Ultra-High-Energy Neutrinos and Their Acoustic Detection in the Sea

Habilitation Thesis

Robert Lahmann
Friedrich-Alexander Universität Erlangen-Nürnberg

August 8, 2011

Contents

Constants and Notation **6**

1 Introduction **7**

2 Ultra-High-Energy Neutrinos:
A Key to the Highest-Energy Universe **10**
2.1 Sources of Ultra High Energy Neutrinos 10
2.1.1 Neutrinos from Acceleration of Hadrons 10
2.1.1.1 Basic Principles 11
2.1.1.2 Active Galactic Nuclei 12
2.1.1.3 Gamma-Ray Bursts 14
2.1.2 Cosmogenic Neutrinos 16
2.1.3 UHE Neutrinos from Non-Accelerator Sources 17
2.1.3.1 *Z*-Burst Neutrinos 17
2.1.3.2 Top-Down Scenarios 18
2.2 Cosmic Rays, the Link to Neutrinos 18
2.2.1 Cosmic Rays Observed on Earth 19
2.2.2 Detection of UHECRs 20
2.2.3 Cosmic Rays Beyond the Ankle 21
2.2.4 Principles of Cosmic Acceleration 23
2.3 Propagation Losses and the “Cosmic Laboratory” 24
2.3.1 Expansion of the Universe and Source Evolution 24
2.3.2 Cosmic Microwave Background 27
2.3.3 Pair Production 28
2.3.4 Photo-Pion Production and the Delta Resonance 28
2.3.5 The GZK Cutoff 30
2.3.6 Combined Propagation Losses for Protons 32
2.3.7 Photo-Disintegration 33
2.4 Production Rate of Cosmic Rays 35
2.4.1 Formalism 35
2.4.2 A Toy Calculation of the Cosmic Ray Energy Production Rate . . . 37
2.4.3 Published Results of the Cosmic Ray Energy Production Rate . . . 38
2.4.4 The Composition of Cosmic Rays 39
2.5 Bounds on Neutrino Production at the Sources of Cosmic Rays 40
2.5.1 Waxman-Bahcall Upper Bound 40
2.5.2 A Discussion of the Waxman-Bahcall Bound 42
2.5.3 Mannheim-Protheroe-Rachen Upper Bound 43

2.5.4 Neutrinos from Cosmic Accelerators of Nuclei 44
2.5.5 Experimental Results from Cherenkov Neutrino Telescopes 45
2.6 Production of Cosmogenic Neutrinos 46
2.6.1 A Calculation for Protons 46
2.6.2 CIB, Cosmic Ray Composition, and Source Evolution 48
2.6.3 Constraints from Diffuse Gamma-Ray Background 50

3 Aspects of Neutrino and Particle Physics 53
3.1 Neutrino Oscillations 53
3.1.1 Oscillations in Vacuum 53
3.1.2 Oscillations over Cosmological Distances 55
3.2 Neutrino Interactions and Cross Sections 56
3.3 Neutrino Propagation through Earth 60
3.4 Energy Deposition in Neutrino Interactions 62
3.4.1 Hadronic Showers 63
3.4.2 Electromagnetic Showers and the LPM Effect 65

4 Acoustic Detection of UHE Neutrinos 68
4.1 Derivation of the Thermo-Acoustic Model 68
4.2 Acoustic Neutrino Signals in Sea Water 71
4.2.1 Generation of Bipolar Signals 71
4.2.2 Attenuation 73
4.2.3 Attenuated Bipolar Pulse 76
4.2.4 The Three-Dimensional Pressure Field 77
4.2.5 Neutrino Signal Properties 78
4.3 The Speed of Sound and Refraction 82
4.4 Neutrino Detection with an Acoustic Detector 85
4.4.1 Event Rates and Effective Volumes 85
4.4.2 Rate Estimate in a Generic Acoustic Neutrino Detector 87
4.4.2.1 Detector Model 87
4.4.2.2 Rate Estimates and Limits 89
4.4.3 Fundamental Design Considerations 91
4.5 Overview of Activities and Target Media 92
4.6 Alternative Detection Methods 96

5 Activities in the Context of the AMADEUS Project 98
5.1 Verification of the Thermo-Acoustic Model 98
5.1.1 Experimental Setup and Beam Characteristics 98
5.1.2 Basic Features of the Measured Signals 100
5.1.3 Simulation of Thermo-Acoustic Signals 101
5.1.4 Comparison of Simulated and Measured Signals 104
5.1.4.1 Proton Beam Experiment 104
5.1.4.2 Laser Beam Experiment 106
5.1.5 Analysis of the Temperature Variation 106
5.1.6 Outcome of the Experiments 108
5.2 The AMADEUS Detector 109
5.2.1 The ANTARES Detector and its Sub-system AMADEUS 109

5.2.2 Acoustic Storeys . . . 111
5.2.3 The Acoustic Sensors . . . 112
5.2.4 Calibration of Acoustic Sensors . . . 115
5.2.5 Off-Shore Electronics . . . 117
5.2.6 The AcouADC Board . . . 118
5.2.6.1 Analogue Signal Processing . . . 120
5.2.6.2 Digital Signal Processing . . . 120
5.2.6.3 AcouADC Board System Characteristics . . . 121
5.2.7 Data Acquisition and Clock System . . . 122
5.2.8 On-Shore Data Processing and System Operation . . . 122
5.2.9 AMADEUS Online Trigger Schemes . . . 123
5.2.10 System Performance . . . 124
5.3 Position Calibration of Acoustic Storeys . . . 125
5.3.1 Position Calibration Using Time Delays . . . 125
5.3.2 Alternative Methods and Effects of Refraction . . . 127
5.4 Acoustic Background in the Deep Sea . . . 130
5.4.1 Ambient Noise and Inherent System Noise . . . 130
5.4.1.1 Spectral Distributions and Correlations with Weather Data 130
5.4.1.2 Daily Variations and Neutrino Detection Threshold . . . 132
5.4.2 Transient Sources . . . 136
5.4.2.1 Source Direction Reconstruction . . . 136
5.4.2.2 Source Position Reconstruction . . . 137
5.4.2.3 Background from Environmental Sources and Interdisciplinary Cooperation . . . 137
5.5 Data Analysis Techniques . . . 137
5.5.1 Source Classification and Identification . . . 138
5.5.1.1 Simulation . . . 138
5.5.1.2 Filtering and Feature Extraction . . . 138
5.5.1.3 Classification . . . 139
5.5.1.4 Results . . . 139
5.5.2 Monte Carlo Simulations . . . 140
5.5.3 Feasibility Study and Neutrino Flux Limit . . . 142

6 Summary and Outlook **144**

A Cosmic Acceleration **148**
A.1 A Generic Model . . . 148
A.2 Fermi Acceleration of Second Order . . . 150
A.3 Shock Acceleration . . . 151

Bibliography **153**

Constants and Notation

Some quantities and constants that are used for numerical calculations throughout this report are listed below. Formulae will be written with the explicit use of the speed of light c and the reduced Planck constant $\hbar$. Mostly, energy units will be based on electron volts, with some notable exceptions where traditionally the cgs unit of erg is used.

Basic notation

Lorentz boost factor	$\gamma = \frac{1}{\sqrt{1-\beta^2}}$ ($\beta =$ velocity relative to c)
year	yr ($\approx \pi \times 10^7$ s)

Prefixes

G (Giga)	factor 10^9
T (Tera)	factor 10^{12}
P (Peta)	factor 10^{15}
E (Exa)	factor 10^{18}
Z (Zeta)	factor 10^{21}

Energy and distance

energy conversion	$1\,\mathrm{TeV} \approx 1.6\,\mathrm{erg}$
light year	$1\,\mathrm{ly} \approx 0.95 \times 10^{16}\,\mathrm{m} \approx 0.31\,\mathrm{pc}$
parsec	$1\mathrm{pc} \approx 3 \times 10^{16}\,\mathrm{m} \approx 3.26\,\mathrm{ly}$

Astrophysical constants (present day values)

Hubble constant	$H_0 = 72(3)\,\mathrm{km\,s^{-1}\,Mpc^{-1}}$
Hubble time	$1/H_0 \approx 14\,\mathrm{Gyr}$
	(close to but not exactly the same as the age of the Universe)
Hubble length	$c/H_0 = 4.228\,\mathrm{Gpc}$
Cosmic Microwave Background temperature	$T_{\mathrm{CMB}} = 2.725\,\mathrm{K}$

Masses

proton (p) mass	$m_p = 938.3\,\mathrm{MeV}\,c^{-2}$
neutron (n) mass	$m_n = 939.6\,\mathrm{MeV}\,c^{-2}$
neutral pion (π^0)mass	$m_{\pi^0} = 135.0\,\mathrm{MeV}\,c^{-2}$
charged pion ($\pi^\pm$) mass	$m_{\pi^\pm} = 139.6\,\mathrm{MeV}\,c^{-2}$
electron (e) mass	$m_e = 0.511,\mathrm{MeV}\,c^{-2}$

Chapter 1

Introduction

Neutrinos, together with high-energy photons (gamma rays) and charged particles (cosmic rays), form the troika of messenger particles that are studied in the field of astroparticle physics. It is commonly accepted that only a multi-messenger approach, combining observations from all three particle types, will deliver a complete picture of the fundamental astrophysical processes taking place throughout the Universe.

The detection of neutrinos with energies of a few tens of MeV [1, 2] from the type II supernova SN1987A in 1987 was the first observation of neutrinos from outside of the Solar System. For the detection of *high-energy* neutrinos, exceeding the energy of supernova neutrinos, a whole new class of detection devices has been conceived and built, the large volume Cherenkov neutrino telescopes. While the energy threshold for "high-energy" neutrinos is not uniquely defined, it is often most convenient to take the detection threshold of Cherenkov neutrino telescopes of several 10 GeV.

High-energy neutrinos detected on Earth are of two different origins: First, atmospheric neutrinos that are mainly produced in the decay of pions and kaons emerging from reactions of cosmic rays or gamma-rays in the upper atmosphere; Second, astrophysical neutrinos that originate from either galactic or extra-galactic astrophysical processes. Candidates for sources of galactic neutrinos are supernova remnants, while Active Galactic Nuclei and Gamma-Ray Bursts are potential extra-galactic neutrino sources. Both the atmospheric neutrino flux and the expected flux from galactic neutrinos roughly follow power laws, resulting in a strongly decreasing flux with increasing energy E. With the spectrum of atmospheric neutrinos being softer, the galactic neutrino flux is predicted to dominate only above a threshold of about $10^{14} \sim 10^{15}$ eV [3]. An upper limit on the flux of extra-galactic neutrinos, the Waxman-Bahcall bound, was derived from the cosmic ray flux observed on Earth. It scales with E^{-2} and becomes dominant over the atmospheric neutrino flux, scaling with about $E^{-3.7}$, at roughly the same energy range.

Existing neutrino telescopes (NT200+ in Lake Baikal [4], ANTARES[1] in the Mediterranean Sea [5] and IceCube [6] at the South Pole) are routinely reconstructing the muon tracks from the interactions of atmospheric muon neutrinos. A "smoking gun" signature of neutrinos from astrophysical sources would either be a reconstructed energy beyond $\sim 10^{14}$ eV for a significant number of events or a clustering of reconstructed neutrinos from a particular direction. Additional evidence can be provided if this direction coincides with that of potential neutrino sources, identified e.g. through detection of gamma-rays by imaging atmospheric

[1] Astronomy with a Neutrino Telescope and Abyss environmental Research

Cherenkov telescopes telescopes (H.E.S.S.[2] [7], MAGIC[3] [8], CANGAROO[4] [9], VERITAS[5] [10]) or by direct observation of the air shower particles (e.g. MILAGRO [11]). No such evidence has yet been found.

One of the central questions of astroparticle physics is the origin of the highest energy cosmic rays observed on Earth, with a spectrum extending to energies in excess of 10^{20} eV. The detection of cosmogenic neutrinos, generated as secondary products in cosmic ray interactions with cosmic background photons, at comparable energies would give important clues about the origin, chemical composition and energy of cosmic rays at their source. Due to propagation effects, a large portion of this information is lost on the way to Earth for the cosmic rays themselves. The energies involved in these processes extend beyond the high-energy region to the *ultra-high-energy* (UHE) domain. Again, "ultra-high energy" is not a clearly defined classification, and different thresholds for cosmic rays, neutrinos and gamma-rays are typically used. Ultra-high-energy cosmic rays (UHECRs) are frequently defined as exceeding 10^{19} eV, since it is commonly accepted that at these energies, they must be of extra-galactic origin. For neutrinos, the threshold is usually set at 10^{18} eV, equivalent to 1 EeV, the order of magnitude of energy a neutrino possesses when created in the reaction of a 10^{19} eV cosmic ray with a low energy photon from the cosmic microwave background (CMB). Gamma-rays, finally, do not reach Earth with energies exceeding the PeV range due to photon-photon interactions at the source and with the CMB during propagation. The term "UHE gamma-ray" is typically used above 100 TeV.

An advantage of the search for neutrinos in the UHE regime is the absence of atmospheric neutrino background. On the other hand, neutrinos at ultra-high energies have very small fluxes, requiring tens of cubic kilometres of target volume to be surveyed for interactions. This makes detection unlikely, even with the next generation of cubic-kilometre sized Cherenkov detectors that are currently in operation (IceCube) or planned (KM3NeT [12, 13]).

Cherenkov detectors require a relatively dense instrumentation, as the spacing between the photomultiplier tubes (PMTs) is determined by the attenuation length of visible light in water or ice of $\mathcal{O}(100\,\mathrm{m})$. Due to this constraint, scaling these devices to even bigger volumes is expensive and technically difficult. New techniques and new detector designs therefore need to be investigated to advance the neutrino branch of astroparticle physics into the ultra-high-energy domain.

The big interest in astrophysical neutrinos in the EeV region is evidenced by the inauguration of the ARENA[6] workshop series in 2005 [14], in which approaches to detect UHE neutrinos are discussed. From a technical point of view, the interest is triggered by the fact that longstanding ideas have finally become technically feasible and because modern detectors, such as the Pierre Auger Observatory [15, 16] or radio telescopes, can extend their research programme and pursue searches for UHE neutrinos with existing hardware.

One of the techniques for a potential future large-scale neutrino telescopes is the acoustic detection which is the main focus of this report. Acoustic neutrino detection utilises the so-called thermo-acoustic effect which implies that a particle shower evolving from a neutrino interaction generates a coherently emitted sound signal with main frequency components between 1 and 50 kHz and a peak emission around 10 kHz. Acoustic detection allows for

[2] High Energy Stereoscopic System

[3] Major Atmospheric Gamma Imaging Cerenkov Telescope

[4] Collaboration of Australia and Nippon for a Gamma Ray Observatory in the Outback

[5] Very Energetic Radiation Imaging Telescope Array System

[6] Acoustic and Radio EeV Neutrino Detection Activities

a wider sensor spacing and potentially simpler sensor design and read-out electronics than the optical Cherenkov technique. The required acoustic sensors are inexpensive and robust devices. Furthermore, underwater arrays of acoustic sensors can be used for other scientific applications besides acoustic detection, such as marine and environmental science.
Given the small fluxes of UHE neutrinos, measurements need to be background free over years. An important task for a novel detection technique such as acoustic detection hence is the study of background intrinsic to the detection method that may produce false neutrino signals. The detection energy threshold of this technique, expected to be of the order of 1 EeV, depends strongly on background conditions and is another subject of study. For these and related investigations, the underwater acoustic array AMADEUS[7] was conceived and build at the Erlangen Centre for Astroparticle Physics (ECAP) and integrated into the ANTARES detector. The description of the AMADEUS device and results obtained since it started operation in December 2007 will be a focus of this report.
This report is organised as follows: In Chapter 2, sources of high-energy neutrinos are discussed. Since the expected fluxes of UHE neutrinos are closely related to the measured fluxes of UHE cosmic rays, the latter are covered in some detail. Further subjects of discussion are energy loss mechanisms of particles propagating over cosmological distances which affect measurements on Earth and have to be taken into account when drawing conclusions about the conditions at the source. The chapter concludes with presenting bounds and estimates for UHE neutrino fluxes expected on Earth, derived from experimental observations of cosmic rays and gamma-rays.
In Chapter 3, aspects of neutrino and particle physics are discussed which are crucial for the detection of neutrinos on Earth. This comprises neutrino oscillations, neutrino interactions and cross sections and the manner in which energy is deposited through hadronic and electromagnetic showers in case of a neutrino interaction.
The subject of acoustic detection of UHE neutrinos is treated in Chapter 4. The theory is introduced and the crucial aspects of the experimental detection are elaborated. Some facets of importance to a potential future acoustic neutrino detector are discussed and expected rates and required volumes are estimated. A short overview of further activities in acoustic detection is given and alternative detection methods are discussed briefly. Neutrino flux limits in the UHE region from some experiments are presented.
Experimental activities in the context of the AMADEUS project are the subject of Chapter 5. This comprises laser and proton beam experiments that were conducted to verify the thermoacoustic effect, a technical description of the AMADEUS device and first results that were obtained with it. In this context, both the ambient background and the background due to transient sources, which could potentially mimic acoustic signals from neutrino interactions, are discussed. The main scientific goal of the AMADEUS device is a feasibility study of a large scale acoustic neutrino detector in the Mediterranean Sea. The current status is summarised and remaining subjects of investigation, in particular a more precise classification of transient sources and Monte Carlo simulations, are discussed. Finally in Chapter 6 the report is summarised and an outlook on the future of the field of acoustic detection is given.
Several parts of Chapters 4 and 5 have been taken (with small adjustments to fit the context) from previous publications of this author: Secs. 4.1 and 5.1 were taken from [17][8], while the remaining sections of Chapter 5 use passages from [18][9], [19], and [20][8].

[7] Antares Modules for Acoustic Detection Under the Sea
[8] This is a publication by the ECAP acoustics group.
[9] The author of the report at hands is the principal author of this publication.

Chapter 2

Ultra-High-Energy Neutrinos: A Key to the Highest-Energy Universe

The first, and so far only, neutrinos detected on Earth that can be clearly assigned to a source outside of the Solar System are neutrinos with energies of a few tens of MeV [1, 2], recorded from the type II supernova SN1987A. However, the observation of cosmic rays on Earth with energies exceeding 10^{20} eV strongly suggest the production of ultra-high-energy (UHE) neutrinos ($E > 10^{18}$ eV). From the observation of UHE neutrinos, conclusions can be drawn about the sources of cosmic rays of highest energies and about the processes that are responsible for the production of these particles. Hence, the search for UHE neutrinos is strongly entwined with the subject of cosmic ray physics. In addition, gamma-rays with energies above the GeV region are expected to be associated with the production of neutrinos, which provide additional clues for the search for UHE neutrinos. Their production and the connection to other messenger particles of astroparticle physics are the subject of this chapter. In Sec. 2.1, an overview of potential sources of UHE neutrinos will be given and the physics processes of their production will be introduced. To allow for qualitative calculations of neutrino fluxes, a deeper understanding of the observation and production of cosmic rays, and of energy-loss mechanisms of particles traversing the Universe is required. These subjects will be addressed in Secs. 2.2 and 2.3, respectively. The calculation of cosmic ray production rates and how their chemical composition at the source is related to observations on Earth will be discussed in Sec. 2.4. With all prerequisites treated, in Sec. 2.5 the neutrino flux associated with cosmic accelerators will be discussed. In Sec. 2.6 finally the cosmogenic neutrino flux, resulting from interactions of cosmic rays with cosmic background photons, will be examined.

2.1 Sources of Ultra High Energy Neutrinos

2.1.1 Neutrinos from Acceleration of Hadrons

Earth is subject to a constant flux of charged particles that ionise the upper parts of the atmosphere. These cosmic rays have experimental signatures of protons or nuclei[1] and their observed energy spectrum extends to energies beyond 10^{20} eV. One possibility to explain

[1] Electrons are not relevant in the context of neutrino production. They do not reach Earth with energies in the TeV region or above and, as will be discussed in Sec. 2.2, are usually not counted as cosmic rays.

this observation is the existence of extremely powerful cosmic accelerators which in the process of accelerating protons or charged nuclei to these remarkable energies should also—according to basic physics principles—generate neutrinos. Potential cosmic accelerators and the connection to neutrino production will be discussed now.

2.1.1.1 Basic Principles

Cosmic rays are presumed to acquire their tremendous kinetic energies through the mechanism of shock acceleration which will be discussed in Sec. 2.2.4. Independent of the details of the acceleration processes, an approximation for the maximum energy $E_{\max}$ of a particle accelerated in a magnetic field can be derived. $E_{\max}$ is determined by the acceleration rate and the time a particle remains in the acceleration process. Hence, for a given size R and magnetic field B of an accelerator, the relation $E_{\max} \sim ZeBR$ for a particle with charge Ze can be derived [21]. An additional factor of γ can be introduced to account for the fact that the observer may not be at rest w.r.t. the accelerator [22]. Following this criterion, the only known sources which presumably are capable of accelerating cosmic rays to energies in excess of 10^{19} GeV are gamma-ray bursts (GRBs) and active galactic nuclei (AGNs). These objects will be discussed below in Secs. 2.1.1.2 and 2.1.1.3.
Only charged particles, i.e. protons, nuclei, and electrons can be accelerated. Photons and neutrinos are secondary particles. Accelerated electrons[2] quickly loose their energy in form of synchrotron radiation. The radiated photons can create new electrons through pair production or their energy can be increased by inverse Compton scattering. The protons interact with photon fields or with protons of the ambient plasma to produce pions according to the reaction

$$p + p/\gamma \rightarrow m\,\pi + X \quad , \tag{2.1}$$

where $m \geq 1$ is the total number of charged and neutral pions created. X denotes further final state particles, most notably protons and neutrons, which are allowed for by kinematics and conservation laws. The produced pions (Eq. 2.1) decay according to

$$\begin{aligned} \pi^+ &\rightarrow \mu^+ + \nu_\mu & (2.2)\\ &\hookrightarrow \mathrm{e}^+ + \nu_\mathrm{e} + \overline{\nu}_\mu & (2.3)\\ \pi^0 &\rightarrow \gamma + \gamma, & (2.4) \end{aligned}$$

where the decay of the π^- is obtained from charge conjugation of Eq. 2.2. The production of charged pions hence leads to the production of neutrinos[3] with a partition of the three generations according to of $N_{\nu_\mathrm{e}} : N_{\nu_\mu} : N_{\nu_\tau} = 1 : 2 : 0$.
In order to gain insights into the processes taking place in the accelerators, flux measurements of cosmic rays, gamma-rays and neutrinos must be combined. Both neutrinos and photons have the advantage over cosmic rays of pointing back to the source since they are not deflected by magnetic fields. Neutrinos furthermore are not affected by reactions with cosmic background photons when propagating from these source towards Earth. High energy photons in contrast loose energy over cosmological distances through the process of pair production on cosmic background photons above the threshold $E_\gamma E_{\mathrm{bkgr}} > m_e^2 c^4$, where E_γ and E_{bkgr} are the energy of the high-energy and background photon, respectively. Hence, interactions with the CMB with a mean energy of $E_{\mathrm{bkgr}} \approx 0.6\,\mathrm{meV}$ (see Sec. 2.3.2) start to

[2]Unless explicitly noted, it will not be distinguished between electrons and positrons.
[3]Unless explicitly noted, it will not be distinguished between neutrinos and anti-neutrinos.

restricts the range of photons for $E_\gamma \gtrsim 100\,\text{TeV}$ and gamma-rays with $E_\gamma \approx 1\,\text{PeV}$ (1 EeV) cannot reach Earth from sources with distances exceeding $\sim$10 kpc (100 kpc) [23].
In conclusion, at ultra-high energies, neutrinos are the only particles which carry information about the processes taking place at the accelerators over cosmological distances directly from the source to Earth, their energy only affected by redshift in an expanding Universe.

2.1.1.2 Active Galactic Nuclei

Active Galactic Nuclei (AGNs) are among the most powerful known cosmological objects, their luminosity appearing to exceed that of a typical galaxy by a factor of up to 10^4 [24]. This observation makes AGNs prime candidates for accelerators of the most energetic cosmic rays.
The unified AGN model [25] is depicted in Fig.2.1(a). It is assumed that a supermassive black hole of $10^6 - 10^{10}$ solar masses is located at the centre of a host galaxy, implying that AGNs are cosmological sources. The host galaxy provides the material for an accretion disk, which is formed in the plane perpendicular to the rotational axis of the black hole. The accretion disk powers the energy emission of the AGN in highly collimated relativistic jets along the rotational axis of the black hole. These jets extend outward for tens of kpc, and in some cases, as much as a Mpc. They offer very favourable conditions for the production of high-energy particles, namely a frozen-in magnetic field and a fully ionised plasma of low density [26]. Outside the jets, winds of high and low velocity gas are forming, referred to as broad line and narrow line region in Fig. 2.1(a), according to their emission line type. An obscuring torus (or other geometrical form) of gas and dust around the accretion disk is hiding the broad line region from some directions.

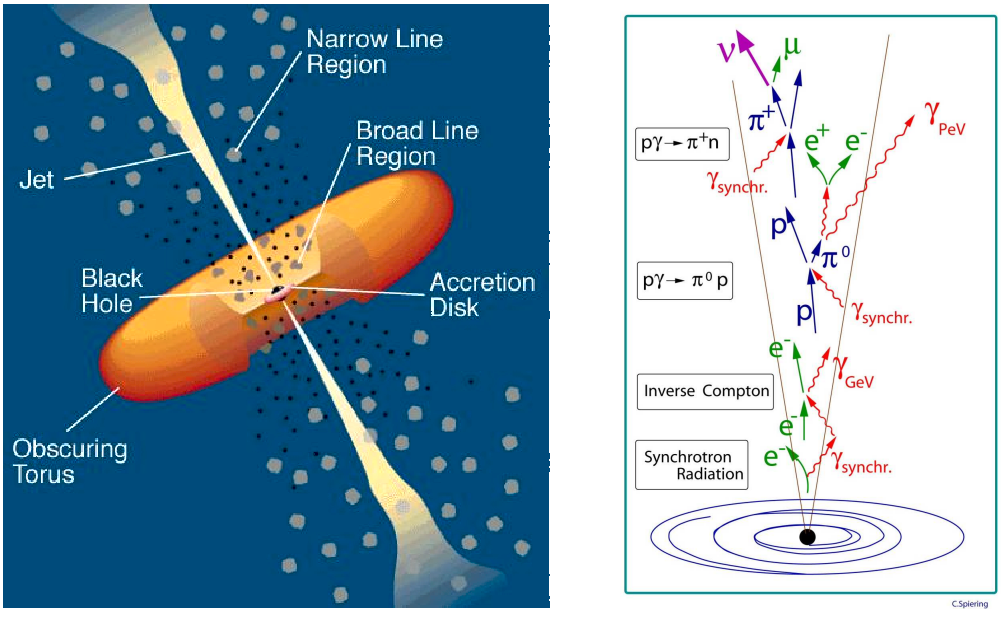

(a) (b)

Figure 2.1: (a) Sketch of an AGN according to the unified AGN model (see text), adapted from [27]; (b) Schematic depiction of particle production by accelerated particles within the magnetic field of the jets of an AGN [28].

Depending on the orientation of the jets w.r.t. Earth and the nuclear matter within the host

galaxy, AGNs appear as rather different objects to an observer. For a subgroup of AGNs called *blazars*, the jet points towards Earth showing flares of luminosity ranging in duration from a fraction of a day to years [22]. Given this directivity, a neutrino flux associated with the production of cosmic rays should be observable on Earth. Different blazar models exist, which have the basic dynamics in common [22]: Relativistic jets are generated with substructures that take the form of "blobs" of matter travelling along the jet with Lorentz factors of 10–100. The photon energy spectrum of blazars observed on Earth is dominated by non-thermal emission and shows two distinct, broad components: A low-energy component from radio through UV or X-rays, and a high-energy component from X-rays to gamma-rays with energies extending to the TeV region, see e.g. [29]. The low energy component is explained by synchrotron radiation of accelerated electrons and the component in the gamma-ray region as the result of either inverse Compton scattering off accelerated electrons (leptonic model) or electromagnetic cascades triggered by the decay of π^0's from proton interactions according to Eq. 2.4 (hadronic model). In the hadronic model, high-energy neutrinos are produced via the decay of charged pions. These processes are summarised in Fig. 2.1(b).
If AGNs are accelerating hadrons and constitute sources of cosmic rays then the observation of a corresponding neutrino flux would be a clear indication of these processes. A recent calculation [30] of the expected neutrino flux from a cosmological distribution of AGNs is shown in Fig. 2.2. Such calculations involve several model assumptions, starting with the acceleration processes at the source. In Fig. 2.2, both the acceleration of protons and iron nuclei at the source and neutrino production from pion decay (Eqs. 2.2 and 2.3) and from the β-decay of neutrons (produced as final state particles according to Eq. 2.1) are considered. The process of disintegration of heavy nuclei into lighter ones and nucleons (see Sec. 2.3.7) reduces the flux of neutrinos from pion decay whereas it enhances that of neutrinos from neutron decay.
The neutrino production rate associated with a given acceleration process depends among other parameters on the density of the target material for the accelerated charged particles. Calculations of the resulting neutrino flux on Earth must furthermore take into account the cosmological evolution of sources and propagation effects over cosmological distances (see Sec. 2.3).
Both the gamma-ray and cosmic ray spectrum measured on Earth can be used as normalisation to calculate the expected neutrino flux since any model will in general predict the neutrino flux relative to the cosmic ray and/or gamma-ray flux. Cosmic rays are usually the better choice because the acceleration of charged particles in a plasma or photon field inevitably leads to the production of neutrinos whereas gamma-rays are also produced in purely leptonic models. Furthermore, the highest measured cosmic ray energies are much closer to the energies of UHE neutrinos than those of gamma-rays. Typically, as was done for Fig. 2.2, calculations are performed for a diffuse flux based on a cosmological distribution of sources. Given the low fluxes of cosmic rays (and gamma-rays) at ultra-high energies, normalisation to individual sources would involve large uncertainties.
Not only the neutrino production rate itself but also its normalisation are affected by the composition of cosmic rays. The composition can neither be easily measured on Earth, nor is the deduced composition at the source unanimous for a given composition determined on Earth.
This discussion has demonstrated some of the challenges in calculating the expected fluxes of neutrinos at ultra-high energies on Earth. The details and several explicit calculations will be treated in the remaining sections of this chapter.

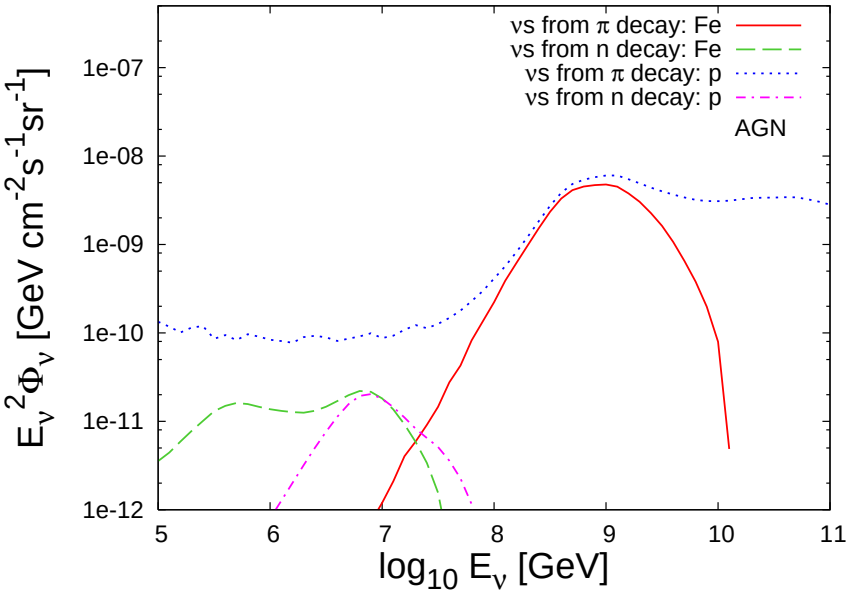

Figure 2.2: Neutrino spectrum produced by protons and iron nuclei accelerated in AGNs. Normalisation has been done assuming a cosmological distribution of sources and an isotropic flux of UHE cosmic rays on Earth that consist exclusively of protons; iron nuclei are disintegrated at the source or on the way to Earth. Figure from [30].

2.1.1.3 Gamma-Ray Bursts

Gamma-ray bursts (GRBs) are flashes of high-energy radiation with timescales ranging from $30\,\mathrm{ms}$ to several minutes [30]. During that short timespan, GRBs are among the most violent events in the Universe. Typically, long-duration ($\gtrsim 2\,\mathrm{s}$) and short-duration GRBs ($\lesssim 2\,\mathrm{s}$) are distinguished [31], where the former are thought to originate from the collapse of a massive star into a black hole [32], while the latter are believed to result from the merger of two compact objects, such as neutron stars, into a black hole [33]. As the engine is thought to be a black hole in both cases, typically the same models are applied to describe them. The energy released in gamma-rays is typically 10^{51} to $10^{54}\,\mathrm{erg}$ for long-duration GRBs, assuming isotropic emission, and about 1% of that for short-duration GRBs [31]. For beamed emission within a solid angle Ω, the energy release must be scaled by a factor $\Omega/(4\pi)$. The emission of the gamma-rays is succeeded by an afterglow of less energetic radiation in the X-ray, optical, and radio bands.

Charged particles are accelerated and neutrinos produced from the decay of charged pions according to the same principles described above for AGNs. Differences arise e.g. from the sizes of the magnetic fields that are employed, from the matter and photon densities and from the size of the Lorentz boost.

Given the short time scales observed in the variability of their light curves, sources of GRBs must be very compact objects with a linear scale of the order of $\sim 10^7\,\mathrm{cm}$ [34]. From dimensional analysis, it follows that in order to obtain energies of $\sim 10^{19}\,\mathrm{eV}$ within these dimensions, the involved magnetic fields must be of the order of $10^{12}\,\mathrm{G}$ [22]. GRBs are assumed to be of cosmological origin, as can be deduced from their apparent isotropic distribution and from redshift determinations of the afterglow or their host galaxies.

Independent of the event that triggers the GRB, a phenomenological description is given by the fireball model (see e.g. [36] for a review) that is shown schematically in Fig. 2.3. In this

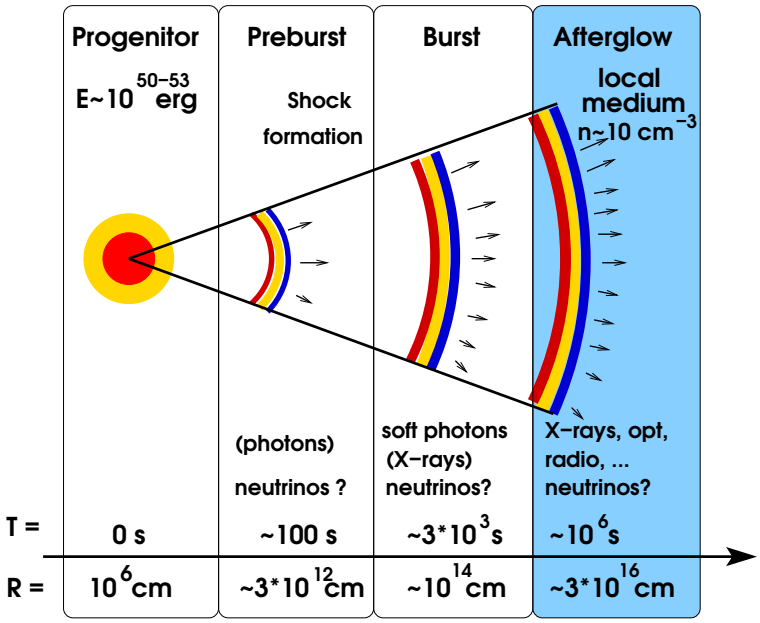

Figure 2.3: Schematic depiction of the fireball model. The fireball is optically thick during the preburst phase, while the characteristic gamma-rays are emitted during the burst phase. Neutrinos with energies exceeding $\mathcal{O}(10^{14}\,\mathrm{eV})$ are believed to be produced during the burst (prompt neutrinos) and afterglow phase. From [35].

model, a "fireball" of $e^{\pm}$ and photons with an optical depth[4] of the order of $\sim 10^{15}$, is ejected, trapping photons within the fireball. A small "load" of baryons (protons or nuclei) is also present. The radiation power results in the highly relativistic expansion of the fireball [22]. The expansion will continue with decreasing velocity until the fireball becomes transparent and the radiation is released. By this time, the expansion velocity has reached highly relativistic values of $\gamma \approx 300$. Charged particles are subject to further acceleration through shocks. Internal shocks can be caused by a succession of plasma ejections at a variable rate where later outflows overtake earlier ones (see [37] and references therein for details) while external shocks will be inevitably created when the fireball extends into the surrounding medium. Electrons accelerated in the internal shocks dissipate their energy via synchrotron or inverse Compton radiation, resulting in the gamma-ray spectrum observed on Earth.
The gamma-rays in the keV–MeV energy region provide the target for protons or nuclei accelerated in GRBs to produce prompt neutrinos in the range of about $10^5 - 10^7$ GeV, see [31] and references therein. While astronomical observations provide information on the gamma-rays, the proton flux is a matter of speculation [22]. For individual GRBs, proton spectra can be deduced by deriving the electron spectrum from the observed photon spectrum and assuming that protons have been subject to the same acceleration process [31]. A definite diffuse neutrino flux can be predicted, in the same fashion as described for AGNs, when assuming that GRBs produce the highest energy cosmic rays observed on Earth. A recent result is shown in Fig. 2.4.
It has been proposed [38] that protons can be accelerated in GRBs to energies above 10^{20} eV resulting in the production of neutrinos in reactions with photons of the afterglow [39]. The

[4]The optical depth τ is the argument of an exponential decay law for the radiation intensity over a given length scale.

energy of these neutrinos would be much higher than that of the prompt neutrinos, roughly one order of magnitude less then the energy of the protons.

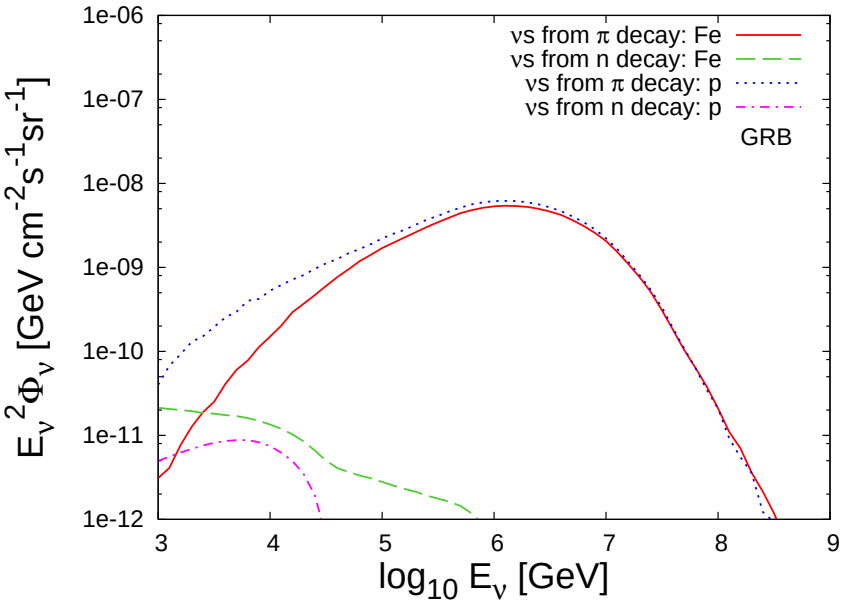

Figure 2.4: Spectrum of prompt neutrinos produced by protons and iron nuclei accelerated in GRBs. Normalisation has been done in the same fashion as described for Fig. 2.2. From [30].

2.1.2 Cosmogenic Neutrinos

Protons ejected from cosmic accelerators have to traverse cosmological distances to reach Earth. As will be discussed in more detail in Secs. 2.3.5 and 2.6, above an energy threshold of about 10^{20} eV photo-pion production (i.e. the production of pions in the reaction of nucleons with photons) with the CMB leads to the production of cosmogenic neutrinos [40]. The corresponding suppression of the cosmic ray flux has been termed *GZK cutoff* (after K. Greisen, G.T. Zatsepin and V.A. Kuz'min), and the experimental verification of its existence is an important task of UHECR physics. Experimental evidence for the cutoff will be discussed in Sec. 2.2.3. The flux of cosmogenic neutrinos has been termed "guaranteed flux" since for a cosmological distribution of proton sources with an energy spectrum exceeding the threshold energy for photo-pion production, neutrinos *must* be produced according to basic and well understood physics principles. However, the calculation of the flux depends strongly on several parameters, most notably the chemical composition of the cosmic rays, their ejection spectrum and energy cutoff and the redshift evolution (see Sec. 2.3.1) of the sources. For some combinations of parameters, which are consistent with cosmic ray observations on Earth, no measurable flux above a neutrino energy of 10^{18} eV is predicted. Nonetheless, even the non-observation of cosmogenic neutrinos in combination with cosmic ray measurements at highest energies would allow for constraining the aforementioned parameters.

If cosmic rays are heavy nuclei, the dominant process of energy loss on the CMB will be photo-disintegration (see Sec. 2.3.7), as opposed to photo-pion production (see Sec. 2.3.4), with strong implications for the neutrino spectrum. Hence, spectra of cosmogenic neutrinos

may reveal information about the cosmic ray composition at the source while the cosmic rays themselves will have lost most of this information when arriving on Earth.
Cosmogenic neutrinos can be considered the prime motivation for UHE neutrino detection. After discussing the parameters that affect their expected flux in more detail, the subject of cosmogenic neutrinos will be revisited in Sec. 2.6 with a more quantitative treatment.

2.1.3 UHE Neutrinos from Non-Accelerator Sources

Alternatively to cosmic accelerators, some theories explain UHECRs as decay products of heavy remnants from the early Universe, see [22] and references therein. These theories usually also predict a flux of UHE neutrinos, which can be used to confirm or disprove a theory, or to constrain its parameter space. Before discussing these so-called top-down models, the Z-burst scenario will be introduced, in which cosmic rays are explained as the result of the decay of Z-bosons, created in the annihilation of neutrino/anti-neutrino pairs.

2.1.3.1 *Z*-Burst Neutrinos

About 1 s after the Big Bang, neutrinos are believed to have decoupled from the rest of matter, see e.g. [41]. These relic neutrinos today constitute the Cosmic Neutrino Background which should show a redshifted blackbody spectrum with a temperature of about $\sim 1.9\,\mathrm{K}$. Unlike the CMB, the Cosmic Neutrino Background has not been experimentally confirmed yet. In the Z-burst scenario, see [42, 43] and references therein, a flux of UHE primary neutrinos interacts with this relic neutrino background. The Z-bosons produced this way decay into quark or lepton pairs, where the branching ratio of the partial to total decay width is about 0.7, 0.1, and 0.2 for hadronic, charged leptonic and invisible (i.e. neutrino) final states, respectively. Standard particle physics predicts that at ultra-high energies, the quarks fragment predominantly into pions and kaons and a relatively small number of protons, see [44] and references therein. The mesons decay further, producing eventually photons, neutrinos and electrons. In addition, the leptonic decay of the Z-boson either yields neutrino/anti-neutrino pairs directly or through the decay of the unstable charged leptons. In total, models that explain the production of cosmic rays by QCD jets, i.e. the Z-burst model and the top-down scenarios discussed below, produce a relatively large number of photons and neutrinos when normalised to the observed cosmic ray spectrum [44], which allows for experimental examination. A cosmic ray composition of heavy nuclei seems difficult to explain in these models.
The energy requirement for the UHE neutrinos at the resonance is $E_\nu^{\mathrm{UHE}} \approx M_Z^2/(2m_\nu^{\mathrm{rel}})$, where m_ν^{rel} is the mass of the relic neutrinos. From cosmological data and neutrino oscillation data, the mass of each of the three neutrino flavours is constrained to $m_\nu \lesssim 0.33\,\mathrm{eV}$, see [45] and references therein. Hence the corresponding energy of the UHE neutrinos is $E_\nu^{\mathrm{UHE}} \gtrsim 10^{22}\,\mathrm{eV}$.
It is problematic to conceive sources of these UHE neutrinos, since they must be produced basically without production of gamma-rays in order to avoid overproduction of the diffuse GeV gamma-ray background. In fact no astrophysical sources are known that meet the requirements of Z-burst models, see [45] and references therein. Even if the sources of the UHE neutrinos are left open, the resulting production of neutrinos associated with the observed cosmic ray flux is difficult to reconcile with existing limits: The upper limit on the

neutrino flux from the GLUE[5] experiment [46] is about a factor of two below the expected peak neutrino flux [47]. The latest results from the ANITA[6] experiment [48] exacerbates the disagreement to more than an order of magnitude. For smaller neutrino masses, the inconsistency increases. The experiments GLUE and ANITA will be discussed in Sec. 4.6.

2.1.3.2 Top-Down Scenarios

So-called top-down scenarios avoid the theoretical problems of accelerating particles to UHE energies by postulating super-heavy particles. These particles, usually denoted X-particles, could at the same time provide a solution for the dark matter problem. The X-particles could be meta-stable relics of the early Universe with lifetimes of the order the current age of the Universe or could be released from topological defects that were produced in the early Universe during symmetry-breaking phase transitions predicted by in Grand Unified Theories (GUTs) [45]. See [22, 44, 49] and references therein for further discussion. Protons, photons and neutrinos are produced in QCD jets or leptonic branches of the X-decay or in the annihilation of an X and anti-X in a similar fashion as described above for the Z-burst scenario.
To explain the observed cosmic ray spectrum, X-particles with masses $M_X \gtrsim 10^{21}\,\mathrm{eV}$ are required [44]. In order for the X-particle to qualify as a super heavy dark matter (SHDM) particle, the observed cosmological density of dark matter determines its mass as $M_X \approx 10^{22-23}\,\mathrm{eV}$ [50].
Top-down models received stimulation by results of the AGASA[7] detector [51] air shower experiment, which measured an excess of UHECRs beyond 10^{20} eV [52] in contrast to the expected GZK cutoff due to reactions of cosmic rays with the CMB. The AGASA experiment will be introduced in Sec. 2.2.2. More recent results with higher statistics however are consistent with the existence of the cutoff, see Sec. 2.2.3. While the search for signatures of top-down models still has strong theoretical motivation, recent experimental results limit their contribution to the UHECR flux to a subdominant level [53].

2.2 Cosmic Rays, the Link to Neutrinos

The definition of cosmic rays is not unambiguous in the literature. Charged nuclei (which includes protons) are always counted as cosmic rays, whereas the inclusion of electrons, gamma-rays and sometimes neutrinos is not treated consistently. In this report, cosmic rays will be defined as consisting of charged nuclei following [54]. Requiring that these charged nuclei originate *outside* the solar system [55] is implicit for UHECRs, since the energy of particles of the solar wind is only of the order of MeV.
Cosmic rays as they are produced at the source are called *primordial cosmic rays* [56]. Cosmic rays arriving on Earth before interacting with the atmosphere are *primary cosmic rays*.
In this section, an introduction of cosmic rays, as observed on Earth, will be given and the mechanism of shock acceleration, which is commonly believed to be the mechanism for the acceleration of cosmic rays, will be briefly described.

[5] Goldstone Lunar Ultra-High Energy Neutrino
[6] Antarctic Impulsive Transient Antenna
[7] Akeno Giant Air Shower Array

2.2.1 Cosmic Rays Observed on Earth

The spectral flux of cosmic rays on Earth in the range from 10^8 eV to the highest measured energies exceeding 10^{20} eV is shown in Figure 2.5. For $E \gtrsim 10^{10}$ eV, the distribution is characterised by a broken power law, $E^{-\alpha}$, where the alteration of the spectral index α with energy shows two characteristic features: The steepening of the spectrum at $\log(E/\mathrm{eV}) \approx 15.5$ is referred to as the "knee" while the following flattening at $\log(E/\mathrm{eV}) \approx 18.6$ is referred to as the "ankle" or (depending on the model to explain the feature) as the "dip". The corresponding values of the spectral index are

$$\alpha \approx \begin{cases} 2.7 & \log(E/\mathrm{eV}) < 15.5 \quad \text{e.g. [23]} \\ 3.3 & 15.5 < \log(E/\mathrm{eV}) < 18.6 \quad [57] \\ 2.6 & \log(E/\mathrm{eV}) > 18.6 \quad [57] \end{cases} .$$

Possibly a second knee at $\log(E/\mathrm{eV}) \approx 17.6$ is present in the spectrum, see e.g. [58] and references therein.

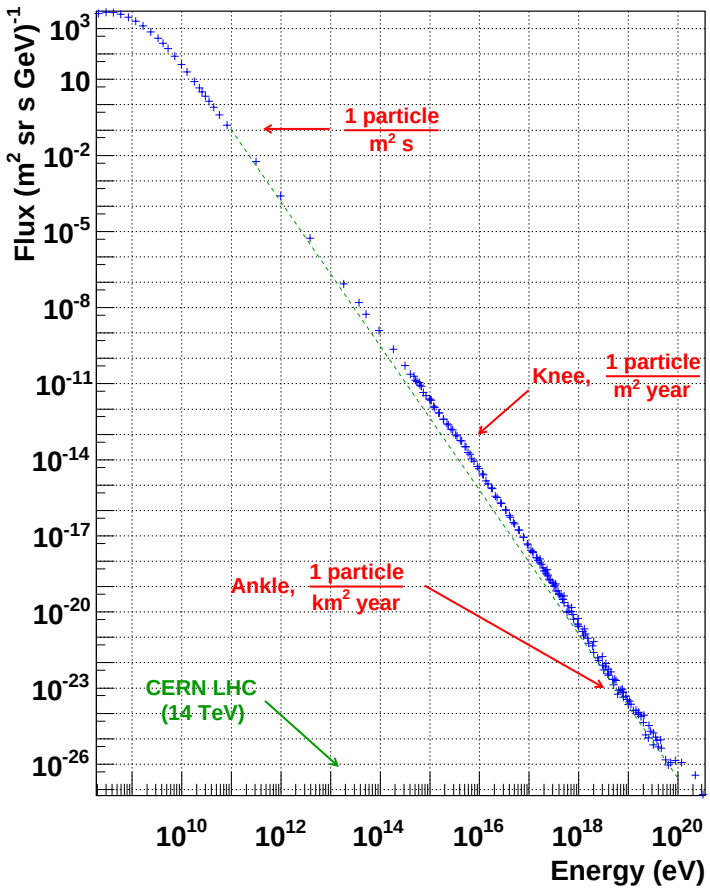

Figure 2.5: Spectral Flux of Cosmic Rays observed on Earth. For the Large Hadron Collider (LHC) the centre of mass energy is shown; in the rest frame of one of the colliding protons, the energy of the other proton is $E \approx 10^{17}\,\mathrm{eV}$. Figure adapted from [59].

While it is generally agreed upon that the transition between galactic and extra-galactic origin of cosmic rays occurs between the knee and the ankle, the origin of these features is

subject to discussion, see e.g. [23, 54] for recent reviews. One popular explanation for the change in the spectral index at the knee is the energy cutoff of particle acceleration in galactic supernovae remnants (SNRs); the cutoff energy is proportional to the atomic number Z of a particle and hence the composition from the knee to the ankle would change from light nuclei (i.e. protons) to increasingly heavy nuclei. Another possible explanation for the knee is a "leaky box model": As particles become more and more energetic, they are more likely to escape the magnetic field of our Galaxy to evade detection on Earth, resulting in a steepening of the energy spectrum. This model would also lead to an increased composition of heavier elements when moving to higher energies from the knee, since the Larmor radius scales with $1/Z$, see Eq. 2.5. Data seem to favour a combination of both explanations [54]. The KASCADE[8] collaboration has measured the flux of cosmic rays with primary energies from 100 TeV to 100 PeV by detecting air showers with an array of ground based detector stations. Using the hadronic interaction models QGSJet [60] and SIBYLL [61], energy spectra for elemental groups representing the chemical composition of primary cosmic rays were derived [62]. For both models the positions of the knee in these spectra are shifted towards higher energy with increasing element number, showing that the knee in the all particle spectrum is due to a steepening of the spectra of light elements. However, neither of the two interaction models describes the measured data consistently over the whole energy range, leaving open questions for the KASCADE-Grande experiment which will measure cosmic rays with primary energies up to 1 EeV [63].
"Ankle" and "dip" refer to the same feature in the cosmic ray spectrum, but the different expressions are usually associated with different models for its cause. In the "ankle model", the feature is the result of the transition between galactic and extra-galactic cosmic rays, see e.g. [54]. In the "dip model", see [64] and references therein, it is due to pair production of protons with the CMB, see Sec. 2.3.3.
The composition of cosmic rays is given in [56] as 85% protons, 12% α-particles and only about 3% of particles with nuclear charge of 3 or higher. Measurements of composition summarised in [65] do not extend to energies beyond 10^6 GeV per nucleus. At higher energies, direct measurements of cosmic rays become impossible due to the steep decrease of the flux and the showering of the cosmic rays in the atmosphere, as will be discussed below. In particular for cosmic rays beyond the ankle, where cosmic rays are assumed to be of extra-galactic origin as will be shown below, the composition is of great interest and subject of contemporary research. The interpretation of the ankle or dip in the cosmic ray spectrum for different chemical compositions of extra-galactic cosmic rays is discussed in [66, 67].

2.2.2 Detection of UHECRs

Primary cosmic rays can be detected with satellite or balloon-borne experiments, before the particles interact in the upper part of the atmosphere. Only relatively high particle fluxes can be measured with these devices as the interaction rate is limited by the fact that only a small detection area can be realised with the available payload. The small flux of about one particle per year and square kilometre for cosmic rays with energies above the "ankle" makes the direct detection of primary cosmic rays impossible. To observe cosmic rays at these energies, Earth's atmosphere is used as detection medium and huge surface detectors are installed on Earth to detect the air showers produced by the interactions of primary particles in the upper

[8] KArlsruhe Shower Core and Array DEtector

parts of the atmosphere. Typically, the air shower of a 10^{19} eV primary cosmic ray consists of roughly 10^{10} particles [68]. In these showers, the primary particle has "disappeared" and a substantial part of the experimental effort of ground based shower detection experiments is the reconstruction of the primary particle type.
For the detection of air showers, surface detector arrays and air fluorescence detectors are traditionally used. The former consist of arrays of particle detectors on the Earth's surface that sample the particles of the air shower reaching the ground. Fluorescence light is emitted by nitrogen molecules in the air that were excited by charged particles of the air shower. Fluorescence detectors observe the longitudinal profile of cosmic ray showers on clear moonless nights. Some detectors, whose results will be referred to in this report, will now be briefly described.
The AGASA in Japan is a pure surface detector array and has been operated since 1990. In its final configuration, the array consists of 111 scintillation detectors of $2.2\mathrm{m}^2$ area each, which are arranged with $1\,\mathrm{km}$ spacing over an area of $100\mathrm{km}^2$.
The HiRes[9] experiment [69, 70] is a pure air fluorescence detector and operated between 1997 and 2003 on the Dugway Proving Grounds in Utah (USA). After the completion of a second site in 1999, the experiment consisted of two sites (HiRes I and II) with a distance of 12.6 km.
The Pierre Auger Observatory [15, 16] located outside the town of Malargüe, in the Province of Mendoza, Argentina, has started a new era in the investigation of Ultra High Energy Cosmic Rays. It is a hybrid detector combining a surface detector array with an air fluorescence detector, providing measurements of the cosmic ray flux for energies beyond the ankle with unprecedented statistics. The surface detector array consists of about 1600 stations covering an area of 3000 km^2 detecting the secondary particles of an air shower by means of the Cherenkov radiation they produce in the water of the detection stations. The ground array is overlooked by 24 air fluorescence telescopes, grouped in four enclosures each consisting of six optical telescopes. Taking data stably since January 2004 while the construction was proceeding, the construction was completed in mid 2008.

2.2.3 Cosmic Rays Beyond the Ankle

Figure 2.6 shows the cosmic ray flux for the region of the ankle and beyond as measured with the Pierre Auger Observatory [57]. Above about $\log(E/\mathrm{eV}) = 19.5$, a flux suppression is detected with high statistical significance. This result is in agreement with measurements of the HiRes experiment [71] shown in the same figure. The suppression is consistent with the GZK cutoff (see Sec. 2.3.5) which limits the distance from which protons with energies above the threshold for photo-pion production with photons of the CMB can reach Earth. This "GZK horizon" is equivalent to a distance of about $100 \sim 200\,\mathrm{Mpc}$. The GZK cutoff is a feature of the cosmic ray spectrum for a cosmological distribution of cosmic ray sources; however, it is also possible that cosmic rays originate predominantly from near-by sources, within the GZK horizon, and the suppression could stem from an energy cutoff of the cosmic accelerators.
Cosmic rays reaching Earth are deflected by the galactic magnetic field with the characteristic Larmor radius r_L,

$$r_L = \frac{p}{Z \cdot e \cdot B} \quad , \tag{2.5}$$

[9] High Resolution Fly's Eye

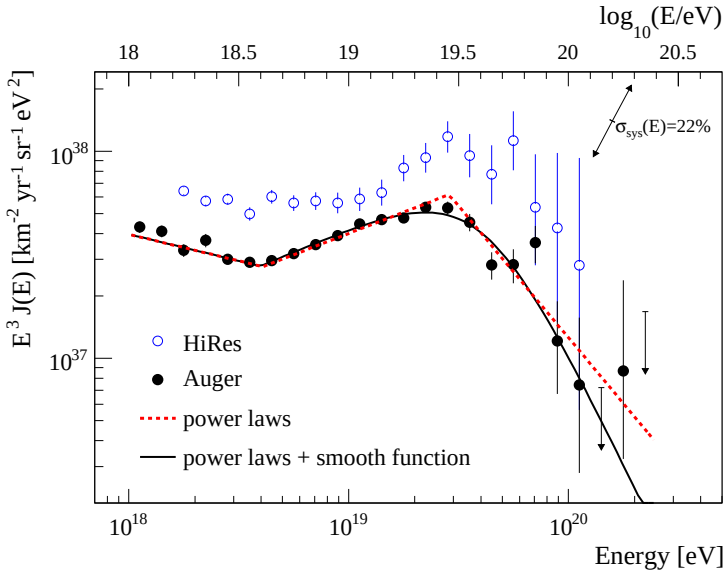

Figure 2.6: The combined energy spectrum measured with the surface and fluorescence detectors of the Pierre Auger Observatory is fitted with two functions as described in [57] and compared to data from the HiRes detector [71]. The systematic uncertainty of the flux scaled by E^3 due to the uncertainty of the energy scale of 22% is indicated by arrows. The Pierre Auger Observatory and HiRes detector will be discussed in Sec. 2.2.2. From [57].

where $p = E/c$ and Z are the momentum and the atomic number of the particle, e is the positive elementary charge and B the galactic magnetic field. Once the Larmor radius exceeds the radius of our galaxy, cosmic rays of galactic origin cannot be magnetically contained. For cosmic rays of galactic origin with sufficiently high energy this would lead to the observation of arrival directions predominantly from within the galactic disc. Equating the Larmor radius from Eq. 2.5 with the radius of the Galactic disc $r \approx 15\,\mathrm{kpc}$, the resulting maximum energy of a particle that can be contained is

$$\frac{E}{[\mathrm{eV}]} \approx 1.4 \times 10^{16} \cdot Z \cdot \frac{B}{[\mu\mathrm{G}]} \quad ,$$

which for $B \approx 3\,\mu\mathrm{G}$ [54] and $Z = 26$ for iron yields $E \approx 1.1 \times 10^{18}\,\mathrm{eV}$, which is below the position of the ankle[10]. AGASA provided clear evidence for the existence of a galactic component of the cosmic ray up to the energy of $10^{18}\,\mathrm{eV}$ by observing an anisotropy of the cosmic rays in the energy range $10^{17} - 10^{18}\,\mathrm{eV}$ with an excess of showers near the directions of the Galactic Centre and the Cygnus region [72]. Furthermore for events above $10^{19}\,\mathrm{eV}$ no significant large-scale anisotropy was found on the celestial sphere, indicating a extra-galactic origin of cosmic rays beyond the ankle [73]. Further measurements of the anisotropy of the arrival directions of cosmic rays are discussed e.g. in [54]. The Pierre Auger Collaboration has investigated the correlation of the highest energy cosmic rays with nearby extra-galactic matter, see [74] and references therein for earlier measurements. For cosmic ray energies above $6 \times 10^{19}\,\mathrm{eV}$, i.e. above the GZK cutoff, the arrival directions are consistent with an anisotropic distribution, with cosmic rays originating predominantly from

[10] No attempt is made here to derive a transition energy between galactic and extra-galactic components of the cosmic rays. The statement is that beyond the ankle, cosmic rays should be of extra-galactic origin; for this reason, $Z = 26$ was chosen as it maximises the cutoff energy.

directions where AGNs within $75\,\mathrm{Mpc}$ are located. This is consistent with the assumption that UHECRs originate indeed from a cosmological distribution of sources.
To conclude, both theoretical and experimental evidence imply that cosmic rays with energies above the ankle are of extra-galactic origin. In order to perform calculations of the emission rate of cosmic rays at the sources, which are required to deduce the associated neutrino production rate, further assumptions are necessary. Typically, it is assumed that the sources have a uniform, i.e. isotropic, cosmological distribution. This is consistent with experimental measurements but at the same time alternative models are not excluded. The production rate of cosmic rays will be discussed in more detail in Sec. 2.4.

2.2.4 Principles of Cosmic Acceleration

The cosmic ray spectrum as shown in Fig. 2.5, imposes the question of the acceleration processes that afford the observed ultra-high energies and the characteristic power law spectrum. A first serious attempt to explain the cosmic ray spectrum was done by Fermi [75] where interactions of charged particles with magnetic clouds were assumed. While resulting in the observed power law spectrum, the theory leads to several problems [76], some of which were already addressed in the original paper. One of these problems is the fact that the interactions considered are of second order in u/c, where u is the velocity of interstellar clouds. Given velocities of interstellar clouds in the Galaxy of $u/c < 10^{-4}$ and a mean free path of the order of $1\,\mathrm{pc}$ [77], this makes the process very slow. To overcome this problem, the mechanism of shock acceleration was devised. A brief discussion is following now while more details are given in Appendix A.
Non-relativistic shock acceleration is thought to take place in SNRs and to be responsible for cosmic rays observed below the knee [23]. In Sec. 2.1.1 relativistic shocks were already introduced as acceleration mechanism in AGNs and GRBs. Qualitatively, in all these cases the standard explanation assumes that a shock front is moving through a plasma, with relativistic particles moving back and forth across the shock front with hardly noticing it at all. The downstream plasma behind the shock front is moving with a lower velocity than that of the shock front itself towards the upstream plasma. The relativistic particles assume an isotropic distribution in the reference frame of the respective plasma they are in, obtaining an energy boost each time they cross the shock front, irrespective of the direction. The energy gain per boost is of first order in u/c and is referred to as first order Fermi acceleration [77]. The appeal of shock acceleration is that it generates a power law spectrum and that in many astrophysical objects, shock fronts are presumed to be moving through regions filled with plasma. However, no theory of shock acceleration, based on basic principles, exists [78]. Furthermore, it is pointed out in [79] that the accelerated particles must generate the magnetic field structure on which they may scatter in order to even reach "moderate" energies around the knee. Hence the "standard explanation" as given in Appendix A must be assumed to simplify the actual processes taking place.
For the source spectra of particles accelerated in shocks, in particular for neutrinos[11], where no flux has been measured yet, frequently a spectral index of 2 is assumed. As will be shown in Appendix A, this value can be derived from kinetic theory by assuming that a portion of the accelerated particles will be "swept away to infinity" by the plasma behind the shock front, never crossing the shock front back into the upstream plasma. This is of course a very

[11] Obviously neutrinos are not accelerated themselves but are produced in the reactions of accelerated charged particles.

simplified model, since charged particles can be removed from the acceleration process in other manners, e.g. by isospin flip of protons in reactions with photons, where the resulting neutron escapes the acceleration region. The neutron can turn into a proton again on the way to Earth through beta decay.

2.3 Propagation Losses and the "Cosmic Laboratory"

Once produced, neutrinos, gamma-rays and cosmic rays propagate over cosmological distance to be detected on Earth. During this propagation, they suffer energy loss due to the expansion of the Universe (all particles) and reactions with the photons of the CMB (cosmic rays and gamma-rays). Adiabatic energy loss due to the expansion of the Universe will be discussed in Sec. 2.3.1. In Sec. 2.3.2 the properties of the CMB as target medium for cosmic rays will be briefly reviewed before turning to the reactions of cosmic rays with the CMB. Understanding these processes is essential for deriving neutrino fluxes both from the sources of cosmic rays and for cosmogenic neutrinos. For protons, the dominant processes for reactions with the CMB are photo-pion production and pair production; Compton scattering can be neglected. These processes will be discussed in Secs. 2.3.3 and 2.3.4, respectively. The GZK cutoff, a feature of photo-pion production on the CMB, is the subject of Sec. 2.3.5. In Sec. 2.3.6 the combined propagation losses from the previously introduced effects will be discussed for protons. For heavy nuclei, the process of photo-disintegration becomes relevant, which will be elaborated in Sec. 2.3.7.
The CMB presents the most significant obstacle to cosmic rays trying to find their way through the Universe toward Earth. The peak value of the extra-galactic energy flux spectrum for infrared, optical and UV background photons is about two orders of magnitude or more below that of the CMB, see e.g. [80, 81]. Hence this background is only relevant for interactions of cosmic ray protons below the threshold for a given process (pair production, photo-pion production, photo-disintegration) with the CMB. Reactions with matter can be ignored completely: The density of baryonic matter in the Universe is $\lesssim 10^{-7}$GeV/cm^3 and that of the local halo/disk is $\sim$1 GeV/cm^3 [65]. Assuming all matter is made of nucleons with masses of $\sim$1 GeV/c^2 leads to negligible densities compared to that of the CMB.

2.3.1 Expansion of the Universe and Source Evolution

In General Relativity, for a homogeneous isotropic Universe, a line element ds is described by the relation

$$ds^2 = c^2dt^2 - R(t)^2 \left(\frac{dr^2}{1-kr^2} + r^2 d\theta^2 + r^2 \sin^2\theta d\phi^2 \right) \quad ,$$

where r is the (dimensionless) radial coordinate, $R(t)$ is the scale of curvature (in units of length), and ϕ and θ are the common azimuthal and polar angular coordinates. The curvature of three-dimensional space is defined by the sign of the constant k while its size depends on the normalisation of R.
In the present epoch, as well as in all past epochs that are relevant for ordinary astrophysics, our Universe is matter dominated, and is commonly referred to as "Robertson Walker Uni-

verse", where the Einstein field equations reduce to

$$\left(\frac{\dot{a}}{a}\right)^2 = H_0^2\left(\frac{\Omega_m}{a^3} + \frac{\Omega_k}{a^2} + \Omega_\Lambda\right) \quad . \tag{2.6}$$

Here the scale $R(t)$ was normalised such that its present day value[12] is given by the Hubble distance, $R_0 \equiv c/H_0$; The scale parameter a is then defined by dividing $R(t)$ by its present day value R_0, that is $a(t) \equiv R(t)/R_0$ and $a_0 = 1$. The Hubble parameter is defined as

$$H(z) \equiv \frac{\dot{a}}{a} \equiv \frac{\dot{R}}{R} \tag{2.7}$$

and its present day value $H_0 = 72\,\mathrm{km\,s^{-1}\,Mpc^{-1}}$ is the Hubble constant. Ω_m and Ω_Λ are the values of the matter density and dark energy density of the Universe, respectively, while Ω_k describes the spatial curvature. These parameters are defined by

$$\begin{aligned}
\Omega_m &= \frac{8\pi G\rho_0}{3H_0^2} \\
\Omega_\Lambda &= \frac{\Lambda R_0^2}{3H_0^2} \\
\Omega_k &= \frac{-k}{3H_0^2} \qquad (k = -1, 0, +1) \quad ,
\end{aligned}$$

where G is the Newtonian gravitational constant, ρ_0 is the present day value of the gravitational matter density and Λ is the cosmological constant.
For the normalisation chosen for R, the curvature constant takes on the three values $k = -1, 0, +1$ for an open, flat, and closed Universe, respectively. Furthermore, since $a_0 = 1$, Eq. 2.6 yield the relation $\Omega_m + \Omega_\Lambda + \Omega_k = 1$ which allows to eliminate Ω_k. Current experimental values are $\Omega_m = 0.26(2)$ and $\Omega_\Lambda = 0.74(3)$ [65] which is consistent with a flat Universe and for the remainder of this report, $\Omega_k = 0$ will be assumed. An approximation that is frequently used is the *Einstein-de Sitter Universe* with $\Omega_m = 1$ and $\Omega_\Lambda = 0$. As will be shown below, this approximation simplifies calculations by allowing for analytical calculations of integrals while yielding decent approximations.
The parameter a is related to the redshift z by the relation

$$a = (1+z)^{-1}$$

such that $\left|\frac{da}{dz}\right| = (1+z)^{-2} \equiv a^2$. Equation 2.6 can then be rewritten, using Eq. 2.7, to relate the Hubble parameter to redshift according to

$$H(z) = H_0\sqrt{\Omega_m(1+z)^3 + \Omega_k(1+z)^2 + \Omega_\Lambda} \quad . \tag{2.8}$$

For a flat Universe with $\Omega_k = 0$, Eq. 2.8 can be written

$$H(z) = H_0\sqrt{\Omega_m(1+z)^3 + \Omega_\Lambda} \quad (k=0) \quad . \tag{2.9}$$

In the context of this report, production *rates* of particles (cosmic rays or neutrinos) are investigated. Assuming a uniform distribution of sources throughout the Universe, a density

[12] The subscript 0 is always used to denote present day values.

of particles can be calculated by integrating the production rate over the relevant production time. This is most conveniently done by using equation 2.6 to relate the time t to the redshift z. Noting that $\dot{a} = \frac{da}{dz}\frac{dz}{dt} = a^2\frac{dz}{dt}$, an expression for dt/dz can be derived:

$$\begin{aligned}\left(\frac{dz}{dt}\right)^2 &= \left(\frac{H_0}{a}\right)^2\left(\frac{\Omega_m}{a^3}+\frac{\Omega_k}{a^2}+\Omega_\Lambda\right)\\ \Rightarrow \left|\frac{dz}{dt}\right| &= H(z)\cdot(1+z)\\ \Rightarrow \left|\frac{dt}{dz}\right| &= \frac{H(z)^{-1}}{1+z} \quad .\end{aligned}$$

Given that going backwards in time is equivalent to increasing z, the sign of $\frac{dt}{dz}$ is negative. Defining distances on cosmological scales in an expanding Universe is not a trivial matter, since the outcome will depend on the measurement method chosen, see e.g. [82]. To establish the redshift-distance relation, the *proper distance* is used (*proper time* times speed of light), i.e.

$$\begin{aligned}d_p(z) &= c\int_0^z \left|\frac{dt}{dz'}\right| dz'\\ &\overset{E.d.S.}{=} \frac{2}{3}\frac{c}{H_0}\left(1-(1+z)^{-3/2}\right) \quad ,\end{aligned}$$

where the second line is for an Einstein-de Sitter Universe (E.d.S.). The age of the Universe is easily calculated as $2/3\,H_0^{-1}$ by using integration bounds of $z = 0$ and ∞ in Eq. 2.10. As the cosmological parameters have only been approximated and it has been ignored that the early Universe was radiation dominated, the resulting value is not correct. The age of the Universe is close to $1/H_0 \approx 14\,\mathrm{Gyr}$. The Einstein-de Sitter Universe has the advantage that the integral can be solved analytical, unlike the most general case with both Ω_m and Ω_Λ different from zero, while yielding reasonably exact results.
A convenient coordinate system is that of *co-moving coordinates*, in which all distances scale with the scale parameter a. Expressed differently, a co-moving distances d_c, i.e. the distance between two objects measured in co-moving coordinates, is defined as proper distance divided by a. For movements along the line of sight (which in practise is always the case for light or particles of distant objects observed on Earth), a factor of $1+z$ is applied such that

$$d_c = c\int_0^z (1+z')\left|\frac{dt'}{dz'}\right| dz' = c\int_0^z \frac{dz'}{H(z')}$$

For $z \ll 1$, the co-moving distance (as well as any other reasonably defined distance) becomes equivalent to the proper distance or to the "normal" distance in Euclidean space and it can be written

$$d \approx \frac{c}{H_0}z \approx z\cdot 4.2\,\mathrm{Gpc} \quad (\text{for z} \ll 1) \quad . \tag{2.10}$$

Co-moving coordinates are particularly useful for the definition of co-moving volumes. In the remaining parts of this chapter, densities based on co-moving volumes are used, which for non-evolving sources leaves the density unchanged throughout the history of the Universe. Source evolution, i.e. the increase of luminosities and/or space densities of sources with redshift, has to be taken into account explicitly. Cosmological source evolution is usually

parametrised by a factor $(1+z)^m$. As no UHE neutrinos have been observed yet, the redshift evolution of their sources is a matter of speculation. An approach that is frequently adopted is to calculate neutrino fluxes under the assumption of no source evolution and the strongest evolution observed for astrophysical objects. The latter is is often parametrised (see [83] and references therein) with $m = 3$ and

$$\begin{array}{ll} (1+z)^m & z < 1.9 \\ (1+1.9)^m & 1.9 \leq z < 2.7 \\ (1+1.9)^m \exp\left([2.7-z]/2.7\right) & z \geq 2.7 \quad . \end{array} \tag{2.11}$$

Finally, the energy of a particle scales with z as

$$E(z) = E_0(1+z) \quad ,$$

where E_0 is the energy observed on Earth. The expansion of the Universe hence leads to an adiabatic energy loss.

2.3.2 Cosmic Microwave Background

The spectral distribution of the photon density of the CMB, n_{CMB}, follows the distribution for blackbody radiation and has the form (see e.g. [84])

$$\frac{dn_{\mathrm{CMB}}}{dE_{\mathrm{CMB}}} = \frac{1}{\pi^2\hbar^3c^3}\frac{E_{\mathrm{CMB}}^2}{\exp(\frac{E_{\mathrm{CMB}}}{k_{\mathrm{B}}T})-1} \quad , \tag{2.12}$$

where $k_{\mathrm{B}} = 8.6 \times 10^{-5}\,\mathrm{eV\,K^{-1}}$ is the Boltzmann constant. To calculate the photon density n_{CMB}, Eq. 2.12 has to be integrated over all energies, which is achieved by using the identity

$$\int_0^\infty \frac{x^{b-1}}{e^{ax}-1}dx = \frac{\Gamma(b)}{a^b}\zeta(b) \quad ,$$

where $\zeta(\cdot)$ is the Riemann zeta function with the explicit value $\zeta(3) \approx 1.202$ and $\Gamma(\cdot)$ is the Gamma function. Hence the photon density can be expressed as

$$n_{\mathrm{CMB}} = \frac{2\zeta(3)(k_{\mathrm{B}}T)^3}{\pi^2\hbar^3c^3} = \frac{120\sigma_{\mathrm{SB}}\zeta(3)}{ck_{\mathrm{B}}\pi^4}T^3 \approx 2.03\times10^7\left(\frac{T}{\mathrm{K}}\right)^3\mathrm{m^{-3}} \quad , \tag{2.13}$$

where $\sigma_{\mathrm{SB}} = \frac{\pi^2\,k_{\mathrm{B}}^4}{60\hbar^3c^2} \approx 1.18\times10^3\,c\ \mathrm{eV\,K^{-4}\,m^{-3}}$ is the Stefan-Boltzmann constant. The CMB temperature of $T_{\mathrm{CMB}} = 2.725\,\mathrm{K}$ yields a photon density of $411\,\mathrm{cm^{-3}}$.
The internal energy U per volume V of a blackbody radiator is given by (see e.g. [85])

$$\frac{U}{V} = \frac{4\,\sigma_{\mathrm{SB}}\,T^4}{c} \approx 4.72\times10^3\frac{\mathrm{eV}}{\mathrm{m^3}}\frac{T^4}{\mathrm{K^4}} \tag{2.14}$$

which for T_{CMB} yields $U/V \approx 0.260\,\mathrm{eVcm^{-3}}$. Hence, the average energy per photon is $0.260\,\mathrm{eVcm^{-3}}/411\,\mathrm{cm^{-3}}$, which more generally can be expressed as the ratio of Eqs. 2.14 and 2.13 as

$$\langle E_{\mathrm{CMB}}\rangle = \frac{\pi^4}{30\zeta(3)}k_{\mathrm{B}}T_{\mathrm{CMB}} \approx 2.7\,k_{\mathrm{B}}T_{\mathrm{CMB}} \approx 0.633\,\mathrm{meV} \quad . \tag{2.15}$$

2.3.3 Pair Production

Cosmic ray proton interact with photons of the CMB to form electron positron pairs according to

$$p + \gamma_{\mathrm{CMB}} \rightarrow p + e^+e^- \quad ,$$

also referred to as Bethe-Heitler process. For a given photon energy E_γ the energy threshold for pair production in head-on collisions of p and γ is

$$E_p \gtrsim \frac{(m_p c^2 + 2m_e c^2)^2 - m_p^2 c^4}{4\,E_\gamma} = \frac{m_p c^2\, m_e c^2}{E_\gamma}(1 + \frac{m_e}{m_p}) \approx 4.8 \times 10^5 \left(\frac{1\,\mathrm{eV}}{E_\gamma}\right) \mathrm{GeV} \quad . \tag{2.16}$$

For the average CMB energy $\langle E_{\mathrm{CMB}} \rangle \approx 0.633\,\mathrm{meV}$ from Eq. 2.15, the threshold energy is $E_p \gtrsim 8 \times 10^{17}\,\mathrm{eV}$. A thorough treatment [86] yields a minimum of the radiation length at $1.4\,\mathrm{Gpc}$, reached at a proton energy of $E_p \approx 10^{19.3}\,\mathrm{eV}$. Below proton energies of $\sim 10^{18}\,\mathrm{eV}$, the radiation length for pair production exceeds the Hubble length, while above about $10^{20}\,\mathrm{eV}$, photo-pion production sets in (see Sec. 2.3.4) which due to its much higher cross section renders the process of pair production insignificant. These two bounds restrict the cosmic ray energy range for which pair production is relevant to less than two orders of magnitude. Furthermore, no neutrino production is associated with this process.
The pair production process has been used to explain the feature of the dip (or ankle) of the cosmic ray flux (see Fig. 2.6) as substantiated in [64, 87] and references therein. In this scenario, cosmic rays in the energy region $10^{18} \sim 10^{19}\,\mathrm{eV}$ are mainly extra-galactic protons, with possibly an admixture of $10 \sim 15$ % of nuclei.

2.3.4 Photo-Pion Production and the Delta Resonance

Photo-pion production is the process of producing pions in nucleon-photon reactions. The threshold for this process is at a centre of mass energy of $m_p c^2 + m_{\pi^0} c^2 = 1079.2\,\mathrm{MeV}$. For a given photon energy, the production threshold for pions for head-on collisions of protons and photons is given as

$$E_p \gtrsim \frac{(m_p c^2 + m_{\pi^0} c^2)^2 - m_p^2 c^4}{4\,E_\gamma} = \frac{m_p c^2\, m_{\pi^0} c^2}{2\,E_\gamma}(1 + \frac{m_{\pi^0}}{2\,m_p}) \approx 6.7 \times 10^7 \left(\frac{1\,\mathrm{eV}}{E_\gamma}\right) \mathrm{GeV} \quad . \tag{2.17}$$

Entering the average energy of a CMB photon, $\langle E_{CMB} \rangle \approx 0.633\,\mathrm{meV}$ for E_γ yields a threshold of $E_p \gtrsim 10^{20}\,\mathrm{eV}$. The (inelastic) cross section for proton-photon interactions peaks at the $\Delta^+(1232)$-resonance,

$$p + \gamma \rightarrow \Delta^+ \rightarrow \pi^+ + n \tag{2.18}$$
$$p + \gamma \rightarrow \Delta^+ \rightarrow \pi^0 + p \quad , \tag{2.19}$$

where for a CMB photon with average energy, the corresponding proton energy at the Δ-resonance[13] for a head-on collision is $E_p \approx 6 \times 10^{20}\,\mathrm{eV}$. Neutrons produced in reaction 2.18 can either decay to protons or react with photons via the $\Delta^0(1232)$-resonance

$$n + \gamma \rightarrow \Delta^0 \rightarrow \pi^- + p$$
$$n + \gamma \rightarrow \Delta^0 \rightarrow \pi^0 + n \quad .$$

[13] The expressions Δ and $\Delta(1232)$ are used synonymously.

Neutrons with energy $E_n \lesssim 4 \times 10^{20}$ eV are however more likely to decay than to interact with the CMB, see Sec. 2.6.1, such that the Δ^+-resonance is mainly responsible for interactions of cosmic rays with the CMB. The charged pions produced in these reactions in turn decay according to the reactions 2.2 and 2.3, yielding the aforementioned number ratios of the three generations of $N_{\nu_e} : N_{\nu_\mu} : N_{\nu_\tau} = 1 : 2 : 0$.

The $\Delta^+(1232)$-resonance has an isospin of $I = \frac{3}{2}$ with $I_3 = \frac{1}{2}$. Writing the isospin states as $|I\, I_3\rangle$ the Δ^+ final state particles can be expressed as $|\pi^+\rangle = |1\,1\rangle$, $|n\rangle = |\frac{1}{2}\,-\frac{1}{2}\rangle$ and $|\pi^0\rangle = |1\,0\rangle$, $|p\rangle = |\frac{1}{2}\,+\frac{1}{2}\rangle$. Using the appropriate Clebsch-Gordan coefficients, the Δ^+-resonance can be expressed in the basis of the final states as $|\Delta^+\rangle = \sqrt{\frac{1}{3}}|\pi^+\rangle|n\rangle + \sqrt{\frac{2}{3}}|\pi^0\rangle|p\rangle$, which means that the branching ratios of the final states involving π^0's a and π^+'s will be $\frac{2}{3}$ and $\frac{1}{3}$, respectively. This is called the Δ-resonance approximation. In this approximation, about $3/4$ of the energy of a charged pion is transferred to neutrinos, the rest to the electron (see Eqs. 2.2 and 2.3). The ratio of yield in electromagnetic energy (electrons from $\pi^\pm$ and photons from π^0) to yield in neutrino energy hence is about $(\frac{3}{4} \times \frac{1}{3})/(\frac{2}{3} + \frac{1}{4} \times \frac{1}{3}) = \frac{1}{3}$. For UHE protons above the pion production threshold traversing the CMB, this approximation however underestimates the energy ratio by a factor of $2 \sim 3$, see [88].
The cross section at the Δ^+-resonance can be parametrised by a Breit-Wigner shape as [84]

$$\sigma(s) = \frac{4m_p^2c^4\, s}{(s - m_p^2c^4)^2} \frac{\sigma_0^{\gamma p\to\Delta^+}\, \Gamma^2\, s}{(s - M_{\Delta^+}^2c^4)^2 + \Gamma^2 s} \quad , \tag{2.20}$$

where s is the square of the invariant mass. The physical parameters of the $\Delta^+(1232)$-resonance are

$$\begin{aligned} M_\Delta &= 1.232\,\mathrm{GeV}/c^2 \\ \Gamma_\Delta &= 0.12\,\mathrm{GeV} \\ \sigma_0^{\gamma p\to\Delta} &= 31.125\,\mu\mathrm{barn} \quad . \end{aligned}$$

For $s = M_\Delta^2 c^4$, the cross section calculates as

$$\sigma(s = {M_\Delta}^2 c^4) = \frac{4\,{m_p}^2}{({M_\Delta}^2 - {m_p}^2)^2} {M_\Delta}^2\, \sigma_0^{\gamma p\to\Delta} \approx 410\,\mu\mathrm{barn} \quad .$$

The cross section for the Δ^0-resonance is roughly 10% higher [84]. This peak cross section and the photon density of the CMB background of $n = 411\,\mathrm{cm}^{-3}$ obtained from Eq. 2.13 can be used to calculate the mean free path λ of a proton according to

$$\lambda = \frac{1}{n\,\sigma} \quad . \tag{2.21}$$

The result is $\lambda \approx 2$ Mpc. Of course, not taking the s-dependence of the $\gamma p \to \Delta^+$ cross section and the spectrum of the CMB photons into account yields only a rough approximation. Nonetheless, it becomes obvious that the mean free path is small compared to the Hubble distance, which is the cause of the GZK cutoff that was introduced above. This point will be addressed in Sec. 2.3.5, where also a more precise calculation of the mean free path will be performed.

For energies beyond the Δ-resonance, multi-pion production becomes dominant [84], e.g. the processes

$$\begin{aligned} p + \gamma &\rightarrow \pi^+\pi^- + p \\ p + \gamma &\rightarrow \pi^+\pi^-\pi^0 + p \\ p + \gamma &\rightarrow 2\pi^+\pi^- + n \\ &\text{etc.} \end{aligned}$$

At higher energies, kaons can also be produced. The photon-proton cross section as a function of the photon energy in the rest frame of the proton is shown in Fig. 2.7. The first and second peak correspond to the $\Delta(1232)$ and $N(1520)$ resonance, respectively. The sum of the cross sections of multi-pion production and the direct channel (i.e. the t-channel exchange of virtual charged mesons near the photo-pion production threshold) is reasonably well approximated by $\sigma \approx 100\,\mu\text{barn}$ above the pion production threshold. Hence, the CMB presents a large cross section to cosmic ray protons beyond the Δ-resonance. This explains the limited validity of the Δ-resonance approximation that was discussed above.

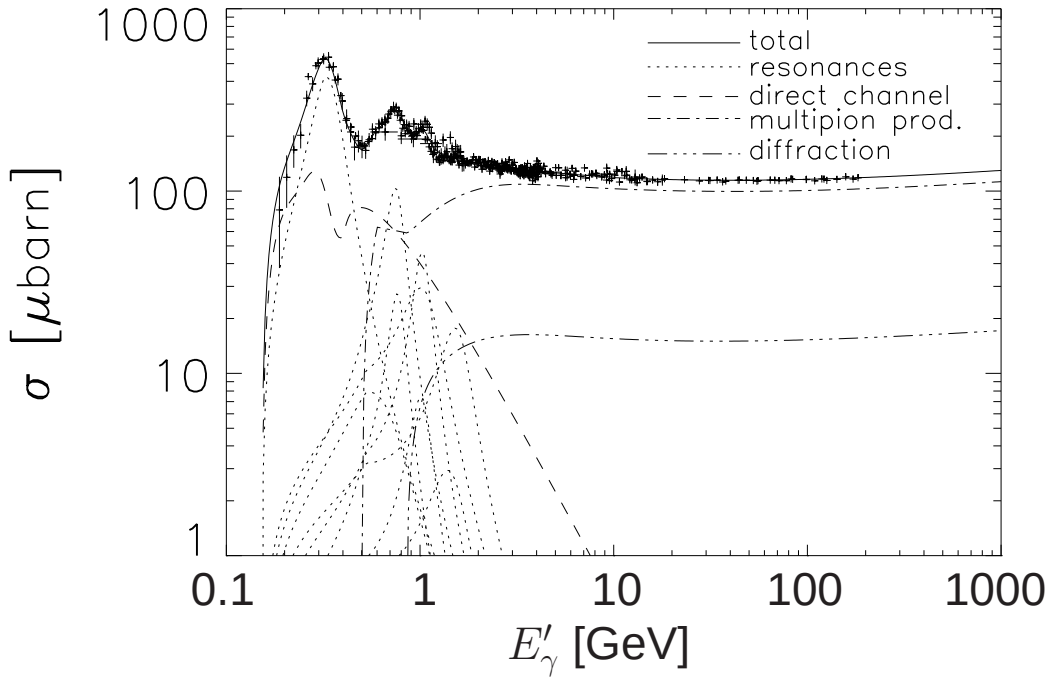

Figure 2.7: The total γp cross section (solid line) with the contributions of baryon resonances (dotted lines), direct pion production processes (dashed line) non-diffractive multi-pion production (dash-dotted line), and diffractive scattering (lower dash-triple-dotted line). Crosses represent experimental data. E'_γ denotes the photon energy in the rest frame of the nucleon. From [84].

2.3.5 The GZK Cutoff

As has been mentioned, photo-pion production with photons of the CMB implies an energy threshold, above which cosmic rays cannot reach Earth except from our "cosmic neighbourhood". The assumption of an extra-galactic origin of cosmic rays at highest energies as

motivated in Sec. 2.2.3 implies that the observed CR flux on Earth should have a cutoff at this energy as was first pointed out in [89, 90]. According to the authors of these papers, K. Greisen, G.T. Zatsepin and V.A. Kuz'min, this threshold has been later termed "GZK cutoff". The production of charged pions implies the production of cosmogenic neutrinos that were introduced in Sec. 2.1.2.
The GZK cutoff was estimated above from Eq. 2.17 as $\sim 10^{11}\,\mathrm{GeV}$ for $\langle E_{CMB}\rangle \approx 0.633\,\mathrm{meV}$. The average mean free path for a proton traversing the CMB is calculated according to

$$\lambda^{-1}(s) = \int \frac{dn}{dE_\gamma}\sigma(s)dE_\gamma \quad ,$$

where the photon energy has been expressed as E_γ. To calculate $\lambda^{-1}(E)$ rather than $\lambda^{-1}(s)$, where E is the proton energy, the average of λ^{-1} over s for a given E needs to be calculated, with E and s related according to

$$s = m_p^2c^4 + 2E_\gamma E(1-\beta\cos\theta) \quad . \tag{2.22}$$

Here β denotes the velocity of the proton in the rest frame of the observer and θ the scattering angle. Following [91, 77], the probability $p(\theta)$ for an interaction under the angle θ is proportional to $(1-\beta\cos\theta)$ from kinematic arguments and proportional to $\sin\theta$ from geometric arguments. Hence $p(\theta) \propto (1-\beta\cos\theta)\sin\theta$, such that

$$\lambda^{-1}(E) = \int\int \frac{dn}{dE_\gamma}\sigma(s)(1-\beta x)dE_\gamma dx \Big/ \int_{-1}^{+1}(1-\beta x)dx \quad ,$$

where the expression was simplified by using $x \equiv \cos\theta$. The normalisation can be easily calculated to yield 2; furthermore, Eq. 2.22 can be used to express $(1-\beta\cos\theta)$ as a function of s and with $ds/dx = -2E_\gamma E\beta$ one can write

$$\begin{aligned}\lambda^{-1}(E) &= \frac{1}{2}\int_{E_\gamma^{\min}}^{\infty}\int_{s_{\min}}^{s_{\max}}\frac{dn}{dE_\gamma}\sigma(s)\frac{(s-m_p^2c^4)}{2E_\gamma E}\frac{1}{2E_\gamma E\beta}dE_\gamma ds \\ &= \frac{1}{8\beta E^2}\int_{E_\gamma^{\min}}^{\infty}\frac{1}{E_\gamma^2}\frac{dn}{dE_\gamma}\int_{s_{\min}}^{s_{\max}}\sigma(s)(s-m_p^2c^4)dE_\gamma ds \quad ,\end{aligned} \tag{2.23}$$

where the minus sign of ds/dx was dropped because the integration bounds were swapped ($x=-1$ corresponds to $s_{\max}$). Eq. 2.23 can also be found in [92]. The integration bounds are

$$\begin{aligned}E_\gamma^{\min} &= \frac{m_\pi c^2(m_\pi c^2 + 2m_p c^2)}{2E(1+\beta)} \\ s_{\min} &= (m_p c^2 + m_\pi c^2)^2 \\ s_{\max}(E_\gamma, E) &= m_p c^4 + 2E_\gamma E(1+\beta) \quad .\end{aligned}$$

Eq. 2.23 can be used for a simple numerical calculation of the mean free path of protons in the CMB as a function of their energy, which demonstrates the basic features of the GZK cutoff. For all numerical calculations, $\beta = 1$ was used. This was done for the cross section of the Δ^+-resonance only, Eq. 2.20, and for the cross section of the Δ^+-resonance plus a constant addition of 100 μbarn (see Sec. 2.3.4) for multi-pion production and the direct channel. The results are shown in Fig. 2.8. When taking only the Δ^+-resonance cross

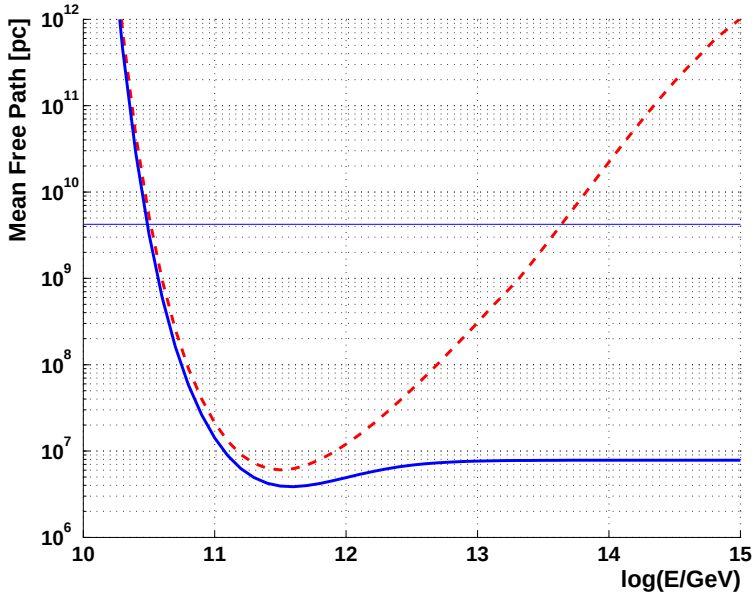

Figure 2.8: Average mean free path according to Eq. 2.23 as a function of the proton energy for reactions with the CMB. For the cross section, in one case only the Δ^+-resonance was used (broken line), whereas in the other case, a constant contribution of 100 μbarn was added to account for multi-pion production and for the direct channel (solid line). The thin straight line shows the Hubble length.

section into account (broken line in Fig. 2.8), the resulting mean free path is 6.0 Mpc at an energy of 3.2×10^{11} GeV. After adding the constant contribution of 100 μbarn (solid line in Fig. 2.8) the mean free path is 3.9 Mpc at an energy of 4.0×10^{11} GeV. The result given in [88] is a minimum mean free path of 3.8 Mpc at an energy of $\sim 6 \times 10^{11}$ GeV.
It can be seen in the figure that the mean free path drops from the Hubble length to a few Mpc within one order of magnitude in proton energy. Due to the cross section from multi-pion production beyond the Δ^+-resonance, the mean free path does not increase strongly again for energies beyond the Δ^+-resonance. The proton energy of about 5×10^{11} GeV at the minimum of the mean free path agrees well with the end of the observed CR flux in Fig. 2.6. After travelling a distance equivalent to the mean free path, a proton looses only a fraction of its energy. In order to have the energy reduced to a value below the pion production threshold, several interactions are necessary. In [93] it is shown that after propagating $\sim$200 Mpc, protons with initial energies between 10^{20} and 10^{22} eV have the same mean energy, below the threshold for photo-pion production, independent of their initial energy. In other words, protons that start off with an energy exceeding the pion production threshold will have their energy reduced to below the threshold after propagating that distance. The distance of $100 \sim 200$ Mpc is typically quoted as the GZK horizon.

2.3.6 Combined Propagation Losses for Protons

The expansion of the Universe introduces a dependence on redshift (z) of the cross section σ and the invariant mass squared s which was neglected in the calculations above. The dependence of the proton mean free path for photo-pion production on z is shown in Fig. 2.9(a) [94] for interaction with the CMB and with the infrared, optical and ultraviolet backgrounds. The

latter three background contributions will be collectively referred to IR/Opt/UV for short. Above the threshold for photo-pion production with the CMB, the effect of the IR/Opt/UV on the propagation of cosmic ray protons becomes insignificant. Even below that threshold, the proton mean free path is $\gtrsim 1\,\mathrm{Gpc}$ and the effect of IR/Opt/UV photons on the proton cosmic ray spectrum observed on Earth is negligible. The effect on cosmogenic neutrinos associated with the propagation of UHE cosmic rays, however, is strong [94], which will be discussed in more detail in Sec. 2.6.2.

The z-dependence of the mean free path for interactions of protons with the CMB is very strong, much stronger than for the IR/Opt/UV. At earlier epochs (larger z), the threshold for photo-pion production sets in at lower energies and the mean free path is decreased. This increases the flux of cosmogenic neutrinos corresponding to a given production rate of primordial cosmic rays when the production occurs at larger values of z. This in turn suggests a strong dependence of the cosmogenic neutrino flux on the cosmological evolution of cosmic ray sources.

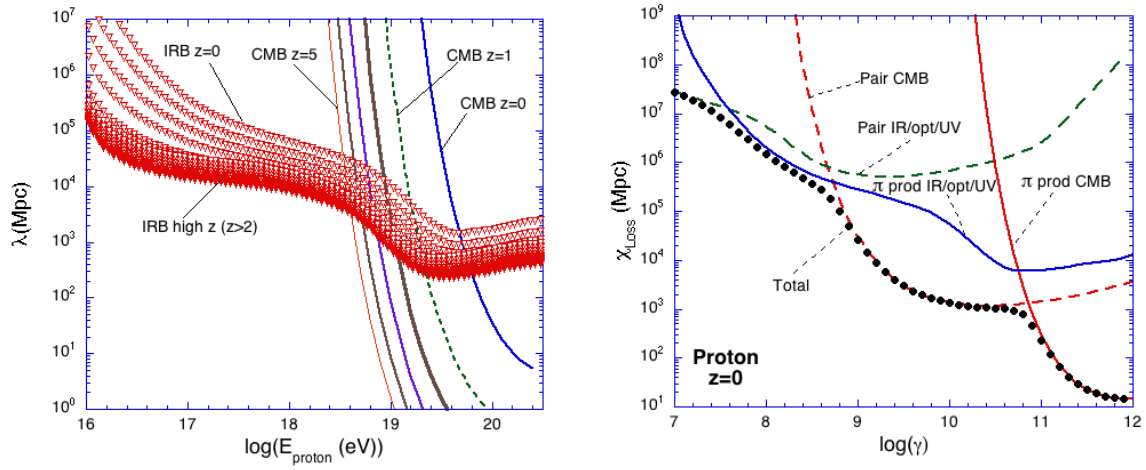

(a) (b)

Figure 2.9: (a) Evolution of the proton mean free path for photo-pion production with the IR/Opt/UV (labelled IRB) and the CMB at redshifts between 0 and 5 as a function of the proton energy observed at $z = 0$; The IR/Opt/UV was calculated for 26 values with $\Delta z = 0.2$. (b) The attenuation length of protons as a function of the energy (logarithm of Lorentz boost factor) at $z = 0$. From [94].

In Fig. 2.9(b), the attenuation length for protons is shown at $z = 0$ when the contribution of pair production is added to that of photo-pion production. For boost factors in excess of $\log(\gamma) \approx 8.7$, pair production of protons with CMB-photons dominates over photo-pion production with the the IR/Opt/UV. However, for $\log(\gamma) \approx 8.7$, the attenuation length exceeds the Hubble length by roughly two orders of magnitude and by higher values for lower energies. Hence, for the attenuation of protons, the effect of the IR/Opt/UV is negligible.

2.3.7 Photo-Disintegration

For heavy nuclei, the process of photo-disintegration, i.e. the disintegration of a nucleus into lighter nuclei and nucleons in reactions with cosmic background photons, becomes relevant. The threshold for photo-disintegration depends on the nucleus but is much lower than for

pair production and photo-pion production, of the order of $10\,\mathrm{MeV}$ [80] in the nucleus rest frame. Hence, photo-disintegration becomes the dominant process of attenuation for heavy nuclei.

The nuclear photo-disintegration process is dominated by the giant dipole resonance (GDR), a collective vibration of the nucleons, which results in the emission of one or two nucleons and α-particles [80, 94]. Around $30\,\mathrm{MeV}$ in the nucleus rest frame and up to the photo-pion production threshold, the quasi-deuteron (QD) process becomes comparable to the GDR [94]. The photo-pion production, or baryonic resonances (BR), of nuclei becomes relevant above the energy $\sim 150\,\mathrm{MeV}$ in the nuclei rest frame, corresponding to the pion mass. For UHE iron nuclei with $A = 56$ interacting with the CMB, the threshold in the observer's rest frame is obtained as $\sim 6 \times 10^{12}\,\mathrm{GeV}$ from Eq. 2.17 with $m_p \to 56\,m_p$ and $E_\gamma \equiv \langle E_{CMB} \rangle \approx 0.633\,\mathrm{meV}$. The effect of photo-disintegration on the mean free path of iron is shown Fig. 2.10(a). For photo-disintegration of nuclei on the way to Earth, the contri-

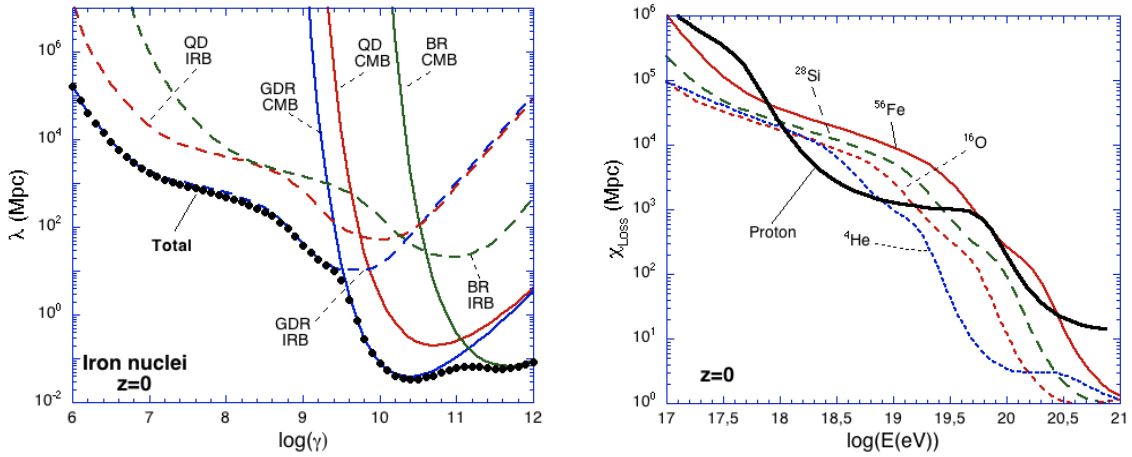

(a) (b)

Figure 2.10: (a) The iron nucleus mean free path for the different photo-disintegration processes and interactions with the CMB and IR/Opt/UV photons (labelled IRB) at $z = 0$. (b) Comparison of the attenuation length of different nuclei at $z = 0$. From [94].

bution of the cosmic infrared background (IRB)[14] radiation become significant, see also [80] and references therein. The energy at which reactions with CMB photons start to set in can be estimated from the threshold for photo-disintegration of $\sim 10\,\mathrm{MeV}$ and the mean energy of the CMB, $\langle E_{\mathrm{CMB}} \rangle \approx 0.633\,\mathrm{meV}$. The resulting boost factor is $\gamma \sim 10^{10}$ corresponding to a cosmic ray energy of $E_{\mathrm{CR}} \sim A \times 10^{10}\,\mathrm{GeV}$. Taking the much higher photon density of the CMB into account, the transition between CIB and CMB occurs at a lower energy of about $\gamma \approx 10^{9.5}$, see Fig. 2.10(a). Fig. 2.10(b) shows the attenuation length for different nuclei, compared to that for protons. The attenuation length of low mass nuclei is smaller than those for protons and heavy nuclei over most of the energy range. Hence, at high energies, the spectrum observed on Earth is expected to be dominated by protons and heavy nuclei [94].

[14]The notation here follows [94]; later in this report, the acronym CIB will be used.

2.4 Production Rate of Cosmic Rays

As discussed above, the production of neutrinos is expected to be associated with the generation and propagation of cosmic rays. In order to estimate expected neutrino fluxes on Earth, a normalisation of the flux to the production rate of primordial cosmic rays is necessary. The formalism to calculate the production rate of primordial cosmic rays from the observed cosmic ray flux on Earth is discussed in Sec. 2.4.1. To demonstrate the procedure, a "toy calculation" of the production rate from measurements of the Pierre Auger Observatory is performed in Sec. 2.4.2 before published results are recapitulated in Sec. 2.4.3.
Assuming that UHECRs are composed of protons simplifies most calculations, but the question of their composition is indeed still open. The implication of the cosmic ray composition for UHE neutrinos is twofold. First, the underlying production rate of primordial cosmic rays will be affected, which is discussed in Sec. 2.4.4. And second, the neutrino production mechanisms associated with cosmic rays will be altered. This will be discussed below in Secs. 2.5 and 2.6.
All calculations presented are based on the assumption of a uniform source distribution over cosmological distances. As discussed in Sec. 2.2.3 this assumption is consistent with data. Alternatively, *single source models* assume that all cosmic rays originate from a nearby source and that isotropy of cosmic rays arriving on Earth is established by (larger than expected) intergalactic magnetic fields. A possible source candidate in this scenario is the superheavy galaxy M87 in the Virgo cluster at $z \approx 0.004$, which is believed to host an AGN [95]. In [96], the majority of the observed ultra-high-energy events is assumed to originate from the radio galaxy Centaurus A at $z \approx 0.002$. In this model the UHECRs are predicted to be heavy nuclei.
Single source models are disfavoured by the data from the Pierre Auger Observatory [74] which claim a correlation between the arrival direction of cosmic rays beyond the GZK cutoff and the directions of several nearby AGNs, see Sec. 2.2.3. However, cosmic rays could still originate from a limited number of nearby sources.

2.4.1 Formalism

If an energy density is denoted by ε, then $\dot{\varepsilon}$ is the rate at which energy per (co-moving) volume is produced, in the case at hands in form of cosmic rays. These cosmic rays have a spectral distribution of their (number) density n per co-moving volume which is denoted by dn/dE. It is assumed here that the source distribution has a value for a given epoch z that is uniform on cosmological scales. Then the spectral distribution of the *energy* density is given by $E\,dn/dE$ and the energy density is calculated as

$$\varepsilon = \int_{E_g^{\min}}^{E_g^{\max}} E_g \frac{dn}{dE_g}\, dE_g \quad , \tag{2.24}$$

where the subscript g was introduced to indicate that this refers to the energies of the cosmic rays when generated. The energy production rate per volume can be written as an integral over the (spectral) particle production rate per volume $Q(E) \equiv d\dot{n}/dE$

$$\dot{\varepsilon} = \int_{E_g^{\min}}^{E_g^{\max}} E_g \frac{d\dot{n}}{dE_g}\, dE_g \quad . \tag{2.25}$$

By omitting a time-dependence it is assumed that cosmic rays on cosmological scales are produced in steady state. The units of $\dot{\varepsilon}$ are $\mathrm{W/m^3}$, or $\mathrm{erg\,Mpc^{-3}\,yr^{-1}}$ as it is more commonly used in astrophysics, which are the units of a power density. Following the literature, this quantity will be simply referred to as energy production rate[15] within the energy range $E_g^{\min}$ to $E_g^{\max}$.
So far, no assumptions about the spectral shape of $d\dot{n}/dE_g$ have been made. Obviously, this quantity cannot be measured directly but must be inferred from observations of the cosmic ray flux on Earth. This must take into account the expansion of the Universe and source evolution (see Sec. 2.3.1), and reactions of the cosmic rays on their way to Earth, most notably photo-pion production with the CMB as discussed in Sec. 2.3.4.
In the following an analytic expression which relates the diffuse cosmic ray flux observed on Earth to the energy production rate of cosmic accelerators will be derived. In practise, the effect of energy loss due to photo-pion production is frequently derived from Monte Carlo simulations since due to the highly stochastic nature of the interaction the continuous loss approximation is not very accurate [97].
Following the discussion in Sec. 2.2.4, a spectral index $\alpha = 2$ will be assumed such that $d\dot{n}/dE_g = AE^{-2}$ with some constant A. This can be inserted into Eq. 2.25 to yield after a simple integration

$$\frac{d\dot{n}}{dE_g} = AE_g^{-2} \;\Rightarrow\; \dot{\varepsilon}\,|_{E_g^{\min}}^{E_g^{\max}} = A\,\ln(E_g^{\max}/E_g^{\min}) \quad . \tag{2.26}$$

From this, an expression for the spectral shape of the underlying particle production rate can be derived,

$$E_g^2 \left(\frac{d\dot{n}}{dE_g}\right)_{\alpha=2} = \frac{\dot{\varepsilon}\,|_{E_g^{\min}}^{E_g^{\max}}}{\ln(E_g^{\max}/E_g^{\min})} \quad . \tag{2.27}$$

Similar expressions follow for a given distribution $d\dot{n}/dE_g = AE_g^{-\alpha}$ with $\alpha \neq 2$. The general form for the particle production rate is then

$$\left(\frac{d\dot{n}}{dE_g}\right)_{\alpha} = \dot{\varepsilon}\,|_{E_g^{\min}}^{E_g^{\max}}\, K_\alpha E_g^{-\alpha} \quad , \tag{2.28}$$

where K_α is the normalisation constant, with $K_\alpha^{-1} = \ln(E_g^{\max}/E_g^{\min})$ for $\alpha = 2$. The particle production rate has to be integrated over the relevant time period to yield a particle density. Then, assuming isotropy, the corresponding diffuse flux can be expressed generically as $\Phi = \text{density} \times c/(4\pi)$. Expressing the time in terms of the redshift z (see Sec. 2.3.2), the diffuse (spectral) cosmic ray flux Φ_{CR} (in units $\mathrm{m^{-2}s^{-1}sr^{-1}eV^{-1}}$) measured on Earth can be expressed by the relation [87]

$$\Phi_{\mathrm{CR}}(E) = \frac{c}{4\pi}\,\dot{\varepsilon}\,|_{E_g^{\min}}^{E_g^{\max}}\, K_\alpha \int_0^{z_{\max}} dz \left|\frac{dt}{dz}\right| (1+z)^m E_g^{-\alpha} \frac{dE_g}{dE} \tag{2.29}$$

where E is the energy observed on Earth and $\frac{dE_g}{dE}$ describes energy losses due to redshift and interactions of the cosmic rays on the way to Earth. The term $(1+z)^m$ describes potential evolution of the sources ($m = 0$ means no evolution). Hence $\dot{\varepsilon}\,|_{E_g^{\min}}^{E_g^{\max}}$ can be calculated by

[15] The quantity $\dot{\varepsilon}$ is also referred to as emissivity in the literature, e.g. in [87], which will not be used here because it is not consistent with the standard definition of the emissivity as a dimensionless quantity.

finding combinations of α and m for which the integral produces the observed flux, and with this value of $\dot{\varepsilon}\,|_{E_g^{\min}}^{E_g^{\max}}$ the quantity $d\dot{n}/dE_g$ is determined according to equation 2.28.
It is tempting to put the ignorance about source evolution into one parameter. For this, the production rate Eq. 2.28 is multiplied by an appropriate time, typically the Hubble time $t_H \equiv H_0^{-1}$ which then approximates the density for a production over the complete history of the Universe. Eq. 2.29 can then be rewritten as

$$\begin{aligned}
\Phi_{\mathrm{CR}}(E) &= \frac{c}{4\pi} \times \frac{dn}{dE_g} \\
\Phi_{\mathrm{CR}}(E) &= \frac{c}{4\pi} \times \left[E^{-\alpha}\, \dot{\varepsilon}\,|_{E_g^{\min}}^{E_g^{\max}}\, K_\alpha\, t_H \right] \times \left[\frac{1}{t_H} \int_0^{z_{\max}} dz \left| \frac{dt}{dz} \right| (1+z)^m \frac{E^\alpha}{E_g^\alpha} \frac{dE_g}{dE} \right] \\
&\equiv \frac{c}{4\pi} \times \left[E^{-\alpha}\, \dot{\varepsilon}\,|_{E_g^{\min}}^{E_g^{\max}}\, K_\alpha\, t_H \right] \times \xi_z \qquad (2.30)
\end{aligned}$$

where the dependence on the redshift is now contained in the dimensionless correction factor[16] ξ_z.
Note that in the density term, the factor $E^{-\alpha}$ contains the energy observed on Earth while $\dot{\varepsilon}\,|_{E_g^{\min}}^{E_g^{\max}}$ and K_α are calculated for specific values of the energy of the cosmic rays at the source. This notation is convenient as typically results are quoted as $\Phi_{\mathrm{CR}}(E)E^{-\alpha}$.

2.4.2 A Toy Calculation of the Cosmic Ray Energy Production Rate

It is instructive to estimate the energy production rate of primordial cosmic rays based on the arguments and physics principles discussed so far; detailed calculations are beyond the scope of this report and published results will be presented in Sec. 2.4.3. For simplicity, it will be assumed that proton propagation has a hard cut-off at $\sim 10^{11}$ GeV due to interactions with CMB photons. For proton energies below the pion production threshold, pair production with the CMB $p + \gamma \rightarrow p + e^+e^-$ limits the range of protons. The radiation length of the process has its minimum of $\sim 1.4\,\mathrm{Gpc}$ for a proton energy of about $10^{19.3}$ eV, see Sec. 2.3.3. This is approximately one third of the Hubble distance of $c/H_0 \approx 4.2\,\mathrm{Gpc}$ and corresponds to a redshift of $z \approx 0.6$ in an Einstein-de Sitter Universe according to Eq. 2.10.
A narrow energy band from $10^{18.5}$ to $10^{19}\,\mathrm{eV}$ is chosen from the cosmic ray fluxes given in [57] and shown in Fig. 2.6. The lower bound ensures that only extra-galactic cosmic ray flux is considered while the upper bound was chosen far below the pion production threshold. Approximating the observed energy spectrum with a spectral index of 2, for the energy range mentioned above the diffuse cosmic ray flux on Earth is estimated as $\Phi_{\mathrm{CR}}(E)\,E^2 \approx 6 \times 10^{18}\,\mathrm{eV\,km^{-2}\,yr^{-1}\,sr^{-1}}$. The pure redshift loss of energy is $E(z) = (1+z)E(z=0)$ and the centre of mass energy squared of the photon-proton system accordingly scales with $(1+z)^2$. The energy band chosen above for the cosmic ray flux observed on Earth is roughly a factor of $10^{0.5}$ below the proton energy of $10^{19.3}$ eV which corresponds to the minimum of a radiation length of $1.4\,\mathrm{Gpc}$. In the proton energy range from 10^{19} to $10^{20}\,\mathrm{eV}$, the radiation length is close to this minimum value [86]. With $10^{0.5} = (1+z)^2$, the peak of the pair production cross section is reached at a redshift of $z_{\max} \approx 0.8$. This corresponds to a distance that is of about the same size as the radiation length at that energy. Hence the energy of protons at $z \approx 0.8$ must actually be *higher* than $10^{19.3}$ eV to reach Earth within the

[16] The definition and notation of ξ_z follows [83].

energy band from $10^{18.5}$ to 10^{19} eV. However, for higher energies the photo-pion production threshold of $\sim 10^{20}$ eV is quickly reached. Therefore, cosmic rays reaching Earth with energies above 10^{18} eV must be relatively close, originating from sources with $z < 1$ [83]. For the estimate done here, $z_{\rm max} = 1$ will be used which should underestimate the resulting energy production rate corresponding to a given cosmic ray flux observed on Earth.
Multiplying Eq. 2.29 by E^2 and inserting the estimated flux one obtains the relation

$$\frac{6 \times 10^{18}\,\mathrm{eV}}{\mathrm{km}^2\,\mathrm{yr\,sr}} \approx E^2\,\frac{c}{4\pi}\,\dot{\varepsilon}\,|_{E_g^{\rm min}}^{E_g^{\rm max}}\,K_\alpha \int_0^{z_{\rm max}} dz \frac{H^{-1}(z)}{1+z}(1+z)^m E_g^{-2}\frac{dE_g}{dE}$$

where a generation spectrum with index $\alpha = 2$ was assumed. Since E^2 does not depend on z, it can be pulled into the integral,

$$\begin{aligned}\frac{4\pi}{c}\,\frac{6 \times 10^{18}\,\mathrm{eV}}{\mathrm{km}^2\,\mathrm{yr}} &\approx \dot{\varepsilon}\,|_{E_g^{\rm min}}^{E_g^{\rm max}}\,K_\alpha \int_0^{z_{\rm max}} dz \frac{H^{-1}(z)}{(1+z)^2}(1+z)^m \\ &= \dot{\varepsilon}\,|_{E_g^{\rm min}}^{E_g^{\rm max}}\,K_\alpha\,\xi_z\,t_H\end{aligned}$$

where $\frac{dE_g}{dE} = \frac{E_g}{E} = (1+z)$ was used, i.e. redshift losses are assumed to be the only energy loss mechanism. The second line follows the notation of Eq. 2.30 with $t_H = H_0^{-1}$. Hence, it remains to calculate ξ_z to obtain

$$\dot{\varepsilon}\,|_{E_g^{\rm min}}^{E_g^{\rm max}}\,K_\alpha \approx \frac{24\pi \times 10^{18}\,\mathrm{eV}}{\mathrm{km}^2\,\mathrm{yr}}\,\frac{H_0}{c}\,\xi_z^{-1} \quad .$$

For an Einstein-de Sitter Universe ($\Omega_m = 1$, $\Omega_\Lambda = 0$), and using $z_{\rm max} = 1$, the integration yields $\xi_z \approx 0.33(0.8)$ for no source evolution (evolution with $m = 3$). For the purposes of this toy calculation, $\xi_z \approx 0.5$ will be used. Inserting the numerical values and transforming units the result is

$$\dot{\varepsilon}\,|_{E_g^{\rm min}}^{E_g^{\rm max}}\,K_\alpha = E_g^2\,\frac{d\dot{n}}{dE_g} \approx 0.4 \times 10^{44}\,\mathrm{erg\,Mpc^{-3}\,yr^{-1}} \quad . \tag{2.31}$$

As will be shown in Sec. 2.4.3, this calculation agrees well with published results.
As can be seen in Eq. 2.31, when assuming a particular spectral index α for the production of cosmic rays, the quantity $\dot{\varepsilon}\,|_{E_g^{\rm min}}^{E_g^{\rm max}}\,K_\alpha$ (or $E^2\,\frac{d\dot{n}}{dE}$ for $\alpha = 2$) contains no explicit dependence on energy. The expression is frequently quoted to characterise the energy production rate of cosmic ray accelerators.

2.4.3 Published Results of the Cosmic Ray Energy Production Rate

The challenge of deducing the production rate and spectrum of primordial cosmic rays from the cosmic ray flux observed on Earth has been addressed by several authors, see e.g. [98] and references therein. In [99], an energy production rate of $\dot{\varepsilon} = 4.4 \pm 1.5 \times 10^{44}\mathrm{erg\,Mpc^{-3}\,yr^{-1}}$ was derived for the energy range 10^{19} to 10^{21} eV, based on results of the Fly's Eye (a precursor experiment of HiRes) and AGASA experiments. The spectral index is given as $\alpha = 2.3 \pm 0.5$, i.e. consistent with a value of 2 that is typically assumed for cosmic accelerators. For $\alpha = 2$, the normalisation constant is $1/\ln(10^{21}/10^{19}) \approx 1/4.6$ so that

$$E^2\frac{d\dot{n}}{dE} \approx 10^{44}\mathrm{erg\,Mpc^{-3}\,yr^{-1}} \quad [99] \tag{2.32}$$

This calculation has most notably been used to derive an upper bound on the neutrino flux from cosmic accelerators that will be discussed in Sec. 2.5.1. An updated calculation [98] including newly available data from the Pierre Auger Observatory found

$$E^2 \frac{d\dot{n}}{dE} = (0.45 \pm 0.15)(\alpha - 1) \times 10^{44}\,\mathrm{erg\,Mpc^{-3}\,yr^{-1}} \quad [98] \tag{2.33}$$

for $E > 10^{19.5}\,\mathrm{eV}$ with $2 \lesssim \alpha < 2.7$. In [30], a cosmic ray production rate of $\dot{\varepsilon} = 2.2 \times 10^{44}\,\mathrm{erg\,Mpc^{-3}\,yr^{-1}}$, based on Pierre Auger Observatory results, is given for the energy range $10^{18.7}$ to $10^{22}\,\mathrm{eV}$. Assuming $\alpha = 2$, this energy production rate yields $E^2 \frac{d\dot{n}}{dE} = 0.3 \times 10^{44}\,\mathrm{erg\,Mpc^{-3}\,yr^{-1}}$, which is consistent with the value of Eq. 2.33.

2.4.4 The Composition of Cosmic Rays

In the calculations so far it has been assumed that extra-galactic UHECRs are composed of protons. Recent results from the Pierre Auger Observatory [100] indicate that with increasing energy above $10^{18}\,\mathrm{eV}$, the cosmic ray composition shifts from protons or light nuclei toward heavy nuclei. The final results of the HiRes Collaboration [101] for the same energy region on the other hand are consistent with a light, mainly protonic composition. These measurements rely heavily on hadronic interaction models used for the simulation of the air showers at highest energies, which are subject to large uncertainties, presumably much larger than suggested by the spread of available Monte Carlo model predictions [102]. Further investigations are needed to conclude on the subject of the cosmic ray composition where measurements of the cosmogenic photon flux may in the future help to resolve the question [103].

If UHECRs would be (at least to a part) composed of heavier nuclei, this would significantly affect the conclusions that can be drawn from cosmic rays observed on Earth about the composition of primordial cosmic rays and their production spectrum. Different compositions of cosmic rays imply different interaction processes, both at the accelerator itself and with cosmic background photons on the way to Earth. This in turn implies different neutrino fluxes.

The energy a particle can obtain in a cosmic accelerator is proportional to the atomic number Z, which makes it easier for heavy nuclei to reach the high energies of cosmic rays observed on Earth. The threshold for pair production (see Sec. 2.3.3) rises for heavy nuclei w.r.t. protons proportionally to the atomic mass A [104] while the energy loss rate increases by a factor of Z^2/A w.r.t. a proton with the same Lorentz factor, see [30] and references therein. Photo-pion production (see Sec. 2.3.4) also takes place for nuclei, albeit again with a threshold increased by a factor of A, see Fig. 2.10(a). Most importantly, for heavy nuclei, the process of photo-disintegration becomes dominant over photo-pion production. Furthermore, as discussed in Sec. 2.3.7, the Cosmic Infrared Background (CIB) contributes significantly to the propagation losses of nuclei with energies near the GZK cutoff. Given the relatively large experimental uncertainties of the spectral density of CIB photons, the rate of photo-disintegration over cosmological distances are accordingly difficult to predict [104]. Further discussions of cosmic ray composition can be found in [30, 105, 106] and references therein.

Important for the cosmic ray composition observed on Earth is the question of how long nuclei are processed in galactic accelerators. In case that charged particles cannot escape the magnetic fields of the accelerators, nuclei are completely disintegrated. Only neutrons are ejected, which decay to protons on their way to Earth. Charged nuclei observed on Earth then

originate only from the fringes of the accelerators [30][17]. Alternatively, different sources of cosmic rays with different compositions could be assumed.
The GZK cutoff as described in Sec. 2.3.5 is a feature of a proton-dominated cosmic ray flux. It is also possible to explain the observed cutoff in the cosmic ray spectrum for a flux of iron nuclei [107, 108] in which case it is the result of photo-disintegration. As the maximum energy a nucleus can obtain in an accelerator scales with Z, in this scenario protons would not be accelerated to energies beyond the photo-production threshold with CMB-photons. The energy per nucleon from photo-disintegration would be below the threshold for photo-production with the photons of the CMB. Fluxes of cosmogenic neutrinos would be strongly suppressed, originating from β-decay of neutrons and from interactions of protons with the extragalactic infrared and optical background [107], with neutrino energies below the UHE regime.
In conclusion it can be said that if heavy nuclei constitute a significant portion of cosmic rays observed on Earth, then even for the case of a concluding measurement of the composition, uncertainties on the expected composition of the cosmic rays at the source will remain. Measurements of UHE neutrino fluxes could help to resolve these uncertainties.

2.5 Bounds on Neutrino Production at the Sources of Cosmic Rays

In this section, different approaches to predict bounds on the expected diffuse flux of neutrinos will be introduced, assuming they are produced in cosmic accelerators together with the cosmic rays observed on Earth. Similar to the discussion in Sec. 2.4.1 for cosmic rays, a uniform density of the neutrino sources n_ν is assumed and an isotropic distribution of the neutrino flux. In Secs. 2.5.1 and 2.5.2, the so-called Waxman-Bahcall upper bound will be discussed and in Sec. 2.5.3, the approach by Mannheim, Protheroe, and Rachen will be introduced. In both cases, a cosmic ray flux composed of protons is assumed. In Sec. 2.5.4, the effect of the cosmic ray composition on the neutrino flux will be discussed and in Sec. 2.5.5, experimental limits from Cherenkov neutrino telescopes will be compared to the bounds.

2.5.1 Waxman-Bahcall Upper Bound

Starting from the primordial cosmic ray energy production rate as discussed in Sec. 2.4, a neutrino flux on Earth can be calculated. In [83] this is done under the following assumptions:

1. The generation spectrum of cosmic rays follows a power law $dn/dE_g \propto E_g^{-2}$.
2. The sources of the high-energy protons are optically thin to photo-pion production and proton-nucleon interactions.
3. The flux of cosmic rays observed on Earth is not affected by magnetic fields throughout the Universe.

[17] In that reference, the argument is applied to protons, but it seems reasonable to generalise it to nuclei.

Assumption 2 assures that the protons in the accelerator, after producing charged pions via one of the processes mentioned, can leave the accelerator to be observed on Earth as cosmic rays[18]. GRBs and AGN jets are discussed as potential sources in [83].
First, the energy production rate of primordial cosmic ray protons (see Sec. 2.4.1) is related to that of muon neutrinos (and anti-neutrinos) as

$$\dot{\varepsilon}_{\overline{\nu}_\mu \nu_\mu}(E_{p,g}^{\min}, E_{p,g}^{\max}) \approx 0.25\,\epsilon\,\dot{\varepsilon}_p|_{E_{p,g}^{\min}}^{E_{p,g}^{\max}} \quad , \tag{2.34}$$

where it has been assumed that high-energy protons produced by extra-galactic sources lose a fraction $\epsilon < 1$ of their energy through production of (charged and neutral) pions before escaping the source. The factor 0.25 arises because about half the energy is carried away by neutral pions and because furthermore for the decay of a pion according to Eq. 2.2, muon neutrinos carry about half of the charged pion energy.
Equation 2.34 was derived for the *total* energy of the produced neutrinos, independent of whether one neutrino is expected at a given energy or two neutrinos at half that energy. Assuming that the neutrino energy spectrum follows that of the protons, the relation can be rewritten for a spectral index $\alpha = 2$ as

$$E_{\overline{\nu}_\mu \nu_\mu, g}^2 \frac{d\dot{n}_{\overline{\nu}_\mu \nu_\mu}}{dE_{\overline{\nu}_\mu \nu_\mu, g}} \ln(E_{\overline{\nu}_\mu \nu_\mu, g}^{\max}/E_{\overline{\nu}_\mu \nu_\mu, g}^{\min}) \approx 0.25\,\epsilon\,E_{p,g}^2 \frac{d\dot{n}_p}{dE_{p,g}} \ln(E_{p,g}^{\max}/E_{p,g}^{\min}) \quad , \tag{2.35}$$

where Eq. 2.28 was used. The normalisation of the neutrino energy is then done by deriving a factor $f < 1$ for $E_\nu = f E_p$. As is obvious from Eq. 2.35, as long as f is independent of the energy, the ratios of the maximum and minimum energy (and therefore the logarithms) are the same for the cosmic ray and neutrino energy and the terms cancel out. As long as no cutoff in the cosmic ray spectrum is assumed, there is also no cutoff in the neutrino spectrum and the factor f enters only as part of the factor ϵ.
The flux of muon neutrinos, scaled by the square of the neutrino energy, is then derived from Eq. 2.30, using Eq. 2.35 with $\ln(E_{\overline{\nu}_\mu \nu_\mu, g}^{\max}/E_{\overline{\nu}_\mu \nu_\mu, g}^{\min}) = \ln(E_{p,g}^{\max}/E_{p,g}^{\min}$ as

$$\begin{aligned} E_{\overline{\nu}_\mu \nu_\mu}^2 \Phi_{\overline{\nu}_\mu \nu_\mu} &= \frac{c}{4\pi}\,\dot{\varepsilon}_{\overline{\nu}_\mu, \nu_\mu}\,|_{E_{\overline{\nu}_\mu \nu_\mu, g}^{\min}}^{E_{\overline{\nu}_\mu \nu_\mu, g}^{\max}} K_\alpha\, t_H\, \xi_z \\ &\approx \frac{c}{4\pi} 0.25 \epsilon E_{p,g}^2 \frac{d\dot{n}_p}{dE_{p,g}}\, t_H \xi_z \qquad (2.36) \\ &< 1.5 \times 10^{-8} \xi_z \mathrm{GeV\ cm^{-2}\ s^{-1}\ sr^{-1}} \quad , \qquad (2.37) \end{aligned}$$

where in the last step it was set $\epsilon = 1$ and the numerical value for $E_p^2 \frac{d\dot{n}_p}{dE_p}$ from Eq. 2.32 was used. Note that the condition for an optically thin source is $\epsilon \ll 1$, such that the upper bound indeed overestimates the expected flux. Strictly speaking, for a given ϵ, the energy available for cosmic rays to reach Earth would be $1 - \epsilon$ at most, so that a factor of $\epsilon/(1-\epsilon)$ instead of ϵ should have been used. However, as long as $\epsilon < 0.5$, it follows $\epsilon/(1-\epsilon) < 1$ and the difference in the scaling does not matter for the estimate of the upper bound.
To calculate the factor ξ_z, an Einstein-de Sitter Universe is assumed and the cases of no source evolution and of strong evolution are calculated. The resulting factors are $\xi_z^{s.e.} \approx 3$

[18] Protons may be confined by strong magnetic fields preventing them from escaping from the accelerator, see e.g. [97, 109]. In this case, neutrons are ejected which then produce the protons observed on Earth via β-decay. In [83] this option is also discussed.

and $\xi_z^{n.e.} \approx 0.6$ for strong evolution (s.e.) and no evolution (n.e.), respectively [83]. The strong evolution case was calculated for an evolution described by Eq. 2.11. The resulting Waxman-Bahcall bound is

$$E_\nu^2 \Phi_{\nu_\mu \overline{\nu}_\mu} < 1.5 \times 10^{-8}\,\mathrm{GeV\ cm^{-2}\ s^{-1}\ sr^{-1}} \begin{cases} \times 0.6 & \text{(no evolution)} \\ \times 3 & \text{(strong evolution)} \end{cases} . \tag{2.38}$$

This bound was calculated without taking into account anti-electron neutrinos which are generated in the β-decay of neutrons, produced together with charged pions at the Δ-resonance (see Eq. 2.18). However, these neutrinos have an energy of roughly two orders of magnitude below the energy of the neutrinos from pion decay, see e.g. Ref. [88]. Hence, if they are produced in similar numbers as neutrinos from pion decay, due to the E^{-2} source spectrum, their flux is exceeded by a factor of $\sim 10^4$ by the neutrinos from pion decay at a given energy. See [30] for a qualitative discussion.

2.5.2 A Discussion of the Waxman-Bahcall Bound

Cherenkov neutrino telescopes are sensitive to the tracks of muons created in reactions of muon neutrinos, which motivates quoting the Waxman-Bahcall bound for that neutrino flavour. Due to the effects of neutrino oscillation (see Sec. 3.1), in fact only half of that flux limit applies to observations on Earth. Acoustic neutrino detection on the other hand, as will be discussed below, is insensitive to the neutrino flavour. Taking the energy going into *all* flavours (i.e. also the electron neutrino) from the decay of charged pions into account, Eq. 2.34 must be multiplied with a factor 3/2.
Furthermore, the bound is directly proportional to the energy production rate of primordial cosmic rays. Using the newer result from Eq. 2.33 instead of Eq. 2.32 reduces the bound by about a factor of 2. However, since the Waxman-Bahcall bound is frequently used as a benchmark to compare the sensitivities of neutrino detectors, usually the values from Eq. 2.38 are kept for consistency.
Note that the value of $t_H = 10^{10}\,\mathrm{yrs}$ which was used to derive the Waxman-Bahcall bound in Eq. 2.37 is smaller than the actual Hubble time (which is very close to the age of the Universe) of $H_0^{-1} \approx 1.4 \times 10^{10}\,\mathrm{yrs}$. However, for the calculation of the parameter ξ_z in Ref. [83], an Einstein-de Sitter Universe is assumed. The age of the Universe in this case calculates as $2/3 H_0^{-1}$, which is very close to $10^{10}\mathrm{yrs}$. Therefore, it seems more consistent to use this value for t_H.
It must be kept in mind that the Waxman-Bahcall bound overestimates the expected neutrino flux by a factor of about $5/\tau$, i.e. at least by a factor of 5 [110], where $\tau < 1$ is the optical depth for nucleons escaping the source. In [30], the Waxman-Bahcall bound is turned into a prediction for neutrino fluxes by making some further assumptions. The results for AGNs and GRBs derived in that reference were already presented in Sec. 2.1.1 and will be discussed in some more detail in the context of neutrino production in accelerators of heavy nuclei in Sec. 2.5.4. It is also pointed out in that reference that for interactions of the cosmic ray protons with the ambient gas (i.e. pp rather than $p\gamma$ collisions), the average fraction of the total pion energy carried by charged pions is 2/3, compared to 1/2 in the photo-pion channel, increasing the upper bound given in Eq. 2.38 by 33%.

2.5.3 Mannheim-Protheroe-Rachen Upper Bound

An alternative calculation of an upper bound on extra-galactic neutrino production is given in [97], referred to as Mannheim-Protheroe-Rachen (MPR) bound. The derivation of this bound is done as follows. It is assumed that protons are confined within the acceleration region, such that only photo-produced neutrons are leaving this region, which in turn produce protons via β-decay. Assumptions 2 and 3 used to derive the Waxman-Bahcall bound in Sec. 2.5.1 are adopted, but no assumption about a particular generation spectrum of cosmic ray sources is made. Instead, consistent with the available data, an upper bound on the extra-galactic cosmic ray proton flux of

$$\Phi_p = 0.8 \times \left(\frac{E_p}{1\,\mathrm{GeV}}\right)^{-2.75} \mathrm{cm}^{-2}\mathrm{s}^{-1}\mathrm{sr}^{-1}\mathrm{GeV}^{-1} \tag{2.39}$$

in the energy range from 3×10^6 GeV to 10^{12} GeV is used for the calculation. Furthermore, no GZK cutoff is assumed.

Then a number of test spectra for proton sources with cutoff energies $E_{\max}$ in the range $10^6\,\mathrm{GeV} < E_{\max} < 10^{12}\,\mathrm{GeV}$ is generated, whose energy production rate is tuned to be consistent with the cosmic ray flux given above. In addition, the diffuse extra-galactic gamma-ray background (EGRB) measured by the satellite experiment EGRET [111] is used to limit the extra-galactic gamma-ray flux from the decay of charged pions. For sources thin to neutrons, this limit however has only a small effect.

Neutrino production rates are calculated by assuming that their spectra follow those of the cosmic ray test spectra at reduced energy. The expected fluxes are then proportional to the production rate and the energy-loss horizon of a particle. Energy-loss horizons are calculated for photons (below 30 GeV), neutrinos and protons. For the former two, the horizon is due to the adiabatic cooling due to the expansion of the Universe. For protons, in addition the interactions with the CMB in form of photo-pion production and pair production have to be included (see Sec. 2.3).

The resulting flux of muon (and anti-) neutrinos times energy squared, $\Phi_{\overline{\nu}_\mu\nu_\mu} E^2_{\overline{\nu}_\mu\nu_\mu}$, is plotted in Fig. 2.11. The underlying $E^{-2.75}$ dependence of the cosmic ray flux on Earth in Eq. 2.39 leads to a decrease of the MPR bound with energy until at $E_\nu \approx 10^7\,\mathrm{GeV}$, a value within a factor of ~ 2 above the Waxman-Bahcall bound for strong evolution is reached. The MPR bound remains within this factor of 2 until it reaches the Waxman-Bahcall bound for $E_\nu \approx 10^9$ GeV. The subsequent rise of the bound for $E_\nu > 10^9$ GeV is a consequence of the strongly increasing ratio of the neutrino and proton energy-loss horizons above that energy, in combination with the assumption that cosmic ray sources are homogeneously distributed in space. In order to account for the cosmic ray flux observed on Earth in the absence of a GZK cutoff, the sources must become more intense, which then increases the neutrino production according to the ratio of the respective energy-loss horizons. If the GZK cutoff enters the calculation, the normalisation of the cosmic ray sources to the cosmic ray flux on Earth reduces the cosmic ray production rate and therefore the neutrino flux is suppressed. This way the MPR bound will be closer to the Waxman-Bahcall bound beyond 10^9 GeV [97]. Considering the GZK cutoff established with the results of the Pierre Auger Observatory, the MPR bound and the Waxman-Bahcall bound are of the same order of magnitude for $E > 10^{18}$ GeV, which is the region of interest for this report.

In addition to the calculation for sources transparent to neutrons discussed so far, sources opaque to neutrons are also considered in [97]. In the latter case, neutrons cannot escape

the source whereas neutrinos can, which leads to a much higher neutrino flux relative to the cosmic ray flux observed on Earth. The bound on the neutrino flux then is essentially derived from the measurement of the EGRB. While by definition an upper bound cannot be disproved by an experimental limit that is lower than that bound, experimental data make it unlikely that the extra-galactic cosmic ray flux on Earth is dominated by sources that are opaque to cosmic rays, see Fig 2.11. For this reason, and due to the agreement with the Waxman-Bahcall bound in the UHE range when the GZK cutoff is taken into account, the Waxman-Bahcall bound will be used for the remainder of this report as a landmark for neutrino fluxes.

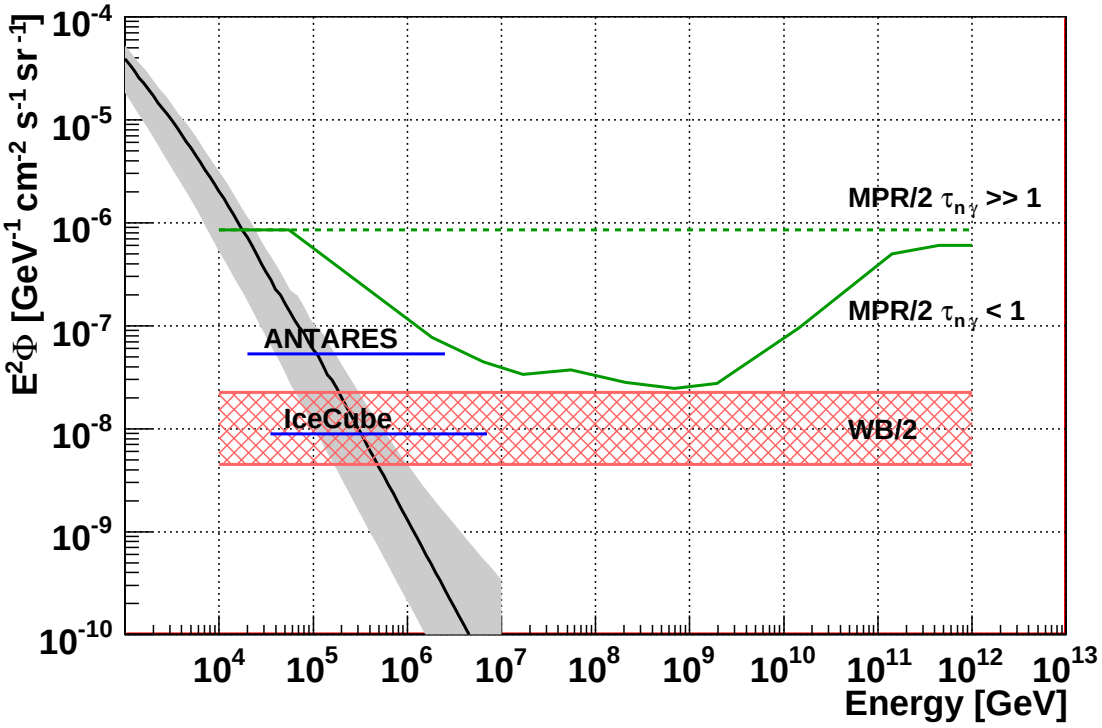

Figure 2.11: Upper bounds on the muon neutrino flux derived from measurements of cosmic ray fluxes and recent experimental limits from Cherenkov neutrino telescopes. The Waxman-Bahcall bound (WB) and the Mannheim-Protheroe-Rachen bound for optically thick (MPR $\tau_{n\gamma} \gg 1$) and thin (MPR $\tau_{n\gamma} < 1$) sources have been scaled by a factor $1/2$ to account for oscillations. For the Waxman-Bahcall bound, the band limited by the two cases of no evolution and strong evolution according to Eq. 2.38 is shown. Experimental limits from ANTARES [112] and IceCube [113] are 90% C.L. upper limits for a flux with spectral index 2. The grey band represents the expected variation of the atmospheric ν_μ flux from [112]: the minimum is the Bartol flux from the vertical direction; the maximum the Bartol+RQPM flux from the horizontal direction, see text. The central line is averaged over all directions.

2.5.4 Neutrinos from Cosmic Accelerators of Nuclei

In Sec. 2.4.4 the implications for sources of cosmic rays were discussed if UHECRs observed on Earth are composed of heavy nuclei. If cosmic ray sources accelerate heavy nuclei which interact with radiation fields at the source, then the nuclei will undergo photo-disintegration.

If this photo-disintegration continues until the nuclei are completely broken up into their constituent nucleons, then the resulting neutrino flux will not differ strongly from the case that protons are accelerated [30]. If this is not the case, fewer nucleons will be available for photo-pion production, reducing the flux of neutrinos. If on the other hand inelastic scattering with ambient gas (rather than photons) dominates, then both protons and nuclei will produce charged pions which in turn decay to neutrinos [30]. In this case, the Waxman-Bahcall bound will remain essentially unchanged for a cosmic ray composition of heavy nuclei. Hence, if heavy nuclei are accelerated at the source, the expected neutrino flux depends strongly on the scattering processes at the source.
In [114] a calculation following that of the Waxman-Bahcall bound described above is performed for the case that cosmic rays are produced as nuclei, assuming photon-nucleus interactions via the giant dipole resonance, see Sec. 2.3.7. The assumption that the sources are optically thin to nucleons (assumption 2 from Sec. 2.5.1) implies for the calculation of the Waxman-Bahcall bound that protons do not lose energy at the source. This assumption is now changed such that UHECR nuclei must survive photo-disintegration (either completely, optical depth ≈ 0, or "almost" with one disintegration process at most) and escape the source without loss of energy. For the best case, i.e. the highest flux, a limit about a factor of 10 below the Waxman-Bahcall bound is found, with only weak dependence on the mass number A of the nucleus.
In [30], AGNs, GRBs and Starburst galaxies are investigated as potential cosmic accelerators of heavy nuclei and the expected neutrino rates are estimated. It is found that in GRBs, most nuclei will undergo complete disintegration, while for AGNs, the rate of disintegration depends on the energy: Below about 10^{19} eV, nuclei escape largely intact, while above that energy an increasing degree of disintegration occurs. The neutrino spectra for AGNs and GRBs according to this model were already shown in Figs. 2.2 and 2.4. The differences in the changes of the spectra for AGNs and GRBs, when shifting from a proton to an iron composition, are reflected in the figures.
Starburst galaxies emit heavy nuclei largely intact, rendering them a potential source for a heavy nuclei flux on Earth, while not producing a significant amount of neutrinos at the source.
A simple estimate can be made by assuming a composition of 75% protons and 25% iron (which is consistent with Pierre Auger Observatory data). The combined flux from AGNs and GRBs of neutrinos of all flavours for this case was estimated in [30] as

$$\Phi_\nu E_\nu^2 \sim 1.0 \times 10^{-9}\,\mathrm{GeV\ cm^{-2}\ s^{-1}\ sr^{-1}}\,.$$

In general, neutrino fluxes due to pion decay in case of heavy nuclei composition of cosmic rays are lower than those for protons such that the Waxman-Bahcall bound remains valid as upper limit.

2.5.5 Experimental Results from Cherenkov Neutrino Telescopes

Here and in the following, it will be assumed that the reader is familiar with the detection technique of Cherenkov neutrino telescopes; an introduction can be found e.g. in [115]. In Fig. 2.11, experimental limits from the ANTARES [112] and IceCube [113] neutrino telescopes are compared to the upper bounds discussed above. The IceCube results are already below the Waxman-Bahcall bound for the case of strong evolution.

The flux of atmospheric neutrinos is also shown in the figure. It is mainly due to neutrinos from the decay of charged mesons (pions and kaons) and in the high-energy region roughly follows $E^{-3.7}$ (see [116] and references therein). A calculation of this flux has been done in [117], referred to as "Bartol flux". An additional component is due to the decays of short-lived hadrons containing charm and bottom quarks. In [112] this component was calculated using the models considered in [118], in particular the Recombination Quark Parton Model (RQPM).
Atmospheric neutrinos constitute a significant background to measurements of the diffuse neutrino flux with Cherenkov neutrino telescopes. At ultra-high energies, background from atmospheric neutrinos becomes negligible.

2.6 Production of Cosmogenic Neutrinos

As already discussed in Sec. 2.1.2, the reaction of cosmic ray protons with cosmic background photons leads to the production of cosmogenic neutrinos, posing a major motivation for the search for UHE neutrinos. Several authors have addressed the question of calculating the cosmogenic neutrino flux, see e.g. [119, 88, 120, 121, 104, 94, 105, 122]. If cosmic ray sources are uniformly distributed, then the GZK cutoff (or photo-disintegration for heavy nuclei) limits the energy of cosmic rays reaching Earth and the spectrum of cosmogenic neutrinos could be a probe of the maximum energy of the cosmic rays at the source [119]. The flux of cosmogenic neutrinos provides information about source evolution since neutrinos reach Earth from much further distances than cosmic rays. On the other hand, a lack of cosmogenic neutrinos could be an indication for a cosmic ray composition of heavy nuclei or for a single source cosmic ray origin.
In Sec. 2.6.1, the calculation of the cosmogenic neutrino flux will be demonstrated for protons reacting with the CMB, and in Sec. 2.6.2 it will be discussed how the flux is affected by the cosmic ray composition, the presence of the CIB, and the evolution of the sources of cosmic rays. While by themselves yielding less stringent results than calculations for cosmic rays, gamma-rays can also be used to constrain the cosmogenic neutrino flux, which will be discussed in Sec. 2.6.3.

2.6.1 A Calculation for Protons

In Sec. 2.4, the production rate of primordial cosmic rays was derived. With this information, in [88] a flux of muon- and electron-neutrinos is derived from the propagation of ultra-high-energy protons, based on simulations of photo-pion production with CMB photons using the Monte Carlo Program SOPHIA[19] [84]. For a given proton energy, the neutrino production rate $\dot{n}_\nu$ is proportional to the production rate of cosmic protons, $\dot{n}_p$. A neutrino with energy E_ν is produced by protons with a range of energy $E_p > E_\nu$, and the flux $\Phi_{\mathrm{CG}\nu}$ of cosmogenic neutrinos can be written as [88]

$$\Phi_{\mathrm{CG}\nu}(E_{\nu_i})E_{\nu_i} = \frac{c}{4\pi}\int\int Y_{\nu_i}(E_{p,g}, E_{\nu_i}, z)\frac{d\dot{n}_p}{dE_{p,g}}\left|\frac{dt}{dz}\right|(1+z)^m dE_{p,g}dz \quad , \tag{2.40}$$

[19] Simulations Of Photo Hadronic Interactions in Astrophysics

where $(1+z)^m$ again describes source evolution. The neutrino yield function Y_{ν_i} for neutrino flavour ν_i is defined as

$$Y_{\nu_i}(E_{p,g}, E_{\nu_i}, z) = E_{\nu_i} \frac{dn_{\nu_i}}{dn_p \, dE_{\nu_i}}$$

and is the number of secondary neutrinos generated per neutrino energy and per proton of energy $E_{p,g}$. The subscript g again denotes the energy at the time of the generation of a particle.

In the following, a coarse estimate of the cosmogenic neutrino flux will be done in order to demonstrate the principal features. For this, it will be assumed that the proton interacts (via the Δ^+-resonance) with the CMB above a sharp threshold E_p^Δ and that the proton interacts only once. Furthermore, the proton energy $E_p(z)$ must exceed some threshold to produce a neutrino of given energy $E_{\nu_i}(z)$; this threshold on the proton energy will be denoted by $E_p^{\rm thd}\left(E_{\nu_i}(z)\right)$. It will be assumed for simplicity that a fixed fraction of the proton energy is transferred to a neutrino. Hence, the yield of muon (and anti-muon) neutrinos is given by $Y_{\nu_\mu,\overline{\nu}_\mu} = 0$ for $E_p(z) < \max(E_p^\Delta(z), E_p^{\rm thd}\left(E_{\nu_i}(z)\right))$ and $Y_{\nu_\mu,\overline{\nu}_\mu} = 2$ for $E_p(z) \geq \max(E_p^\Delta(z), E_p^{\rm thd}\left(E_{\nu_i}(z)\right))$.

This of course underestimates the neutrino yield for high energies, since the cosmic rays will interact multiple times. Given the short mean free path of protons near the Δ^+-resonance, the adiabatic energy change of the proton between its production and the reaction with the CMB that creates the neutrino will be ignored. To simplify the notation, $E_p^{\rm thd}(z)$ will be use instead of $\max(E_p^\Delta(z), E_p^{\rm thd}(z))$, where it is understood that the proton energy is above the threshold for the Δ^+-resonance. Assuming furthermore a spectral index of 2, i.e. $\frac{d\dot{n}_p}{dE_{p,g}} = A\, {E_{p,g}}^{-2}$, the flux from Equation 2.40 for neutrino energies resulting from interactions of proton with energies exceeding $E_p^\Delta(z)$ can be written as

$$\begin{aligned}
\Phi_{\rm CG\nu}(E_{\nu_\mu\overline{\nu}_\mu})E_{\nu_\mu\overline{\nu}_\mu} &\approx \frac{c}{4\pi}\int_{z=0}^{z_{\rm max}}\int_{E_p^{\rm thd}}^{\infty} 2\,A\,E_{p,g}(z)^{-2}\left|\frac{dt}{dz}\right|(1+z)^m dE_{p,g}dz \\
&= \frac{c}{4\pi}\,2\,A\int_{z=0}^{z_{\rm max}} E_p^{\rm thd}(E_{\nu_i}(z))^{-1}\left|\frac{dt}{dz}\right|(1+z)^m dz \\
&= \frac{c}{4\pi}\,\frac{2\,A}{E_p^{\rm thd}(E_{\nu_i}(z=0))}\int_{z=0}^{z_{\rm max}}(1+z)^{-1}\left|\frac{dt}{dz}\right|(1+z)^m dz \\
&= \frac{c}{4\pi}\,\frac{2\,A}{E_p^{\rm thd}(E_{\nu_i}(z=0))}\,t_H\xi_z \quad . \qquad (2.41)
\end{aligned}$$

In the last step, the integral over z has been expressed as $t_H\,\xi_z$ following Eq. 2.30. In this simple estimate, the integral over proton energy was evaluated from a sharp starting energy up to infinity. A smooth transition of $\Phi_{\rm CG\nu}$ is introduced at lower energies, near the production threshold of cosmogenic neutrinos, due to the Planck spectrum of the CMB; at higher energies, usually a cutoff of the source spectrum according to $\frac{d\dot{n}}{dE} \propto E^{-\alpha} \times \exp(-E/E_{\rm max})$ is introduced ($E_{\rm max} = 10^{21.5}$ eV in [88]) which leads to a roll-off of the proton flux, and hence the neutrino flux, toward high energies. Equation 2.41 can therefore be seen as a peak value of the cosmogenic neutrino flux, where the neutrino energy $E_{\nu_\mu\overline{\nu}_\mu}^{\rm max}$ at which this peak value is reached is not specified.

Assuming that about 5% of the proton energy goes into each neutrino from pion decay [83],

i.e. $E_{\nu_i}(z) \approx E_p^{\rm thd}(E_{\nu_i}(z))/20$ and substituting $A \equiv {E_{p,g}}^2 \frac{d\dot{n}_p}{dE_{p,g}}$, yields the approximation

$$\Phi_{\mathrm{CG}\nu}(E^{\max}_{\nu_\mu\overline{\nu}_\mu}){E^{\max}_{\nu_\mu\overline{\nu}_\mu}}^2 \approx \frac{c}{4\pi}\frac{2}{20}\left[{E_{p,g}}^2\frac{d\dot{n}_p}{dE_{p,g}}\right] t_H \xi_z \quad . \tag{2.42}$$

Assuming the same primordial cosmic rays are generating neutrinos at the source and cosmogenic neutrinos, this result can be compared to the Waxman-Bahcall bound. It is lower by only a factor of about $2 \sim 3$ than the expression in Eq. 2.36 with $\epsilon = 1$. As mentioned above, the flux in Eq. 2.42 is underestimated due to the approximation of the neutrino yield function $Y_{\nu_\mu\overline{\nu}_\mu}$. For proton energies $E_p > 10^{20}$ eV, a more realistic value is $Y_{\nu_\mu\overline{\nu}_\mu} \approx 6 \sim 8$ [88], where obviously the proton energy and hence the neutrino energy is reduced in each interaction. The flux of cosmogenic neutrinos at its maximum value is therefore similar to the value of the Waxman-Bahcall bound at that energy. This is in fact not too surprising: For this *upper* bound, $\epsilon = 1$ was chosen, which would mean that all energy goes into neutrinos and none is left for the cosmic rays. However, this is what is happening for UHECRs with energies much bigger than the threshold for photo-pion production.

The results for the cosmogenic neutrino flux from [88] are shown in Fig. 2.12 and compared to the Waxman-Bahcall bound[20]. The normalisation of the source flux was done with the value from Eq. 2.32 which was also used to derive the Waxman-Bahcall bound. The flux is obviously directly proportional to the cosmic ray energy production rate and would consequently be reduced by a factor of about 2 when using the flux from Eq. 2.33.

For $\sim 6 \times 10^{20}\,\mathrm{eV}$ protons, at which energy the mean free path for photo-pion production with the CMB has its lowest value, the peak of the cosmogenic neutrino flux is expected to occur at $\sim 6 \times 10^{20}/20\,\mathrm{eV} \approx 3 \times 10^{19}\,\mathrm{eV}$. The energy will be further reduced due to redshift effects[21].

The neutrons produced according to Eq. 2.18 can produce anti-electron neutrinos via β-decay. The neutron decay length $\gamma c \tau_{\rm n}$ for the neutron life time of $\tau_{\rm n} = 885.7 \pm 0.8\,\mathrm{s}$ equals the neutron mean free path (which is about the same as the proton mean free path) of $\sim 4\,\mathrm{Mpc}$ for $\gamma \approx 4 \times 10^{11}$, i.e. at about $E_n \approx 4 \times 10^{20}$ eV. Neutrons of lower energy are more likely to decay than to interact [88]. This leads to a peak of electron anti-neutrinos between 10^{16} eV and 10^{17} eV [88, 119].

The cosmogenic neutrino flux can exceed the Waxman-Bahcall bound for harder ejection spectra or stronger source evolution [120]. In this case, either the protons creating neutrinos at the source and cosmogenic neutrinos would have to come from different sources (or possibly from different processes within the same source) or in principle the Waxman-Bahcall bound would have to be adjusted as well. Furthermore, the effects of the CIB and of cosmic ray composition have not been taken into account yet. This will be discussed now.

2.6.2 CIB, Cosmic Ray Composition, and Source Evolution

The CIB will lead to an additional neutrino peak of the cosmogenic neutrino flux at lower energies [123, 94]. This peak is in fact expected to exceed the peak from the interaction with the CMB due to the increase of the cosmic ray flux according to $E^{-\alpha}$ towards lower cosmic

[20] The lower bound of the Waxman-Bahcall flux of $0.9 \times 10^{-8}\,\mathrm{GeV\,cm^{-2}\,s^{-1}\,sr^{-1}}$, see Eq. 2.38, is underestimated in the figure by a factor of about 2.8, see *ftp://ftp.bartol.udel.edu/../seckel/ess-gzk/gzk_update.pdf*.

[21] Note that the peak shifts in the graphic depiction depending on whether the flux Φ is displayed as Φ, ΦE, or ΦE^2.

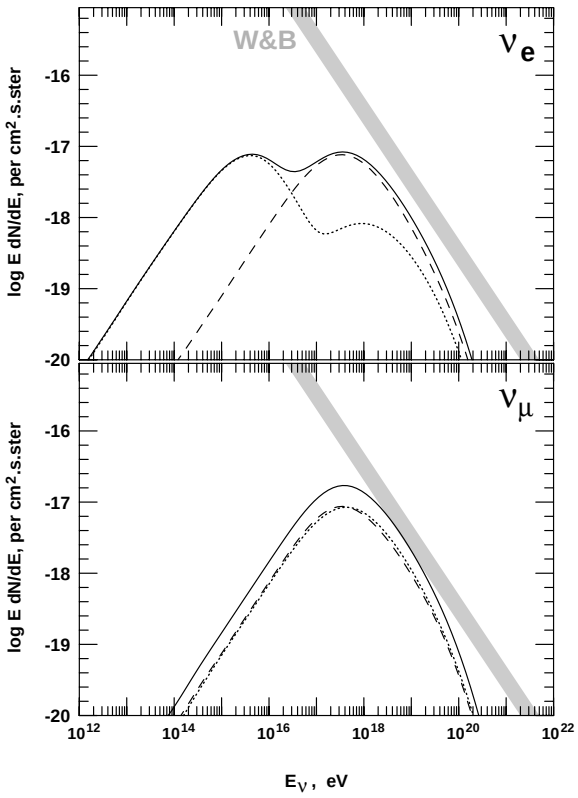

Figure 2.12: Fluxes of electron/muon neutrinos (dashed lines) and their anti-neutrinos (dotted lines) and the sum (solid line), generated in the propagation of protons. Fluxes for electron (anti-) neutrinos are shown in the upper panel, those for muon (anti-) neutrinos in the lower one. The shaded band shows the Waxman-Bahcall bound for muon neutrinos and anti-neutrinos given in Eq. 2.38. A spectral index of $\alpha = 2$ is assumed for the source spectrum, and a source evolution that corresponds to the upper limit of the Waxman-Bahcall bound (strong evolution). The flux of cosmogenic neutrinos is normalised to the same cosmic ray flux, given in Eq. 2.32, as the Waxman-Bahcall bound. In both cases, an Einstein-de Sitter Universe is assumed. From [88].

ray energies and the size of this peak depends strongly on the assumed spectral index of the source. For cosmic ray energies above the GZK cutoff, which by definition is the energy at which photo-pion production of protons with the CMB sets in, interactions with the CIB can be neglected.

For the cosmic ray composition, the principal statements about its effect on reactions of cosmic rays with photons from Sec. 2.5.4 remain valid and the composition strongly affects the expected rates of cosmogenic neutrinos [104, 124, 94, 105]. Given the uncertainties of the cosmic ray composition, results obtained for the flux of protons can again be regarded as an upper bound. The flux of cosmogenic neutrinos from photo-pion production for heavy nuclei with atomic mass A depends strongly on the energy cutoff at the sources: If the cutoff is high enough for the energy of the nucleons (which will in average be reduced by a factor of A w.r.t. the energy of the nucleus) created in photo-disintegration to exceed the threshold for photo-pion production with the CMB, then the flux is significantly enhanced w.r.t. an energy per nucleon below that threshold [104]. In Fig. 2.13, the neutrino flux on Earth for

several source compositions, consistent with Pierre Auger Observatory measurements, is shown [105]. A flat universe with $\Omega_\Lambda = 0.7$ and source evolution equivalent to Eq. 2.11 were assumed.
Since neutrinos (unlike cosmic rays) lose energy only through redshift losses when traversing cosmological distances, the horizon (or redshift z) up to which they can be observed is much increased w.r.t. cosmic rays. Hence, the evolution of their sources has a large effect on the observed fluxes of cosmogenic neutrinos[22]. To derive the upper bound for strong evolution described in Sec. 2.5.1, the evolution for quasars was used. Using enhanced rates of cosmological evolution for GRBs, the cosmogenic neutrino flux is consequently increased [125].
In conclusion, a measured spectrum of cosmogenic neutrinos would help to resolve questions about the CIB spectrum, source evolution and the composition of primordial cosmic rays and their maximum energy.

2.6.3 Constraints from Diffuse Gamma-Ray Background

The neutral pions created in interactions of cosmic ray protons with photons of the CMB, see Eq. 2.19, decay into photons. These interact with CMB photons to produce e^+e^- pairs which in turn engage in inverse Compton scattering with the CMB. The combined effect of these processes is a pile-up of gamma-rays at GeV–TeV energies, just below the threshold for further pair production. These photons should show up in the diffuse extra-galactic gamma-ray background (EGRB). The Large Area Telescope (LAT) installed on the Fermi Gamma-Ray Space Telescope spacecraft (Fermi-LAT for short) has measured the EGRB spectrum [126]. The measurement indicates a less intense and softer EGRB than previously measured with EGRET (see Sec. 2.5.3). Just as for the proton flux, the EGRB resulting from a given evolution model and energy spectrum at the cosmic ray sources can be compared to observation. This way, a bound on the neutrino flux based on EGRB measurements alone can be derived or the flux predictions obtained from the cosmic ray flux alone can be tightened [127, 128].
An upper bound on the all-flavour neutrino flux can be estimated by assuming that the complete photon energy density corresponding to the Fermi-LAT measurement is due to proton interactions with the CMB, namely through photo-pion production and pair production. The former process yields electromagnetic energy from the decay of neutral pions and from the electrons released in the decay of charged pions. Assuming the energy released in electromagnetic and neutrino radiation is about equal[23], the following *cascade bound* on the neutrino flux is found [128]:

$$E_\nu^2 \Phi_\nu(E_\nu) \leq \frac{c}{4\pi} \frac{\varepsilon_{\rm cas}^{\rm max}}{\ln(E_{\rm max}/E_{\rm min})} \frac{1}{1+\varepsilon_{\rm cas}^{e^+e^-}/\varepsilon_{\rm cas}^{\pi}} \quad ,$$

where a neutrino source spectrum proportional to E_ν^{-2} was assumed with maximum and minimum values $E_{\rm max}$ and $E_{\rm min}$ of the proton injection spectrum[24]. The total cascade energy density derived from the Fermi-LAT measurement of the EGRB spectrum is $\varepsilon_{\rm cas}^{\rm max} = 5.8 \times 10^{-7} {\rm eV\,cm^{-3}}$ [128] while $\varepsilon_{\rm cas}^{e^+e^-}$ and $\varepsilon_{\rm cas}^{\pi}$ are the cascade energies from pair production and photo-pion production, respectively.

[22] This is of course also true for the fluxes of neutrinos produced at the sources of the cosmic ray acceleration.

[23] In Sec. 2.3.4, a ratio of $1/3$ was derived for the Δ-resonance approximation. For energies far beyond the resonance, a ration closer to 1 is expected [88].

[24] As discussed in Sec. 2.5.1, the ratio of maximum and minimum values should be the same for the corresponding neutrino spectrum.

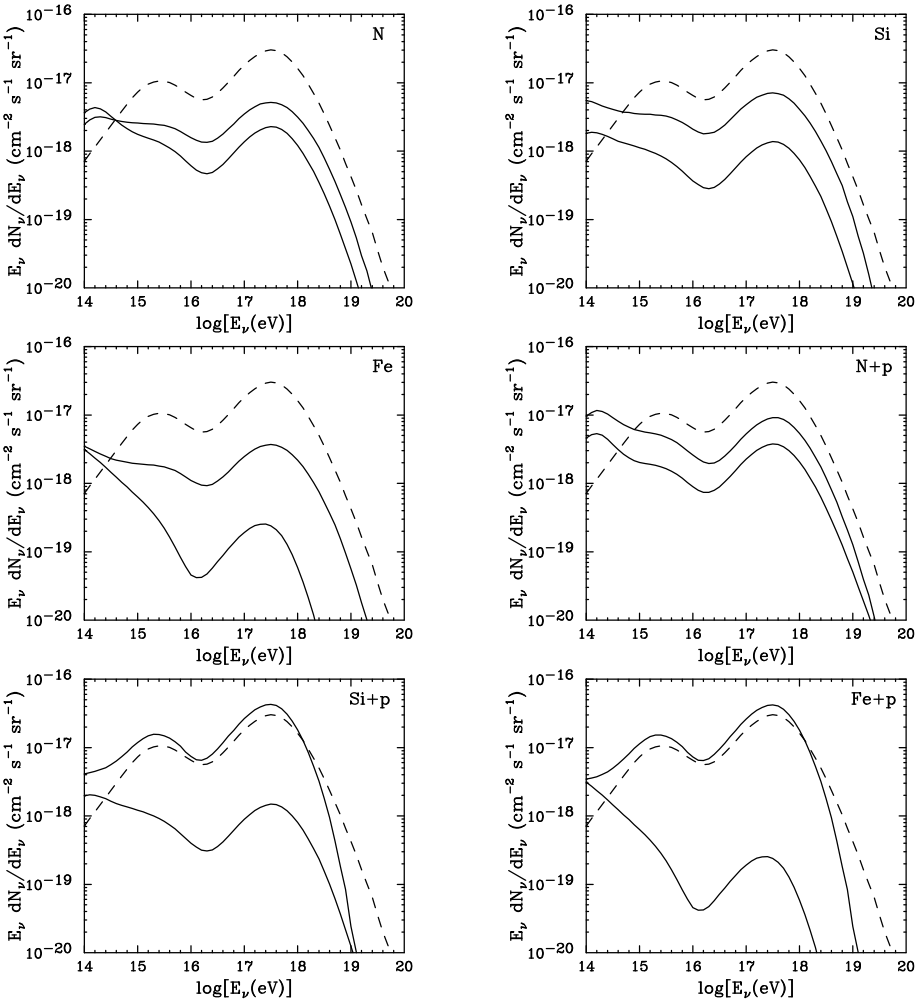

Figure 2.13: The range of cosmogenic neutrino spectra for various chemical species which are consistent with both the spectrum and composition measurements with Pierre Auger Observatory; data were obtained from publications predating [57, 100], see [105] for details. In each case, model parameters in the range $\alpha = 1.4 - 3.0$ and $E_{\rm max} \times 26/Z = 10^{20} - 10^{22}$ eV were considered (although models with $E_{\rm max} \times 26/Z$ below approximately 10^{21} eV were found to be inconsistent with the data). In the N+p, Si+p and Fe+p frames, the results for combinations of injected nuclei and protons are shown. In each frame, for comparison as a dashed curve the prediction for an all-proton spectrum with $\alpha = 2.2$ and $E_{\rm max} = 10^{22}/26$ eV is shown. The solid lines denote the models with the maximal and minimal spectra in terms of the expected event rate in a neutrino telescope. From [105].

The cascade energy density $\varepsilon_{\rm cas}$ for a given model depends on the energy cutoff and spectral index of the proton source, and on the source evolution. If the resulting value of $\varepsilon_{\rm cas}$ exceeds the value of $\varepsilon_{\rm cas}^{\rm max}$ from above, the model can be excluded. In this fashion, strong source evolution, with evolution index $m \gtrsim 3$ for integration up to $z_{\rm max} \gtrsim 4$, can be excluded [128]. Refer to the expression for the cosmic ray flux in Eq. 2.29 for a definition of these parameters. It is furthermore concluded that a cosmogenic neutrino flux can become detectable only in the case of source evolution ($m > 0$) in combination with a large value of $E_{\rm max}$.
In [127], the extra-galactic proton flux is calculated in dependence of the crossover energy between galactic and extra-galactic flux ($10^{17.5}$ eV to 10^{19} eV), the evolution index m and the spectral index α. The resulting proton flux is then fitted to the HiRes data [129] and consistency with the Fermi-LAT measurement of the EGRB is required. The cosmogenic neutrino flux is rather sensitive to the assumed cutoff energy of the proton spectrum at the source, the proton spectrum observed on Earth however is not, as a consequence of the GZK-cutoff. But with increasing cutoff energy, the number of photo-produced high-energy π^0's is also increased, which in turn enhances the density of the EGRB. Hence, the Fermi-LAT measurements constrain the energy cutoff of the cosmic ray sources [130]. In [127] a cutoff at $E_{\rm max} = 10^{21}$ eV is used[25].
The best fits yield spectral indices $\alpha \approx 2.5$ and evolution indices $m = 3.2 - 4.6$, depending on the crossover energy. The allowed range of the cosmogenic neutrino flux increases with the crossover energy. For all crossover energies considered, the range of models is at the 99% C.L. consistent with existing neutrino flux limits. Experimental data published after [127], in particular from ANITA [48] and IceCube [113] (see Fig. 2.11) do not change this statement; only for a crossover energy of $10^{17.5}$ eV, the IceCube flux limit is slightly below the 99% C.L. flux limit band[26] for a small range of neutrino energies around 10^9 GeV.
Results from [127] and [128] for combined fits to the cosmic ray and EGRB flux show some differences, those from [127] being larger by up to a factor of $\sim$30 for the same sets of parameters [127].

[25] This cutoff is again implemented using an exponential function as described on p. 47.
[26] If the IceCube limit is extended to 10^9 GeV.

Chapter 3

Aspects of Neutrino and Particle Physics

In this chapter, several aspects of neutrino and particle physics that are relevant for the detection of UHE neutrinos will be discussed. As neutrinos are known to posses mass, oscillations affect observations on Earth: the ratios of the neutrino flavours differ between production and observation. This will be discussed in Sec. 3.1. In Sec. 3.2, interactions of neutrinos will be discussed and the interaction processes as well as the formulae for calculating the relevant cross sections will be presented. At ultra-high energies, the cross section of neutrino-nucleon reactions becomes large enough to make Earth opaque to neutrinos. This affects the observation strategy for UHE neutrinos and will be the subject of Sec. 3.3. Finally, in Sec. 3.4, the deposition of the neutrino energy in the medium of the interaction through hadronic and electromagnetic showers, which is the prerequisite for the acoustic detection of neutrinos, will be discussed.

3.1 Neutrino Oscillations

Given the experimental finding that neutrinos have masses, the ensuing questions about their masses, oscillations and flavour mixing have been the subject of intense research. In the following, this subject will be discussed only very briefly in as far as necessary to explain the remarkable circumstance that the aforementioned generation of neutrinos in the ratios $N_{\nu_\mathrm{e}} : N_{\nu_\mu} : N_{\nu_\tau} = 1 : 2 : 0$ (see Sec. 2.1.1.1) will lead to a ratio observed on Earth of almost exactly $\tilde{N}_{\nu_\mathrm{e}} : \tilde{N}_{\nu_\mu} : \tilde{N}_{\nu_\tau} = 1 : 1 : 1$ [131].

3.1.1 Oscillations in Vacuum

Assuming three-flavour oscillations, i.e. in particular the absence of sterile neutrinos, the unitary 3×3 mixing matrix U is defined to fulfil

$$|\nu_\alpha >= \sum_{i=1}^{3} U_{\alpha i} |\nu_i > \quad , \tag{3.1}$$

where $|\nu_\alpha >$ corresponds to one of the flavour eigenstates of the neutrino $|\nu_\mathrm{e} >, |\nu_\mu >, |\nu_\tau >$ and $|\nu_i >$ denotes the mass eigenstates with $i \in \{1, 2, 3\}$. The matrix U is conventionally decomposed into three separate mixing terms:

$$U \equiv \begin{pmatrix} 1 & 0 & 0 \\ 0 & c_{23} & s_{23} \\ 0 & -s_{23} & c_{23} \end{pmatrix} \cdot \begin{pmatrix} c_{13} & 0 & s_{13}e^{-i\delta} \\ 0 & 1 & 0 \\ -s_{13}e^{-i\delta} & 0 & c_{13} \end{pmatrix} \cdot \begin{pmatrix} c_{12} & s_{12} & 0 \\ -s_{12} & c_{12} & 0 \\ 0 & 0 & 1 \end{pmatrix} \tag{3.2}$$

where s_{ij} and c_{ij} are short for $\sin\theta_{ij}$ and $\cos\theta_{ij}$, respectively, and δ is the CP-phase[1]. The three mixing angles θ_{12}, θ_{13} and θ_{23} have to be determined experimentally. Assigning the CP-violating term to the matrix element of θ_{13} is purely conventional. It can be shown that δ will be zero (i.e. no CP violation present) if any $\theta_{ij} \equiv 0$ or any two neutrino masses are identical. Since θ_{13} has been measured to be the smallest of the three mixing angles, and in fact to be consistent with zero, it is sensible to assign the CP-violating term to the matrix element of that angle.

After a flavour eigenstate $|\nu_\alpha>$ has been produced in a weak interaction, the mass eigenstates $|\nu_i>$ with energies E_i propagate and evolve in time from their time of production $t_0 = 0$ to a given time t according to

$$|\nu_i(t)> = e^{-i(E_i/\hbar)t}|\nu_i(0)> . \tag{3.3}$$

Using Eqs. 3.1 and 3.3, one can calculate the probability for a flavour state $|\nu_\alpha>$ to change into a flavour state $|\nu_\beta>$ after a time t according to

$$P_{\nu_\alpha \to \nu_\beta} \equiv |<\nu_\alpha(0)|\nu_\beta(t)>|^2 \quad .$$

it will be assumed that CP violation is negligible, and therefore all elements of the matrix U are real. Approximating the energy of ultrarelativistic particles by

$$E_i \approx |\vec{p}|c + \frac{m_i^2 c^4}{2|\vec{p}|c}$$

and denoting $E \equiv |\vec{p}|c$, the flavour changing probability can be written as

$$P_{\nu_\alpha \to \nu_\beta} = \delta_{\alpha\beta} - 4\sum_{i>j} U_{\alpha i}U_{\beta i}U_{\alpha j}U_{\beta j}\sin^2\left(\frac{\Delta m_{ij}^2 c^4}{4E\hbar}\frac{x}{c}\right) \tag{3.4}$$

where $\Delta m_{ij}^2 \equiv |m_i^2 - m_j^2|$ and the time t has been replaced by the distance from the source according to $t = x/c$. In the equation above, $\delta_{\alpha\beta}$ denotes the Kronecker symbol and must not be confused with the CP phase used in Eq. 3.2. From the symmetry of Eq. 3.4 it is clear that

$$P_{\nu_\alpha \to \nu_\beta} = P_{\nu_\beta \to \nu_\alpha} \quad . \tag{3.5}$$

The oscillation length for the transition between mass eigenstates $|\nu_i>$ and $|\nu_j>$ is defined as

$$L_{ij} \equiv \frac{4\pi E\hbar c}{\Delta m_{ij}^2 c^4} \quad . \tag{3.6}$$

[1]For simplicity it is assumed here that neutrinos are Dirac particles. For Majorana particles, two additional complex phases have to be introduced.

In a recent review [132], the following values for the neutrino mixing parameters are quoted:

$$\begin{aligned} \sin^2\theta_{12} &= 0.30 \pm 0.02 \qquad & (\theta_{12} &= 33.2^\circ \pm 1.3^\circ) \\ \sin^2\theta_{23} &= 0.50 \pm 0.07 \qquad & (\theta_{23} &= 45^\circ \pm 4^\circ) \\ \sin^2 2\theta_{13} &< 0.13 \qquad & (\theta_{13} &< 10^\circ) \end{aligned}$$

$$\begin{aligned} \Delta m^2_{13} &= 2.40^{+0.12}_{-0.11} \times 10^{-3}\mathrm{eV}^2 \\ \Delta m^2_{12} &= 7.6 \pm 0.2 \times 10^{-5}\mathrm{eV}^2 \end{aligned}$$

3.1.2 Oscillations over Cosmological Distances

Since neutrino sources are assumed to be distributed over cosmological distances that are huge compared to L_{ij}, and since neutrinos are produced over wide ranges of energy, the sine term involving the distance x of the source in Eq. 3.4 averages out:

$$\frac{1}{L_{ij}} \int_0^{L_{ij}} \sin^2(\frac{2\pi x}{2L_{ij}})\, dx = \frac{1}{2}\,.$$

It follows that only the three mixing angles of the matrix U from Eq. 3.2 are relevant to calculate the flavour oscillations.
Now substituting $\theta_{13} = 0^\circ$ and $\theta_{23} = 45^\circ$ (i.e. $\sin\theta_{23} = \cos\theta_{23} = 1/\sqrt{2}$), Eq. 3.2 simplifies to

$$U \equiv \begin{pmatrix} \cos\theta_{12} & \sin\theta_{12} & 0 \\ -\sin\theta_{12}/\sqrt{2} & \cos\theta_{12}/\sqrt{2} & 1/\sqrt{2} \\ \sin\theta_{12}/\sqrt{2} & -\cos\theta_{12}/\sqrt{2} & 1/\sqrt{2} \end{pmatrix}\,.$$

The last two rows of the matrix—representing the composition of the states $|\nu_\mu>$ and $|\nu_\tau>$, respectively, with the mass eigenstates—are up to sign factors of the matrix elements identical. It follows immediately that

$$P_{\nu_\mu\to\nu_\mu} = P_{\nu_\tau\to\nu_\tau}\,.$$

Furthermore,

$$P_{\nu_\mathrm{e}\to\nu_\mu} = P_{\nu_\mathrm{e}\to\nu_\tau}\,,$$

which follows from the condition $U_{\alpha 3} = 0$ for the state $|\nu_\mathrm{e}>$.
Combining it all, the relative numbers of neutrinos arriving on Earth, $\tilde{N}_{\nu_\mathrm{e}}, \tilde{N}_{\nu_\mu}, \tilde{N}_{\nu_\tau}$, can be calculated without explicit knowledge of θ_{12}:

$$\begin{aligned} \tilde{N}_{\nu_\mathrm{e}} &= 2P_{\nu_\mu\to\nu_\mathrm{e}} + P_{\nu_\mathrm{e}\to\nu_\mathrm{e}} \\ &= 2P_{\nu_\mu\to\nu_\mathrm{e}} + (1 - P_{\nu_\mathrm{e}\to\nu_\mu} - P_{\nu_\mathrm{e}\to\nu_\tau}) \\ &= 2P_{\nu_\mu\to\nu_\mathrm{e}} + (1 - 2P_{\nu_\mathrm{e}\to\nu_\mu}) \\ &= 1 \quad . \end{aligned}$$

$\tilde{N}_{\nu_\mu} = 1$ and $\tilde{N}_{\nu_\tau} = 1$ can be calculated in a similar fashion. This result is independent of the neutrino energy as long as the distances over which the neutrinos propagate are large compared to L_{ij}. For a 10^{21} eV neutrino, the larger of the two oscillation length is $L_{12} \approx 1\,\mathrm{kpc}$. Hence the derived results are valid also in the UHE region.

3.2 Neutrino Interactions and Cross Sections

By virtue of the fact that neutrinos interact only via the weak force, neutrino interactions have very low cross sections which makes them difficult to detect, requiring huge detection volumes. In the following, all neutrino interactions within the Standard Model are discussed,

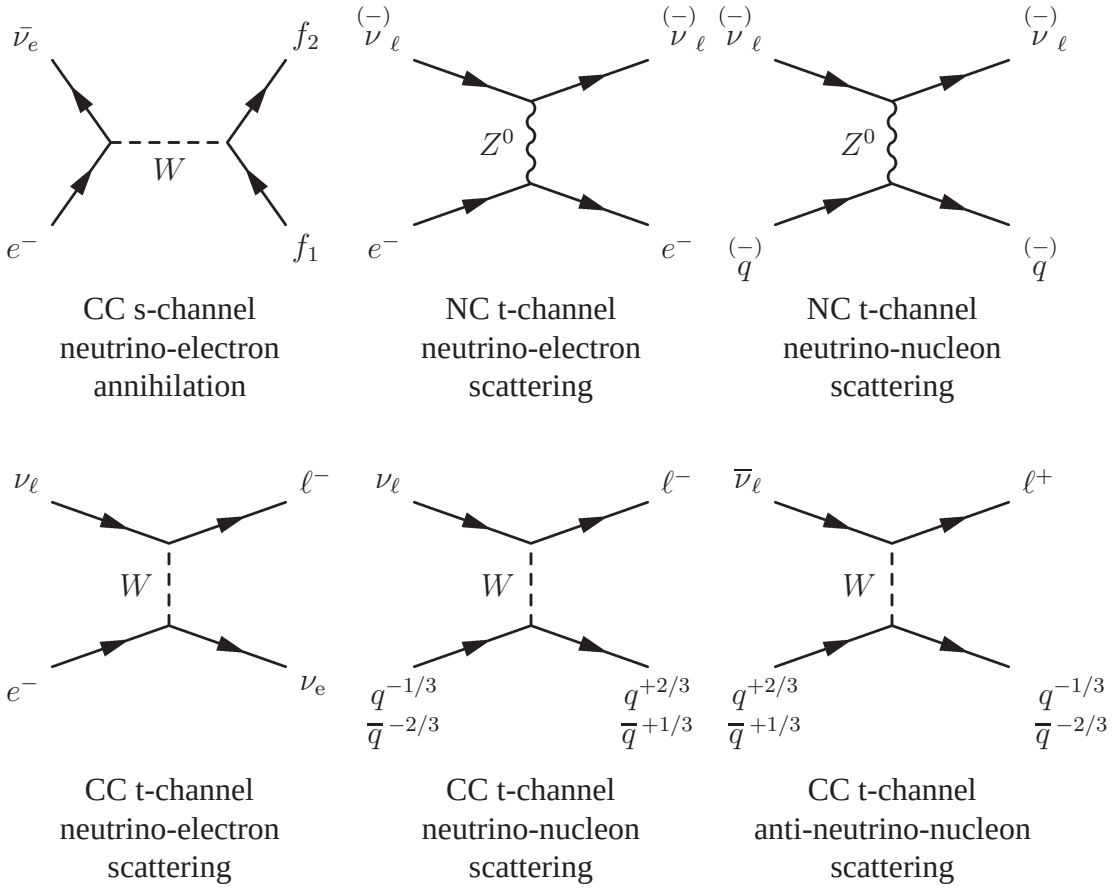

Figure 3.1: The Born level Feynman diagrams for reactions of neutrinos (ν_ℓ) and anti-neutrinos ($\bar{\nu}_\ell$) with matter. Time axis is pointing to the right. ℓ denotes any charged lepton, $q(\bar{q})$ any quark (anti-quark), where in some cases the charge is given as superscript. For the CC neutrino annihilation diagram the outgoing fermion f_1 can be any of $\bar{\nu}_\ell, q^{+2/3}, \bar{q}^{+1/3}$ and the other fermion f_2 accordingly $\ell^-, q^{-1/3}, q^{-2/3}$.

and for those which are relevant for UHE neutrino detection cross section formulae are given. Figure 3.1 shows Feynman diagrams for all neutrino interactions with matter on Born level and for single fermions, meaning quarks are not treated within their composite structure inside a proton or neutron. Weak eigenstates of the quarks coupling to the weak vector boson are obtained by applying the Cabibbo-Kobayashi-Maskawa (CKM) matrix.
A neutrino or anti-neutrino[2] of any flavour can interact with the electron or with a nucleon of a water atom via the exchange (t-channel) of a weak vector boson, either the Z^0 (neutral current, NC) or the $W^\pm$ (charged current, CC). The s-channel (annihilation) diagram is only

[2]In this section (Sec. 3.2) it will distinguished between neutrinos and anti-neutrinos.

relevant for the interaction of an incoming electron anti-neutrino with a shell electron of the target molecule.
For the calculation of cross sections, the square of the relevant matrix elements has to be calculated. For the matrix element, the propagator of the massive vector bosons introduces a term of the form

$$\text{vector boson propagator} \propto \frac{1}{q^2 - M_V^2} \quad , \tag{3.7}$$

where q is the 4-momentum transfer between the incoming particles and the mass of the vector boson M_V is either the mass of the Z-boson, M_Z, or of the W-boson, M_W. For the annihilation of two particles (s-channel) the relation $q^2 = s$, holds, where s is the square of the invariant mass. The resulting cross section peaks when $\sqrt{s}$ equals the mass of the massive vector boson, M_Z or M_W and is described by a Breit-Wigner shape (see e.g. Eq. 2.20).
For boson exchange (t-channel), the peak is "smeared out" as q^2 becomes negative and can take on any value between 0 and $-s$. More specifically the relation $Q^2 \equiv -q^2 = xys$ holds, where the new kinematic variables x and y have been introduced, both of which range from 0 to 1. For elastic scattering, $x \equiv 1$ holds, such that y and Q^2 are just two different ways to express the same kinematic situation. This is the case for neutrinos scattering off pointlike particles, in particular electrons.
For inelastic scattering, in particular for neutrino-nucleon scattering in the deep inelastic scattering (DIS) regime, y is commonly referred to as "inelasticity" and in the rest frame of the proton is given by the energy difference of the neutrino[3] before and after the emission of the vector boson, relative to its initial energy. Expressed differently, a fraction $(1 - y)$ of the initial energy E_ν of the neutrino will be carried by the lepton after the reaction, the rest is transferred to the nucleon. The quantity x is the Bjorken scaling variable and within the framework of the quark parton model (see e.g. [133]), this quantity can be identified with the momentum fraction of the proton which is carried by the quark that is participating in the interaction. Loosely formulated, for given values of s and y of a reaction, the vector boson with four-momentum q "picks out" quarks which carry a fraction $-q^2/ys$ of the proton momentum. In the centre of mass frame of the electron-quark system, the inelasticity y can also be expressed as $y = (1 - \cos\theta)/2$, where θ is the scattering angle For neutrino-electron scattering with $x \equiv 1$, the same expression for y is valid.
In the rest frame of the target proton with $s = 2m_N E_\nu$ the propagator now takes the form

$$\text{t} - \text{channel DIS propagator} \propto \frac{1}{M_V^2 + 2m_N E_\nu xy} \quad , \tag{3.8}$$

and clearly, for high neutrino energies E_ν and some average value of y, the value of x must be small in order for the expression 3.8 to be sizable. If $\langle y \rangle = 0.2$ is used, which will be motivated below, and $Q^2 \approx M_W^2$ is assumed as a typical momentum transfer, then for $E_\nu = 10^9$ GeV, the average value $\langle x \rangle = \frac{M_W^2}{2E_\nu m_N \langle y \rangle} \approx 1.7 \times 10^{-5}$ is found. This value is at the edge of the region so far investigated experimentally. Now neutrino electron reactions will be briefly discussed before turning to the more relevant case of neutrino-nucleon reactions.

Neutrino-electron scattering In the absence of inner structure, calculating neutrino-electron scattering cross sections within the Standard Model is fairly straight forward. The total

[3] In case of a CC reaction, the neutrino is transferred into a charged lepton, but in the highly relativistic regime, their mass difference is negligible.

cross section is calculated by integrating the squared matrix element over the scattering angle θ, or the related quantity y, respectively. Explicit calculations are performed in [134] and (based on that publication) in [135].
Of all neutrinos or anti-neutrinos interacting with matter, only the reaction $e^-\overline{\nu}_\mathrm{e}$ has an s-channel contribution, see Fig. 3.1. The resonance curve for that process peaks at a cross section of $5.02 \times 10^{-31}\,\mathrm{cm}^2$ for all final states combined [135]. This is indeed two orders of magnitude higher than the cross section for (anti-) neutrino scattering off nucleons at the same energy. However, in the rest frame of the electron, the peak in the cross section occurs at a neutrino energy of $E_\nu = 6.3\,\mathrm{PeV}$. For acoustic neutrino detection, this energy is below the detection threshold. Beyond the resonance, however, the cross section then falls off with $1/s$ (see e.g. the Breit-Wigner parametrisation in Eq. 2.20). Hence, for ultra high energies, namely $E_\nu \gtrsim 10^{18}\,\mathrm{eV}$, the effect of the resonance is not significant.
Turning to the t-channel, it should first be noted that the matrix element for the process $e^-\overline{\nu}_\mathrm{e} \to e^-\overline{\nu}_\mathrm{e}$ contains the contribution from both the t-channel *and* the s-channel. Hence, the cross section contains also an interference term between the two channels such that their contributions to the cross section strictly speaking cannot be separated. However, near the resonance, the s-channel contribution will be dominant while for $\sqrt{s} \gg M_V$, the t-channel contribution will dominate. For $\sqrt{s} \ll M_V$, the contributions are expected to be of similar size, in accordance with Eq. 3.7, where for $|q^2| \ll M_V^2$ the contribution from q^2 becomes negligible.
Calculations of cross sections at small energies $\sqrt{s} \ll M_V$ for neutrinos or anti-neutrinos of any flavour off electrons can e.g. be found in [136, 137]. In this regime, the propagator can be approximated by $1/M_V^2$ and, independent of the flavour of the neutrino or anti-neutrino, the integration of the differential cross section introduces a factor s from the particle four-vectors in the matrix element. In the rest frame of the electron, this factor is proportional to $m_e E_\nu$ where m_e is the electron mass. Hence in the case of heavier particles (e.g. a proton treated as a pointlike particle), the cross section scales with the mass.
For the case of leptons, for which $x \equiv 1$, the calculation for t-channel scattering for the case $\sqrt{s} \gg M_V$ leads to a flattening of the cross section with increasing neutrino energy, approaching a constant value [134]. For the process $e^-\overline{\nu}_\mathrm{e} \to e^-\overline{\nu}_\mathrm{e}$, this cross section is given as $2 \times 10^{-35}\,\mathrm{cm}^{-2}$ and is essentially constant for $E_\nu \gtrsim 10^{18}\,\mathrm{eV}$. For pointlike particles with higher mass, the flattening would set in at a lower energy. This however is not the case for neutrino-nucleon scattering, where the presence of sea quarks for high values of Q^2 leads to targets within the proton with small values of x, which in turn increases the cross section due to bigger values of the t-channel propagator, see Eq. 3.8. Neutrino-nucleon scattering will be discussed now. To conclude, neutrino-electron scattering is not relevant for UHE neutrino physics due to the pointlike structure of the electrons.

Neutrino-nucleon scattering The double differential CC and NC cross sections in the DIS regime can be expressed in terms of the structure functions F_2, xF_3 and F_L as[4]

$$\frac{d^2\sigma_i(\nu N)}{dxdQ^2} = \frac{G_F^2 M_V^4}{2\pi x(Q^2+M_V^2)^2}\left(Y_+ F_2^{\nu N,i}(x,Q^2) - y^2 F_L^{\nu N,i}(x,Q^2) \pm Y_- x F_3^{\nu N,i}(x,Q^2)\right) \tag{3.9}$$

[4]Frequently, the double differential cross section is expressed as $d^2\sigma/dxdy$, which introduces a factor $dQ^2/dy = sx$ on the right hand side.

where the $+(-)$ sign applies to neutrino (anti-neutrino) scattering and $Y_\pm \equiv 1 \pm (1-y)^2$. The Fermi constant is defined as $G_F = \frac{\sqrt{2}}{8}\frac{g^2}{M_W^2}(\hbar c)^3$, where g is the coupling constant of the weak interaction. The index i denotes either the CC or NC process and M_V is again the mass of the corresponding vector boson. The longitudinal structure function F_L is zero in leading order and negligible in NLO, except for $y \approx 1$. The structure function F_2 is related to the parton distribution functions (PDFs) $q_i(x, Q^2)$ of the quarks and $\overline{q}_i(x, Q^2)$ of the anti-quarks,

$$F_2 = \sum_i \left(\zeta_i^2 q_i(x, Q^2) + \tilde{\zeta}_i^2 \overline{q}_i(x, Q^2) \right) \quad , \tag{3.10}$$

where the sum runs over all (anti-) quarks that couple to the vector boson and ζ_i ($\tilde{\zeta}_i$) describes the coupling of the vector boson to the quark (anti-quark). Unlike the situation for couplings to photons, for the weak vector bosons the coupling strengths for quarks and anti-quarks do not simply differ by a sign. In particular, they can be finite for the one and zero for the other. Of the valence quarks within a nucleon, neutrinos (anti-neutrinos) couple only to the down (up) quark for CC coupling. Hence, neutrino-proton and neutrino-neutron scattering involve different structure functions F_2. For neutrino-nucleon scattering, for which cross sections will be presented below, these functions are averaged. The sea quark contributions, which dominate at ultra-high energies, do not depend on isospin, so that in this energy regime F_2 does not differ significantly for neutrino-proton and neutrino-neutron scattering.
Note that for NC interactions, in Eq. 3.9 the substitution $M_V = M_Z$ is made, whereas in the definition of the Fermi constant, the mass of the W-boson remains, which may seem inconsistent. However, one obtains $G_F^2 M_Z^4 = \frac{g^4}{32}\frac{M_Z^4}{M_W^4} = \frac{g^4}{32}\frac{1}{\cos^4\theta_W}$, where θ_W is the Weinberg angle, which is equivalent to replacing the coupling strength g for CC interactions by that for NC interactions, $g/\cos\theta_W$, with no M_W-terms remaining. Further factors present for the vertex factor of the Z-boson are absorbed in the factors ζ_i and $\tilde{\zeta}_i$ in Eq. 3.10.
For the parity violating structure function xF_3, which is specific to weak interactions, the PDFs of quarks enter the sum with a positive sign, those of anti-quarks with a negative sign, so that the result is small compared to F_2, see e.g. [138].
The relevant PDFs have been measured at the electron-proton collider HERA at DESY. In the low-x region, the contribution of the valence quarks becomes less and less important, as the contribution of the sea quarks, resulting from gluon splitting $g \to q\overline{q}$ becomes dominant. This leads to the effect that νN and $\overline{\nu} N$ cross sections for high energies show no significant difference. For low x and high Q^2, the gluon momentum distribution can be parametrised by $xg(x, Q^2) \propto x^{-\lambda}$ where $\lambda \sim 0.3 - 0.4$ [138]. As hinted above, the x values relevant for UHE neutrino scattering are much lower than the region $x \gtrsim 10^{-5}$, which has been probed by collider experiments. Taking the relatively modest energy of $E_\nu = 5.3 \times 10^9$ GeV, the relevant x-region is $10^{-8} \lesssim x \lesssim 10^{-4}$ [138]. Hence, the parametrisation of $xg(x, Q^2)$ requires extrapolations over several orders of magnitude, introducing large systematic uncertainties to the resulting cross section calculations. Three different parametrisation of neutrino-nucleon cross section will be discussed now.

Cross section formulae for neutrino-nucleon scattering In this paragraph, three different calculations for neutrino-nucleon cross sections are presented, shown in Fig. 3.2.

In [139], cross sections for CC and NC interactions are given separately for νN and $\overline{\nu} N$ interactions, the difference however being less than 1%. The averaged values are:

$$\sigma_{CC} = 5.53 \times 10^{-36}\mathrm{cm}^2 \left(\frac{E_\nu}{1\,\mathrm{GeV}}\right)^{0.363} \tag{3.11}$$

$$\sigma_{NC} = 2.30 \times 10^{-36}\mathrm{cm}^2 \left(\frac{E_\nu}{1\,\mathrm{GeV}}\right)^{0.363} \tag{3.12}$$

(Label “Gandhi et. al." in Fig. 3.2)

for the energy range $10^7\,\mathrm{GeV} \leq E_\nu \leq 10^{12}\,\mathrm{GeV}$.

In [140], values for the cross sections σ_{CC} and σ_{NC} are tabulated for $10\,\mathrm{GeV} \leq E_\nu \leq 10^{14}\,\mathrm{GeV}$ in steps of $\Delta \log(E/\mathrm{GeV}) = 1$. A parametrisation of the values with the form

$$\log\left(\frac{\sigma}{1\,\mathrm{pb}}\right) = a + b\left[\log\left(\frac{E}{\mathrm{GeV}}\right)\right]^c \tag{3.13}$$

(Label “fit to Berger et. al.” in Fig. 3.2)

with the parameters

$$CC: \quad a = 9.19 \quad b = -14.55 \quad c = -0.464 \tag{3.14}$$

$$NC: \quad a = 8.93 \quad b = -14.9 \quad c = -0.464 \tag{3.15}$$

deviates from the tabulated values by less than 5% in the range $10^6\,\mathrm{GeV} \leq E_\nu \leq 10^{14}\,\mathrm{GeV}$ and by less than 10% in the range $10^4\,\mathrm{GeV} \leq E_\nu \leq 10^6\,\mathrm{GeV}$.

Using the most recent results from the HERA-experiment ZEUS [138], the following CC cross section parametrisation is found to fit the calculated cross sections to better than 10% in the range $10^7\,\mathrm{GeV} \leq E_\nu \leq 10^{12}\,\mathrm{GeV}$:

$$\ln\left(\frac{\sigma_{CC}}{\mathrm{pb}}\right) = \ln(10^{-36}) - 98.8\left[\ln\left(\frac{E_\nu}{1\,\mathrm{GeV}}\right)\right]^{-0.0964} \quad . \tag{3.16}$$

(Label “Cooper S. & Sarkar” in Fig. 3.2)

At high energies, where only the sea quark contributions are relevant, quark and anti-quark PDFs are the same and the structure functions $F_2(x, Q^2)$ for CC and NC neutrino-nucleon interactions will differ by a constant factor. If both bosons had the same mass, one would therefore expect a constant ratio between the respective total cross sections.
For the values tabulated in [140], the ratio σ_{NC}/σ_{CC} increases from 0.40 to 0.43 between $E_\nu = 10^7$ GeV and 10^{12} GeV. For the cross sections from [139], the ratio is readily calculated from Eqs. 3.11 and 3.12 to be 0.416. Hence, by scaling the CC results from [138] for the range $10^7\,\mathrm{GeV} \leq E_\nu \leq 10^{12}\,\mathrm{GeV}$ by 0.415, it is expected that the results for the NC cross section are (relative to the CC cross section) correct within a few percent.

3.3 Neutrino Propagation through Earth

The relation $\lambda = 1/(n\sigma)$ (Eq. 2.21) can be used to calculate the mean free path of neutrinos traversing Earth. For this, the density of scattering centres n will be approximated by $n =$

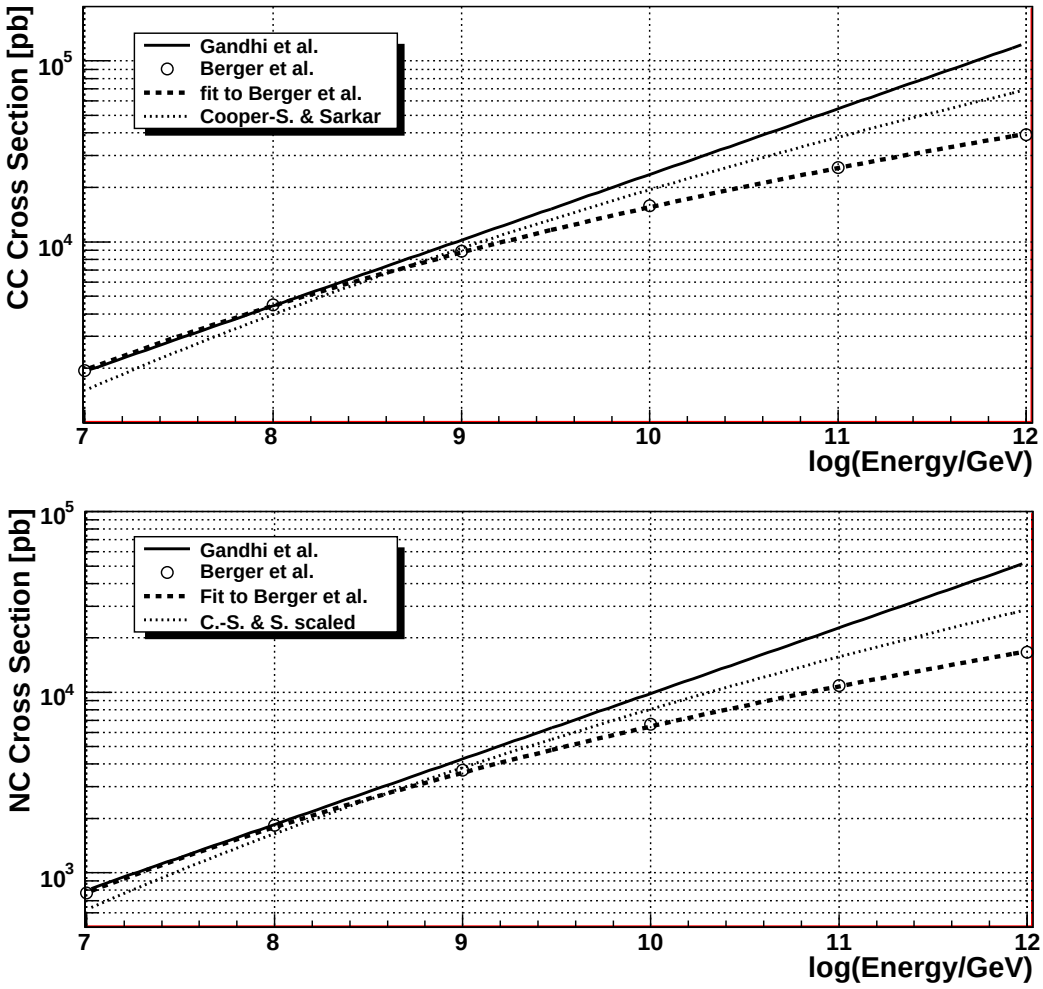

Figure 3.2: CC cross sections (top) and NC cross sections (bottom) for neutrino-nucleon scattering. The curves are labelled as follows: "Gandhi et al." corresponds to Eq. 3.11 (CC) and Eq. 3.12 (NC), respectively; "Berger et al." to the tabulated values from [140], and "fit to Berger et al." to Eq. 3.13 with the respective parameters for CC and NC interactions; "Cooper-S. & Sarkar" to Eq. 3.16 for CC interactions and "Cooper-S. & S. scaled" to Eq. 3.16 multiplied by 0.415 as described in the text.

ρ/m_N, where $\rho = 5.52\,\mathrm{g\,cm^{-3}}$ is the mean density of the Earth. The cross sections according to Eqs. 3.13 and 3.16 are used and CC and NC contributions are added. Results are shown in Fig. 3.3. For neutrinos with energies of interest for acoustic detection, $E_\nu \gtrsim 10^{18}$ eV, Earth is opaque, i.e. only neutrinos from the upper hemisphere can be detected. This is in contrast to optical detection of neutrinos at lower energies, but since tracks of atmospheric muons do not present a background for acoustic detection, this fact poses no problem for the method of acoustic neutrino detection.
In Fig. 3.3 the depth profile of the Earth has not been taken into account. The density of the Earth varies from $\rho = 3.5 - 13\,\mathrm{g\,cm^{-3}}$, see [136] and references therein, with the highest density in the core and the lowest in the crust. A parametrisation of the density profile of the Earth can be found in [141]. Hence, neutrinos skimming the outer parts of the Earth would in fact have a longer mean free path (and hence neutrinos from a larger angle below the horizon could reach the detector) which is not taken into account in the lower plot of Fig 3.3. On the other hand it is assumed that the detector is located at the top at a perfectly spherical Earth. Assuming a detector in $\sim$2 km depth would affect the angle in the opposite direction.

3.4 Energy Deposition in Neutrino Interactions

For both NC and CC reactions, the breakup of a nucleus within a water molecule inevitably leads to the formation of a hadronic shower, which is dominated by inelastic hadronic interactions. Acoustic detection, as will be described in Chapter 4, is sensitive to the energy deposited in the water in terms of heat, i.e. through particle showers. Hence, in stark contrast to optical detection, acoustic detection is about equally sensitive to CC and NC reactions. Hadronic showers are discussed in Sec. 3.4.1.
In the CC reaction of a neutrino, a charged lepton is furthermore created. For muons, the critical energy is at several hundred GeV [65] such that muons resulting from the interactions of UHE neutrinos lose their energy predominantly through radiative effects. These processes are characterised by small cross sections, hard spectra, large energy fluctuations, and the generation of electromagnetic and (in the case of photonuclear interactions) hadronic showers [65]. These showers in principle are detectable acoustically. To estimate the size of the effect, the energy loss of muons will be parametrised according to $-dE/dx = a(E) + b(E)\,E$ [65], where $a(E)$ and $b(E)$ are energy-dependent constants. In [142], for the region $E > 35.3\,\mathrm{TeV}$, values of $a(E) = -6.50 \times 10^{-3}\,\mathrm{GeV}\frac{\mathrm{cm^2}}{\mathrm{g^{-1}}}$ and $b(E) = 3.66 \times 10^{-6}\frac{\mathrm{cm^2}}{\mathrm{g}}$ for muons in water are given. From an extrapolation in the relevant figures in [65] for muons traversing copper and iron with energies beyond $10^5\,\mathrm{GeV}$, the approximation $-dE/dx \approx 9 \times 10^{-6}\,\frac{\mathrm{cm^2}}{\mathrm{g}}\,\rho\,E$ can be estimated, where ρ is the density of water. Hence for $-dE/dx \approx E/10^3\,\mathrm{m}$, which should overestimate the effect, the energy loss is spread out over a distance of the order of a kilometre while the hadronic showers from the breakup of the nucleus are rather compact in size, of the order of several metres. As will be shown in Chapter 4, the acoustic signal is sensitive to the *density* of the energy deposition. Hence, radiation from UHE muons is not expected to contribute to an acoustic signal. However, treating the radiative energy losses of muons as a continuous process for many purposes is not adequate.
Tau leptons, with a mass of $m_\tau \approx 1.78\,\mathrm{GeV}/c^2$, have a boost factor of $\gamma \gtrsim 5.6 \times 10^9$, for energies of interest for acoustic detection, $E \gtrsim 10^{18}\,\mathrm{GeV}$. Hence, for a lifetime of $t_\tau \approx 3.3 \times 10^{-13}\,\mathrm{s}$, in the rest frame of the observer a tau in average travels a distance of at least $\gamma c t_\tau \approx 560\,\mathrm{km}$. The particle can therefore be regarded as "stable" for purposes of

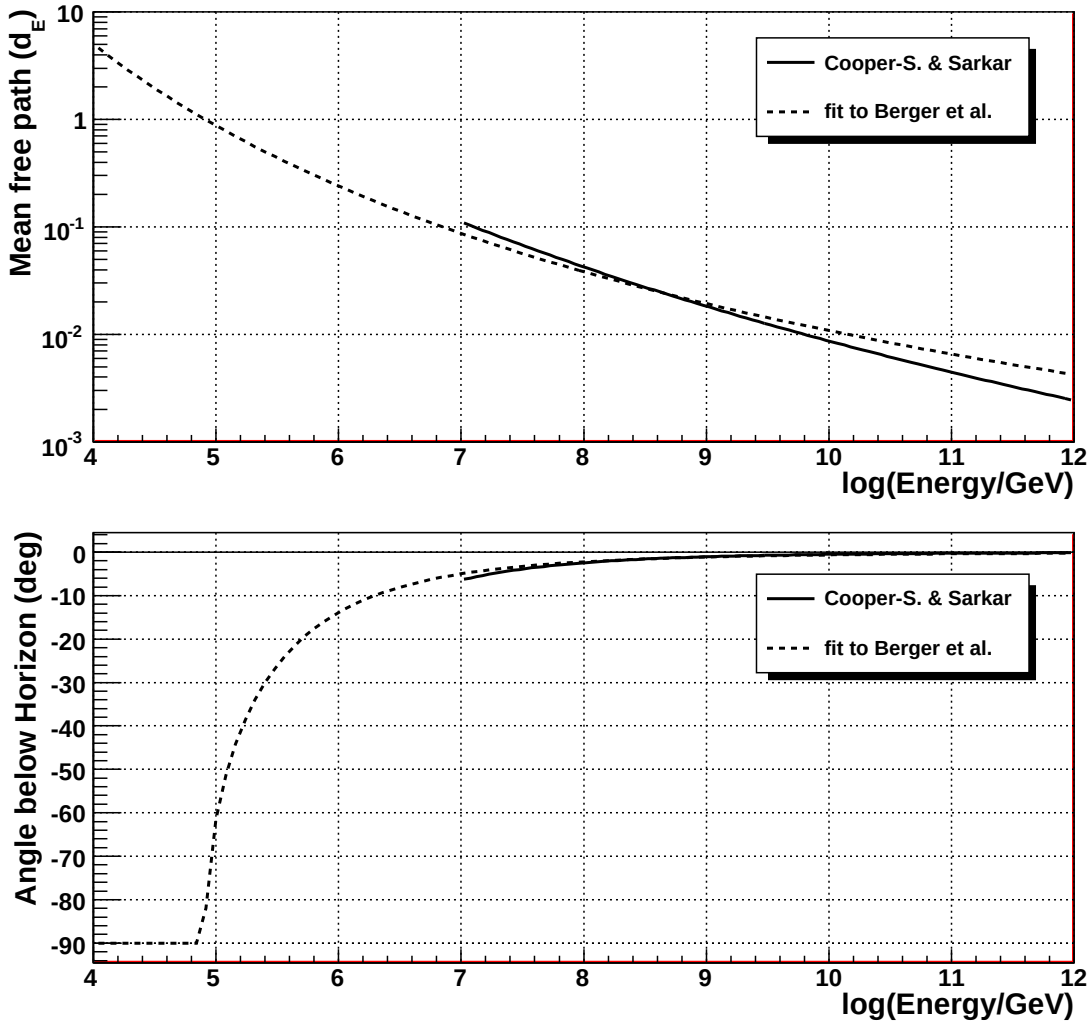

Figure 3.3: Mean free path for neutrinos traversing Earth in units of Earth diameters (top) and the angle below the horizon at which the Earth presents one mean free path's worth of material to an Earth-skimming neutrino. The detector is assumed at the surface and a constant density of the Earth has been assumed.

acoustic detection. Due to the higher mass, the critical energy is expected to be higher and radiative effects smaller than for muons. Hence, for all the charged leptons produced in CC interactions, only the energy deposited in electromagnetic showers resulting from the interaction of an electron neutrino is available for acoustic detection. Electromagnetic showers will be discussed in Sec. 3.4.2.

3.4.1 Hadronic Showers

As discussed in Sec. 3.2, the energy transferred to the nucleon, and therefore into the hadronic shower, in the reaction of a neutrino with energy E_ν is given by yE_ν. The y-dependence of the cross section can be obtained by expressing the double differential cross section, Eq. 3.9, as $\frac{d^2\sigma}{dxdy}$ and performing the integral over x. Hence, the y-distribution depends on the x-parametrisation with its uncertainties at low values, affecting calculations of cross sections for UHE neutrinos. The differential cross section $d\sigma/dy$ and the resulting average values $\langle y \rangle$

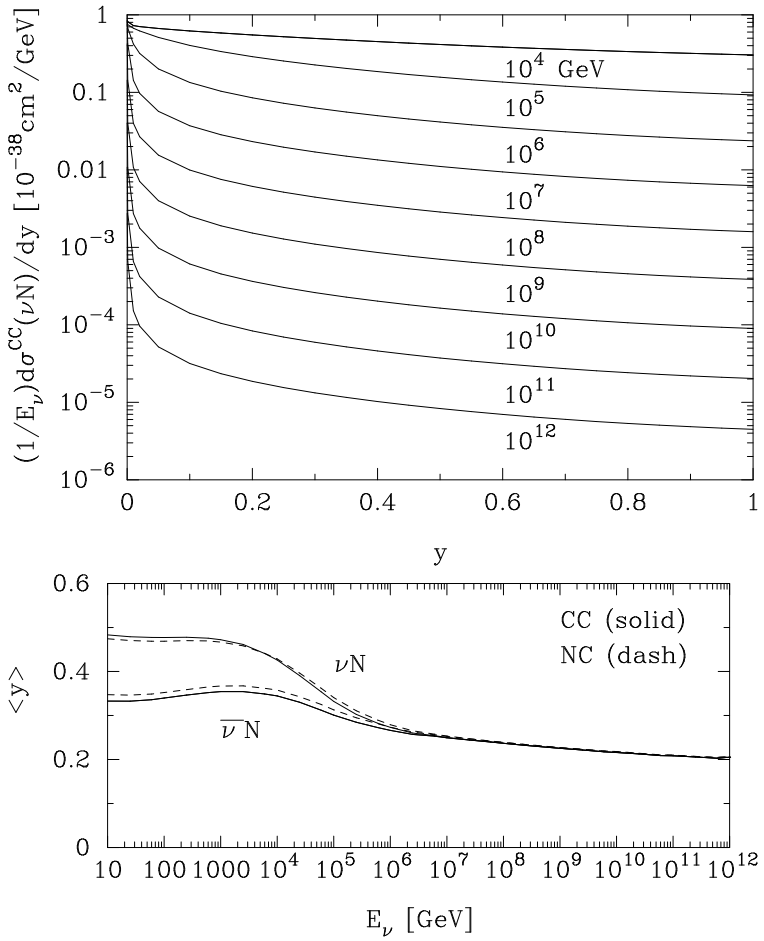

Figure 3.4: Top: Differential cross section for CC neutrino-nucleon scattering, scaled by the neutrino energy, for neutrino energies between 10^4 and 10^{12} GeV. Bottom: Energy dependence of the average of the inelasticity y for CC (solid lines) and NC (dashed lines) interactions of neutrinos and anti-neutrinos with nucleons as a function of the incident neutrino energy. From [135].

from [135] are shown in Fig. 3.4. Typically, a mean value of $\langle y \rangle \approx 0.2$ is assumed for UHE neutrinos.

Secondary particles produced in hadronic showers are mostly pions and nucleons, produced in the decay of excited nuclei. The decay of a π^0 leads to the production of two photons and the subsequent formation of an electromagnetic shower, which therefore are also always present in hadronic showers.

Event-by-event fluctuations of energy deposition (for a given value of y) and of spatial distributions of hadronic showers are large. This has several reasons. Depending on how early in the showers the first π^0's are produced, a more or less sizable fraction of the energy goes into electromagnetic showers. Furthermore, energy going e.g. into muons and neutrinos produced by charged pions is lost to the energy of the shower. And the energy going into the excitation and breakup of nuclei is sizable and subject to large event-by-event fluctuations.

No universally used parametrisation for hadronic shower exists. Frequently, the parametrisation for electromagnetic showers (see below) or similar ones are used. The scale of the longitudinal shower profile of hadronic showers is given by the nuclear interaction length

which for water is $\lambda_I = 83.3\,\mathrm{cm}$. As will become clear in Chapter 4, the energy distribution within the shower, most notably the lateral distribution, is a crucial quantity that determines the size of the acoustic pulse generated in a neutrino interaction. But shower simulations can be validated in fixed target experiments only up to the TeV-region[5]. Hence, simulations of showers and their event-by-event fluctuations pose a great theoretical challenge to the subject of acoustic detection of neutrinos.

3.4.2 Electromagnetic Showers and the LPM Effect

Electromagnetic showers, i.e. the cascading effects of bremsstrahlung and pair productions, at energies $E \lesssim 10^{15}$ eV have a longitudinal profile that is relatively easily parametrised by the radiation length X_0, and two energy and material dependent parameters a and b according to

$$\frac{dE}{dz} = E_0 b X_0 \frac{(bz/X_0)^{a-1}\exp(-bz/X_0)}{\Gamma(a)} \tag{3.17}$$

where the Gamma function $\Gamma(a)$ normalises the total shower energy to E_0. For water, $X_0 = 36.08\,\mathrm{g/cm^2}$, which is smaller than the nuclear interaction length by roughly a factor of 2.
In the conventional description of the electron scattering process, the interaction is treated as occurring at a single point. In dense media and at ultra-high energies, this approximation is not valid anymore and it must be taken into account that the emission of bremsstrahlung takes place over a distance where multiple scattering occurs. This perturbation acting on the particle within the coherence length leads to destructive interference, suppressing radiation and extending the size of the shower. Similar arguments can be applied to the related process of pair creation. This effect has been termed Landau-Pomeranchuk-Migdal (LPM) effect according to the first semi-classical description [143, 144, 145].
The formation length (or coherence length) over which the interaction spreads out can be approximated by [146]

$$l_f = \frac{2E_e E_e' \hbar c}{(m_e c^2)^2 E_\gamma} \quad ,$$

where E_e is the electron energy before the interaction, E_γ the energy of the emitted photon and $E_e' = E_e - E_\gamma$ the electron energy after the interaction. The mean angle of the multiple scattering ϑ_{MS} at some length l is [146]

$$\vartheta_{\mathrm{MS}} \;=\; \frac{E_S}{E_e}\sqrt{\frac{l}{2\rho X_0}} \tag{3.18}$$

with

$$E_S \;\equiv\; m_e c^2 \sqrt{\frac{4\pi}{\alpha}} \quad . \tag{3.19}$$

For $\vartheta_{\mathrm{MS}} \gtrsim 1/\gamma$ multiple scattering is expected to affect the interaction. The condition can be rewritten as $\frac{4\pi l}{2\alpha\rho X_0} \gtrsim 1$ using $\gamma = E_e/(m_e c^2)$ and Eqs. 3.19 and 3.18. Substituting the formation length for l yields $E_e(E_e - E_\gamma) \gtrsim E_\gamma E_{\mathrm{LPM}}$ where [147]

$$E_{\mathrm{LPM}} \equiv \frac{(m_e c^2)^2 \alpha \rho X_0}{4\pi\,\hbar\,c} = (7.7\,\frac{\mathrm{TeV}}{\mathrm{cm}} \times \rho X_0) \quad .$$

[5]Validation and testing results for hadronic physics are given on the GEANT4 web page *http://geant4.cern.ch/index.shtml*.

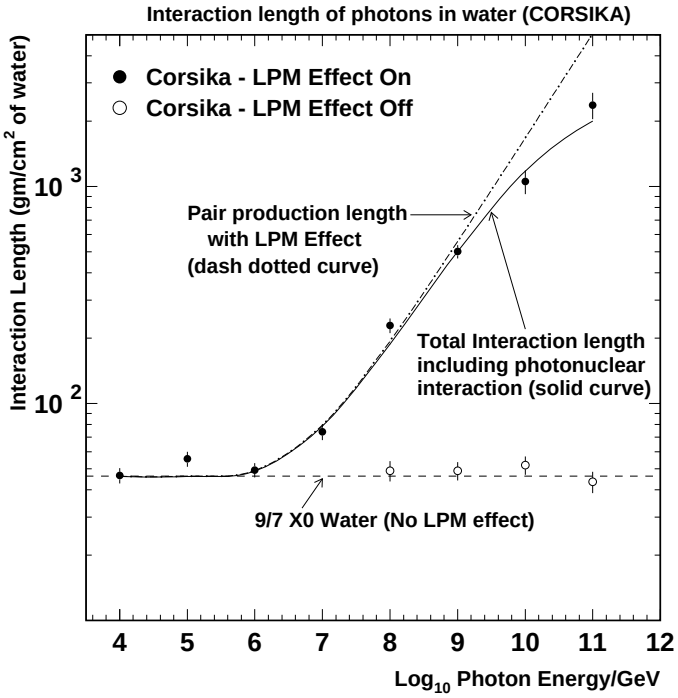

Figure 3.5: The interaction length for high-energy photons versus the photon energy measured with the simulation code CORSIKA (data points with statistical errors). The dash dotted curve shows the pair production length computed from the LPM effect using the formulae of Migdal [145]. The solid curve shows the computed total interaction length, including both pair production and photonuclear interactions with the cross section from CORSIKA. The dashed line labelled $9/7X_0$ shows the expected pair production length without the LPM effect. Here X_0 is the radiation length of the material. From [148].

Using $E_\gamma = E_e/2$ yields the relation $E_e \gtrsim E_{\mathrm{LPM}}$ such that E_{LPM} can be seen as the energy at which the LPM effect sets in. In water, $E_{\mathrm{LPM}} \approx 3 \times 10^{14}$ eV.
Fig 3.5 [148] shows the interaction length of high-energy photons as a function of energy [148] obtained with a modified version of the the simulation tool CORSIKA[6] [149]. At 10^{18} eV, the interaction length is already more than a factor of 10 bigger than the low energy value.
In Fig. 3.6, the longitudinal energy distribution of electromagnetic showers as obtained from a GEANT4[7] simulation is shown for energies in the LPM regime [150]. Up to $\sim 10^{17}$ eV, the parametrisation of Eq. 3.17 is valid, albeit above $\sim 10^{15}$ eV with parameters a and b that deviate from a simple extrapolation from lower energy values [150]. Then above $\sim 10^{18}$ eV the energy distribution becomes stochastic. While the LPM effect has been verified in collider experiments [151], simulations at UHE energies again have to be taken with caution as they lack experimental verification. See [150] and references therein for a detailed discussion.
Due to the electromagnetic component present in hadronic showers, the latter in principle should also show an elongation due to the LPM effect. However, as discussed in [152],

[6]COsmic Ray SImulations for KAscade, *http://www-ik.fzk.de/corsika/*

[7]GEometry ANd Tracking, a toolkit for the simulation of the passage of particles through matter *http://www.geant4.org*

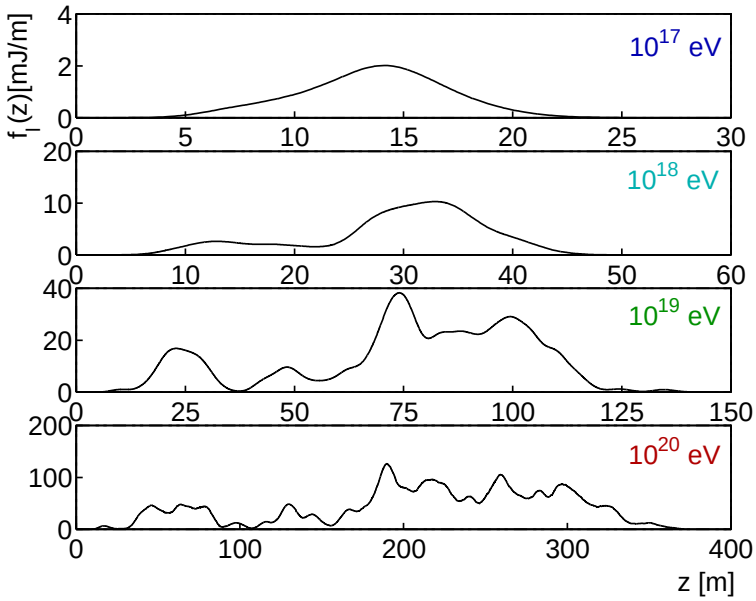

Figure 3.6: Examples of longitudinal energy distribution $f_l(z) \equiv dE/dz$ of LPM extended electromagnetic showers for shower energies of 10^{17}, 10^{18}, 10^{19}, and 10^{20} eV. From [150].

the fraction of the hadronic shower energy that goes into the first generation of photons in average is much smaller than for electromagnetic showers. Therefore the LPM effect is not relevant for hadronic showers.
For the CC interaction of a ν_e or $\overline{\nu}_e$, the complete energy of the neutrino is deposited in the water through hadronic and electromagnetic showers, where both components generate acoustic signals. This will be discussed now in Chapter 4.

Chapter 4

Acoustic Detection of UHE Neutrinos

In the previous chapters, the search for ultra-high-energy neutrinos was motivated and the underlying physics aspects were investigated. In this chapter, the acoustic detection of neutrinos will be discussed as one option to investigate the ultra-high-energy region. In Sec. 3.4, the deposition of energy in water through hadronic and electromagnetic showers, produced in the interaction of neutrinos with nuclei, was discussed. The resulting temperature change induces an expansion or contraction of the medium depending on its volume expansion coefficient. According to the thermo-acoustic model, the accelerated expansion of the heated volume—a micro-explosion—creates a pressure pulse of bipolar shape which propagates in the surrounding medium. The thermo-acoustic model is described in Sec. 4.1 and in Sec. 4.2, the formation of the signal in the environment of the ANTARES detector in the Mediterranean Sea will be discussed. In this context, the characteristic bipolar shape of the sound waves is derived and it is shown, how the shape is affected by frequency-dependent attenuation over large distances. The three-dimensional signal propagation within a characteristic flat, disk-like volume, typically referred to as "pancake", will be introduced and the essential signal properties will be discussed. As the speed of sound is pressure-dependent, signal propagation over large distances in deep bodies of water will be affected by refraction. This will be discussed in Sec. 4.3. In Sec. 4.4, the properties of a potential acoustic neutrino detector will be deduced. The properties of the sound signal that mainly affect the detection efficiency are the particular three-dimensional shape of the pressure field and the large attenuation length of acoustic signals in sea water. As will be discussed, this leads to the definition of an effective volume in which neutrino reactions can be recorded by an acoustic neutrino detector beyond its geometric volume. Using an estimate of the effective volume for a generic acoustic neutrino detector, detection rates will be estimated before general design criteria for an acoustic neutrino detector will be discussed. Finally, in Sec. 4.5 an overview of current and recent projects for the investigation of acoustic particle detection is given and in Sec. 4.6 alternative detection methods for UHE neutrinos are briefly discussed.

4.1 Derivation of the Thermo-Acoustic Model

In the following, the thermo-acoustic model [153, 154] is derived from basic assumptions, using a hydrodynamic approach. Starting point are the Euler Equations for a compressible

fluid with the three coordinates $i = 1, 2, 3$,

$$\frac{\partial(\rho v_i)}{\partial t} = -\sum_{j=1}^{3} \frac{\partial \Pi_{ij}}{\partial x_j} \,, \tag{4.1}$$

with mass density ρ, velocity vector $\vec{v} = (v_1, v_2, v_3)$ of the fluid and momentum-density tensor

$$\Pi_{ij} = p\delta_{ij} - \rho v_i v_j \tag{4.2}$$

including the pressure p. Equation 4.1 can be derived from momentum conservation. Taking the partial derivative $\partial/\partial x_i$ of component i of Eq. 4.1 and using the continuity equation

$$\frac{\partial \rho}{\partial t} + \vec{\nabla}(\rho \vec{v}) = 0 \,, \tag{4.3}$$

a non-linear wave equation can be derived:

$$\frac{\partial^2 \rho}{\partial t^2} = \sum_{i,j=1}^{3} \frac{\partial^2 \Pi_{ij}}{\partial x_i \partial x_j} \,. \tag{4.4}$$

To find a solution to this equation, the problem is approached in two separated spacial regions: First, a region I ("interaction"), where the energy is deposited in the particle interactions with the medium and thus the wave excited. Second, a hydrodynamic ("acoustic") region A, where the acoustic wave propagates through the medium. This splitting can be applied to the momentum density tensor, rewriting it as $\Pi_{ij} = \Pi^A_{ij} + \Pi^I_{ij}$.
In thermodynamics, the entropy S in a reversible system is related to the heat Q and the temperature T via the equation

$$dS = \frac{\delta Q}{T} \,.$$

Furthermore, assuming the mole number N is constant, the heat capacity at constant pressure C_p, and the specific heat capacity at constant pressure c_p are defined for a given mass m as

$$C_p \equiv m\, c_p = T \frac{\partial S}{\partial T}\bigg|_p \,,$$

and the bulk volume expansion coefficient α is given by

$$\alpha = \frac{1}{V}\frac{\partial V}{\partial T} \,.$$

The density of the medium, whose change with time "drives" the wave equation, is composed of a part due to heat injected (or withdrawn) from the system and due to a dynamic part, resulting from the change of the pressure. Choosing S, p, and N to characterise the state, the total derivative of ρ can be expressed as

$$d\rho = \frac{\partial \rho}{\partial p}\bigg|_{S,N} dp + \frac{\partial \rho}{\partial S}\bigg|_{p,N} dS \,.$$

For a reversible transformation, the integral $\int \delta Q/T$ is independent of the path (see e.g. [85]). Hence, for a reversible isothermal expansion, the heat deposition can be expressed using

the exact differential dQ. Clearly, the process under investigation is not isothermal, as the temperature change is responsible for the expansion of the water and hence for the pressure wave. However, the temperature change resulting from the interaction of a 1 EeV neutrino is only about $1\,\mu$K[1] at an absolute temperature around 300 K, so that the relative change of temperature is only a 10^{-8} effect.
Using finally the definition of the adiabatic sound velocity,

$$c_s = \sqrt{\frac{\partial p}{\partial \rho}}\,,$$

it follows

$$\begin{aligned} d\rho &= \frac{1}{c_s^2}dp + \frac{\partial\rho}{\partial V}\frac{\partial V}{\partial T}\frac{\partial T}{\partial S}\frac{dQ}{T} \\ &= \frac{1}{c_s^2}dp - \frac{m}{V^2}\left(\alpha V\right)\frac{T}{mc_p}\frac{dQ}{T} \\ &= \frac{1}{c_s^2}dp - \frac{\alpha}{c_p}\frac{dQ}{V} \qquad (4.5) \\ \Rightarrow dp &= c_s^2 d\rho + c_s^2\frac{\alpha}{c_p}\frac{dQ}{V}\,, \qquad (4.6) \end{aligned}$$

which splits a pressure change into an acoustic part $dp_A = c_s^2 d\rho$ and an energy (or interaction) part $dp_I = c_s^2\alpha/c_p d\epsilon$ with energy deposition density $\epsilon \equiv Q/V$ and bulk volume expansion coefficient α. The quantities c_s, α and c_p will be assumed to be constant when performing integrations.
In Eq. 4.4, the acoustic part of the moment density tensor can be expressed as $\Pi_{ij}^A = p_A\delta_{ij} = c_s^2\rho\delta_{ij}$, using Eq. 4.2 with the term $-\rho v_i v_j$ being neglected. The latter seems justified as v_i can be assumed to be small compared to c_s and to be constant or only slowly varying with x_i.
As pressure changes will only be measured in the acoustic region, in the following $p \equiv p_A$ will be used to formulate the wave equation. Using $\Pi_{ij} = p\delta_{ij} + \Pi_{ij}^I$ and $d\rho = c_s^{-2}dp$, Eq. 4.4 translates for pressure differences $p' = p - p_0$ (p_0 being the static pressure) to

$$\vec{\nabla}^2 p' - \frac{1}{c_s^2}\frac{\partial^2 p'}{\partial t^2} = \frac{\partial^2\Pi_{ij}^I}{\partial x_i \partial x_j}\,.$$

The general solution for the wave in the acoustic region can be written as [155]

$$\begin{aligned} p'(\vec{r},t) &= \frac{1}{4\pi}\int_V dV' \frac{1}{|\vec{r}-\vec{r}\,'|}\frac{\partial^2\Pi_{ij}^I(\vec{r}\,',t')}{\partial x_i' \partial x_j'} \\ &\approx \frac{1}{4\pi c_s^2}\int_V dV' \frac{\delta_{ij}\cdot\ddot{\Pi}_{ij}^I(\vec{r}\,',t')}{|\vec{r}-\vec{r}\,'|}\,, \end{aligned}$$

where for the last conversion, partial integration and the total derivative $\frac{d}{dx_i} = \frac{\partial}{\partial x_i} + \frac{1}{c_s}\frac{\partial}{\partial t}$ have been used repeatedly and terms which are suppressed more than linear in $|\vec{r}-\vec{r}\,'|$ were

[1] This number follows from a simple calculation assuming 20% of the neutrino energy is deposited in the hadronic shower within a cylindrical volume of 10 m length and 4 cm diameter. The shower dimensions will be discussed later in this chapter.

neglected. In the affected terms, the expressions have to be evaluated at the retarded time t' which is given by $t' = t - |\vec{r} - \vec{r}\,'|/c_s$.
For the momentum density tensor in the interaction region, an isotropic energy deposition without momentum transfer to the medium through the term $-\rho v_i v_j$ in Eq. 4.2 is again assumed, yielding

$$\Pi_{ij}^I = p_I \delta_{ij} = c_s^2 \frac{\alpha}{C_p} \epsilon \delta_{ij} \; .$$

Under these assumptions, a thermo-acoustic wave, generated by heating up the medium is described by

$$p'(\vec{r}, t) = \frac{1}{4\pi} \frac{\alpha}{c_p} \int_V \frac{\mathrm{d}V'}{|\vec{r} - \vec{r}\,'|} \; \frac{\partial^2}{\partial t^2} \; \epsilon \left(\vec{r}\,', t' \right) . \tag{4.7}$$

The pressure field resulting from a particle interaction in a medium is thus determined by the spatial and temporal distribution of the energy deposition density ϵ. The amplitude of the resulting acoustic wave is governed by the thermodynamic properties c_s, C_p and α, which depend primarily on the temperature of the medium. A controlled variation of these parameters in laboratory experiments and a study of the resulting pressure signals therefore allows for a precise test of the validity of the thermo-acoustic model. Experiments conducted with this aim will be discussed in Sec. 5.1.

4.2 Acoustic Neutrino Signals in Sea Water

The energy of the hadronic shower resulting from the interaction of a UHE neutrino is deposited within a volume of roughly the shape of a long, thin cylinder with radius of several centimetres and length of several metres. In this section, the specific features of neutrino-induced acoustic signals, resulting from the energy deposition according to the thermo-acoustic model, will be discussed. As attenuation is frequency-dependent, it affects the signal shape and will be part of the discussion.

4.2.1 Generation of Bipolar Signals

The energy deposition of the hadronic shower leads to a local heating of the medium which is instantaneous with respect to the hydrodynamic time scales. The dissipation of the heat then is slow compared to the hydrodynamic time scales. Hence, the energy deposition (of the hadronic shower) can be decomposed into a temporal and spatial part and the former approximated by a Heaviside step function Θ

$$\epsilon(\vec{r}, t) = \epsilon_{\vec{r}}(\vec{r}) \, \Theta(t - t_0) \quad \Rightarrow \quad \frac{\partial}{\partial t} \epsilon(\vec{r}, t) = \epsilon_{\vec{r}}(\vec{r}) \, \delta(t - t_0) \tag{4.8}$$

where t_0 is the time of the energy deposition and $\delta(t - t_0)$ is the Dirac delta function. The expression for the partial derivative of ϵ from Eq. 4.8 can be inserted into Eq. 4.7 to yield

$$\begin{aligned} p'(\vec{r}, t) &= \frac{1}{4\pi} \frac{\alpha}{c_p} \int_V \frac{\mathrm{d}V'}{|\vec{r} - \vec{r}\,'|} \; \frac{\partial}{\partial t} \; \epsilon_{\vec{r}}(\vec{r}\,') \, \delta(t' - t_0) \\ &= \frac{c_s^2}{4\pi} \frac{\alpha}{c_p} \frac{\partial}{\partial R} \int_{S_{\vec{r}}^{R_{t_0}}} \frac{\mathrm{d}S'}{R_{t_0}} \epsilon_{\vec{r}}(\vec{r}\,') \; . \end{aligned} \tag{4.9}$$

In the second step, the volume integral has been decomposed into an integration over $R \equiv |\vec{r}-\vec{r}\,'|$ and a surface integral over the surface $S_{\vec{r}}^{R}$ with distance R from point $\vec{r}$. The retarded time t' is related to R as $R = c_s(t-t')$ and the delta function "picks out" the value $R_{t_0} \equiv c_s(t-t_0)$ for the integration over R. Here a constant speed of sound c_s was assumed, such that the surface $S_{\vec{r}}^{R_{t_0}}$ is a sphere. As will be elaborated in Sec. 4.3 the speed of sound shows a depth profile, such that over large distances this assumption in general does not hold.
Eq. 4.9 can be used to derive the bipolar shape of the pressure pulse and to better understand the dependence of the signal shape (and hence the frequency spectrum) on the radial extension of the shower profile [154, 156]. The direction of the shower axis shall be denoted as z-axis and the origin of the coordinate system shall be located at the maximum of the energy distribution along the z-axis. The energy deposition clearly has a cylindrical symmetry around the z-axis and for the energy density in the xy-plane, a Gaussian distribution is assumed. Assuming further that the distribution is uncorrelated between the three coordinates, an energy density

$$\epsilon_{\vec{r}}(x,y,z) = \frac{E_0}{N_z(\sigma_\rho\sqrt{2\pi})^2}\exp\left(-\frac{1}{2}\frac{(x^2+y^2)}{\sigma_\rho^2}\right) f(z)$$

can be postulated, where $f(z)$ denotes the energy density along the z-axis and N_z its normalisation. The standard deviation of the Gaussian distribution in the xy-plane has been denoted by σ_ρ. An observer (listener) is located at a distance x_0 along the x-axis which is far enough from the shower to approximate the surface $S_{\vec{r}}^{R_{t_0}}$ cutting through the shower by a flat surface in the yz-plane. Equation 4.9 can then be rewritten

$$p'(x_0\vec{e}_x,t) \;=\; \frac{c_s^2}{4\pi}\frac{\alpha}{c_p}\frac{\partial}{\partial R}\int_{yz}\frac{\mathrm{d}y'\,\mathrm{d}z'}{R_{t_0}}\,\epsilon_{\vec{r}}(x,y',z')\bigg|_{R=R_{t_0}}$$

and assuming that for the longitudinal extension of the shower σ_z the relation $x_0 \gg \sigma_z$ holds[2], the approximation $\epsilon_{\vec{r}}(x_0,y,z)/R \approx \epsilon_{\vec{r}}(x_0,y,z)/x_0$ is valid in the region where $\epsilon_{\vec{r}}$ differs significantly from zero. The surface integral can then be calculated yielding a linear energy density

$$\begin{aligned}\epsilon_x(x) &\equiv \int_{yz}\mathrm{d}y'\,\mathrm{d}z'\,\epsilon_{\vec{r}}(x,y',z') \\ &= \frac{E_0}{\sigma_\rho\sqrt{2\pi}}\exp(-\frac{1}{2}\frac{x^2}{\sigma_\rho^2}) \qquad (4.10)\end{aligned}$$

in the direction x. The relative pressure amplitude can be approximated by

$$\begin{aligned}p'(x_0\vec{e}_x,t) &\approx \frac{c_s^2}{4\pi}\frac{\alpha}{c_p}\,\frac{1}{X}\frac{d}{dX}\epsilon_x(x)\bigg|_{X=c_s(t-t_0)} \qquad (4.11)\\ &\approx \frac{c_s^2}{4\pi}\frac{\alpha}{c_p}\frac{1}{x_0}\,\frac{d}{dX}\epsilon_x(x)\bigg|_{X=c_s(t-t_0)} \qquad (4.12)\end{aligned}$$

where $X = x_0 - x$ has been defined as the one-dimensional analogue to the variable R. Performing the differentiation $d/dX \equiv -d/dx$ one obtains

[2] $\sigma_z \gg \sigma_\rho$ is furthermore implied.

$$p'(x_0\vec{e}_x,t) \approx \frac{c_s^2}{4\pi}\frac{\alpha}{c_p}\frac{1}{x_0}\frac{E_0}{\sigma_\rho\sqrt{2\pi}}\frac{x}{\sigma_\rho^2}\exp\left(-\frac{1}{2}\frac{x^2}{\sigma_\rho^2}\right)\Bigg|_{X=c_s(t-t_0)} . \quad (4.13)$$

It is convenient to define $t_0 = -x_0/c_s$ such that the expression is evaluated at $x = -c_s t$ yielding

$$\begin{aligned} p'(x_0\vec{e}_x,t) &\approx \frac{c_s^2}{4\pi}\frac{\alpha}{c_p}\frac{1}{x_0}\frac{E_0}{\sigma_\rho\sqrt{2\pi}}\frac{-c_s t}{\sigma_\rho^2}\exp\left(-\frac{1}{2}\frac{(c_s t)^2}{\sigma_\rho^2}\right) \\ &= -\frac{\gamma_G}{4\pi x_0}\frac{E_0}{\sqrt{2\pi}}\frac{c_s t}{\sigma_\rho^3}\exp\left(-\frac{1}{2}\frac{(c_s t)^2}{\sigma_\rho^2}\right) . \end{aligned} \quad (4.14)$$

The dimensionless quantity

$$\gamma_G \equiv c_s^2\alpha/c_p$$

is the Grüneisen parameter, to which the amplitude of the acoustic pulse will be proportional. Eq. 4.14 describes the typical bipolar shape of an acoustic pulse, so far of course under some simplified assumptions. As can be easily verified, Eq. 4.14 has its maximum and minimum for $\sigma_\rho^2 = c_s^2 t^2$, such that

$$p'_{\max} = \frac{\gamma_G}{4\pi x_0}\frac{E_0}{\sqrt{2\pi}}\frac{1}{\sigma_\rho^2}\exp\left(-\frac{1}{2}\right) . \quad (4.15)$$

The maximum pulse height is proportional to the deposited energy, the inverse of the square of the radial energy distribution, the inverse of the distance and the Grüneisen parameter. While the Grüneisen parameter can be easily derived from the properties of a medium, the equally important radial energy distribution must be simulated and contains potentially large systematic errors, as extrapolations over large ranges of energy are involved, see Sec. 3.4. Furthermore, so far attenuation has not been taken into account, which depends on the medium. In Sec. 4.5, an overview of activities and target media for acoustic detection will be given and the Grüneisen parameters for different bodies of water will be compared.

4.2.2 Attenuation

Attenuation in distilled water is caused by viscous absorption. In sea water, in addition ionic relaxation of chemical compounds solved in the water contributes. The latter effect is due to the dependence of the association $\rightleftharpoons$ dissociation process of the chemical compounds on temperature and pressure [158]. At a given pressure and temperature, the rates of dissociation and reassociation will be at an equilibrium. Since energy is required for dissociation, this process contributes part of the specific heat capacity of sea water [159], implying absorption of energy. Changes in the temperature and pressure induced by a sound wave will distort the equilibrium, inciting a dissociation or reassociation with a relaxation time that is specific to the substance. The inverse of the relaxation time is the relaxation frequency $f_j = \omega_j/(2\pi)$, for the j-th chemical compound.
The compression or rarefaction of the chemical compound lags behind the applied pressure, which is expressed in terms of a complex compressibility [158]. Following the same arguments, the specific heat is also expressed as a complex quantity. From these quantities,

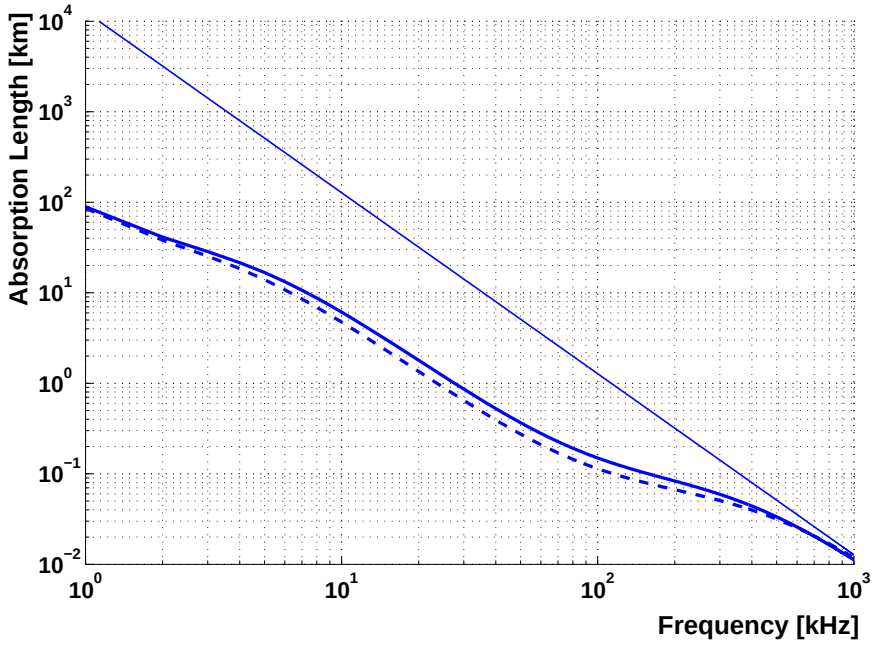

Figure 4.1: Absorption length according to the parametrisation given in [157] for conditions at the ANTARES site with temperature $T = 13.2°$ C, salinity of 3.8 % and a pH-value of 8. The solid thick curve is for a depth of 2000 m, the broken thick curve for a depth of 100 m. The straight thin line is the absorption length for pure water (last term in Eq. 4.16) at a depth of 2000 m.

the complex attenuation coefficient $\tilde{\mu}$ can be derived and the propagation of a plane wave expressed as

$$p_{\mathrm{att}} = p_0 \exp\left(i\omega(t - \frac{x}{c_s}) - \frac{\tilde{\mu}(i\omega)}{2}x\right) \ .$$

The factor $1/2$ has been applied to $\tilde{\mu}$ since the attenuation coefficient is defined for power, which is proportional to the square of the pressure. Splitting the complex attenuation coefficient into a real and imaginary part, $\tilde{\mu}(i\omega) \equiv \mu(\omega) + i\mu_{\mathrm{im}}(\omega)$, yields

$$p_{\mathrm{att}} = p_0 \exp\left(i\omega\left(t - \left[\frac{1}{c_s} + \frac{\mu_{\mathrm{im}}(\omega)}{2\,\omega}\right]x\right) - \frac{\mu(\omega)}{2}x\right) \ .$$

Hence, the imaginary part introduces a dispersion and in effect a delay of the propagation of a neutrino induced bipolar pulse [156]. For chemical component j the complex absorption coefficient can be parametrised as [158, 150]

$$\tilde{\mu}(i\omega) = a_j \frac{i\omega}{\omega_j + i\omega} \quad .$$

Although NaCl is the principal constituent of salt in sea water and magnesium sulphate $MgSO_4$ only amounts for a fraction of 4.7 % by weight of the total dissolved salts in sea water, it is the latter that dominates the absorption process for frequencies above a few kHz, up to about 100 kHz [160], i.e. in the region relevant for acoustic detection.

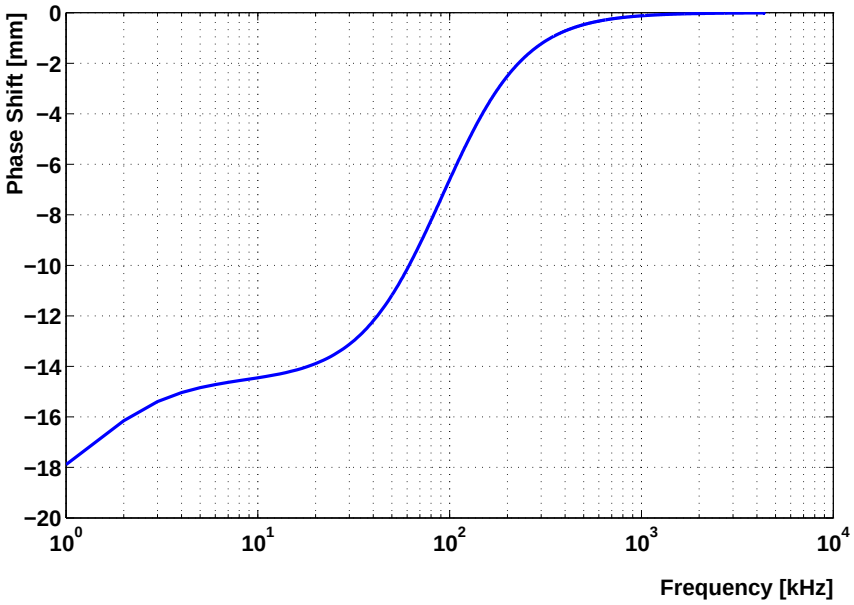

Figure 4.2: Phase shift due to complex attenuation at a distance of 1 km for the same conditions described in Fig. 4.1 for the ANTARES site at a water depth of 2000 m. A speed of sound of 1500 m/s has been assumed to transfer the phase shift from radians to distance.

Boric acid $B(OH)_3$ further reduces the attenuation length at frequencies below a few kHz. For frequencies in excess of 100 kHz, the attenuation length approaches the ω^2 dependence of fresh water.
Combining all three contributions, the complex attenuation can be written as [156, 150]

$$\tilde{\mu}(i\omega) = a_1 \frac{i\,2\pi\,\omega\,\omega_1}{\omega_1 + i\omega} + a_2 \frac{i\,2\pi\,\omega\,\omega_2}{\omega_2 + i\omega} + \frac{\omega^2}{c_s\,\omega_0} \quad , \tag{4.16}$$

where the last term describes viscous absorption of pure water. The real part of Eq. 4.16, which causes attenuation, is readily calculated as

$$\mu(\omega) = a_1 \frac{2\pi\,\omega_1\omega^2}{\omega_1^2 + \omega^2} + a_2 \frac{2\pi\,\omega_2\omega^2}{\omega_2^2 + \omega^2} + \frac{\omega^2}{c_s\,\omega_0} \quad . \tag{4.17}$$

The factors 2π have been introduced for compatibility of the parameters a_j with the more common definition of equation 4.17 as a function of frequency in the literature, e.g. [161, 162]. The quantities a_j, ω_j depend in a non-trivial matter on the temperature, pressure (i.e. depth) and salinity, and in case of boric acid in addition on the acidity. Parametrisations, based on a collection of measurements in various bodies of water, have been derived in [161, 162]. A simplified version of these parametrisations is given in [157], specifying the parameters of Eq. 4.17. The resulting absorption length is shown in Fig. 4.1. The parameters can then be directly transferred to the complex attenuation in Eq. 4.16 [156]. The imaginary part of the complex attenuation coefficient introduces a delay of the bipolar pulse from a neutrino interaction, $\sim 10\,\mu\mathrm{s}$ at $1\,\mathrm{km}$, combined with small distortions as the delay is frequency-dependent. The phase shift, transferred into a spatial delay, is shown in Fig. 4.2.
Note that most references, including [157], quote the attenuation coefficient in units of dB per distance, whereas in the context of this report the attenuation length λ according to

$I = I_0 e^{-x/\lambda}$ is given. Here the intensity I is equivalent to power per solid angle or area (depending on the type of wave), such that effects of the emitted power spreading out over larger areas with distance are compensated. The relation between the two quantities is $\lambda^{-1} = \frac{\mu}{10\log(e)} \equiv \frac{\mu \ln(10)}{10}$, where λ^{-1} then has the same units of distance as μ.

4.2.3 Attenuated Bipolar Pulse

Equation 4.11 can now be transformed into the frequency domain in order to apply the effect of attenuation. Performing the Fourier transform

$$\mathcal{F}\{p(t)\} \equiv \hat{p}(\omega) = \int_{-\infty}^{\infty} e^{-i\omega t} p(t) dt \tag{4.18}$$

for a pressure pulse as described by Eq. 4.12 yields the expression

$$\hat{p}(\omega) = \frac{\gamma_G}{4\pi} \frac{1}{x_0} \times \int_{-\infty}^{\infty} e^{-i\omega t} \frac{1}{c_s} \frac{d}{dt} \epsilon_x(x(t))\, dt \quad . \tag{4.19}$$

By partial integration, using that $\epsilon_x(x(t))$ will be zero at the integration bounds $t = \pm\infty$, the expression can be rewritten[3]

$$\begin{aligned} \hat{p}(\omega) &= -\frac{\gamma_G}{4\pi c_s} \frac{1}{x_0} \times \int_{-\infty}^{\infty} \epsilon_x(x(t)) \frac{d}{dt} e^{-i\omega t} dt \\ &= -\frac{\gamma_G}{4\pi c_s} \frac{1}{x_0} \times \int_{-\infty}^{\infty} \epsilon_x(x(t)) (-i\omega) e^{-i\omega t} dt \\ &= \frac{\gamma_G}{4\pi c_s} \frac{1}{x_0} \times i\omega \times \mathcal{F}\{\epsilon_x(x(t))\} \quad . \end{aligned} \tag{4.20}$$

Equation 4.11 can in fact be generalised for an arbitrary position of the observer, using causality and the rotational symmetry of the problem [163], in which case $\epsilon_x(x(t))$ is replaced by an effective linear energy density $\epsilon_r(r(t))$. In the frequency domain, the attenuation at a distance r_0 between the observer and the shower centre, replacing the quantity x_0 can now be simply multiplied to the right hand side of Eq. 4.20 to obtain the attenuated pressure pulse,

$$\hat{p}_{\mathrm{att}}(\omega) = i\omega \frac{\gamma_G}{4\pi c_s} \frac{1}{r_0} \mathcal{F}\{\epsilon_r(r(t))\} \exp\left(-\frac{\tilde{\mu}(i\omega)}{2} r_0\right) \quad . \tag{4.21}$$

As mentioned above, all calculations have been made in the far field region, where the $1/r$-dependence of the signal amplitude on the distance r from the source has been established. The extension of the near field is frequency-dependent and can be estimated by the relation $\sigma_z \ll r \ll \sigma_z^2/\lambda$ for a wavelength λ [153]. In the near field, for the sound emission from a "line source" , a $1/\sqrt{r}$-dependence of the signal amplitude is expected. This has been observed in simulations [150], where for the simulation of a 10^{20} eV hadronic cascade the transition from near to far field is observed between radial distances of 100 m and 2 km. This is consistent with previous calculations [154]. As has been furthermore pointed out in [154], the broadband frequency content of the bipolar pulse leads to a $1/r^2$-dependence

[3] The expression for $\hat{p}(\omega)$ can also be derived from basic theorems of Fourier transformations.

of the amplitude in the attenuation zone, which is a much slower decrease with distance than the naively expected exponential behaviour. This can be demonstrated most easily for fresh water by writing the viscous term of Eq. 4.17 as $\mu(\omega) = \hat{\mu}\,\omega^2$ with $\hat{\mu} = 1/c_s\,\omega_0$, i.e. ignoring the effect of the chemical compounds for simplicity. Equation 4.21 then can be expressed as

$$\hat{p}_{\mathrm{att}}(\omega) \quad \stackrel{\text{fresh water}}{\longrightarrow} \quad i\omega\frac{\gamma_G}{4\pi c_s}\,\frac{1}{r_0}\mathcal{F}\{\epsilon_r(r(t))\}\,\exp\left(-\frac{\hat{\mu}}{2}\omega^2\,r_0\right) \quad . \tag{4.22}$$

The Fourier transformation of $\epsilon_r(r(t))$ from Eq. 4.10 with $x \rightarrow r, \sigma_\rho \rightarrow \sigma_r$ can now be performed, using $r = -c_s t$ as in Sec. 4.2.1, yielding

$$\mathcal{F}\{\epsilon_r(r(t))\} = \frac{E_0}{c_s}\exp\left(-\frac{\sigma_r^2\omega^2}{2c_s^2}\right)$$

and

$$\hat{p}_{\mathrm{att}}(\omega) \quad = \quad i\omega\frac{\gamma_G}{4\pi c_s^2}\,\frac{E_0}{r_0}\exp\left(-\frac{\sigma_r^2\omega^2}{2c_s^2} - \frac{\hat{\mu}}{2}\omega^2\,r_0\right) \quad .$$

Hence, when transforming back into the time domain, the result will be equivalent to Eq. 4.14 with σ_ρ^2 substituted according to $\sigma_\rho^2 \rightarrow \sigma_r^2 + \hat{\mu}\,c_s^2\,r_0$ and $x_0 \rightarrow r_0$. The maximum amplitude from Eq. 4.15 can then be written

$$p'_{\mathrm{max,att}}(r_0) = \frac{\gamma_G}{4\pi r_0}\frac{E_0}{\sqrt{2\pi}}\frac{1}{(\sigma_r^2 + \hat{\mu}\,c_s^2\,r_0)}\exp\left(-\frac{1}{2}\right) \quad , \tag{4.23}$$

which in the attenuation zone with $r_0 \gg \frac{\sigma_r^2}{\hat{\mu}\,c_s^2}$ becomes

$$p'_{\mathrm{max,att}}(r_0)\big|_{r_0 \gg \frac{\sigma_r^2}{\hat{\mu}\,c_s^2}} = \frac{\gamma_G}{4\pi\,r_0^2}\frac{E_0}{\sqrt{2\pi}}\exp\left(-\frac{1}{2}\right) \quad . \tag{4.24}$$

Hence, in the attenuation zone, the amplitude of the bipolar pulse falls off only as $1/r^2$ and not exponentially as the individual frequencies. This qualitative statement remains valid when taking complex attenuation into account, even though the amplitude itself will be modified.

For the high frequency components of the acoustic signal from the hadronic cascade, with the absorption length in the Mediterranean Sea dropping below 2 km for frequencies above $\sim$20 kHz (see Fig. 4.1), attenuation sets in before the far field conditions have been fully established [150]. For UHE electromagnetic cascades, due to the large extension of LPM-extended cascades, near field conditions for UHE electromagnetic showers directly cross over into the attenuation zone.

4.2.4 The Three-Dimensional Pressure Field

Coherent superposition of the elementary sound waves, produced over the volume of the energy deposition leads to a propagation within a flat disk-like volume, the so-called "pancake" in the direction perpendicular to the axis of the particle cascade. This is an application of Huygens's principle and in order for coherence to occur, the wavelength of the pressure pulse must exceed the radial dimension of the shower.

The strongly directed propagation of the pressure signal can be understood by evaluating Eq. 4.9 along the z-axis. The maximum shower amplitude then follows from Eq. 4.15 by replacing σ_ρ by σ_z, i.e. the standard deviation of the energy distribution in z-direction for an observer located along the shower axis. For σ_ρ on the order of a few centimetres and σ_z on the order of a few metres, it follows $\sigma_z/\sigma_\rho \approx 10^2$ and the maximum of the pressure pulse in z-direction is reduced by a factor 10^4 for the same distance.
After the signal has traversed a volume, to each point of the volume the maximum pulse height that was present over the propagation time of the pulse can be assigned. A given isobar of this pressure field then shows the disk-like shape referred to as "pancake". To quantify the opening angle of the "pancake" it is most convenient to look at the energy contained in the pressure wave as a function of the polar angle distribution, once far field conditions have been established [156, 164]. The opening angle is then defined[4] as the FWHM of the square root of the pulse energy vs. polar angle and is about $\pm 0.5^\circ$ [156], essentially independent of the energy of the hadronic shower above 10^5 GeV. For reactions of electron neutrinos, for which in addition an electromagnetic shower develops, the opening angle is larger, due to the LPM effect [164].
The three-dimensional pressure field will be affected by refraction which will be the subject of Sec. 4.3. Signal shapes as measured with an individual sensor, discussed now in Sec. 4.2.5, are not affected by refraction, except that the distance between the source and the sensor would need to be defined as the length of an acoustic ray connecting the two points.

4.2.5 Neutrino Signal Properties

Simulations of acoustic pulses originating from hadronic showers performed by the ACoRNE[5] collaboration [148, 156] will now be used to discuss the basic neutrino signal properties. To simulate the showers, the air shower program CORSIKA was adapted for neutrino interactions in sea water. Results obtained with this code have already been shown for the discussion of the LPM effect in Sec. 3.4.2 . From simulations of hadronic showers with this code, a dedicated parametrisation was derived and then applied to describe the average differential energy deposition in longitudinal and lateral direction. The acoustic pulse at an arbitrary position[6] is then calculated according to a formula equivalent to Eq. 4.21. To describe complex attenuation, the parameters from [157] were used together with Eq. 4.16. The linear energy density $\epsilon_r(r(t))$ was calculated in the following fashion: First a three-dimensional distribution of points was generated according to the energy density distribution. For each volume element, the point density is then proportional to the underlying energy density. Subsequently for each point, the signal propagation time to the observer was calculated and the points were binned accordingly, yielding the sought after linear energy density. Simulations were performed with the expected equal proportions of all neutrino flavours for the diffuse flux on Earth (see Sec. 3.1) and with the ratio of CC to NC reactions of roughly 2:1, see Sec. 3.2.
As pointed out in Sec. 3.4.1, hadronic showers are subject to large event-by-event fluctuation of both the absolute value and the spatial distribution of the deposited shower energy. Hence, for realistic Monte Carlo simulations of a detector response to acoustic neutrino pulses, these fluctuations have to be taken into account. A method of parametrising the fluctuations, rather

[4] Different definitions are possible, of course.
[5] Acoustic Acoustic Cosmic Ray Neutrino Experiment
[6] Due to rotational symmetry, this position can be defined in any plane containing the shower axis.

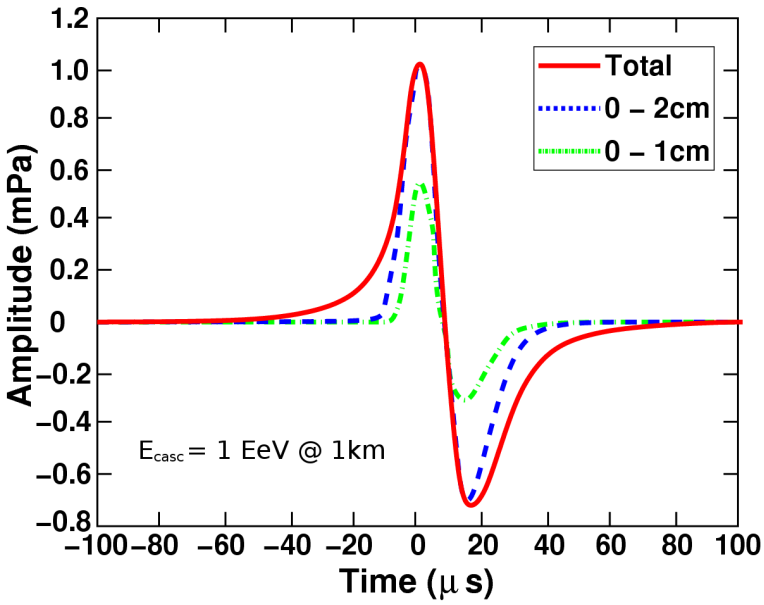

Figure 4.3: Simulated bipolar pressure pulse from a 10^{18} eV hadronic shower at a radial distance of 1 km. Roughly half of the pressure pulse is produced within a radius of 1 cm (dash-pointed line) of the cascade, whereas the energy distribution within a radius of 2 cm (dashed line) is nearly completely responsible for the final signal shape (solid line). Figure adapted from [148].

then working with a large sample of generated showers, is described in [156]. Results presented here are average values. Monte Carlo simulations in the context of the AMADEUS project will be further discussed in Sec. 5.5.2.

A typical bipolar pulse obtained in the fashion just described is shown in Fig. 4.3. For a summary of earlier calculations see [165] and references therein. The most notable difference of this pulse w.r.t. the simple derivation in Eq. 4.14 is the asymmetric shape of the signal. In the far field, where the shower can be approximated by a point source, this is due to the non-linear frequency dependence of the phase shift, or delay, introduced by the complex attenuation according to Eq. 4.16 [156]. In the near field, due to interference of the emission from different parts of the shower, the signal is close to monopolar [150].

In Fig. 4.4 some properties of the acoustic pulse generated by the hadronic shower of a neutrino interaction are shown [156]. Figures 4.4(a) and (b) show the maximum and minimum pulse amplitude $|P_{\max}|$ and $|P_{\min}|$, respectively. As expected, the amplitude decreases with distance and most of the energy is radiated within a narrow region with opening angle of about $\pm 0.5°$, i.e. within the "pancake". The asymmetry, defined as $(|P_{\max}| - |P_{\min}|)/(|P_{\max}| + |P_{\min}|)$ is shown in Fig. 4.4(c). As was discussed above, the asymmetry is predominantly positive, due to the effect of the complex attenuation.

In the far field at distances $\gtrsim 1$ km, the asymmetry (unlike the pulse amplitudes $|P_{\max}|$ and $|P_{\min}|$ from which it is derived) does not show a symmetric behaviour w.r.t. the direction of zero degrees. Clearly, whereas from 1 km to 30 km the amplitude drops by 60 dB, i.e. three orders of magnitude in pressure, the asymmetry varies in the same range from about -0.1 to 0.2, i.e. from a $\sim$5 % excess of $|P_{\min}|$ to a $\sim$10 % excess of $|P_{\max}|$. Differences on this level are not visible in Figs. 4.4(a) and (b).

In Fig. 4.4(d), the mean frequency is shown to decrease with distance. This is due to ab-

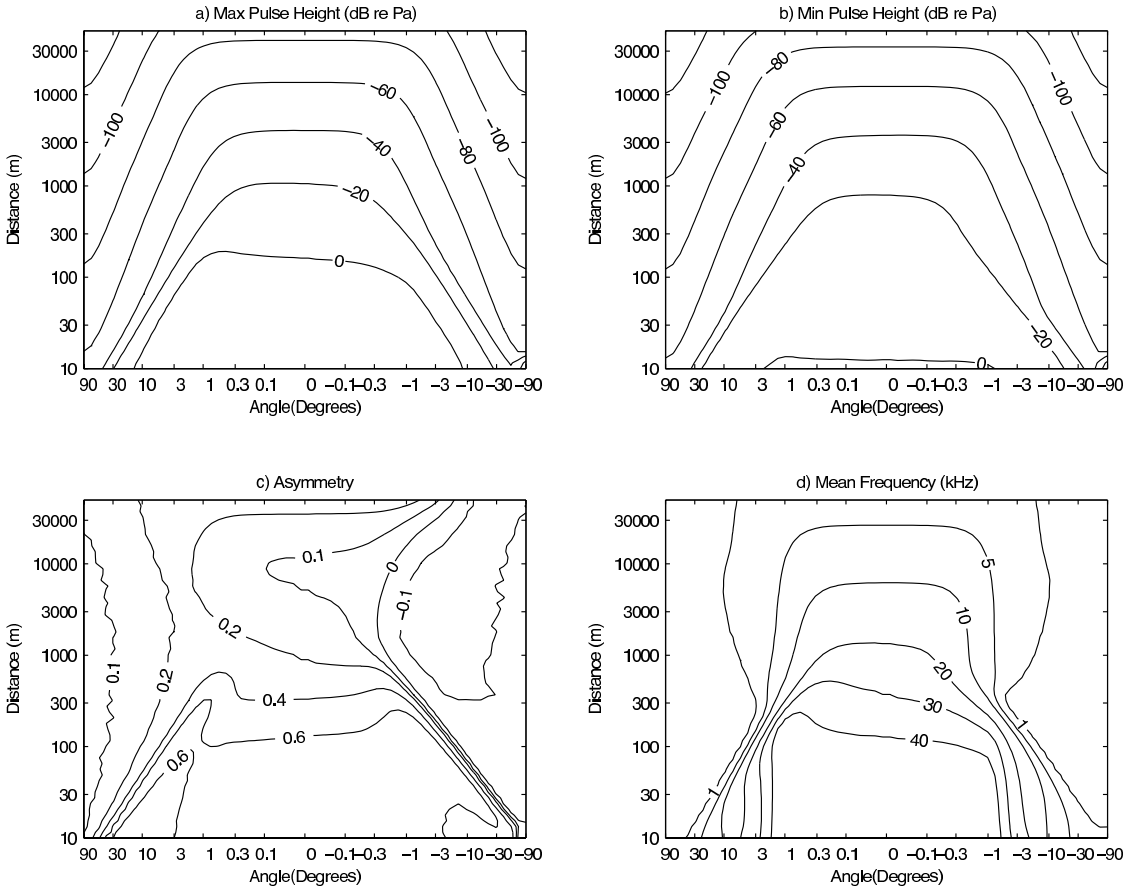

Figure 4.4: Maximum and minimum pressures (a,b), asymmetry (c) and mean frequency (d) versus angle and distance for a 10^{11} GeV shower using the ACoRNE complex attenuation (temperature 15°C, salinity 37 ppt, pH=7.9). Refraction has been ignored. From [156].

sorption which affects higher frequencies stronger than lower ones at a given distance, see Fig. 4.1. As a result, the spectrum and hence the shape of the signal depends strongly on the distance of the observer from the source. The power spectrum of a 10^{11} GeV energy cascade is shown in Fig. 4.5 for several distances of the observer. In consistency with Fig. 4.4(d), the distribution can be seen to become stronger and stronger peaked at low frequencies with increasing distance, leading to a decrease of the mean frequency. After propagating $\sim$1 km in sea water, the peak of the frequency spectrum is at $\sim$10 kHz.

Figure 4.6 shows the dependence of the power spectrum on the angle of the observer with respect to a plane perpendicular to the shower axis intersecting the shower maximum. Towards increasing angles, the spectral distribution gets stronger peaked at lower frequencies, i.e. longer wavelengths. This result is qualitatively expected if the shower is thought of as an emitter of superposing spherical waves. For increasing angles w.r.t. zero degrees from the z-axis, coherence is first lost for short wavelengths.

Assuming equal partition of all neutrino flavours and a ratio of CC to NC cross sections of $\sigma_{NC}/\sigma_{CC} = 0.415$ (see Sec. 3.2), roughly 1/4-th of the neutrino interactions generate an electron in the final state, producing an electromagnetic shower. For these interactions, the full energy of the neutrino is deposited in the water through hadronic and electromagnetic showers. However, the LPM-extended electromagnetic showers (see Sec. 3.4.2) produce a

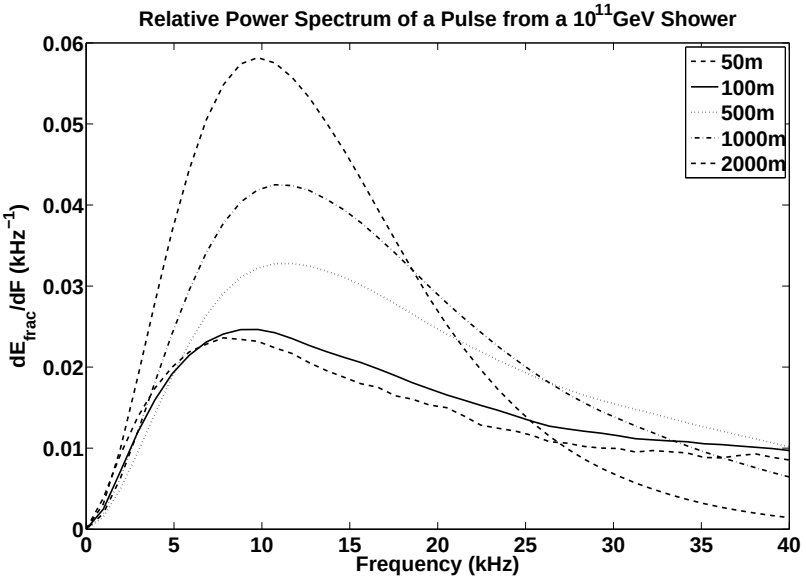

Figure 4.5: Power spectrum of a pulse from a 10^{11} GeV shower for different distances from the shower axis. The area under the curve has been normalised. The pulse shape was evaluated at $z = 0$, i.e. in the plane through the shower maximum at right angles to the axis of the shower. From [148].

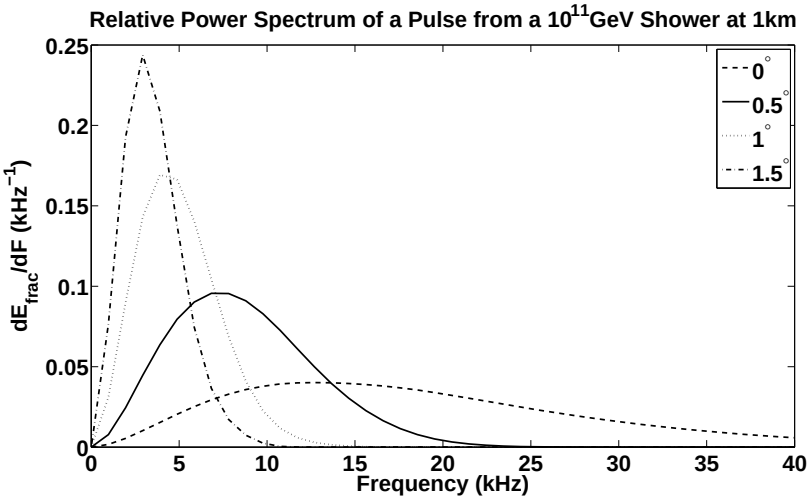

Figure 4.6: Power spectrum of a pulse from a 10^{11} GeV shower at a distance of 1 km. The area under the curve has been normalised. The angle of 0° corresponds to the plane through the shower maximum at right angles to the axis of the shower. Remaining angles are with respect to this plane. In the far field for small angles, difference between the spectra at the same angles above and below the plane at 0° are negligible. From [148].

pressure field that has a much larger opening angle than the "pancake" for a hadronic shower. For a shower energy of 10^{20} eV at a distance of 1 km, a typical opening angle of $\sim 15^{\circ}$ is obtained [164] from simulations based on [166, 167]. The asymmetry of the pulse is much larger than that from a hadronic shower at the same distance. At a distance of 1 km, the peak-to-peak pressure for a 10^{20} eV electromagnetic shower at the angle of its largest value is given as ~ 0.1 Pa while for the largest peak-to-peak value of the hadronic shower (which will be at a different angle) for the same shower energy is ~ 0.8 Pa. Assuming that on average 20% of the neutrino energy is deposited in the hadronic shower (see Sec. 3.4.1) the ratio of the maximum signals from hadronic and electromagnetic showers is about 2:1[7]. Hence, the hadronic shower component generates the dominant contribution to the acoustic signal.

4.3 The Speed of Sound and Refraction

The speed of sound in water depends on the temperature, salinity, and pressure (i.e. depth). The phase shift resulting from complex attenuation, see Fig. 4.2, introduces small dispersion effects over distances of several hundreds of metres that are usually ignored. For the following investigations, the speed of sound was calculated numerically using the parametrisations of water properties from [169]. The geographic position of the ANTARES detector is 42°48'N 6°10'E. The required measurements of salinity and temperature as a function of depth were obtained from sea campaigns conducted within one nautical mile of the ANTARES site in August of 2007 [170] and in March of 2010 [171]. The temperature profile measured in the two campaigns is shown in Fig. 4.7(a). Only the upper ∼100 m of the water are strongly affected by seasonal variations while further down to about 700 m, seasonal differences of maximally 0.5°C can be observed. Below that depth, the temperature is quite stable and independent of the season, ranging from 13.1 °C to 13.6 °C. Sound channelling, which will be discussed below, is not a significant effect for acoustic measurements near the ANTARES site. This is quite different from the situation in oceans, where typically the uppermost kilometre of water shows a temperature decrease with depth. This is shown in Fig. 4.7(b) where temperature profiles for the geographic position 24°30'N and 72°30'W in the Atlantic Ocean are shown. Data were obtained from [172] where the choice of the geographic position was limited due to available data. A position about 500 km East of the town of Nassau on the Bahamas was chosen on a 5°-grid. For this position, sufficient data were available for both the average of the summer months and winter months. Note that the depth up to which data were available is not necessarily the true depth at the given geographic position.

The speed of sound as a function of depth is shown in Fig. 4.8 for the same locations and seasonal conditions as in Fig. 4.7. For the ANTARES site (Fig. 4.8(a)), once the temperature is stable, the speed of sound increases almost linearly with depth. For the ocean (Fig. 4.8(b)) a minimum of the speed of sound is reached at about 1200 m, providing the conditions for sound channelling.

The paths of acoustic signals resulting from the speed of sound profiles shown in Fig. 4.8 (values from summer) are shown in Fig. 4.9, assuming open water models, i.e. assuming that

[7] As pointed out in [168], the value of the volume expansion coefficient is too high by a factor of 8 in [164]. This overestimates the pulse amplitude by the same factor while the value for their ratio as well as the opening angles should be unaffected.

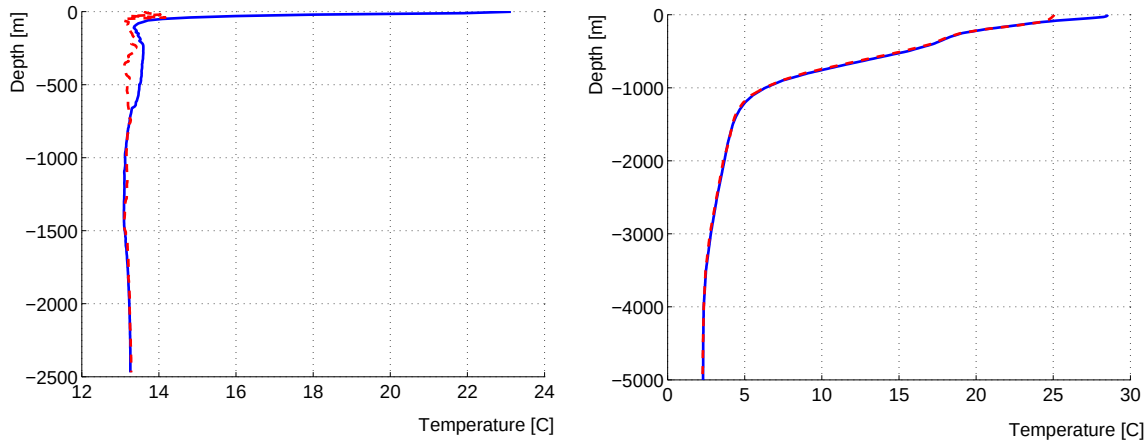

(a) (b)

Figure 4.7: Temperature as a function of the depth below the sea surface, for different seasons at two different sites: (a) Measurement from the ANTARES site in August 2007 [170] (solid blue line) and in March 2010 [171] (dashed red line); (b) Temperature profile in the tropical ocean [172], 24°30'N and 72°30'W, for the average of the three summer months (solid blue line) and the three winter months (dashed red line).

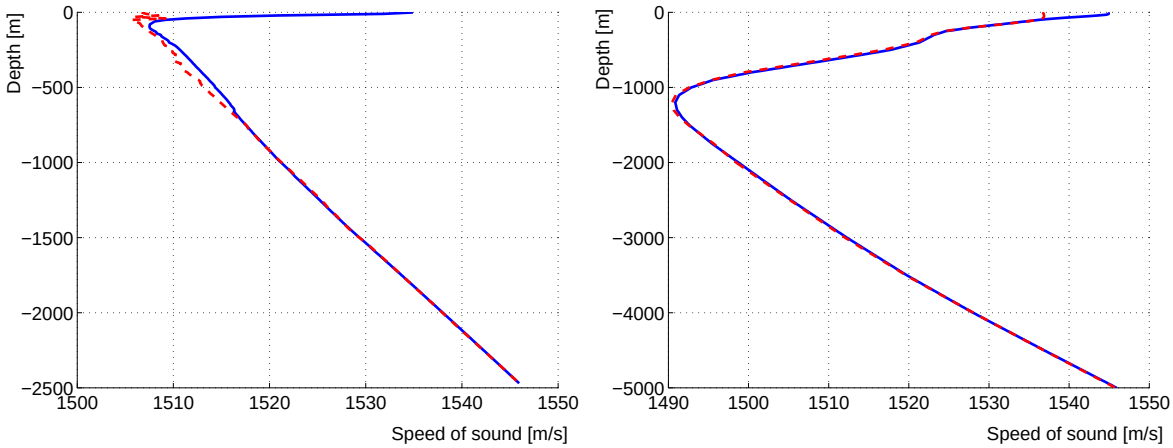

(a) (b)

Figure 4.8: Speed of sound as a function of the depth below the sea surface, for the seasons and sites as in Fig. 4.7 derived using the parametrisations of water properties from [169]: (a) Profile of the speed of sound at the ANTARES site in August 2007 [170] (solid blue line) and in March 2010 [171] (dashed red line); (b) Profile of the speed of sound in the tropical ocean [172], 24°30'N and 72°30'W, for the average of the three summer months (solid blue line) and the three winter months (dashed red line).

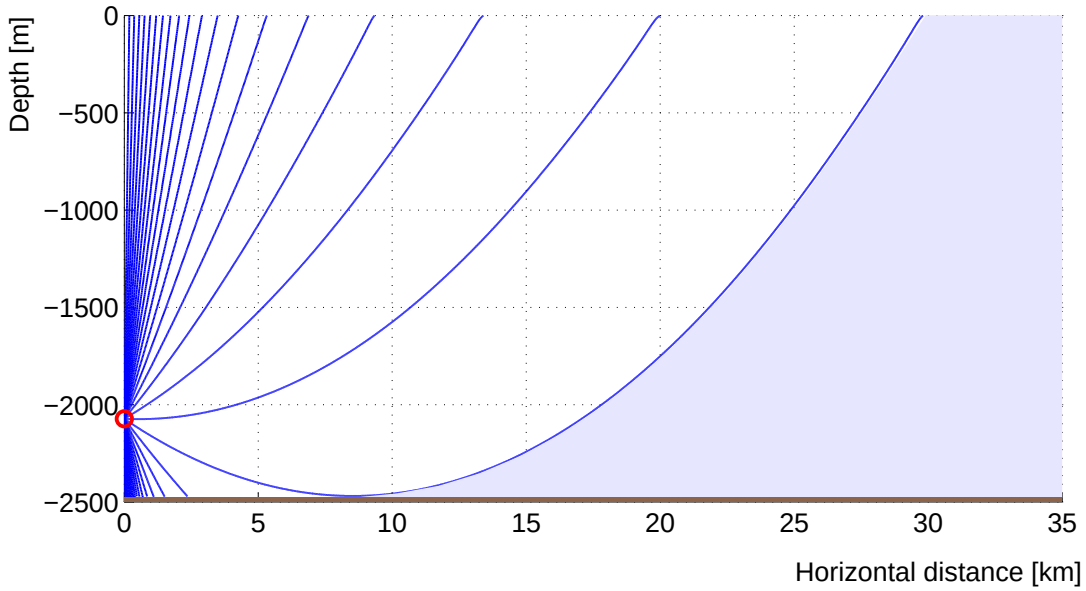

(a) ANTARES site

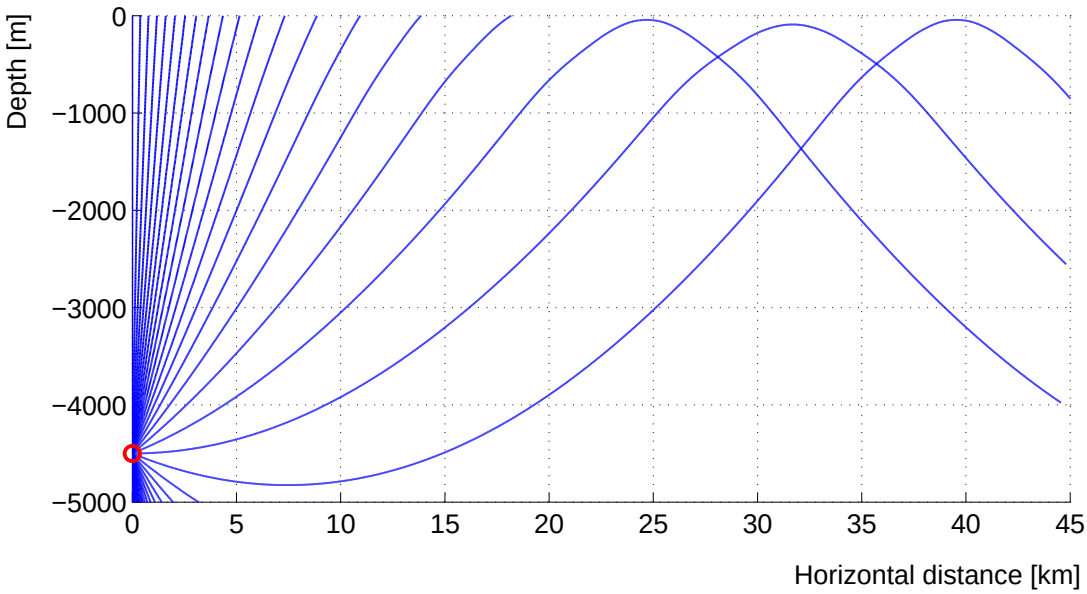

(b) Tropical ocean

Figure 4.9: Ray tracing of acoustic signals for the speed of sound profiles from Fig. 4.8 (summer values). Open water models with a constant depth were assumed (see text). (a) Model for the ANTARES site assuming a constant depth of 2478 m. The shaded area indicates the region from which signals cannot reach the receiver. The position of the receiver is 410 m about the sea floor, which is the nominal position of the highest acoustic storey of the AMADEUS device. (b) Model for a site with a constant depth of 5500 m and the water properties of the tropical ocean at 22°30' N and 72°30' W. An acoustic receiver 500 m above the sea floor is assumed.

the temperature gradient and the depth of the sea surrounding the location of an acoustic receiver do not vary. In this model, for the ANTARES site a constant depth of 2478 m and a position of the receiver of 410 m above the sea floor is assumed. As will be discussed in Sec. 5.2.1, this corresponds to the nominal position of the acoustic storey of the AMADEUS device with the highest elevation above the sea floor. As can be seen in Fig. 4.9(a), the furthest distance from which an acoustic signal originating from the surface can reach the AMADEUS device is about 30 km. The refracted signal will reach the uppermost sensor from an angle of about $-5.5°$, i.e. from below the horizontal. A signal originating at the surface and reaching the detector within the horizontal plane will have a distance of about 20 km. Signals from the shaded area in the figure cannot reach the detector unless through reflection at the sea floor or surface. The volume from which signals can directly reach (the uppermost storey of) the AMADEUS device in this simple model is $\sim 4200\,\mathrm{km}^3$. The validity of the open water model at the ANTARES site will be discussed in Sec. 5.4.2.1.
Figure 4.9(b) shows the typical situation in the ocean: The specific profile of the speed of sound, see Fig. 4.8(b) leads to sound channelling, i.e. the effect that rays of sound propagate over large distances within a depth range around the depth of the minimum of the speed of sound. In this case areas exist also from where signals cannot reach the receiver, but the distance from which a signal can be received in principle is not limited. Note that rays of sound propagation intersect, meaning that the sound from a source at such an intersection will reach the receiver from more than one direction.

4.4 Neutrino Detection with an Acoustic Detector

4.4.1 Event Rates and Effective Volumes

Knowing the flux and the interaction cross section of UHE neutrinos the interaction rate in a given volume can be calculated. In practise, however, the rate of *detected* events is of interest which, as will be discussed below, depends on the detection process and the detector setup. For a most general approach, the cross section formula from [173],

$$\frac{d^3(\delta N)}{dEdtd\Omega}[GeV^{-1}s^{-1}sr^{-1}] = \Phi[GeV^{-1}m^{-2}s^{-1}sr^{-1}] \times A[m^2] \times n[m^{-3}] \times \sigma[m^2] \times \delta x[m] \quad , \tag{4.25}$$

is taken as a starting point, where units are given for better comprehensibility. The density of scattering centres is denoted by n and δx is the (small) thickness of the material along the direction of the particle flux Φ. δN is the number of interactions taking place within δx over the area A of the target, perpendicular to the particle flux, that is traversed by that flux. The ranges of energy, time and solid angle, in which particles are counted, are denoted by dE, dt, and $d\Omega$, respectively.
In general the detector geometry will introduce a dependence of the interaction rate on the solid angle through variations of A and of the distance $x = \int \delta x$ that the neutrino will traverse within the sensitive volume. As will be discussed below, both A and x will have to be replaced by effective values, specific to the detection process and the detector, which in general differ from the geometric values.
As was already shown in Eq. 2.21, the quantity $n\sigma$ is equivalent to the inverse of the mean free path λ for a constant density of scattering centres n and cross section σ. The dimensionless quantity $\delta x/\lambda$ can be interpreted as the reaction probability dp over the thickness δx of

the material. The probability for a particle of the incident flux to have not interacted after a distance $x = m\delta x$ is[8] $\lim_{m\to\infty}(1 - x/(\lambda m))^m = \exp(-x/\lambda)$, such that the probability for a reaction after the distance x is $P(x) = 1 - \exp(-x/\lambda)$ and the expression for the number of neutrino interactions inside the detector volume can be written as

$$N_i = \int dt \int d\Omega \int dE\, \Phi(E)\, A(\Omega)\, P_x(E, \Omega) \quad . \tag{4.26}$$

It has been neglected here that over the area A the distance x and therefore P_x, the probability for an interaction over a distance x, in general will vary. Hence the formula implies an averaging of P_x over the the area A. Furthermore, it has been assumed that the flux is isotropic and independent of time, so that it only depends on the energy. Since $x \ll \lambda$, the approximation $P_x(E, \Omega) \approx x/\lambda$ holds such that

$$N_i = T \int d\Omega \int dE\, \Phi(E)\, A(\Omega)\, \frac{x(\Omega)}{\lambda(E)} \quad . \tag{4.27}$$

In Eq. 4.27, $\Phi(E)$ is the flux at the detector surface and not that at the surface of the Earth, where the latter has been the subject of discussion in Secs. 2.5 and 2.6. These fluxes will be different for high-energetic neutrinos which traverse the Earth where the interaction probability inside the Earth has to be taken into account [174]. However, for UHE neutrinos, which are of interest for acoustic detection, Earth is opaque (see Sec. 3.3). Therefore, it will be assumed that all neutrino entering the detector volume are coming from the upper hemisphere only. Attenuation losses of the neutrino flux near the horizon can be taken into account when calculating effective volumes using Monte Carlo simulations, as will be discussed below.
To move from the interaction rate inside the detector volume to the event rate registered by the detector, two further aspects need to be taken into account. First, the efficiency for the detection of neutrino reactions inside the detector volume has to be accounted for. And second, neutrinos reacting outside the instrumented volume can be detected. For an optical neutrino telescope, the latter point is typically accounted for by replacing the geometric dimension x of the detector volume by $x \to \tilde{x} = x + l$ where l is the track length of the muon. This quantity is clearly energy dependent. The quantity Ax from Eq. 4.27 is hence replaced by an effective volume $V_{\text{eff}}(E) = V_{\text{geo}} \times f_{\text{eff}}(E) \times f_{\text{det}}(E)$, where V_{geo} is the geometric (instrumented) volume, $f_{\text{eff}}(E) > 1$ accounts for the increase of the geometric volume to the volume in which neutrinos can be detected and $f_{\text{det}}(E) < 1$ describes the detection efficiency. For acoustic detection, the effective dimension $\tilde{x}$ will not differ much from the geometric quantity x. However, due to the strongly directed emission pattern of the sound waves from a neutrino interaction and due to the large absorption length of sound in water, the area A has to be replaced by an effective value $\tilde{A}$ that is significantly larger than A. Formally, the effective volume can then be introduced as $V_{\text{eff}}(E) = \Omega^{-1} \int_\Omega \tilde{A}(\Omega', E)\tilde{x}(\Omega', E)d\Omega'$. In practise, $\tilde{A}$ and $\tilde{x}$ are not explicitly determined and V_{eff} is calculated from Monte Carlo simulations by generating a number of N_{gen} events over a sufficiently large volume V_{gen} containing the detector (referred to as can volume). The effective volume is then calculated as $V_{\text{eff}} = N_{\text{rec}}/N_{\text{gen}} \cdot V_{\text{gen}}$ where N_{rec} is the number of events recorded by the detector. . Equation 4.27 can then be written, now describing the *detected* events over the time T, as

[8] It is assumed that the particle can react only once which in principle is not true for NC reactions, in which case the neutrino with reduced energy can react again. Given the small reaction probability this case does not have to be taken into account.

$$N_d = 2\pi T \int dE\, \Phi(E) \frac{V_{\text{eff}}(E)}{\lambda(E)} \quad , \tag{4.28}$$

where the factor 2π implies a neutrino flux recorded over the upper hemisphere. The event rate in a given detector can now be calculated if the effective volume is known.

4.4.2 Rate Estimate in a Generic Acoustic Neutrino Detector

4.4.2.1 Detector Model

Effective volumes have been calculated for generic acoustic neutrino detectors of $1\,\text{km}^3$ size [175, 176]. For the instrumentation, a random distribution of sensors over the volume was assumed; this eliminates symmetries which will always lead to a reduced efficiency of the detector. To find the maximally required density of sensors, the density was increased in the simulations until the efficiency for neutrino detection (and hence the effective volume) did not increase any further. In this fashion, an instrumentation with 200 acoustic sensors per km^3 has been derived as the optimal choice [175]. This corresponds to distances of $\sim$200 m between sensors. In [176] it is concluded that the required density of acoustic sensors is closer to 400 per km^3; the factor of two in volume however only corresponds to a factor of $\sim$1.25 in distance.

For a real detector, the detection threshold of individual hydrophones for bipolar signals depends on the ambient noise at the detector site, on the signal recognition techniques and on the sensitivity of the hydrophones, which in general will be a function of frequency and solid angle. These topics therefore need to be carefully investigated. For the AMADEUS device, this will be discussed in Chapter 5.

In the following, the effective volumes calculated in [175] are used. In that reference, a detection threshold of acoustic signals in terms of a pressure level is assumed for each acoustic sensor to decide if the sensor recorded a "hit". A reconstruction algorithm is subsequently applied to the hits and a neutrino is counted as "detected" if the algorithm converges. Figure 4.10 shows the effective volume calculated in this fashion for an optimistic detection threshold of 5 mPa and a more pessimistic threshold of 35 mPa. The detector is assumed to be of cylindrical shape, located at the bottom of the sea in 2.5 km depth with 1 km height and a radius of $\sqrt{1/\pi}$ km. Clearly reconstruction algorithms also depend strongly on the properties of the detector and on the background conditions. For interactions in a distance of several kilometres, only the edges of the disk-like structure of the pressure field will reach the detector. Whether or not these can be identified as originating from neutrino interactions depends among other things on the background of bipolar signals in the deep sea—another topic to be investigated with AMADEUS. The effective volume used here hence describes an idealised situation.

The effective volume in Fig 4.10 shows a strong dependence on energy and is in fact *smaller* than the geometric volume for neutrino energies $E \lesssim 10^{19}\,\text{eV}$ for a 5 mPa threshold. This is due to the fact that the fraction of energy transferred from the neutrino to the hadronic shower shows a large spread and is in average only 20 % (see Sec. 3.4.1). Hence for neutrino energies around the detection threshold, the energy transferred into the shower will with great probability be below the detection threshold.

Figure 4.10 furthermore shows the differential event rate as a function of energy for a flux corresponding to the Waxman-Bahcall bound, both for the geometric volume of 1 km and

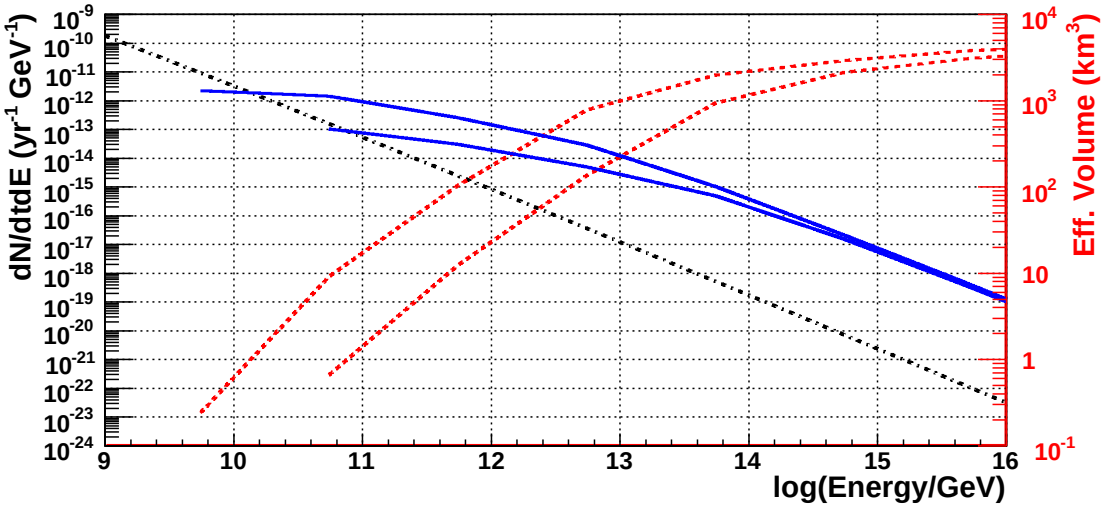

Figure 4.10: Spectral event rate $dN/dtdE$ for a unit effective volume of 1 km^3 (black dash-dotted line, left scale), effective volume for the 1 km^3-size detector (200 sensor clusters) described in [175] (red dotted line, right scale) and the product of the two (blue solid line, left scale), corresponding to the expected spectral event rate of the detector. The upper (lower) graphs for the effective volume and the corresponding differential event rate are for a 5 mPa (35 mPa) threshold, respectively. A flux of neutrinos according to the Waxman-Bahcall bound as described in the text is assumed.

for the effective volumes shown in the same figure. For this flux, the value from Eq. 2.38 without correction for evolution was used and multiplied by 1.5 to account for all neutrino flavours. The resulting value $\phi E^2 = 2.2510^{-8}\mathrm{GeV}^{-1}\mathrm{s}^{-1}\mathrm{cm}^{-2}\mathrm{sr}^{-1}$ is too small by a factor of 3 in case of strong evolution but roughly a factor of 2 too high in case measurements by the Pierre Auger Observatory are used for normalisation (see Sec. 2.5.2).
For the cross section, contributions from CC and NC reactions according to Eq. 3.13 ("fit to Berger et al.") were added. The mean free path required for Eq. 4.28 is then calculated as described in Sec. 3.3. Note that these cross sections were only calculated up to energies of 10^{14} GeV whereas Fig. 4.10 extends up to 10^{16} GeV. The effect of the region beyond 10^{14} GeV on the resulting event rate is very small though and can be neglected.
The low energy threshold for the detection of neutrinos is given by the detection threshold of the acoustic sensors. For the detector model assumed here, the energy with $V_{\mathrm{eff}} = V_{\mathrm{geo}}$ is at neutrino energies of $E \approx 10^{10}$ GeV ($E \approx 10^{11}$ GeV) for detection thresholds of 5 mPa (35 mPa).
The differential event rate for the fixed volume of 1 km^3 is falling with energy approximately according to a power law with exponent ~ -1.85; The flux corresponding to the Waxman-Bahcall bound contributes a spectral index of 2 while the neutrino cross section scales roughly with $E^{0.15}$. The effective volume on the other hand is increasing strongly above the detection threshold, mitigating the effect of the decreasing event rate. The volume, from which acoustic signals can reach the detector, is limited to a maximum value due to the effect of refraction (see Sec. 4.3). In [175], this volume is calculated from simplified geometric arguments as $5726\,\mathrm{km}^3$ for a detector of $1\,\mathrm{km}$ height in $2.5\,\mathrm{km}$ depth. In Sec. 4.3, a volume of $\sim 4200\,\mathrm{km}^3$ was estimated for the AMADEUS device.
Once the effective volume is close to its maximum value and does not increase significantly

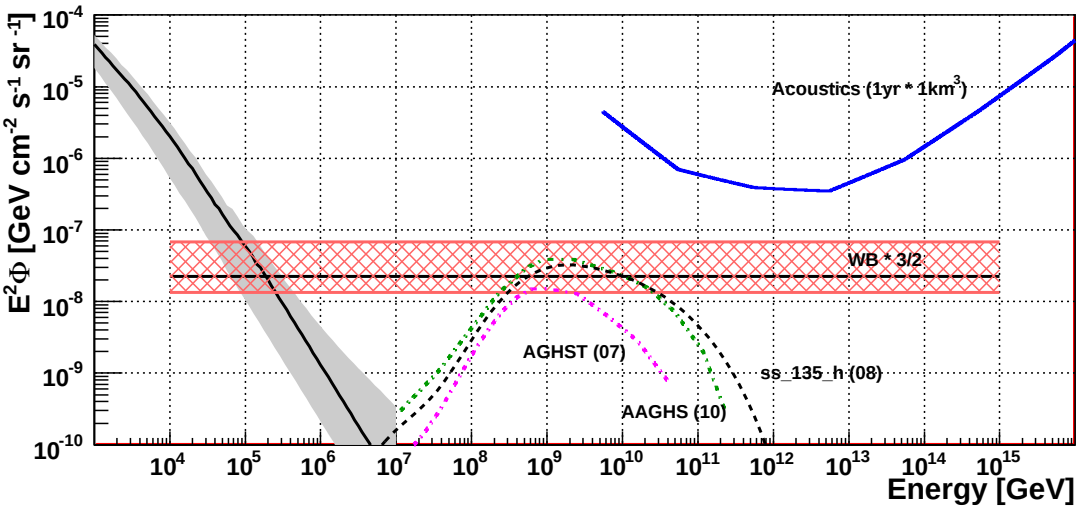

Figure 4.11: Model independent flux limit for a "generic" 1 km^3 acoustic neutrino detector as described in the text and an observation time of 1 year. (blue solid line). The effective volume for the 5 mPa detection threshold was used. For the Waxman-Bahcall bound, scaled by 3/2 to take all neutrino flavours into account, the base value (dashed line) and the range (cross hatched area) resulting for no evolution (factor 0.6) and strong evolution (factor 3) are shown. The models for the expected cosmogenic neutrino flux for a pure proton composition of cosmic rays, labelled ss_135_h(08) [178], AGHST(07) [105], and AAGHS(10) [127] are described in the text. The grey band represents the background from atmospheric neutrinos, and is identical to that shown in Fig. 2.11. It is irrelevant in the energy range exploited by acoustic detection.

anymore, the decrease of the differential event rate is not compensated anymore and the differential event rates for the geometric and the effective volume differ by a constant factor.

4.4.2.2 Rate Estimates and Limits

To calculate a model dependent limit on a given flux for a confidence level (CL) of x%, the corresponding flux is given as

$$\Phi_x(E) = \frac{N_x}{N_{\mathrm{mod}}(E_1, E_2, T)} \Phi_{\mathrm{mod}}(E) \quad , \tag{4.29}$$

where $N_{\mathrm{mod}}(E_1, E_2, T)$ is the number of events expected for the model flux Φ_{mod} during the time T within the energy range $E_1 < E < E_2$ according to Eq. 4.28. If no events are detected, then N_x is the maximum of the true mean number of events that for a given CL is consistent with a non-observation of events. In other words, the confidence interval is $[0, N_x]$. Once $N_{\mathrm{mod}} \geq N_x$, the model flux Φ_{mod} can be excluded for the chosen CL. For a Poissonian distribution of events with low statistics and in the absence of background, the values are $N_x = 2.44\ (3.09)$ for 90% (95%) CL [177].
A model independent flux limit is typically calculated according to [179] as

$$\Phi_x(E) = \frac{N_x}{2\pi\, T\, E\, [V_{\mathrm{eff}}(E)/\lambda(E)]} \quad , \tag{4.30}$$

Flux	Detection thd (pressure)	Detection thd (energy)	ν/year ($V_{\rm eff}$)	T(years) (90% CL)	ν/year ($V_{\rm geo}$)
WB-equiv	5 mPa	5.5×10^9 GeV	0.98	2.5	0.05
WB-equiv	35 mPa	5.5×10^{10} GeV	0.19	12.8	0.01
cosmogenic	5 mPa	5.5×10^9 GeV	0.075	32.5	0.03
cosmogenic	35 mPa	5.5×10^{10} GeV	0.0034	720	0.0009

Table 4.1: Estimated all-flavour neutrino rates for a flux corresponding to the Waxman-Bahcall bound and for the cosmogenic flux labelled AAGHS(10) in Fig. 4.11. The threshold on the neutrino energies is given by the model of the acoustic detector. Rates are given for the effective volume discussed in the text and for the interactions taking place only within the geometric volume. The time required to measure an event or exclude the model at the 90% CL are given for the event rate of the effective volume.

where the factor 2π enters for an isotropic flux over the upper hemisphere. The corresponding limit for the 1 km^3 detector described and for an observation time of 1 year is shown in Fig. 4.11. The limit is compared to the Waxman-Bahcall bound and to three different flux estimates for cosmogenic neutrinos. All models assume a pure proton composition at the source and take all neutrino flavours into account. The flux estimate ss_135_h(08) was taken from the file ss_135_h.txt of [178][9], AGHST(07) is the pure proton flux given in [105] (see Fig. 2.13), and AAGHS(10) is the flux from [127] for a transition of galactic and extragalactic cosmic ray fluxes fixed at 10^{19} eV, which is the most optimistic case. The models differ most notably in the assumed cutoff energy at the source and in the normalisation. The effect of different cutoff energies assumed at the source are visible in Fig. 4.11: The model AGHST(07)[10] assumes a cutoff energy of $E_{\rm max} = 10^{22}/26 \approx 4 \times 10^{20}$ eV whereas for model AAGHS(10) a cutoff of $E_{\rm max} = 10^{21}$ eV was implemented. For model ss_135_h(08), $E_{\rm max} = 10^{21.5}$ eV was used. The measurement of a flux of UHE neutrinos could help to determine the energy cutoff of the source.

In Table 4.1 the expected neutrino rates are shown for a flux equivalent to the Waxman-Bahcall bound and for a cosmogenic neutrino flux from a pure proton composition of cosmic rays according to the model labelled AAGHS(10) in Fig. 4.11 as described above. This model was chosen for the neutrino flux as it is the most recent one of the three discussed models.

Rates were calculated for the generic 1 km^3 acoustic neutrino detector discussed above, both for the effective volume and for the geometric volume only. In the latter case when $V_{\rm eff} < V_{\rm geo}$ for low energies, the effective volume was used as well. For the neutrino detection rates within the effective volume, the number of years required to measure a neutrino flux (or exclude it at 90% CL) was calculated by dividing N_{90} from above by the number of neutrinos expected to be detected within one year.

The low counting rate shown in Table 4.1 has a number of implications. First, to maximise the detection efficiency, it is important to push the detection threshold as low as possible. Second, it is important to extend the measurement to an as large as possible effective volume. As already indicated, the effective volume used for the calculations above was derived for idealised conditions. It will be important to derive the effective volume for a "real" detector

[9] The flux calculations described on the cited web page are updates of [88].

[10] This model is outdated and was superseded by AAGHS(10), but is shown here to demonstrate the effect of the cutoff energy. See Secs. 2.6.2 and 2.6.3 for more details on these models.

geometry and instrumentation from Monte Carlo simulations.
The next-generation optical neutrino telescope in the Mediterranean Sea, a multi-cubic-kilometre device that will be part of the future deep-sea research infrastructure KM3NeT, will also provide the possibility to pursue acoustic neutrino detection. Whether an acoustic neutrino detector of that size will be big enough to measure a signal from acoustic neutrino interactions will depend strongly on the effective volume and on the energy detection threshold.

4.4.3 Fundamental Design Considerations

Compared to an optical neutrino telescope, the major advantage of acoustic detection is the large attenuation length of sound in sea water of about 6 km (2 km) for 10 kHz (20 kHz) signals (see Fig. 4.1). This is one to two orders of magnitude larger than for visible light with a maximum attenuation length of about 60 m and hence allows for a less dense instrumentation of an acoustic neutrino detector.[11] On the other hand, the pressure pulse propagates only within a thin (several tens of metres) disk-like volume and the geometry and instrumentation of a detector has to be adapted to this emission pattern.
Obviously, a random distribution of sensors as it was assumed in Sec. 4.4.2 is difficult to realise for a large volume acoustic detector. In the deep sea, technical reasons will require acoustic sensors to be mounted on some vertical structures, anchored to the sea bed. A part of the "pancake" pressure pattern must be contained within the geometric detector volume in order to identify the neutrino interaction by the resulting characteristic pressure field and to perform a reconstruction of the interaction position. A layout of sensors on the seabed is not optimal solution for this purpose [168]. Signals from a minimum of four sensors are required to reconstruct the position of a source if the emission pattern is known to be a spherical wave. To reconstruct the "pancake" shape with some certainty, signals in ~ 10 sensors are required. From a physics point of view there is no reason to install an acoustic neutrino detector in the deep sea. In fact, acoustic sensors near the surface for a given depth would extend the distance from which signals could reach the sensors in the presence of refraction, see Sec. 4.3. It is however advantageous to monitor a volume below some depths, where anthropogenic and environmental sources of sound are strongly reduced, see Sec. 5.4.2; for the Mediterranean Sea, this depth is below around $500\,\mathrm{m}$. Furthermore, as any sizable acoustic neutrino detector potentially constructed in the foreseeable future is likely to be integrated into an optical neutrino telescope, it can be presumed to be located at great depth.
It is obvious that as the size of a potential acoustic neutrino detector increases, the detection of contained events, i.e. those for which the interaction is taking place within the instrumented volume, will eventually dominate. A detector aiming for the detection of contained events would not be strongly affected by distortions of the pressure field due to refraction, see Sec. 4.3. How strongly refraction will affect the detection efficiency for detectors relying on a large effective volume needs to be investigated.
In the following, some further considerations for the case of a cubic-kilometre size acoustic neutrino detector are made. For such a device, most detected neutrino interactions will occur outside of the geometric volume but within a much larger effective volume. Since sea water as target medium will extend further into the horizontal than into the vertical direction, it is most probable that the "pancake" is oriented approximately horizontally if the sound waves

[11] Another advantage, the more compact sensor design and simpler readout electronics for acoustic measurements will be part of the discussion of the AMADEUS device in Sec. 5.2.

are reaching the detector from outside of the geometric volume. Reflection at the sea surface and the sea floor affect this argument. Preliminary investigations indicate that for surface reflections, the reflected amplitude is reduced by about a factor of 0.75, while for the sea floor, the factor is about $0.1 - 0.2$. Hence the loss of signal amplitude for reflections at the sea surface is not very high. This increases the range of polar angles of incident neutrinos for which the acoustic signals resulting from an interaction in the water can reach the detector. It is important to study how reflections affect the design of a potential large-scale acoustic neutrino detector; however, if the effective volume is assumed to be extending much further in horizontal than in vertical direction, the argument from above about the orientation of the "pancake" remains intact. Therefore, reflections will be ignored in this qualitative treatment. The opening angle of about $\pm 0.5^\circ$ of the "pancake" corresponds to an extension of about 20 m at 1 km distance. Assuming this angle remains constant with distance, an extension of about 1 km, i.e. the size similar to the vertical dimension of the presumed acoustic neutrino detector is reached for a distance of $\sim$57 km. It is unlikely that neutrino signals will reach the detector from even greater distances as effects due to both attenuation and refraction (see Sec. 4.3) will become significant. This results in a detector geometry in which acoustic sensors are spaced at distances of several tens of metres along vertical structures. For a length of about 1 km (which is of the order of the attenuation length), a spacing of the structures of several per kilometre should, for most directions of the incident neutrino, provide a signal on several structures for contained events. For non-contained events, the design should allow for the reconstruction of the "pancake" structure of the pressure field. Symmetries should be avoided as far as possible in the arrangement of the acoustic sensors.
In practise, the cost of an acoustic neutrino detector will be essentially determined by the number of vertical structures. To determine the layout of the structures on the sea floor, in particular their spacing, taking requirements for both contained and non-contained events into account, Monte Carlo simulations are necessary.

4.5 Overview of Activities and Target Media

The acoustic detection of UHE neutrino reactions in principle works in any dense homogeneous medium. In addition to water and ice, which are the media of acoustic detection test experiments presently or recently conducted, acoustic detection in salt domes [180, 181] and in permafrost [182] has been discussed.
In the context of the DUMAND[12] experiment, ideas about adding a large scale acoustic detector to a deep-sea optical neutrino telescope were already considered in the 1970s [183]. As the DUMAND experiment was not realised beyond a prototype phase, acoustic particle detection was subsequently pursued by the parasitic use of military arrays. In an early effort starting in 1997 by the SADCO[13] collaboration, a Russian Navy stationary antenna near Kamtchatka consisting of 2400 hydrophones was used for acoustic particle detection studies [184] (see also [185] and references therein).
Besides sea water, which is the medium under investigation in the case of the AMADEUS project, ice and fresh water are currently investigated as media for acoustic detection of neutrinos. An overview of experiments that are currently taking data or have done so until recently is shown in Table 4.3. Below, the individual projects will be discussed in some more

[12] Deep Underwater Muon and Neutrino Detection
[13] Sea Acoustic Detector of Cosmic Objects

Experiment	Location	Medium	Sensor Channels	Host Experiment
SPATS	South Pole	Ice	80	IceCube [6]
Lake Baikal	Lake Baikal	Fresh Water	4	Baikal Neutrino Telescope [4]
OνDE	Mediterranean Sea (Sicily)	Sea Water	4	NEMO [186]
AMADEUS	Mediterranean Sea (Toulon)	Sea Water	36	ANTARES [5]
ACoRNE	North Sea (Scotland)	Sea Water	8	Rona military array
SAUND	Tongue of the Ocean (Bahamas)	Sea Water	$7/49^{(\star)}$	AUTEC military array

Table 4.3: Overview of existing and recent acoustic detection test sites.
$^{(\star)}$ The number of hydrophones was increased from 7 in SAUND-I to 49 in SAUND-II, see text.

detail.

The **AMADEUS (ANTARES Modules for the Acoustic Detection Under the Sea)** project is the main subject of this report and will be described in detail in Sec. 5.2.

The **SPATS (South Pole Acoustic Test Setup)** project [187, 188], deployed up to a depth of 500 m in the upper part of four boreholes of the IceCube Neutrino Observatory, has continuously monitored the noise in Antarctic ice at the geographic South Pole since January 2007. As acoustic properties, in particular the absorption length and the speed of sound, have been subject to much less experimental studies for ice than for water, these properties have been instigated with SPATS [189, 190]. Based on 8 month of observation, a limit on the neutrino flux above 10^{11} GeV has been derived [191], see Fig. 4.12.

In **Lake Baikal**, an antenna consisting of four hydrophones in a tetrahedral arrangement with equal interspacings of the hydrophones of $1.5\,\mathrm{m}$ has been placed in 150 m depth [192]. Fresh water has the advantage over sea water that the attenuation length is roughly one order of magnitude larger in the frequency range of 10 to 100 kHz (see Fig. 4.1). However, conditions in Lake Baikal are not particularly favourable for acoustic neutrino detection, since in the deep zone of the lake the water temperature is only $1.5 - 2^{\circ}\mathrm{C}$ higher than the maximum density at the respective depth [193, 194]. The thermal expansion coefficient hence is close to zero and the Grüneisen parameter small. The observed noise level depends mostly on surface conditions and in the frequency range of 5 to 20 kHz has a value of a few mPa.

The **OνDE (Ocean noise Detection Experiment)** project at the site of the NEMO[14] Cherenkov neutrino detector [186] has performed long term noise studies at 2050 m depth, 25 km east of Catania (Sicily) in the Mediterranean Sea at the location 37°30.008'N, 15°23.004'E. Phase I operated from January 2005 until November 2006. It employs 4 hydrophones

[14] Neutrino Mediterranean Observatory

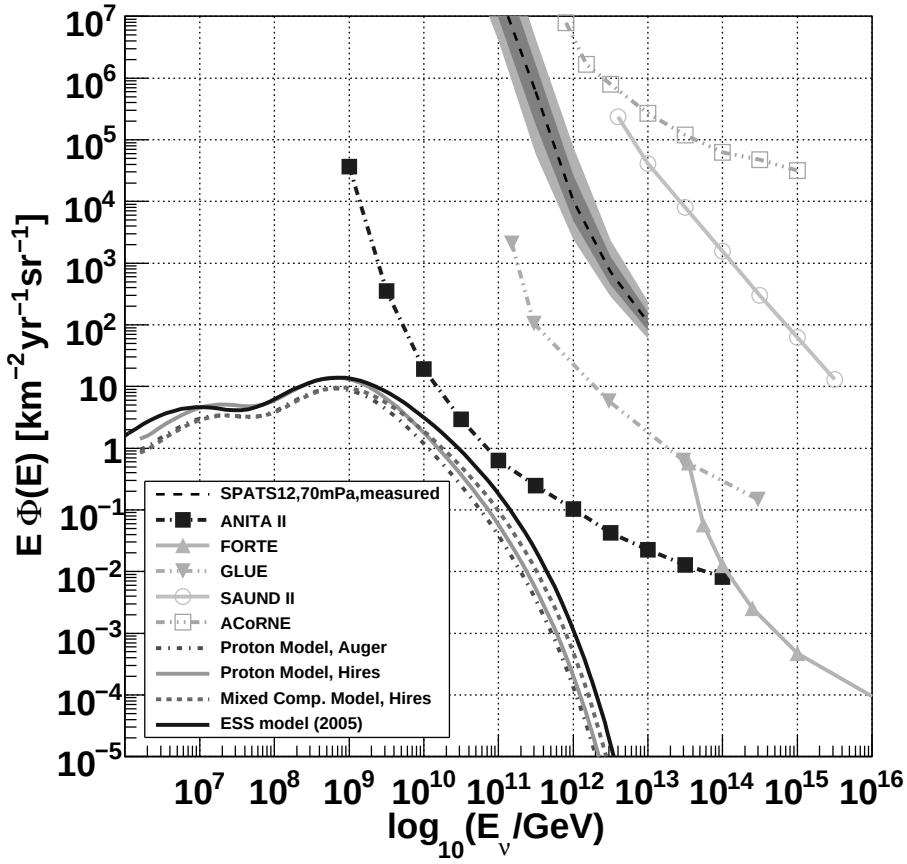

Figure 4.12: The neutrino flux limit of the 2009 SPATS configuration (70 mPa threshold, $\geq$ 5 hits per event) from [191]. The dark grey band (50 to 100 mPa threshold) around the limit considers uncertainties in absolute noise. The even broader light grey band includes additional uncertainties due to the choice of different acoustic models. Experimental limits on the flux of ultra-high-energy neutrinos are from ANITA II [48], FORTE [179], GLUE [46], SAUND II [196], ACoRNE [197]. Different models for the cosmogenic flux are shown [178]. Figure from [191].

forming a tetrahedral antenna with side lengths of about 1 m. In an analysis carried out with data recorded during 13 months between May 2005 and November 2006 [195], the average acoustic sea noise in the band 20 to 43 kHz was measured as $5.4 \pm 2.2\,(\mathrm{stat}) \pm 0.3\,(\mathrm{sys})\ \mathrm{mPa}\,(\mathrm{RMS})$. In 2011, the deployment of a new hydrophone antenna is planned in the context of the NEMO-II project.

The **SAUND (Study of Acoustic Ultra-high energy Neutrino Detection)** experiment [164] employed a large hydrophone array in the U.S. Navy Atlantic Undersea Test And Evaluation Center (AUTEC) [164]. The array is located in the Tongue of the Ocean, a deep tract of sea in the Bahama islands at approximately 24°30'N and 77°40'W. In the first phase SAUND-I, 7 hydrophones arranged over an area of $\sim$250 km^2 where used for the studies of UHE neutrino detection. The hydrophones were mounted on 4.5 m booms standing vertically on the ocean floor at about 1600 m depth. The horizontal spacing between central and pe-

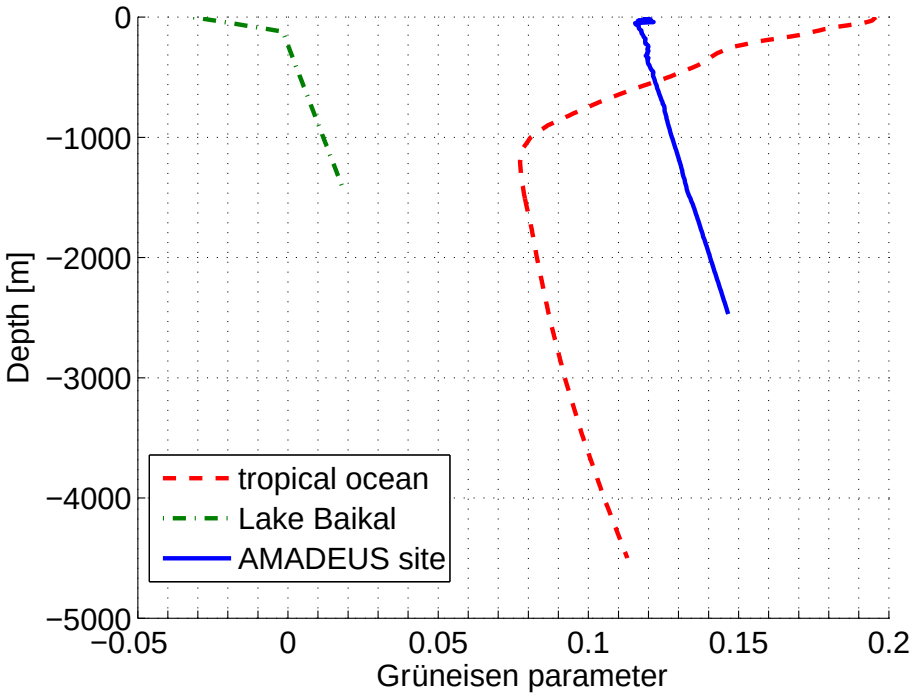

Figure 4.13: Grüneisen Parameter for Lake Baikal, Mediterranean Sea at the ANTARES site, and tropical ocean waters.

ripheral hydrophones was between 1.50 km and 1.57 km. After the upgrade of the array, 49 hydrophones that are mounted 5.2 m above the ocean floor, at depths between 1340 and 1880 m where available. The upgraded array spans an area of $\sim$ 20 km $\times$ 50 km with spacing of 3 to 5 km. This array was used in the second phase SAUND-II. Neutrino flux limits were derived with SAUND-I for a lifetime of 195 days [168] and for SAUND-II for an integrated lifetime of 130 days [196], see Fig. 4.12.

The **ACoRNE (Acoustic Acoustic Cosmic Ray Neutrino Experiment)** project [198] utilises the Rona hydrophone array, situated near the island of Rona between the Isle of Skye and the Scottish mainland. At the location of the array, the sea is about 230 m deep. The ACoRNE Experiment uses 8 hydrophones, anchored to the sea bed and spread out over a distance of about 1.5 km. Six of these hydrophones are approximately in mid-water, one is on the sea bed while the last one is about 30 m above the sea bed. The ACoRNE collaboration has derived a flux limit on UHE neutrinos [197] which is shown in Fig. 4.12.

To compare the acoustic properties at different sites, in Fig. 4.13, the Grüneisen parameter is plotted vs. depth for three different bodies of water. In each case, the value was calculated from temperature, pressure (i.e. depth) and salinity according to the parametrisations given in [169]. The temperature in Lake Baikal was parametrised following [194] as rising linearly from 0° to 3.5°C for a depth between 0 m and 125 m. At greater depth, the temperature is taken as constant at 3.5°C, which models the data to better than 0.2°C. For the Mediterranean Sea at the ANTARES site and for the tropical ocean at 22°30' N and 72°30' W, the same data were used as discussed in Sec. 4.3: For the ANTARES site the measurement from March

2010 [171] and for the tropical ocean the summer values.
As mentioned above, a Grüneisen parameter near zero for Lake Baikal strongly suppresses signals resulting from the thermo-acoustic effect. Compared to sea water, the effect is partially compensated by the increased attenuation length, see Fig. 4.1. In shallow water, properties are most favourable in the tropic ocean whereas beyond a depth of about 1000 m, the Grüneisen parameter for the Mediterranean Sea exceeds that for the ocean by about 50%.
Compared to Mediterranean water, the Grüneisen parameter of ice is bigger by a factor of roughly 10 [156]. The lateral distribution of the shower energy from a neutrino interaction, which is another crucial parameter for the maximum pulse height of a neutrino-induced pressure pulse (see Eq. 4.15), is expected to be similar for water and ice. Hence for a given shower energy, pressure pulses are expected to be higher in ice than in water at small distances. For ice at the South Pole, measurements of the attenuation length [190] on the other hand indicate that the amplitude falls off much more rapidly with distance than in water for the relevant frequency range. Hence the advantage is lost for large distances between acoustic sensors.

4.6 Alternative Detection Methods

While the the acoustic detection method is the main focus of this report, it is not the only technique under investigation for the detection of UHE neutrinos. In this section, some alternative techniques will be briefly described.
In most general terms, alternative methods use different signatures of particle showers (both hadronic and electromagnetic) in various media and typically require that the shower develops deep in that medium, where the only particles that can initiate a reaction are neutrinos. Frequently, detection of UHE neutrinos is the extension of an existing program to detect particle showers from cosmic rays and consequently the same methods for the detection are used.
The radio Cherenkov method is based on the detection of electromagnetic radiation with frequencies of about 100 MHz - 1 GHz, which is coherently emitted from the excess of electrons present in (hadronic or electromagnetic) showers interacting in dense media [199]. The radio Cherenkov method has been applied at the South Pole where the emission from neutrino-induced showers is searched for by antennas deployed inside the ice by the RICE[15] Experiment [200, 201], and by the balloon-borne experiment ANITA [48]. Several follow-up experiments and extensions to the existing programmes are currently planned or designed [202, 203]. The FORTE[16] satellite [179] recorded bursts of electromagnetic waves arising from near the Earth's surface in the radio frequency range of 30 to 300 MHz with a dual polarisation antenna. For data recorded in the period from September 1997 to December 1999, an effective time of observation of about three days was spent on searching for electromagnetic emission generated in the Greenland ice sheet. The resulting limit on the UHE neutrino flux is shown in Fig. 4.12.
A further target medium that is searched for radio Cherenkov signals is the lunar regolith. Recent experiments employing radio telescopes for the search are GLUE [46] (using the JPL/NASA Deep Space Network antennas at Goldstone, California, USA) the experiment at

[15] Radio Ice Cherenkov Experiment
[16] Fast On-orbit Recording of Transient Events

the radio telescope in Kalyazin, Russia [204], NuMoon (using the Westerbork Synthesis Radio Telescope, Netherlands) [205], LUNASKA[17] [206] (using the Parkes radio telescope in New South Wales, Australia) and RESUN[18] [207] (using the Very Large Array in New Mexico, USA). As the next step of the NuMoon experiment, radio detection of emission from the lunar regolith is investigated in the context of the LOFAR[19] experiment [208] that is currently under construction in the Netherlands. Furthermore, the detection of radio Cherenkov radiation from neutrino-induced showers in salt domes is investigated by the SalSA[20] [209] and HASRA[21] [210] collaborations.

An alternative to the detection of radio signals is the detection of Cherenkov and/or fluorescent light from neutrino-induced extended air showers. Exploiting this option, the surface detectors of the Pierre Auger Observatory have been used to search for neutrinos produced by two mechanisms. First, upgoing, "Earth skimming" tau neutrinos, which interact inside the Earth, produce an upgoing tau lepton. If the tau decays hadronically, an upgoing shower is registered in the Pierre Auger Observatory, which would be a clear signature of an underlying neutrino reaction. Second, neutrinos of any flavour can be identified by down-going, nearly horizontal showers that start deep inside the atmosphere, i.e. after a distance of several interaction lengths up to which a cosmic ray could not propagate without initiating a shower beforehand. Limits on the neutrino flux obtained with both methods have been published [211, 212]. It is furthermore under investigation if an extension to the Pierre Auger Observatory for the detection of radio signals from air showers can be used for the detection of neutrinos, see [213] for a summary. In air, the geosynchrotron model predicts that coherent radio emission originates from electron-positron pairs in the shower as they move through the geomagnetic field [214].

JEM-EUSO[22] [215], a proposed observatory on board of the Japanese Exploration Module of the International Space Station, is taking the observation of extended air showers into space. It will monitor the atmosphere, a target volume of $\sim 10^{12}$ tons, for fluorescent UV photons from extended air showers. JEM-EUSO can detect neutrinos through their LPM dominated extended air showers evolving deep in the atmosphere.

[17] Lunar UHE Neutrino Astrophysics with the Square Kilometre Array
[18] Radio EVLA Search for UHE Neutrinos
[19] Low Frequency Array
[20] Salt Sensor Array
[21] Hawaii Askaryan in Salt Radio Array
[22] Japanese Experiment Module - Extreme Universe Space Observatory

Chapter 5

Activities in the Context of the AMADEUS Project

As was discussed at the end of the previous chapter, various activities are ongoing to push forward the development of acoustic detection techniques both in water and ice. One of the major advantages over an optical neutrino telescope that motivates the pursuit of investigations towards acoustic detection of neutrinos, the much larger attenuation length, was discussed in the previous chapter. A second advantage, the more compact sensor design and simpler readout electronics for acoustic measurements, will become evident in this chapter in the detailed description of the AMADEUS design.
In this chapter, the activities in the context of the AMADEUS setup within the ANTARES detector in the Mediterranean Sea will be discussed. In Sec. 5.1 preparatory studies are discussed, verifying the thermo-acoustic model, which were performed by depositing energy by means of a laser and a proton beam in water. The AMADEUS detector itself will be described in Sec. 5.2. In the next two sections, first experimental results obtained with the AMADEUS data will be presented: In Sec. 5.3 the position calibration of the acoustic sensors within the ANTARES detector will be discussed and in Sec. 5.4 investigations of the acoustic background in the deep sea will be presented. Finally, in Sec. 5.5 data analysis techniques are discussed which will eventually permit an assessment of the feasibility of a future large-scale acoustic neutrino detector.

5.1 Verification of the Thermo-Acoustic Model

In 1957 G.A. Askaryan pointed out that ionisation and cavitation along a track of an ionising particle through a liquid leads to hydrodynamic radiation [216]. Starting in the late 1970s, theoretical and experimental studies have been performed on the hydrodynamic radiation of beams and particles transversing dense media [153, 154, 217, 218, 219, 220]. In this section, recent measurements performed in preparation for the AMADEUS project will be discussed.

5.1.1 Experimental Setup and Beam Characteristics

The experiments presented in this section were performed with a pulsed infrared Nd:YAG laser facility ($\lambda = 1064\,\mathrm{nm}$) located at the Erlangen Centre for Astroparticle Physics (ECAP) of the University of Erlangen, and the $177\,\mathrm{MeV}$ proton beam of the “Gustaf Werner Cy-

clotron" at the "Theodor Svedberg Laboratory" in Uppsala, Sweden. The beam properties allow for a compact experimental setup. In both cases, the beams were dumped into a dedicated $150 \times 60 \times 60\,\mathrm{cm}^3$ water tank, where the acoustic field was measured with several position-adjustable acoustic sensors (see Fig. 5.1). The sensors could be positioned within the tank with absolute uncertainties below 1 cm. The temperature of the water could be varied between $1°\mathrm{C}$ and $20°\mathrm{C}$ with a precision of $0.1°\mathrm{C}$. The temperature was brought to a particular value by first cooling the water with ice; subsequently the whole water volume was heated to the desired temperature in a controlled, gradual procedure. Once the water temperature had been established, at least 10 min remained for measurements until the water volume heated up by $0.1°\mathrm{C}$ through heat transfer from the environment. This time span was sufficient for all measurements conducted at water temperatures below the ambient temperature.

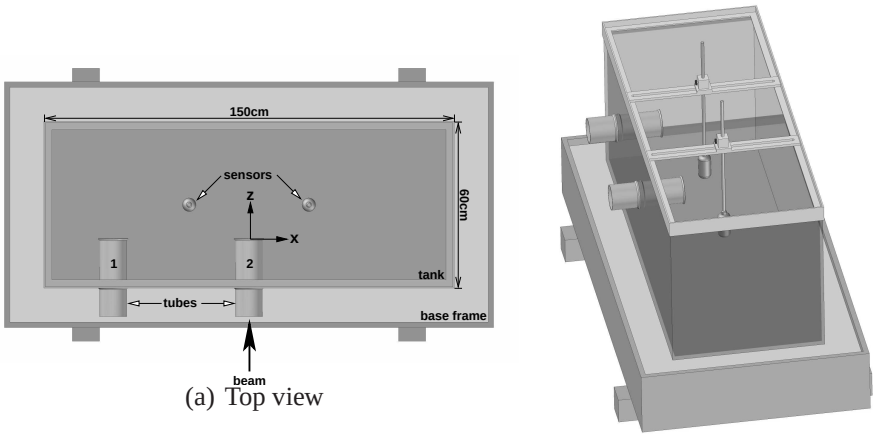

(a) Top view

(b) Isometric view

Figure 5.1: Schematic view of the experimental setup. Beams can enter the water volume through a thin foil (proton beam) or glass window (laser beam), which are set away from the tank walls via two air-filled tubes to minimise effects of surface reflections on the recorded signals.

The explored range of spill energies for the proton beam was from $10\,\mathrm{PeV}$ to $400\,\mathrm{PeV}$, the beam diameter was approximately $3\,\mathrm{mm}$ and the spill time $t_s \approx 30\,\mu\mathrm{s}$. For $177\,\mathrm{MeV}$ protons, the energy deposition in the water along the beam axis (z-axis, beam entry into the water at $z = 0\,\mathrm{cm}$) is relatively uniform up to $z = 20\,\mathrm{cm}$ ending in the prominent Bragg-peak at $z \approx 22\,\mathrm{cm}$ (see Fig. 5.2).
For the laser experiment, the pulse energy was adjusted between $0.1\,\mathrm{EeV}$ and $10\,\mathrm{EeV}$ at a beam diameter of approximately $2\,\mathrm{mm}$, the pulse length was $9\,\mathrm{ns}$. For the infrared light used, the laser energy density deposited along the beam axis has an exponential decrease with an absorption length of $(5.9 \pm 0.1)\,\mathrm{cm}$.
For both beam types the lateral energy deposition profile was Gaussian (the given beam diameters are the σ-values of the profiles). The two experiments allow for the use of different spatial and temporal distributions of the energy deposition as well as two different mechanisms of energy transfer into the medium. For both beams, energy is deposited via atomic excitation, in addition the medium is ionised in the case of the proton beam.
For the signal recording, sensors based on the piezo-electric effect [221] were used. A full

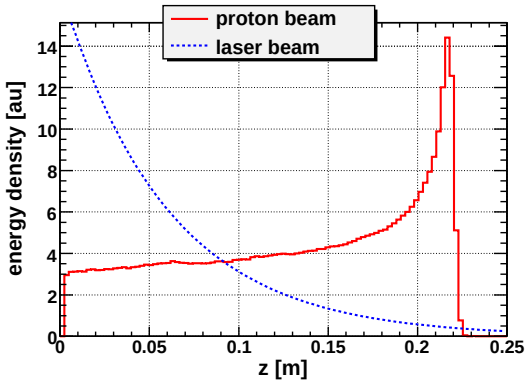

Figure 5.2: Simulated energy deposition density along the beam axis (z-axis) for the two beam types (integral normalised to 1). For the proton beam the Bragg peak is prominent at 0.22 m, for the laser beam the decrease is exponential with an attenuation length of 0.059 m.

characterisation of these sensors had been performed prior to the experiments. They are linear in amplitude response, the frequency response is flat starting from a few kHz up to the main resonance at $40\,\mathrm{kHz}$ with a sensitivity of $-155\,\mathrm{dB\,re\,1V/\mu Pa}$ (~ 0.02 V/Pa). The main resonance is more sensitive by $\sim 5\,\mathrm{dB\,re\,1V/\mu Pa}$ and sensitivity drops rapidly at higher frequencies. The absolute uncertainty in the determination of the sensitivity is at a level of 2 dB, at frequencies above 90 kHz—were the sensitivity has dropped by 20 dB—the uncertainty exceeds 5 dB. To calculate the response of the sensors to an external pressure pulse a parametrised fit of an equivalent circuit model as described in [221] was used. The sensitivity dependence on water temperature was measured and the relative decrease was found to be less than 1.5% per $1°\mathrm{C}$.
For every set of fixed experimental parameters (temperature, energy, sensor position, etc.) the signals of 1000 beam pulses were recorded with a digital oscilloscope, at a sampling rate in excess of $1\,\mathrm{MHz}$, sufficient for the signals with spectral components up to 100 kHz, where the sensitivity of the sensors becomes negligibly small. These individual pulses were averaged to reduce background and environmental noise in the analysis, thereby obtaining a very high statistical precision.

5.1.2 Basic Features of the Measured Signals

Figure 5.3 shows typical signals measured in the proton and the laser experiment using the same sensors and experimental setup. The general shapes of the two signals differ: a typical signal for the proton beam shows a bipolar signature, the one for the laser deviates from such a generic form. The laser signal has high frequency components up to several MHz due to the high energy deposition density at the point of beam entry and the almost instantaneous energy deposition compared to the µs-pulse of the proton beam; therefore the resonance of the sensor is excited causing a ringing in the measured signal. The spatial distribution of the energy density ϵ deposited by the laser leads to the two separate signals: the first originates in the beam area at the same z-region as the sensor placement (*"direct signal"*), the second from the beam entry, a point of discontinuity where most of the energy is deposed (*"beam entry signal"*).

The signal of the proton beam is deteriorated with respect to an ideal bipolar signal primarily by three factors: the recorded signal starts before the expected onset of the acoustic signal (55.2 µs for the given position, see Fig. 5.3, given by the sonic path length); reflections of the acoustic wave on the beam entry window overlay the original wave starting in the first rarefaction peak; and finally there are frequency components of the signal exciting a resonant response of the sensor, causing a slight change in the signal shape and ringing. The first factor was studied and found to be consistent with an electric charge effect in the sensors caused by the proton beam. Its starting time is always coincident with the beam pulse entry into the water, even at sensor distances of up to 1 m, hinting at an electromagnetic origin. Its shape is consistent with the integrated time-profile of the beam pulse with a subsequent exponential decay. This deformation of the signal is considered a systematic uncertainty on the signal properties and treated as such in the analysis. For the most part, it was subtracted from the signal.
In order to minimise the impact of the signal deformation given by the described effects on the analysis of the recorded signals, robust characteristics were used: the peak-to-peak amplitude and the signal duration from maximum to minimum of the signal. For the laser experiment these features were extracted for the direct signals only.

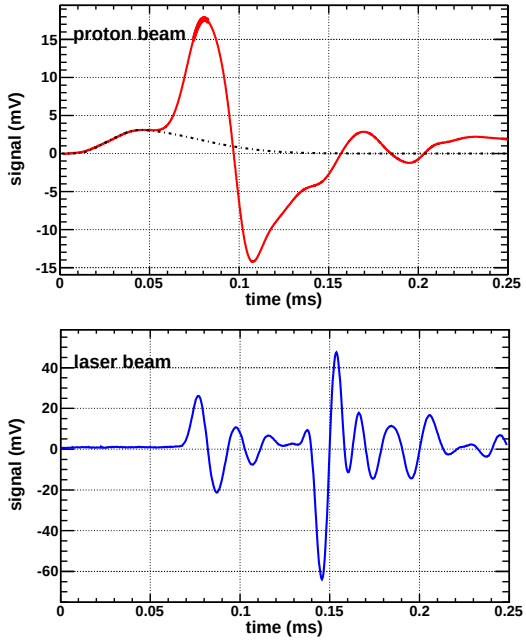

Figure 5.3: Typical signals measured in the proton (upper graph) and laser (lower graph) experiment. Both signals (solid lines) were taken at a sensor position near x=10 cm and z=20 cm and are shown within the same time interval. The dash-dotted line in the upper graph indicates the charge effect described in the text.

5.1.3 Simulation of Thermo-Acoustic Signals

For an in-depth validation of the thermo-acoustic model, comparisons of the signal properties with simulation results based on the model are essential. To this aim, a simulation of the expected signals was developed. It is based on the thermo-acoustic model using a numeric

solution of Eq. 4.7. Note that the assumption of instantaneous energy deposition that was made for neutrino interactions in Eq. 4.8 is not valid for the proton beam.
The input parameters to the simulation were either measured at the experiments, i.e. medium temperature and beam profiles, or simulated, i.e. the energy deposition of the protons (using GEANT4). The thermodynamic parameters bulk expansion coefficient, heat capacity and sound velocity were derived from the measured water temperature using standard parametrisations. Tap water quality was assumed.
A series of simulations was conducted, where the input parameters were varied individually in the range given by the experiment including uncertainties. Especially the spatial and temporal beam profile has a substantial impact on signal amplitude, duration and shape. Simulated signals and the respective sensor response corresponding to the measured signals of Fig. 5.3 are shown in Fig. 5.4. To minimise systematic effects from the setup caused e.g. by reflections on the surfaces, the sensor response was convoluted onto the simulated signals, rather than deconvoluted from the measured ones. Thus in the analysis voltage signals are compared.

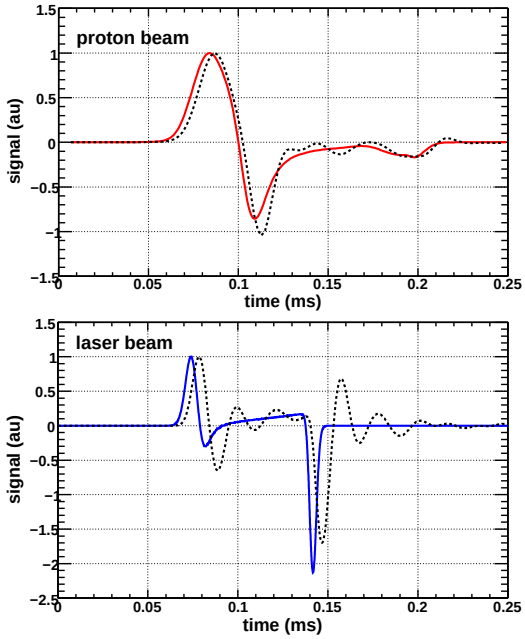

Figure 5.4: Simulated signals for the proton (upper graph) and laser experiment (lower graph). Both signals (solid lines) were calculated for the experimental conditions of Fig. 5.3. The corresponding dashed-lined signals mark the simulated signals after convolution with the sensor response. For better comparability, the signal maxima were normalised to 1.

The shapes of the simulated pulses are distorted by the sensor response, especially the high-frequency components above the resonant frequency of the sensor. In the case of the laser pulse, mostly the resonance of the sensor is excited, leading to a strong ringing. For the proton beam, the primarily bipolar shape is again prominent, whereas the laser pulse is segmented into the two parts described above. The direct pulse of the laser experiment exhibits a bipolar shape as well, albeit less symmetric than for the proton beam.
Figure 5.5 exemplifies the dependency of the signal amplitude on the input parameters of

the simulation: water temperature, pulse energy, beam profile in x and y, pulse length and the position of the sensor. All parameters were varied by $\pm 50\%$ around the value of the best agreement with measurement, i.e. the values used for the simulations of the signals shown in Fig. 5.4.

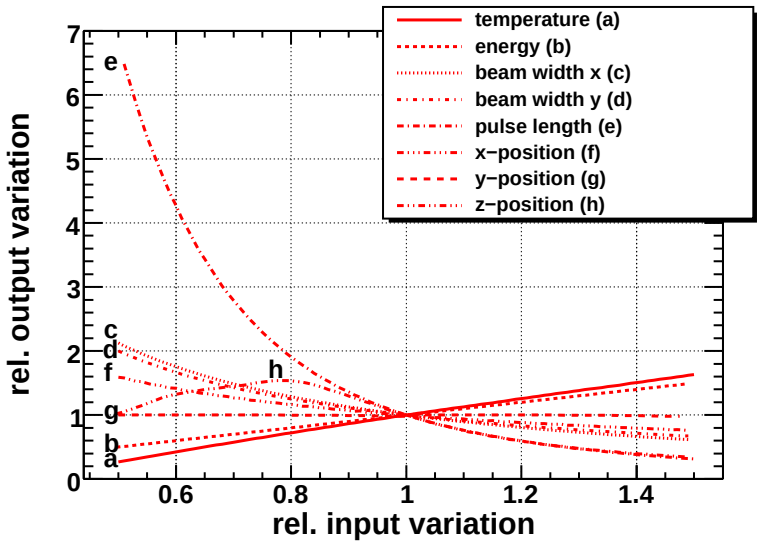

(a) Proton beam simulation results

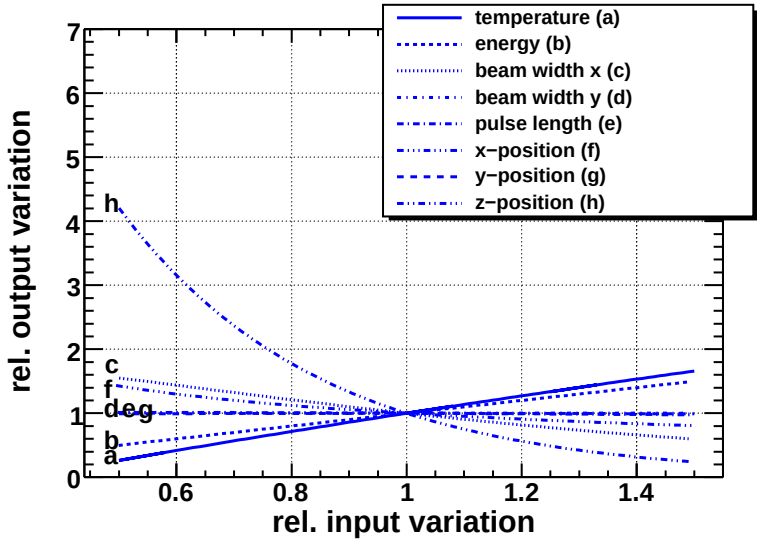

(b) Laser beam simulation results

Figure 5.5: Dependency of the simulated signal amplitude on variation of the simulation input parameters (labelled a – h) for the proton (upper graph) and the laser experiment (lower graph).

The main characteristics of thermo-acoustic sound generation are observable. As was discussed in Sec. 4.2.1, the dependence on temperature is proportional to α/c_p and the dependence on energy strictly linear. The dependency on the beam pulse parameters is diverse. It is governed by the integral in Eq. 4.7 and therefore on both the spatial and the temporal beam profiles and the interaction of the particles with the water. For a given point in space and time, the elementary waves produced in the volume of energy deposition may interfere constructively or destructively depending on the beam properties. E.g. the spill time (or pulse

length) of the laser pulse has no influence on the amplitude, as with 9 ns it is shorter than the transit time of the acoustic signal through the energy deposition area. For the several ten µs long proton spill, the spill time is comparable to the transit time. Thus the acoustic signal shows a strong dependence on the spill time. The dependence of the amplitude on the radial coordinate w.r.t. the beam axis r (corresponding to the x-position in the experiments) follows roughly the expected $1/\sqrt{r}$ or $1/r$ fall-off of a cylindrical source in the near and the far field, respectively. The y-position was varied between -2 and $2\,\mathrm{cm}$, as the signals were recorded within the xz-plane. The resulting change in amplitude is below 1% and can therefore be neglected. The z-dependency for the laser experiment follows the exponential fall-off expected from the light absorption. The one for the proton experiment shows a non-monotonic behaviour due to the form of the energy deposition with the prominent Bragg peak.
Using these dependencies the uncertainties of the simulation can be obtained using the experimental uncertainties of the various parameters. The main uncertainty for the proton beam is given by the temporal profile of the proton pulse, which was simplified to a Gaussian profile for this study. For the laser beam experiment this parameter influences the signal amplitude only on a one percent level. The second main influence on the amplitude is the position along the beam axis (z-direction).
Table 5.1 gives the parameters and their uncertainties (ΔV) used for the simulation of the signals. The resulting systematic uncertainties in the amplitude (ΔA) are given as well. The combined uncertainties are $^{+34\%}_{-29\%}$ for the proton signal and $^{+26\%}_{-24\%}$ for the laser signal, respectively.

5.1.4 Comparison of Simulated and Measured Signals

5.1.4.1 Proton Beam Experiment

Figure 5.6 shows a comparison between simulated and measured signals for the proton beam experiment at different sensor positions. For better visibility only the main part of the signals (first bipolar part) is plotted. The input parameters of the simulation were varied within the experimental uncertainties until the best agreement in amplitude and duration was obtained for the reference point at x=0.40 m and z=0.11 m. The other signals are simulated with the same parameter set, only the sensor position is changed. The signal shapes differ for different z-positions due to the geometry of the energy deposition profile described in Sec. 5.1.1 with cylindrical form in the xy-plane and flat energy density in z-direction up to the Bragg peak at $z = 0.22\,\mathrm{m}$. Due to this geometry an almost cylindrical wave is excited in the medium, with coherent emission perpendicular to the beam axis. In the region $z \lesssim 0.2\,\mathrm{m}$ the signals are of bipolar shape. Along the beam axis ($x \approx 0.0\,\mathrm{m}$, $z > 0.25\,\mathrm{m}$) the main part of the observed signal originates from the Bragg peak as a nearly spherical source and no clear bipolar shape evolves.
The agreement between simulation and measurement is good for all positions. Not only amplitude and duration match but also the signal shape is reproduced to a very high degree. The small discrepancies, primarily in the rare-faction part of the bipolar pulse, are influenced by a non-ideal sensor calibration and reflections on the tank surfaces. However, a significant part of the discrepancies may lie in the beam pulse modelling or even the thermo-acoustic model itself.

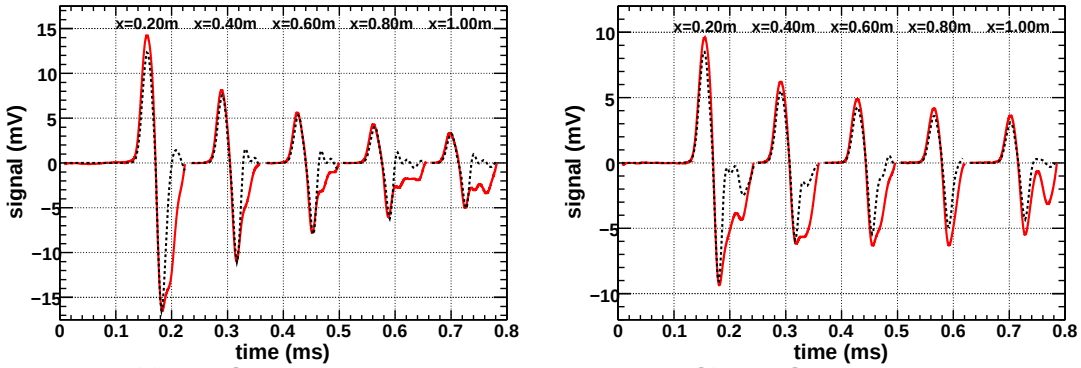

(a) Signals at $z = 0.11\,\mathrm{m}$

(b) Signals at $z = 0.21\,\mathrm{m}$

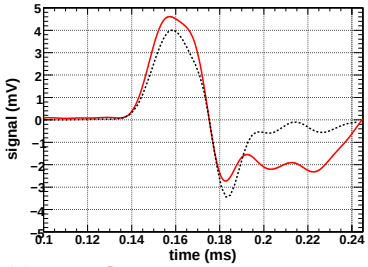

(c) Signal at $x = 0.01\,\mathrm{m}$, $z = 0.41\,\mathrm{m}$

Figure 5.6: Comparison of measured (solid line) and simulated (dashed line) signals at different sensor positions for the proton beam experiment. The reference signal for tuning the simulations is at $z = 0.11\,\mathrm{m}$ and $x = 0.40\,\mathrm{m}$. The coordinate system is given in Fig. 5.1. See text for a detailed description.

Parameter	Proton value (ΔV)	ΔA	Laser value (ΔV)	ΔA
temperature	$12.0°\mathrm{C}$ ($\pm 8\%$)	$^{+10\%}_{-11\%}$	$12.0°\mathrm{C}$ ($\pm 8\%$)	$\pm 11\%$
energy	$4.1 \cdot 10^{17}$ eV ($\pm 10\%$)	$\pm 10\%$	$5.2 \cdot 10^{17}$ eV ($\pm 10\%$)	$\pm 10\%$
beam width (x-direction)	3.0 mm ($\pm 14\%$)	$^{-14\%}_{+19\%}$	5.0 mm ($\pm 15\%$)	$^{-14\%}_{+16\%}$
beam width (y-direction)	3.0 mm ($\pm 14\%$)	$^{-12\%}_{+16\%}$	5.0 mm ($\pm 15\%$)	$\pm 0\%$
pulse length	$1.0 \cdot 10^{-5}$ s ($\pm 11\%$)	$^{-13\%}_{+16\%}$	$6.9 \cdot 10^{-7}$ s ($\pm 50\%$)	$^{-2\%}_{+2\%}$
x-position	0.10 m ($\pm 7\%$)	$^{-4\%}_{+5\%}$	0.11 m ($\pm 6\%$)	$^{-3\%}_{+4\%}$
y-position	0.0 m (± 1 cm)	$^{-2\%}_{+0\%}$	0.0 m (± 1 cm)	$^{-1\%}_{-1\%}$
z-position	0.22 m ($\pm 4\%$)	$\pm 9\%$	0.17 m ($\pm 5\%$)	$^{-11\%}_{+13\%}$
combined		$^{+34\%}_{-29\%}$		$^{+26\%}_{-24\%}$

Table 5.1: Beam parameters used for the simulated signals in Fig. 5.4 with their associated experimental uncertainties (ΔV) and resulting uncertainty in signal amplitude (ΔA). The pulse length of the laser is set to a value much higher than in the experiment, to save calculation time. The resulting uncertainty in the signal amplitude is below 2%

5.1.4.2 Laser Beam Experiment

The prominent feature of the energy deposition of the laser beam is at the beam entry into the medium. Otherwise, the geometry of this deposition is mainly a cylindrical one in the xy-plane, as for the proton beam, with coherent emission perpendicular to the beam axis (direct signal). The signal from the discontinuity at the beam entry is emitted almost as from a point source (beam entry signal). In contrast to the proton beam, the shapes of signals at different position along the z-axis do not vary much, only the relative timing between the two signal components. Therefore, Fig. 5.7 shows only signals for a z-position in the middle of the water tank. Here, both signal parts are well described by the simulation. The beam entry part of each signal is less well reproduced in the simulation due to its high frequency components where the sensor calibration has high uncertainties.
For the laser signal, only the amplitude from the direct signal part is considered in the following.

5.1.5 Analysis of the Temperature Variation

The main feature of the thermo-acoustic model is its dependence on the temperature of the medium. Figures 5.8 and 5.9 show the temperature dependence of the signal peak-to-peak amplitude, where a positive (negative) sign denotes a leading positive (negative) peak of the signal. The two data sets shown in each figure were recorded by two sensors simultaneously,

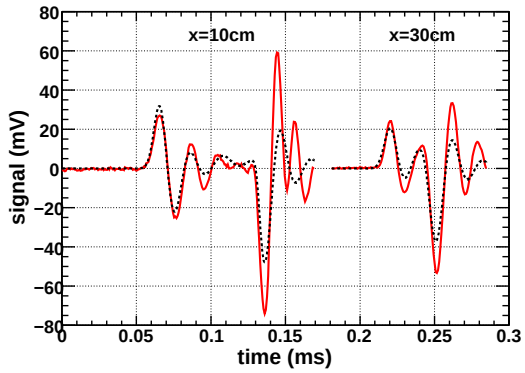

Figure 5.7: Comparison of measured (solid line) and simulated (dashed line) signals for the laser beam experiment at $z = 0.17\,\mathrm{m}$ for different sensor positions along x (reference at $x = 0.10\,\mathrm{m}$). For more details see text.

which were positioned at $x = 0.10\,\mathrm{m}$ perpendicular to the beam axis and at $z = 0.11\,\mathrm{m}$ and $z = 0.21\,\mathrm{m}$ along the beam axis, respectively. In the case of the proton beam setup the hydrophone positions correspond roughly to the z-position of the Bragg-peak and a z-position half way between the Bragg-peak and the beam entry into the water, respectively. For comparability, the same positions and the same sensors were chosen for the laser experiment.
The laser beam signal shown in Fig. 5.8 changes its polarity at about $4°\mathrm{C}$, as expected from the thermo-acoustic model. The theoretical expectation for the signal amplitude, which is proportional to α/c_p and vanishes at $4°\mathrm{C}$, is fitted to the experimental data. In the fit, an overall scaling factor and a shift in temperature (for the experimental uncertainty in the temperature measurement) were left free as fit parameters. The fit yielded a zero-crossing of the amplitude at $(3.9 \pm 0.1)°\mathrm{C}$, where the error is dominated by the systematic uncertainty in the temperature setting. Analysing the proton data in the same way resulted in a fit that slightly deviated from the model expectation, and a zero-crossing significantly different from $4.0°\mathrm{C}$ at $(4.5 \pm 0.1)°\mathrm{C}$. In view of the results from the laser beam measurements, the residual signal of tripolar shape at $4.0°\mathrm{C}$ was subtracted from all signals, which has an amplitude of 5% of the $15.0°\mathrm{C}$ signal. Thus a non-temperature dependent effect on top of the thermo-acoustic signal was assumed. The resulting amplitudes shown in Fig. 5.9 are well described by the model prediction.
The production mechanism of the underlying signal at $4.0°\mathrm{C}$, which was only observed at the proton experiment, could not be unambiguously determined with the performed measurements. From the model point of view, the main simplification for the derivation of Eq. 4.7 was to neglect all non-isotropic terms and moment transfers to the medium in the momentum density tensor Π^I_{ij}. E.g. near-field effects or dipole radiation could contribute significantly near the disappearance of the volume expansion coefficient. Also other non-thermo-acoustic signal production mechanism have been discussed in the literature which could give rise to an almost temperature independent signal, see e.g. [153]. The obvious difference to the laser experiment are the charges involved both from the protons themselves and the ionisation of the water which could lead to an interaction with the polar water molecules. Another difference are the massive protons compared to massless photons. Residual signals at $4.0°\mathrm{C}$ were found in previous works as well [217, 218, 219], where the temperature of zero amplitude is ranging from 2.5 to $6.0°\mathrm{C}$.

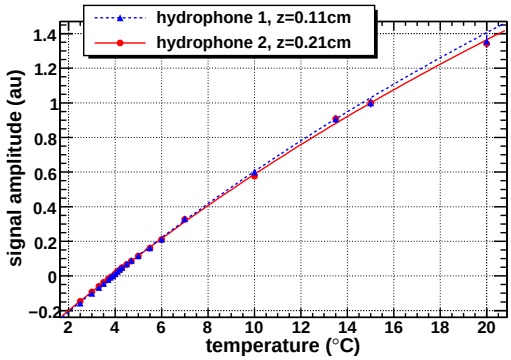

Figure 5.8: Measured signal amplitude of the bipolar acoustic signal induced by laser pulses at different temperatures fitted with the theoretical expectation as described in the text. All amplitudes were normalised to 1 at 15.0°C.

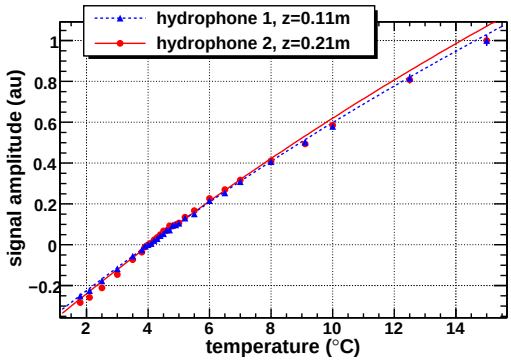

Figure 5.9: Measured signal amplitude of the bipolar acoustic signal induced by proton pulses at different temperatures fitted with the model expectation as described in the text. The non-thermo-acoustic signal at 4.0°C was subtracted at every temperature. The amplitudes were afterwards normalised to 1 at 15.0°C.

For clarification further experiments are needed either with ionising neutral particles (e.g. synchrotron radiation) or with charged particles (e.g. protons, α-particles) with more sensors positioned around the Bragg-peak. With such experiments it might be possible to distinguish between the effect of ionisation in the water and of net charge introduced by charged particles.

5.1.6 Outcome of the Experiments

It was demonstrated that the sound generation mechanism of intense pulsed beams is well described by the thermo-acoustic model. In almost all aspects investigated, the signal properties are consistent with the model. The biggest uncertainties of the experiments are on the 10% level. One discrepancy is the non-vanishing signal at 4°C for the proton beam experiment, which can be described by an additional non-temperature dependent signal with 5% of the amplitude at 15°C. The model allows for calculations of the characteristics of sound pulses generated in the interaction of high-energy particles in water with the input of the energy deposition of the resulting particle shower. The performed measurements confirm the principal possibility of the acoustic detection of UHE neutrinos. The investigation of

the experimental feasibility in the Mediterranean Sea with the AMADEUS project will be discussed in the next section.

5.2 The AMADEUS Detector

The AMADEUS project was conceived to perform a feasibility study for a potential future large-scale acoustic neutrino detector. For this purpose, a dedicated array of acoustic sensors was integrated into the ANTARES neutrino telescope [5, 222]. In the context of AMADEUS, the following aims are being pursued:

- Long-term background investigations (levels of ambient noise, spatial and temporal distributions of sources, rate of neutrino-like signals);
- Investigation of spatial correlations for transient signals and for persistent background on different length scales;
- Development and tests of data filter and reconstruction algorithms;
- Investigation of different types of acoustic sensors and sensing methods;
- Studies of hybrid (acoustic and optical) detection methods.

In particular the knowledge of the rate and correlation length of neutrino-like acoustic background events is a prerequisite for estimating the sensitivity of a future acoustic neutrino detector.
In this section, the AMADEUS system within the ANTARES detector will be described. First (Secs. 5.2.1 and 5.2.2) an overview of the system is given, with particular emphasis on its integration into the ANTARES detector. Subsequently the acoustic sensors and their calibration in the laboratory are described (Secs. 5.2.3 and 5.2.4). The remaining system components are described in Secs. 5.2.5 to 5.2.8 and in Section 5.2.10 the system performance is discussed. The characteristic features of the AMADEUS system are mainly determined by the acoustic sensors (Sec 5.2.3) and the custom-designed electronics board, which performs the off-shore processing of the analogue signals from the acoustic sensors. The electronics board is described in Sec. 5.2.6.

5.2.1 The ANTARES Detector and its Sub-system AMADEUS

AMADEUS is integrated into the ANTARES neutrino telescope [5, 222], which was designed to detect neutrinos by measuring the Cherenkov light emitted along the tracks of relativistic secondary muons generated in neutrino interactions. A sketch of the detector, with the AMADEUS modules highlighted, is shown in Figure 5.10. The detector is located in the Mediterranean Sea at a water depth of about 2500 m, about 40 km south of the town of Toulon on the French coast and was completed in May 2008. It comprises 12 vertical structures, the *detection lines*. Each detection line holds up to 25 *storeys* that are arranged at equal distances of 14.5 m along the line, starting at about 100 m above the sea bed and interlinked by electro-optical cables. A standard storey consists of a titanium support structure, holding three *Optical Modules* [223] (each one consisting of a photomultiplier tube (PMT) inside a water-tight pressure-resistant glass sphere) and one *Local Control Module (LCM)*.

The LCM consists of a cylindrical titanium container and the off-shore electronics within that container, see Sec. 5.2.5.
A 13th line, called *Instrumentation Line (IL)*, is equipped with instruments for monitoring the environment. It holds six storeys. For two pairs of consecutive storeys in the IL, the vertical distance is increased from 14.5 to 80 m. Each line is fixed on the sea floor by an anchor equipped with electronics and held taut by an immersed buoy at about 2000 m below the sea surface. An interlink cable connects each line to the *Junction Box* from where the main electro-optical cable provides the connection to the shore station.
The ANTARES lines are free to swing and twist in the undersea current. In order to determine the positions of the storey with a precision of about 20 cm—which is necessary to achieve the required pointing precision for neutrino astronomy—the detector is equipped with an acoustic positioning system [224]. The system employs an acoustic transceiver at the anchor of each line and four autonomous transponders positioned around the 13 lines. Along each detection line, five positioning hydrophones receive the signals emitted by the transceivers. By performing multiple time delay measurements and using these to triangulate the positions of the individual hydrophones, the line shapes can be reconstructed relative to the positions of the emitters. Currently, the sequence of positioning emissions is repeated every 2 minutes and lasts for about 10 seconds.
In AMADEUS, acoustic sensing is integrated in the form of *acoustic storeys* that are modified versions of standard ANTARES storeys, in which the Optical Modules are replaced by custom-designed acoustic sensors. Dedicated electronics is used for the digitisation and pre-processing of the analogue signals.

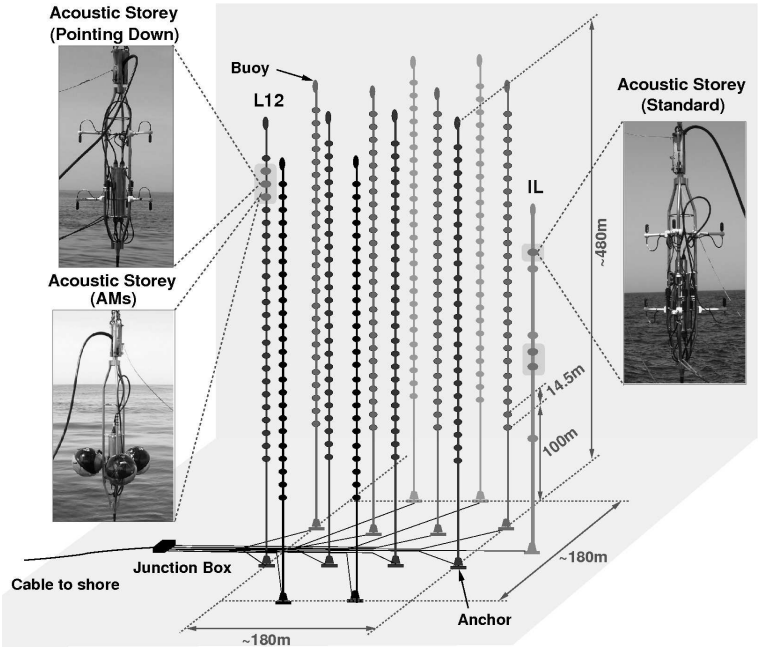

Figure 5.10: A sketch of the ANTARES detector. The six acoustic storeys are highlighted and their three different setups are shown (see text for details). L12 and IL denote the 12th detection line and the Instrumentation Line, respectively.

The AMADEUS system comprises a total of six acoustic storeys: three on the IL, which started data taking in December 2007, and three on the 12th detection line (Line 12), which was connected to shore in May 2008. AMADEUS is now fully functional and routinely

taking data with 34 sensors. Two out of 36 hydrophones became inoperational during their deployment. In both cases, the defect was due to pressurisation.
The acoustic storeys on the IL are located at 180 m, 195 m, and 305 m above the sea floor. On Line 12, which is anchored at a horizontal distance of about 240 m from the IL, the acoustic storeys are positioned at heights of 380 m, 395 m, and 410 m above the sea floor. With this setup, the maximum distance between two acoustic storeys is 340 m. AMADEUS hence covers three length scales: spacings of the order of 1 m between sensors within a storey; intermediate distances of 14.5 m between adjacent acoustic storeys within a line; and large scales from about 100 m vertical distance on the IL up to 340 m between storeys on different lines. The sensors within a storey allow for efficient triggering of transient signals and for direction reconstruction. The combination of the direction information from different acoustic storeys yields (after verifying the consistency of the signal arrival times at the respective storeys) the position of an acoustic source [225]. This concept of spatially separated clusters of acoustic sensors allows for the reduction of the required processing time without sacrificing the advantages given by the large attenuation length,

5.2.2 Acoustic Storeys

Two types of sensing devices are used in AMADEUS: hydrophones and *Acoustic Modules* (AMs). The sensing principle is in both cases based on the piezo-electric effect and is discussed in Sec. 5.2.3. For the hydrophones, the piezo elements are coated in polyurethane, whereas for the AMs they are glued to the inside of standard glass spheres which are normally used for Optical Modules. In each case, six acoustic sensors per storey were implemented. This number was the maximum compatible with the design of the LCM and the bandwidth of data transmission to shore. Furthermore, the acoustic storeys were designed such that their size did not exceed the size of the standard ANTARES storeys in radial dimension, hence assuring compatibility with the deployment procedure of the ANTARES lines. Figure 5.11 shows the design of a standard acoustic storey with hydrophones.

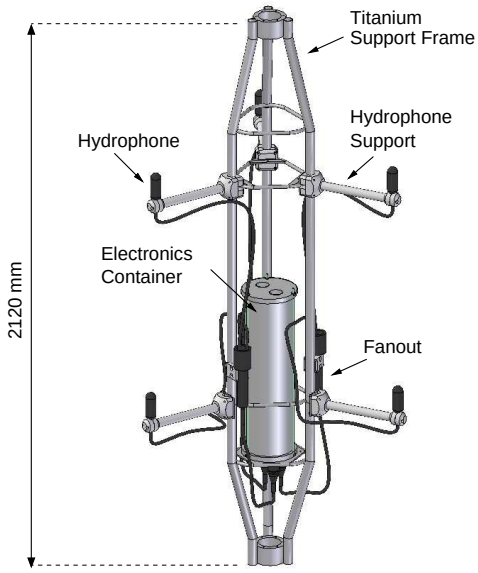

Figure 5.11: Drawing of a standard acoustic storey with hydrophones.

Figure 5.12 shows pictures of the three different designs of acoustic storeys installed in AMADEUS. The acoustic storeys on the IL house hydrophones only, whereas the lowermost acoustic storey of Line 12 holds AMs. The hydrophones are mounted to point upwards, except for the central acoustic storey of Line 12, where they point downwards. The sensitivity of the hydrophones is largely reduced at their cable junctions and therefore shows a strong dependence on the polar angle. The different configurations allow for investigating the anisotropy of ambient noise, which is expected to originate mainly from the sea surface (see Sec. 5.4.1).
Three of the five storeys holding hydrophones are equipped with commercial models, dubbed "HTI hydrophones"[1], and the other two with hydrophones, described in detail in Sec. 5.2.3, developed and produced at the Erlangen Centre for Astroparticle Physics (ECAP).

(a) (b) (c)

Figure 5.12: Photographs of three different storeys of the AMADEUS system during their deployment: (a) A standard storey, equipped with hydrophones pointing up; (b) the central acoustic storey on Line 12 with the hydrophones pointing down; (c) the lowermost acoustic storey on Line 12 equipped with Acoustic Modules.

5.2.3 The Acoustic Sensors

The fundamental components of both the hydrophones and the AMs, collectively referred to as acoustic sensors, are piezo-electrical ceramic elements, converting pressure waves into voltage signals [221], and preamplifiers. Compared to PMTs used for optical detection of neutrinos, the more compact sensor design and simpler readout electronics is an advantage of acoustic sensors.
A schematic drawing of an ECAP hydrophone is shown in Figure 5.13. For these hydrophones[2], two-stage preamplifiers were used: adapted to the capacitive nature of the piezo elements and the low induced voltages, the first preamplifier stage is charge integrating while

[1] Custom produced by High Tech Inc (HTI) in Gulfport, MS (USA).

[2] For the commercial hydrophones, details were not disclosed by the manufacturer, but the main design is similar to the one described here.

the second one is amplifying the output voltage of the first stage. The shape of the ceramics is that of a hollow cylinder.
The piezo elements and preamplifiers of the hydrophones are coated in polyurethane. Plastic endcaps prevent the material from pouring into the hollow part of the piezo cylinder during the moulding procedure. The ECAP as well as the HTI hydrophones have a diameter of 38 mm and a length (from the cable junction to the opposite end) of 102 mm.
The equivalent inherent noise level in the frequency range from 1 to 50 kHz is about 13 mPa for the ECAP hydrophones and about 5.4 mPa for the HTI hydrophones. This compares to 6.2 mPa of the lowest expected ambient noise level in the same frequency band for a completely calm sea [226], referred to as *sea state 0* [227]. The ambient noise and the choice of a frequency range for its evaluation that is better adapted to acoustic neutrino detection will be discussed in Sec. 5.4.1.

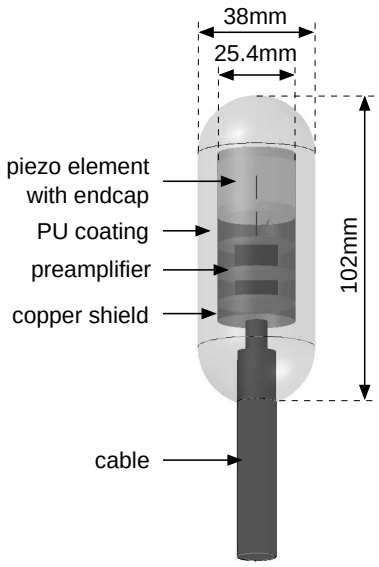

Figure 5.13: Schematic drawing of an ECAP hydrophone. Piezo element and preamplifier (consisting of three circular circuit boards, interconnected by pin connectors) are moulded into polyurethane (PU).

For the AMs, the same preamplifiers are used as for the ECAP hydrophones. The piezo elements have the same outer diameter but are solid cylinders in case of the AMs. Two sensors are glued to the inside of each sphere. This design was motivated by the idea to operate the piezo elements at low pressure and also to investigate an option for acoustic sensing that can be integrated together with a PMT in the same glass sphere. In order to assure a good acoustic coupling, the space between the curved sphere and the flat end of the piezo sensor of the AMs was filled with epoxy. A photograph of an Acoustic Module and a schematic drawing of the sensors glued to the inside of the glass sphere are shown in Figures 5.14(a) and 5.14(b), respectively.
In order to obtain a 2π azimuthal coverage, the six sensors are distributed over the three AMs of the storey within the horizontal plane defined by the three centres of the spheres as shown in Figure 5.14(c). The spheres have outer diameters of 432 mm.

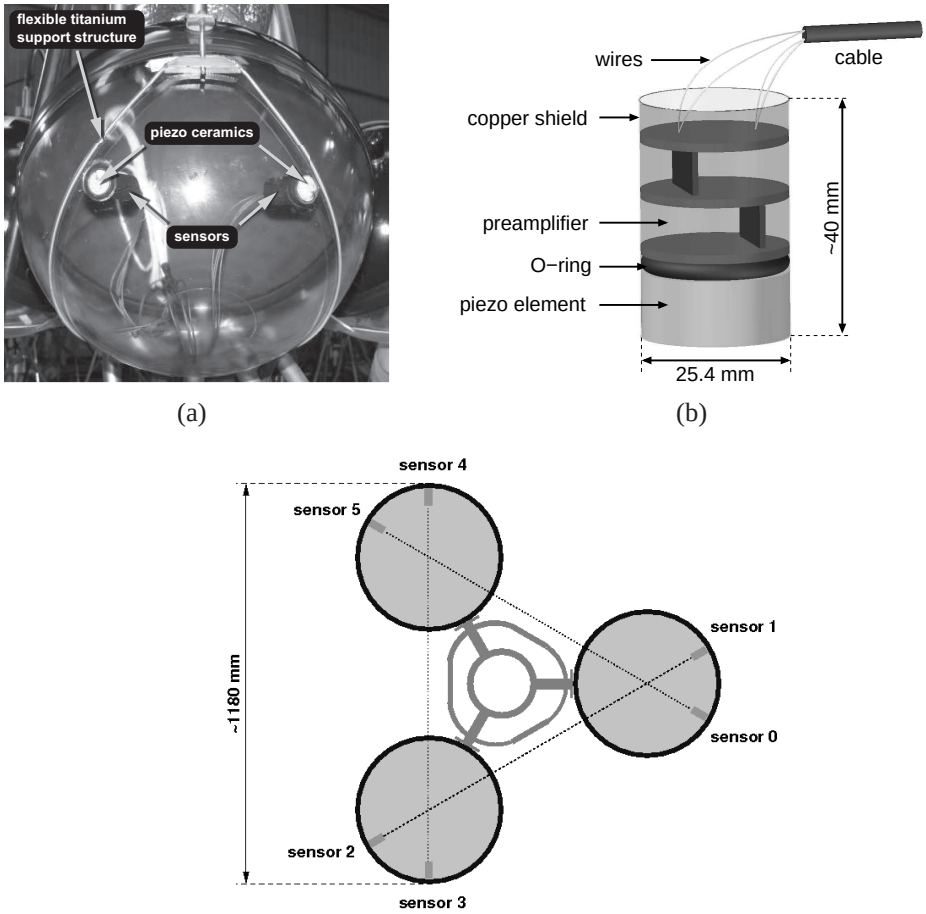

(a) (b)

(c)

Figure 5.14: (a) Photograph of an Acoustic Module (AM) before deployment; (b) schematic drawing of an AM sensor; (c) horizontal cross-section of an acoustic storey holding Acoustic Modules in the plane of the sensors. The dotted lines are collinear with the longitudinal axes of the sensors and indicate the arrangement of the sensor within the storey. The lines intersect at angles of 60° at the centres of the glass spheres.

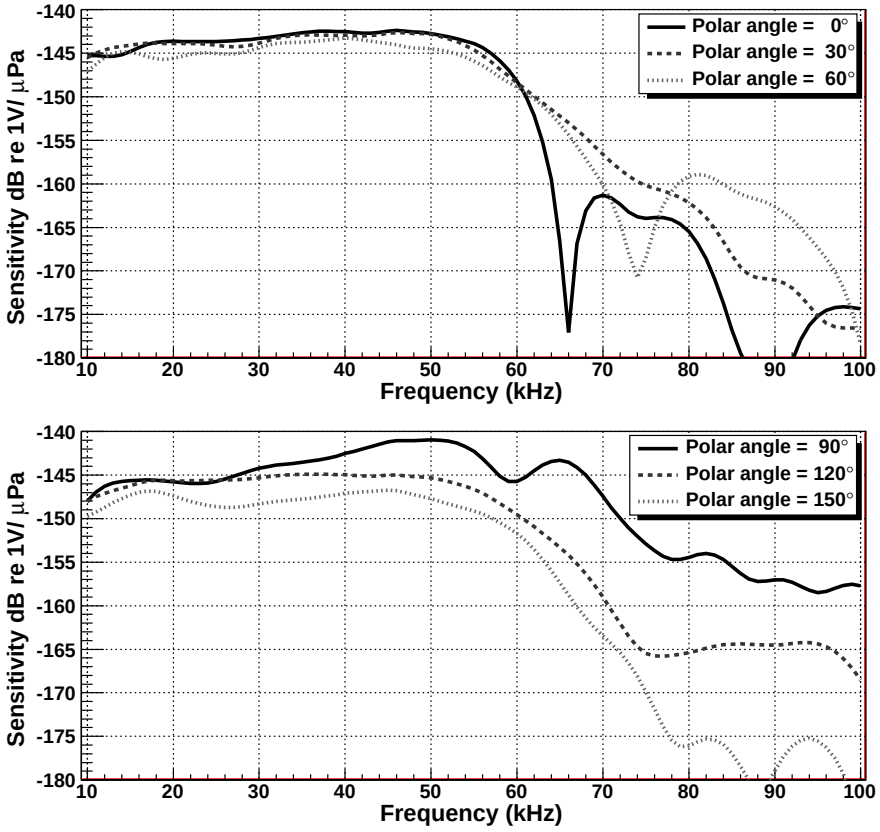

Figure 5.15: Typical sensitivity of an HTI hydrophone as a function of frequency for different polar angles, averaged over the azimuthal angle. Systematic uncertainties below 50 kHz are 2 to 3 dB.

5.2.4 Calibration of Acoustic Sensors

All sensors are tuned to have a low noise level and to be sensitive over the frequency range from 1 to 50 kHz with a typical sensitivity around -145 dB re 1V/μPa (including preamplifier). The sensitivities of all sensors as a function of frequency, polar angle and azimuthal angle were measured before deployment in a water tank, using a calibrated emitter. The analysis was restricted to frequencies above 10 kHz. Towards lower frequencies, measurements become increasingly less significant. This is due to the quadratic frequency dependence of the emitter's transmit voltage response and to the increasingly adverse effect of reflections for increasing wavelengths. In accordance with the expected behaviour of the piezo elements, the sensitivity is assumed to be constant below 10 kHz.
The sensitivity of one of the commercial hydrophones is shown in Figure 5.15 as a function of frequency for different polar angles [228]. For frequencies below 50 kHz, where the sensitivity of all acoustic sensors shows a relatively flat behaviour, the sensitivity decreases once the polar angle approaches 180°, which defines the direction at which the cable is attached to the hydrophone. The beginning of this trend can be seen for the polar angle of 150°.
The sensitivity as a function of the azimuthal angle for a given frequency is essentially flat at the 3 dB level for all hydrophones. The sensitivity as a function of polar angle and frequency shows deviations of less than 2 dB between different HTI hydrophones in the frequency range

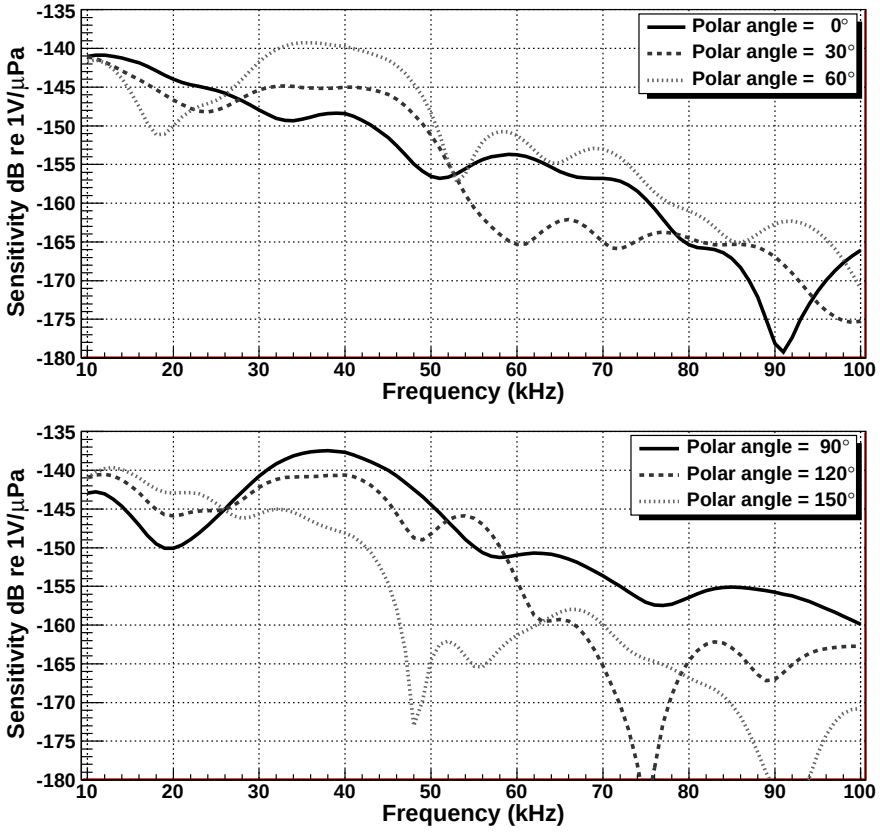

Figure 5.16: Typical sensitivity of an ECAP hydrophone as a function of frequency for different polar angles, averaged over the azimuthal angle. Systematic uncertainties below 50 kHz are 2 to 3 dB.

from 10 to 50 kHz. The deviations for the hydrophones produced at ECAP are at a level of 3 to 4 dB. The sensitivity of an ECAP hydrophone is shown in Figure 5.16. Compared to the HTI hydrophones, the sensitivity in the frequency range from 10 to 50 kHz is higher but less uniform, both as a function of frequency and as a function of polar angle.
As a consequence of their design, the solid angle over which the sensors of the AMs are sensitive is smaller compared to the hydrophones. Furthermore, reflections and resonances within the glass sphere affect the signal shape and frequency dependence, making laboratory measurements more difficult to interpret. The calibration was performed by varying the position of the emitter along a half circle, such that each emitter position has the same distance to the piezo element. Angles were then given by the position of the emitter along the half circle with respect to the longitudinal axis of the piezo sensor, which defined the angle of 0°. Results are shown in Figure 5.17. The higher sensitivity compared to the ECAP hydrophones is due to the different piezo element that is used and the acoustic coupling between water, the glass sphere and the piezo sensor.
All sensitivity measurements were done at normal pressure. A verification with an in situ calibration has not yet been carried out at the time of the writing of this report.
For the calibration, Gaussian signals were emitted which in the frequency domain cover the range of the calibration. In addition, the response of the sensors to bipolar pulses was recorded. This is shown in Figure 5.18. The agreement between the different sensor types is quite good. The asymmetry of the input pulse, i.e. the ratio of the pulse heights at the

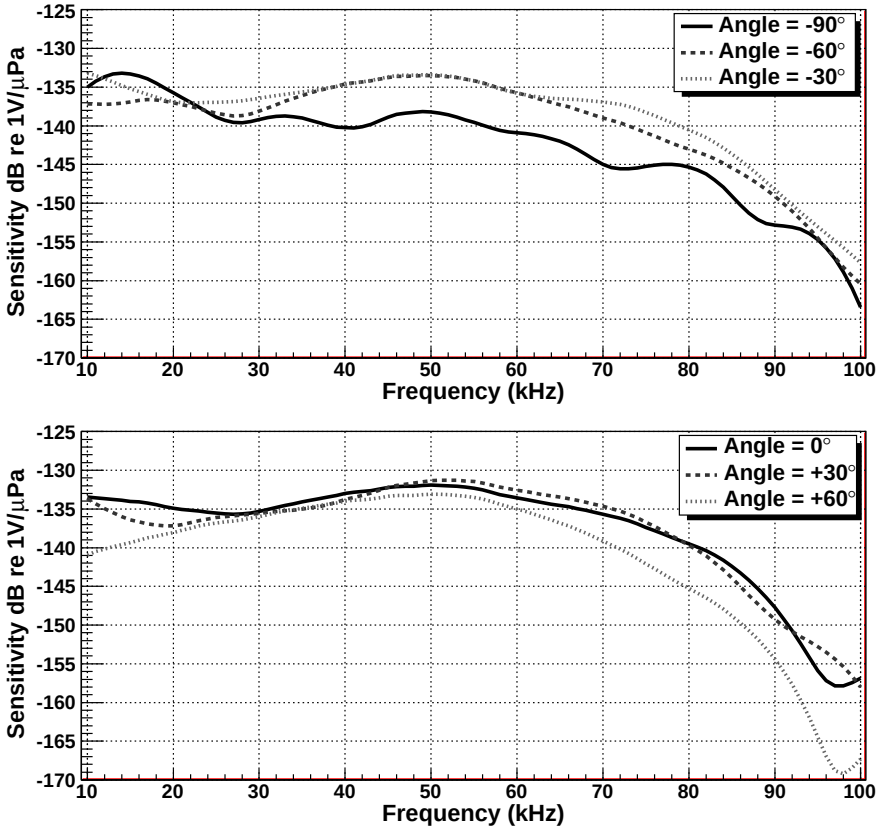

Figure 5.17: Sensitivity of an AM sensor as a function of frequency for different angles with respect to the longitudinal axis of the sensor. Systematic uncertainties below 50 kHz are 2 to 3 dB.

positive and negative peaks, can be seen to be diminished in the response of the sensors. This is due to the excitation of oscillations of the piezo elements.

5.2.5 Off-Shore Electronics

In the ANTARES data acquisition (DAQ) scheme [229], the digitisation is done within the off-shore electronics container (see Sec. 5.2.1). Each LCM contains a backplane that is equipped with sockets for the electronics cards and provides them with power and data lines. A standard LCM for processing the data from PMTs contains the following electronics boards:

- Three *ARS motherboards*, each comprising two Analogue Ring Sampler (ARS) ASICs, for conditioning and digitisation of the analogue signals from the PMTs [230];
- A *DAQ board*, which reads out the ARS motherboards and handles the communication to shore via TCP/IP;
- A *Clock board* that provides the timing signals to correlate measurements performed in different storeys (see Sec. 5.2.7);
- A *Compass board* to measure the tilt and the heading of the storey.

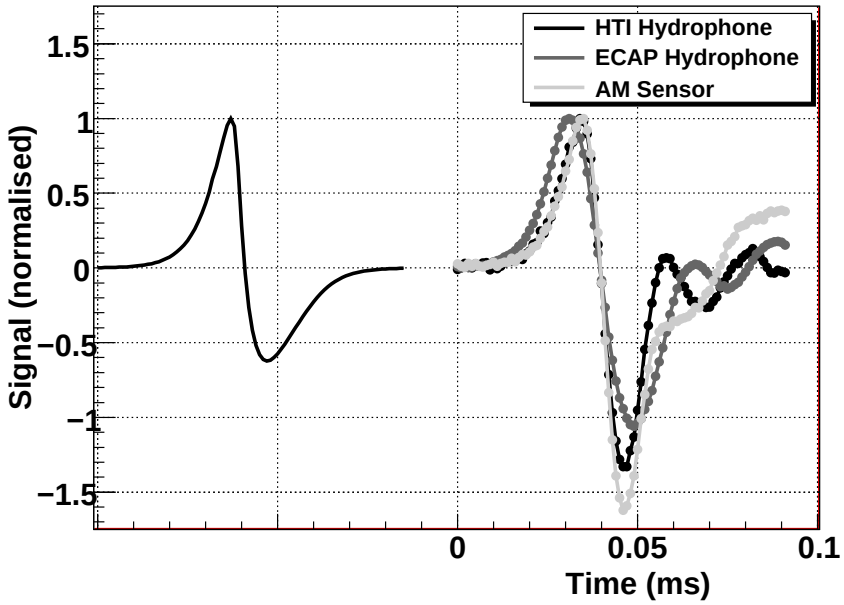

Figure 5.18: Comparison of the response of different acoustic sensor types to a bipolar pulse. The emitted signal is shown on the left. The response of the hydrophones was measured for a polar angle of 90°, the response of the AM sensor for an angle of 0°. The first peak of each pulse (including the emitted one) was normalised to 1 and the time axis of each received signal was adjusted such that the times of the zero crossings coincide. The time offset between emitted and received pulses in the depiction is arbitrary.

The transmission of data to shore is done through a *Master LCM (MLCM)* which—in addition to the components of an LCM described above—contains an ethernet switch and additional boards for handling incoming and outgoing fibre-based optical data transmission. Up to five storeys form a *sector*, in which the individual LCMs transmit the data to the MLCM. For the digitisation of the acoustic signals and for feeding them into the ANTARES data stream, the *AcouADC board* was designed. These boards are pin-compatible with the ARS motherboards and replace them in the acoustic storeys. Figure 5.19 shows the fully equipped LCM of an acoustic storey.

5.2.6 The AcouADC Board

Each AcouADC board serves two acoustic sensors and has the following major tasks:

- Pre-processing of the analogue signals (impedance matching, application of an anti-alias filter, selectable gain adjustment);
- Digitisation of the analogue signals and preparation of the digitised data stream for transmission to the DAQ board;
- Provision of stable low-noise voltage (6.0 V) for power supply of the acoustic sensors;
- Provision of an interface to the on-shore slow control software.

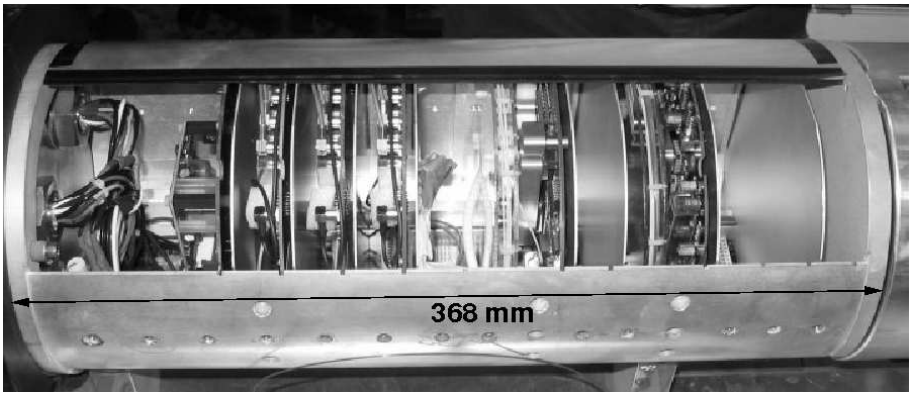

Figure 5.19: An LCM during assembly, equipped with AcouADC boards before insertion into the titanium container. The sockets for external connection (not visible in this picture) are attached to the lid of the container on the left-hand side of the photograph. From left to right, the following boards are installed: a Compass board; three AcouADC boards; a DAQ board; a Clock board.

A photograph of an AcouADC board is shown in Figure 5.20. The board consists of an analogue and a digital signal processing part. Each board processes the differential voltage signals from two acoustic sensors. The two signals are processed independently and in parallel for the complete (analogue and digital) data processing chain.
A main design criterion for the board was a low inherent noise level, so that even for sea state 0 no significant contribution to the recorded signal originates from the electronics of the board.

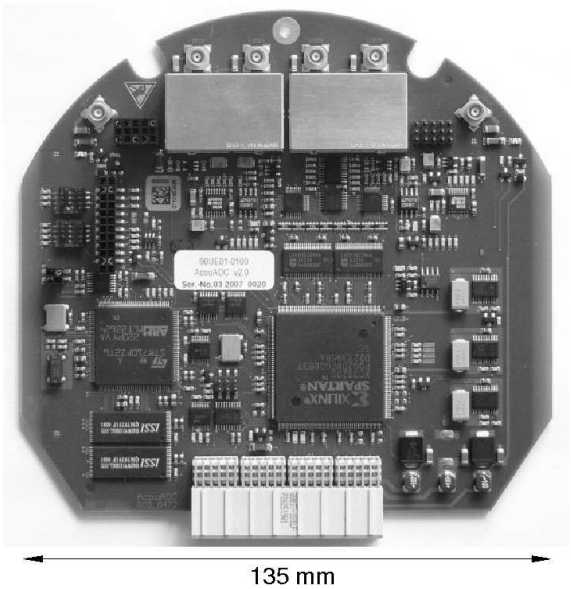

Figure 5.20: Photograph of an AcouADC board. The four connectors for the two differential input signals are located at the top, the analogue signal processing electronics is covered by metal shields.

5.2.6.1 Analogue Signal Processing

The analogue signal is amplified in two stages. The first stage applies a coarse gain with nominal amplification factors of 1, 10 or 100. The gain factor 1 is used for recording dedicated runs with large signal amplitudes, e.g. from the emitters of the ANTARES acoustic positioning system (see Sec. 5.2.1), whereas the factor of 100 was only foreseen for the case that the sensitivity of the hydrophones would degrade after deployment.
The second amplification stage, the fine gain, is intended to adjust the gains of different types of hydrophones. Gain factors of 1.00, 1.78, 3.16, and 5.62 (corresponding to 0, 5, 10, and 15 dB, respectively) are selectable by switching between four appropriate resistors in the feedback loop of the operational amplifier. Combining the two stages, the gain factor can be set to one of 12 values between 1 and 562. The standard setting is an overall gain factor of 10, yielding the approximate sensitivity of $-125\,\mathrm{dB\,re\,1V/\mu Pa}$.
Several RCL elements within the analogue signal chain form an additional band-pass filter. Its low-frequency 3 dB point is at about 3 kHz and cuts into the trailing edge of the low-frequency noise of the deep-sea acoustic background [160], protecting the system from saturation. The high-frequency 3 dB point is above 1 MHz and was introduced to comply with the input requirements of active components of the circuitry. After amplification, the signal is coupled into a linear-phase 10th-order anti-alias filter[3] with a root-raised cosine amplitude response and a 3 dB point at a frequency of 128 kHz. The output is referenced to 2.0 V and fed into a 16-bit analogue-to-digital converter (ADC) that will be described below.

5.2.6.2 Digital Signal Processing

The digital part of the AcouADC board digitises the acoustic signals and processes the digitised data. It is flexible due to the use of a micro controller (μC)[4] and a field programmable gate array (FPGA)[5] as data processor. All communication with the shore is done via the DAQ board; the μC handles the slow control[6] and the FPGA the data transfer. The μC is accessed from the on-shore control software and is used to adjust settings of the analogue part and the data processing. It can also be used to update the firmware of the FPGA.
For each of the two input channels, the digitisation is done at 500 kSps (kilosamples per second) by one 16-bit successive approximation ADC[7] with output range from -32768 to $+32767$ counts. The two ADCs are read out in parallel by the FPGA and further formatted for transmission to the DAQ board.
In standard mode, the sampling rate is reduced to 250 kSps in the FPGA, corresponding to a downsampling by a factor of 2 (DS2). Currently implemented options are DS1 (i.e. no downsampling), DS2, and DS4, which can be selected from the shore. For each downsampling factor an adapted digital anti-alias filter, compliant with the Nyquist-Shannon sampling theorem, is implemented in the FPGA as a finite impulse response (FIR) filter with a length of 128 data points. For DS2, the frequency spectrum between the 3 dB points at 2.8 and 108.8 kHz passes the filter.

[3] Filter LTC1569-7 from Linear Technology, http://www.linear.com/
[4] STR710 from STMicroelectronics, http://www.st.com/
[5] Spartan-3 XC3S200 from XilinX, http://www.xilinx.com/
[6] The slow control provides the off-shore components with initialisation and configuration parameters and it regularly monitors whether the operational parameters are within their specified ranges.
[7] ADS8323 from Analog Devices, http://www.analog.com/

5.2.6.3 AcouADC Board System Characteristics

The complex response function of the AcouADC board (i.e. amplitude and phase) was measured in the laboratory prior to deployment for each board and a parametrisation of the function was derived [226]. Figure 5.21 shows the frequency response of the AcouADC board. The measurement was done by feeding Gaussian white noise into the system and analysing the digital output recorded by the board. Without downsampling (DS1), the roll-off at high frequencies is governed by the analogue anti-alias filter. For DS2 and DS4, the digital FIR filters are responsible for the behaviour at high frequencies. At low frequencies, the effect of the band-pass filter described above can be seen. Figure 5.21 furthermore demonstrates that within each passband, the filter response is essentially flat. The comparison of the recorded data with the parametrisation shows excellent agreement.

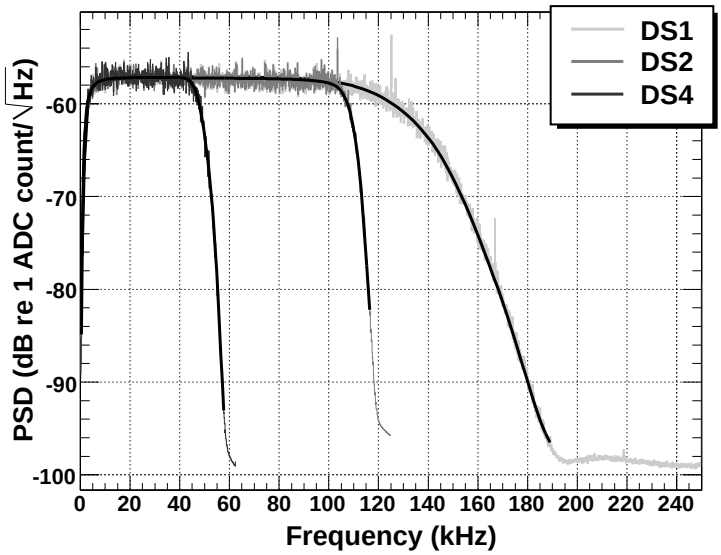

Figure 5.21: The AcouADC board filter response, characterised by a power spectral density (PSD) as a function of frequency, measured for the three different downsampling factors. For each of the three measurements, the parametrisation is shown as a black line.

The parametrisation of the response function allows to calculate the response of the system to any input pulse and vice versa the reconstruction of the original shape of any recorded pulse. Figure 5.22 shows a comparison of the measured and calculated response of the analogue signal processing part of the AcouADC board to a generic bipolar input pulse as it would be expected from a neutrino-induced particle shower. The digital FIR filter introduces an additional time offset of 128 µs of the digitised data for DS2 and DS4.
The ADCs of the AcouADC board were investigated in detail [226]. For each individual ADC, the transfer curve from input voltage to ADC counts was measured and distortions from the ideal linear behaviour quantified in terms of the differential non-linearity (DNL) and integral non-linearity (INL). The distribution of the DNL values for all bins of all calibrated signal channels shows negligible deviations from the ideal situation (i.e. a peak at zero) with a mean of -0.02 ADC counts and a standard deviation of 0.06 ADC counts, corresponding to 3.4 µV. The values of the INL of the ADCs stay within ± 50 ADC counts for all signal channels over the full input range from about $-2.0\,\mathrm{V}$ to $2.0\,\mathrm{V}$, corresponding to $\pm 3.1\,\mathrm{mV}$.

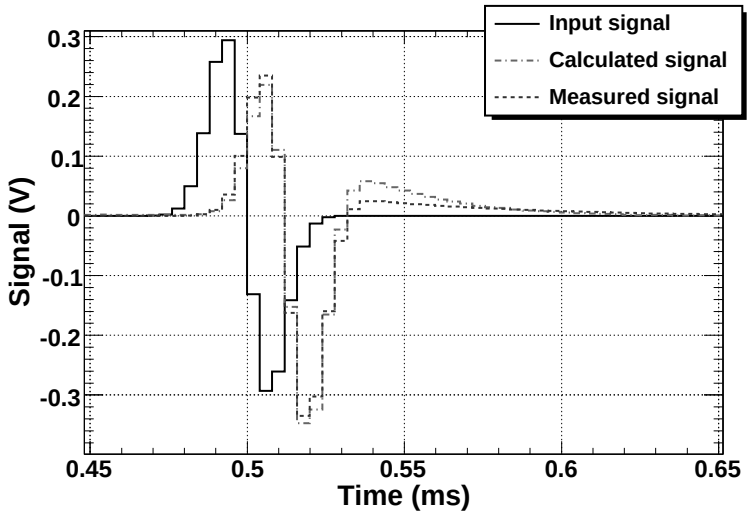

Figure 5.22: The response of the analogue part of an AcouADC board to a bipolar input pulse. Shown are the measured output signal and the output signal calculated from the parametrised response function. The measured output signal was obtained with an oscilloscope at the input of the ADC. The measurement was done for a nominal gain factor of 1.

5.2.7 Data Acquisition and Clock System

AMADEUS uses the same DAQ system and follows the same "all data to shore" strategy [229] as the ANTARES neutrino telescope, i.e. all digitised data are transmitted to shore via optical fibres using the TCP/IP protocol. The data stream from the sender DAQ board is tagged with the IP address of the receiving on-shore server. In the control room, the acoustic data are routed to a dedicated computer cluster by using the transmitted IP address. The ANTARES clock system operates separately from the DAQ system, using a different set of optical fibres to synchronise data from different storeys. The system provides a highly stable 20 MHz synchronisation signal, corresponding to a resolution of 50 ns[8], which is generated by a custom-designed system at the ANTARES control room. The synchronisation of this internal clock with the UTC[9] of the GPS system is established with a precision of 100 ns.
The synchronisation signal is broadcast to the off-shore clock boards and from there transmitted further to the FPGA of the AcouADC board. Based on this signal, the data packages sent from the AcouADC board to shore via the DAQ board receive a timestamp which allows for correlating the data from different storeys. The 50 ns resolution of the timestamp by far exceeds the requirements given by the standard sampling time of 4 μs corresponding to DS2. Differences in the signal transit times between the shore station and the individual storeys are also smaller than 4 μs and do not need to be corrected for.

5.2.8 On-Shore Data Processing and System Operation

The AMADEUS system is operated with its own instance of the standard ANTARES control software called *RunControl* [229]. This is a program with a graphical user interface to control

[8]The much higher precision that is required for the synchronisation of the optical signals from the PMTs is provided by a 256-fold subdivision of the 20 MHz signal in the ARS motherboards.

[9]Coordinated Universal Time

and operate the experiment. It is Java™-based and reads the configuration of the individual hard- and software components from the ANTARES database, allowing for an easy adaption of individual run parameters for the AMADEUS system. Via the clock system the absolute time of the run start is logged in the database with the aforementioned precision of 100 ns. The end of a run is reached if either the data volume or the duration exceed predefined limits (in which case a new run is started automatically) or the run is stopped by the operator. The data of one AMADEUS run are stored in a single file in *ROOT* [231] format. The typical duration of a run ranges from 2 to 5 hours. AMADEUS is controlled remotely via the Internet. Data are centrally stored and are remotely available.
For the computing requirements of AMADEUS, a dedicated on-shore computer cluster was installed. Among other tasks, the AMADEUS trigger[10] is running on the cluster, which searches the data by an adjustable software filter; the events thus selected are stored to disk. This way the raw data rate of about 1.5 TB/day is reduced to about 10 GB/day for storage. The AMADEUS trigger schemes will be discussed now.

5.2.9 AMADEUS Online Trigger Schemes

Currently, three trigger schemes are in operation [232]: A *minimum bias trigger* which records data continuously for about 10 s every 60 min, a *threshold trigger* which is activated when the signal exceeds a predefined amplitude, and a *pulse shape recognition trigger*. For the latter, a cross-correlation of the signal with a predefined bipolar signal, as expected for a neutrino-induced particle shower, is performed. The trigger condition is met if the output of the cross-correlation operation exceeds a predefined threshold. With respect to a matched filter, this implementation reduces the run time complexity while yielding a comparable trigger performance.
As discussed in Sec. 4.2.5, for pressure pulses induced by neutrino interactions the amplitude, asymmetry and frequency spectrum depend on the position of the observer with respect to the particle shower. The predefined bipolar signal used for the pulse shape recognition trigger corresponds to the pulse shape expected at a distance of roughly 300 m from the shower centre in the direction perpendicular to the shower axis, i.e. where the maximum signal within the flat volume of sound propagation is expected. The cross correlation with pulses whose shape differs from the implemented one changes the peak in the cross correlation output: it is broadened and diminished as compared to the filter response on the predefined signal. This effectively increases the trigger threshold in terms of pressure amplitude for such pulses. As will be described below, the final trigger decision requires coincidences within an acoustic storey, which allows the trigger threshold for the cross correlation output of each individual acoustic sensor to be set to a low value. Given that the main purpose of the AMADEUS system is the investigation of background noise, this implementation is very efficient in recording a wide range of bipolar and multipolar events. Dedicated searches for neutrino signals—which are difficult due to the geometry of the acoustic storeys within the AMADEUS system—are done offline, taking into account the variations of the pulse shapes with distance and direction.
Both the threshold and the pulse shape recognition trigger are applied to the individual sensors and are self-adjusting to the ambient noise, implying that all trigger thresholds are defined in terms of a signal-to-noise ratio. The trigger thresholds are software parameters and

[10] While this functionality might be more commonly referred to as filtering, it is ANTARES convention to refer to the "on-shore trigger".

therefore can be set at will. The noise level is calculated from and applied to the data of the *frame* that is currently being analysed. A frame denotes the structure in which data are buffered off-shore by the DAQ board before being sent to shore and contains data sampled during an interval of about 105 ms [229]. If either the threshold or the pulse shape recognition trigger condition is met, an additional trigger condition is imposed, which requires coincidences of a predefined number of acoustic sensors on each storey. Within the ANTARES data processing scheme, the coincidence window is fixed to the length of a frame. Currently, the coincidence trigger requires that the threshold or pulse shape recognition trigger conditions have been met for at least four out of six sensors of a storey.
In the ANTARES DAQ system, the frames start at fixed intervals with respect to the run start. Trigger conditions are imposed on temporally corresponding frames from all storeys simultaneously, whereupon the frames are discarded and data not selected by the trigger are lost. Processing subsequent frames at the same time is not possible. Given the distances of typically 1 m between sensors within one storey, time delays between signals from a given source are always less than 1 ms. Therefore, the number of sources for which the signals extend over two frames, and hence the coincidence trigger may not be activated, is small. The disadvantage of a large trigger window, the increased probability for random coincidences, leads only to a small increase of the recorded data volume. The coincidence trigger can be optionally extended to require coincidences between different storeys on the same line. With distances between storeys ranging from about 10 to 100 m (corresponding to delays of the order of 10 to 100 ms) signals originating from above or below are suppressed. This trigger is currently not enabled.
The data of all sensors that have fired a coincidence trigger are stored within a common time window that covers all triggered signals. Its minimum length is 1.536 ms for 4 μs sampling time (corresponding to 384 data samples) and its maximum length corresponds to the length of a frame.

5.2.10 System Performance

AMADEUS is continuously operating and taking data with only a few operator interventions per week. The up-time of each sensor is typically better than 90%. Its ability to continuously send unfiltered data, sampled at high frequency, to shore for further analysis renders the AMADEUS system a multipurpose apparatus for neutrino feasibility studies, acoustic positioning and marine research.
The concept of acoustic clusters (i.e. the acoustic storeys) is very beneficial for fast online processing. By requiring coincident signals from at least four sensors within a storey, the trigger rate is significantly reduced, improving the purity of the sample selected with the pulse shape recognition trigger.
The stability of the system response is excellent. This was verified prior to deployment as well as in situ. It was quantified by observing the mean of the ambient noise distribution as a function of time. In situ, the 10 s of continuous data recorded every hour with the minimum bias trigger were used to calculate the mean. The standard deviation of this value for the first year of operation is less than 2×10^{-5} of the full range.
All sensor types described in Sec. 5.2.2 are well suited for the investigation of acoustic particle detection methods. The signals recorded with the three different types of acoustic sensors on Line 12 for a common source is shown in Figure 5.23. The signals were recorded in May 2010 and were received under an angle of about 65° with respect to the direction

pointing vertically upwards. The agreement between the signal shapes can be seen to be very good. For the second positive peak at about 0.20 to 0.25 s, the AM sensor shows a differing behaviour from the hydrophones, which can be attributed to the coupling of the sensor to the glass sphere.

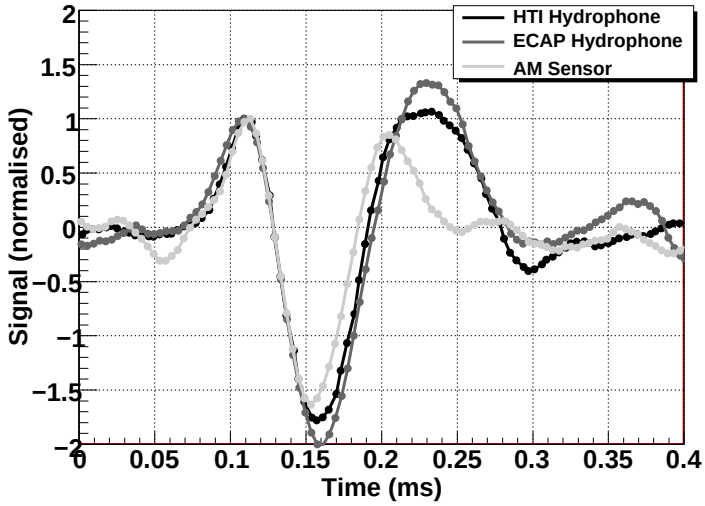

Figure 5.23: Comparison of the signals originating from a common source as recorded by three different types of acoustic sensors, each one located on a different storey of Line 12. For better comparability, the first peak of each signal has been normalised to 1 and the time axis of each signal adjusted such that the times of the zero crossings between the first positive and negative peak coincide.

The maximal pressure amplitude that can be recorded for a gain factor of 10 without saturating the input range of the ADC is about 5 Pa. Usually, only anthropogenic signals originating close to the detector reach this pressure level at the positions of the hydrophones.

5.3 Position Calibration of Acoustic Storeys

5.3.1 Position Calibration Using Time Delays

The relative positions of the acoustic sensors within the AMADEUS setup have to be continuously monitored. This is done by using the emitter signals of the ANTARES acoustic positioning system (see Sec. 5.2.1). Figure 5.24 shows such a signal as recorded by four typical sensors. The delays between the signal arrival times are clearly visible: short delays of less than 1 ms within each storey and a long delay of about 10 ms between the signals arriving in two different storeys.
The time shown in the figure is given in seconds since the start of the run and can be converted into UTC using the data recorded by the clock system (see Sec. 5.2.7). As the emission times of the positioning signals are also recorded in UTC, the time difference between emission and reception of the signal can be calculated. Using the signals from multiple emitters and their known positions at the anchors of the lines, the positions of the AMADEUS sensors can be reconstructed. And finally, from the reconstructed positions of the individual sensors,

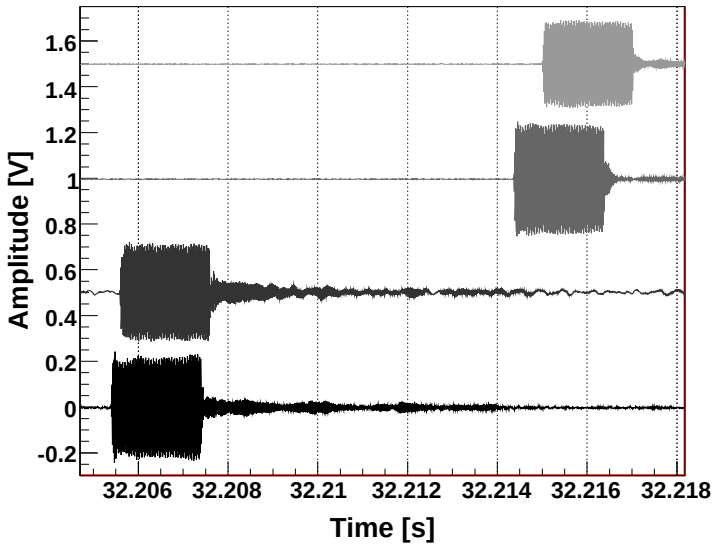

Figure 5.24: Typical signals of the ANTARES acoustic positioning system as recorded with four sensors of the AMADEUS system for gain factor 1 of the AcouADC board. For better clarity an offset, starting with 0 V and incremented by 0.5 V with respect to the previous one, is added to the amplitude of each sensor. The first two signals along the time axis were recorded by the acoustic storey holding AMs (see Figure 5.10). The following two signals were recorded with two hydrophones on the acoustic storey just above—one hydrophone mounted at the bottom and the other one at the top of the storey. The time is counted since the start of the run.

the six degrees of freedom (centre of mass coordinates and the three Euler angles) of each storey can be obtained.
The position calibration has statistical uncertainties of a few millimetres for each hydrophone. Systematic uncertainties due to the size of the receiving piezo elements, the knowledge of their relative positions within the acoustic storey, the knowledge of the speed of sound in sea water and the position uncertainties of the emitters are still under study. For the AMs, the position reconstruction is less precise and has a statistical uncertainty of the order of a centimetre.
Figure 5.25 shows the comparison of the *heading* as measured with the acoustic sensors on a storey and with the compass board installed in that storey. The heading is defined as the rotational angle of a well defined horizontal reference axis within the storey around the vertical axis. A heading of zero degrees then corresponds to the reference axis pointing north, with angles counting clockwise from $0°$ to $360°$. The periodic structure of the heading is due to the sea currents which change in accordance to the Coriolis force, which at a geographic latitude ϕ affects the direction of sea currents with a period of $T = T_0 \sin\phi$, where $T_0 \approx 24\,\mathrm{h}$ is the period of a sidereal day on Earth and therefore $T \approx 16.3\,\mathrm{h}$.
Both the acoustic measurement and the measurement of the compass board have an offset of their zero degree position w.r.t. the cardinal direction of north: When measuring zero degrees, the compass board points to the North Magnetic Pole while the direction derived from the acoustic measurements points along the *northing axis* of the UTM grid. At the location of ANTARES, this difference is 2.5° where the UTM northing axis points further

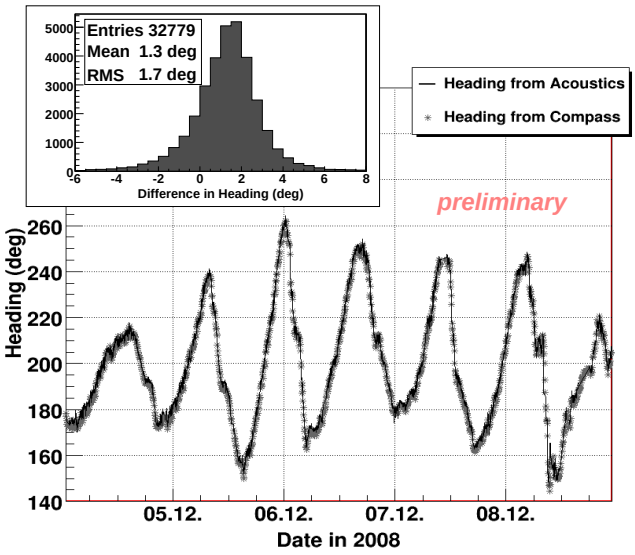

Figure 5.25: Comparison of the heading measured with the sensors of the uppermost storey of IL07 and with the compass board in the same storey over a period of five days. In the insert at the top left, the resolution between the two measurements is shown.

westwards than the direction of the North Magnetic Pole. The difference shown in Fig 5.25 is not corrected for these offsets, the mean value of the distribution after this correction is therefore $-1.2°$. The offsets from the six storeys have a spread of about $1°$ around zero.
The RMS deviation between the two measurements is 1.7° (0.03 rad) or 3% when quantifying the corresponding circle segment w.r.t. the distance of a source from the ANTARES line on which the sensor is installed. Here the residual offset between compass board and angle reconstruction with the AMADEUS sensors were ignored. On the other hand, the RMS deviation is the quadratic sum of the resolution of the compass board and of the AMADEUS measurement, resulting in an overestimation of the RMS resolution. Since the two effects are of about the same size, they will roughly compensate each other.
For a measurement of the density of bipolar events, the absolute positioning of the acoustic storeys is not important. The precision of the measurement of source positions (which then determines the error of the density and limits the distance up to which a surveillance is possible) is determined by the resolution of the angular reconstruction of a source position and by that of the distance between the storeys. The horizontal distance between the IL07 and Line 12 is about 240 m. Preliminary studies, comparing the positions that are reconstructed with AMADEUS and with the ANTARES positioning system, indicate that the distance between the centre of mass positions of two storeys on the two lines can be reconstructed with a precision of much better than 1 m. The resulting precision of $\Delta(\,\vec{r}_{L12} - \vec{r}_{IL07}\,)/|\,\vec{r}_{L12} - \vec{r}_{IL07}\,| \ll 1\%$ indicates that the dominant contribution to the error on the position reconstruction will stem from the angular resolution of the source position reconstruction.

5.3.2 Alternative Methods and Effects of Refraction

In Sec. 5.3.1 position calibration was based on the time delay between the emission and reception of a signal. This method has two disadvantages: First, the emission time needs to be know. This is not problematic for the reconstruction of the positions of the acoustic

storeys. However, when trying to reconstruct the positions of arbitrary sources, this method is not applicable. Second, the method depends strongly on the speed of sound. An error of only 0.1 % for the speed of sound over a distance of 500 m introduces an error of 0.5 m in the position of the storey. Here the AMADEUS system has the potential to cross check and possibly improve the position calibration of the optical storeys within the ANTARES detector, for which an error of 0.2 m already deteriorates the pointing precision for muon tracks. Hence it is worthwhile to alternatively apply the *time difference of arrival* (TDOA) method for the position calibration of the acoustic storeys of AMADEUS. According to this method, the direction of an acoustic emitter is reconstructed from the differences between the arrival times in the six hydrophones of a storey. Then the reconstructed directions (polar angle θ and azimuth ϕ) of the emitters are matched to the geometric pattern of the emitters on the sea floor. The TDOA method was investigated in [233]. A detailed, high-statistics comparison with the time delay method is still pending.

The resolution of the position reconstruction depends strongly on the spatial arrangement of the emitters. In order to compare the precision of the two methods, the size of the error will be roughly estimated from basic considerations. For the time delay method, the statistical error of the reconstruction of a sensor position is of the order $\Delta t c_s/\sqrt{n-1} \approx 6\,\mathrm{mm}/\sqrt{n-1}$, where n is the number of emitters and Δt is the resolution of the measurement of the time delay. Numerically, $c_s \approx 1.5\,\mathrm{mm}/\mu\mathrm{s}$ and $\Delta t \approx 4\mu s$ at the receiver side for 250 kHz sampling. Typical values of n are $7 \sim 8$ and Δt can be reduced by interpolating between data points. Therefore, the experimentally measured error is an order of magnitude larger than this estimate (see Sec. 5.3.1), because several sources or errors were omitted, such as the timing precision of the emission of the signal. Furthermore, the position of the receiver will not be stable on a millimetre level over the duration of an emitter cycle of several seconds.

For the TDOA method, the resolution of the reconstructed position of a storey is (in the horizontal plane) of the order $\Delta\Phi d/\sqrt{n-1} \approx 2\,\mathrm{m}/\sqrt{n-1}$. Here a (horizontal) distance of $d = 100\,\mathrm{m}$ between emitter and receiver was assumed and an error on the heading of $\Delta\phi = 1^\circ$. This assumed error of the heading is indeed too optimistic. While it is consistent with the value shown in Fig. 5.25, which contains both the error of the acoustic position reconstruction and of the reconstruction with the compass board, the error from the acoustic position reconstruction is already reduced by combining measurements from several emitters. The error on the reconstruction of the azimuthal angle of a source with a single acoustic storey is about 3°, see Sec. 5.4.2.1. In conclusion it is clear that the precision of the position reconstruction with the TDOA method is much worse than with the time delay method. Whether for high statistics a test of the precision of the speed of sound with the TDOA method is possible needs to be investigated. Note that the angular resolution of the reconstruction of the storey orientation is expected to be of about the same size for both methods. This is due to the fact that effectively the orientation of the storey in terms of polar angle and azimuth is calculated for the time delay method using time differences of a signal between the sensors on a storey.

So far, refraction effects were not taken into account for the position calibration. Table 5.2 shows systematic effects resulting from refraction for the two methods, calculated for the speed of sound profile derived from the August 2007 measurements of water properties at the ANTARES site [170], see Fig. 4.8(a). The systematic errors were determined in the following fashion: A ray was traced from the position of an acoustic sensor at a height of $\Delta z = 410\,\mathrm{m}$ above the sea floor at $z = 2478\,\mathrm{m}$ for a given starting angle θ. The z-position of the sensor corresponds to the nominal position of the uppermost acoustic storey on Line

angle (deg)	error (m) from time delay	distance error on sea floor from TDOA (m)	angle (deg)	error (m) from time delay	distance error on sea floor from TDOA (m)
25	0.024	-10.61	60	0.013	-0.67
30	0.021	-6.08	65	0.013	-0.49
35	0.019	-3.79	70	0.012	-0.36
40	0.017	-2.51	75	0.012	-0.25
45	0.016	-1.74	80	0.012	-0.16
50	0.015	-1.24	85	0.012	-0.08
55	0.014	-0.91	90	0.012	0.00

Table 5.2: Error in the reconstruction of emitter positions due to refraction using the time delay and time difference of arrival (TDOA) methods. The methods and the calculation of the errors are explained in the text. The error from the time delay method refers to the distance between emitter and receiver, whereas for the TDOA method, the error in the horizontal direction on the sea floor is given. Errors were calculated as reconstructed distance minus true distance. Angles are those at which the ray reaches the acoustic sensor with 0° and 90° referring to rays arriving horizontally and vertically from below, respectively. The position of the sensor is assumed at $\Delta z = 410\,\mathrm{m}$ above the sea floor at $z = 2478\,\mathrm{m}$ and water properties are that of the Mediterranean Sea at the ANTARES site.

12 of ANTARES. The angle θ is measured w.r.t. the horizon where $\theta = 90^\circ$ corresponds to the downwards direction. The ray tracing was continued until the sea floor was reached at a horizontal distance Δx from the acoustic sensor along the sea floor. The ray connecting the sensor and the point on the sea floor is then the path of a sound signal that is emitted from the position on the sea floor, reaching the sensor at its given position at a polar angle θ.
The systematic error of the TDOA method was calculated by finding the intersection with the sea floor of the tangent of the ray at the position of the sensor, i.e. $\Delta x_{\mathrm{rec}} \equiv \Delta z / \tan\theta$. Therefore Δx_{rec} is the horizontal distance of a potential emitter on the sea floor from the receiver, whose signal would reach the acoustic sensor at the angle θ in the absence of refraction. The systematic error due to refraction of the TDOA method is then given by $\Delta x_{\mathrm{rec}} - \Delta x$.
For the absolute time method, the time t_{path} was calculated along the refracted path from the acoustic sensor to the sea floor for the given angle θ. Then the average speed of sound $\overline{c}_s$ was calculated according to $2/\overline{c}_s = 1/c_s^{\mathrm{floor}} + 1/c_s^{\mathrm{sens}}$ where c_s^{floor} and c_s^{sens} are the speed of sound at the sea floor and at the position of the acoustic sensor, respectively. The path length of the ray is estimated by $d_{\mathrm{path}} = \overline{c}_s t_{\mathrm{path}}$. This is the calculation performed for the reconstruction of the positions of the AMADEUS storeys. The systematic error of this method is then given by $d_{\mathrm{path}} - \sqrt{\Delta x^2 + \Delta z^2}$. Note that the approximation of the average speed of sound introduces a systematic error even if a ray is not refracted for the case $\theta = 90^\circ$.
Within the AMADEUS setup, angles between emitter and receiver are ranging from $\sim 35^\circ$ (for a receiver on the lowest acoustic storey on the IL and the most distant acoustic emitter on the anchor of Line 12) to 90° for signals received from the transceiver at the anchor of the same line.

5.4 Acoustic Background in the Deep Sea

It is important to realise that there are two kinds of background which need to be understood to assess the feasibility of an acoustic neutrino detector: First, there is ambient noise which can be described by its characteristic power spectral density. This noise is determined by environmental processes and defines the minimum pulse heights that can be measured, if a given signal-to-noise ratio can be achieved with a search algorithm. To measure this background, in principle one hydrophone is sufficient and the synchronisation among multiple hydrophones is not crucial. Second, there are neutrino-like signals, i.e. signals which have the characteristic bipolar pulse shape but have a different origin. These transient signals are very diverse and originate from anthropogenic and biological sources as well as weather-correlated sources. It is important to measure the spatial, temporal and pulse-height distribution of such bipolar events in order to asses the probability for random coincidences that mimic the characteristic "pancake" structure of a neutrino sound wave. For this kind of measurement, a hydrophone array is required and the synchronisation among the hydrophones is crucial.

5.4.1 Ambient Noise and Inherent System Noise

5.4.1.1 Spectral Distributions and Correlations with Weather Data

As summarised in [234], three main sources of underwater ambient noise have been identified in various studies: Surface agitation (including the effects of precipitation, bubbles and spray), marine life and anthropogenic sources. In the absence of the latter two sources, underwater ambient noise levels have been shown [235] to depend on wind force and sea state, where the studies have been performed for frequencies between 100 Hz and 25 kHz. This region shows a large overlap with the frequency range of interest for acoustic neutrino detection. The so-called Knudsen curves [235] describe the frequency dependence of the noise power spectral density (PSD) with a slope of -5 to -6 dB/octave. These results are however not necessarily applicable to the depths of 2000 m and more at which the AMADEUS system is installed. Several authors, e.g. [160, 234], distinguish between shallow water and deep water, where the former is defined as a depth of up to 183 m [234]. However, since the absorption length decreases with frequency (see Fig. 4.1), e.g. from about 6 km at 10 kHz to less than 2 km at 20 kHz, it will make a substantial difference if a measurement is performed at 200 m or 2000 m despite the fact that both measurements are performed in the deep water region according to the definition from above. From the frequency dependence of the absorption length it is expected that the roll-off of the noise in depths of several hundreds of metres is steeper than predicted by the Knudsen curves. This behaviour was indeed observed at the site of the SAUND experiment [236].
Studies of the power spectral density of the ambient noise at the ANTARES site have been performed using the minimum bias trigger data (see Sec. 5.2.9). Figure 5.26 shows the noise levels recorded with representative HTI and ECAP hydrophones and with one AM sensor on Line 12 over several time periods with a combined duration of six months. For each sensor, the power spectral density was calculated for the 10 s intervals of continuous data and then for each 1 kHz bin, the median and the 0.27% quantile (corresponding to a 3σ deviation from the median) were derived for the complete set of measurements. For each sensor, one can observe a characteristic frequency above which the 0.27% quantile of the noise level shows a

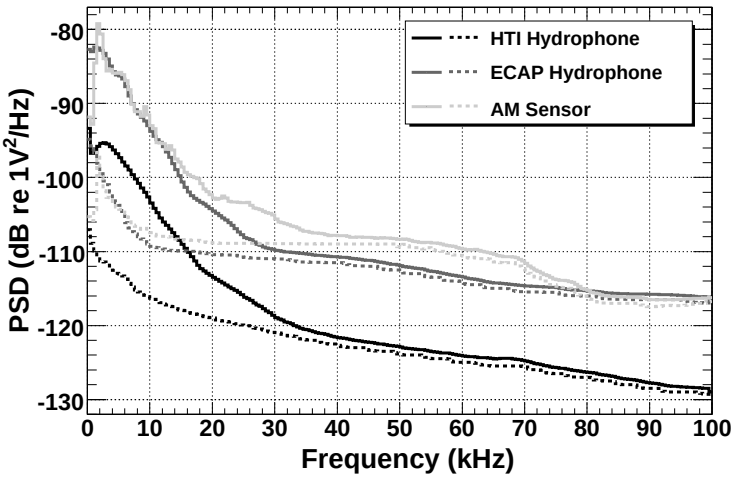

Figure 5.26: Power spectral density (PSD) of the noise level recorded in situ. Solid lines represent the median, dotted lines the 0.27% quantile (corresponding to a 3σ deviation from the median). The voltage used is the calibrated input voltage of the AcouADC board.

constant difference to the median. The corresponding frequencies are about 35 kHz, 30 kHz, and 40 kHz for the HTI hydrophones, ECAP hydrophones and AM sensors, respectively. For higher frequencies, the noise is dominated by the intrinsic electronics noise, limiting the capability to study the acoustic noise.

The noise floor is the lowest for the HTI hydrophones, the difference in the power spectral density to the ECAP hydrophones and AM sensors being 10 to 15 dB. When recording transient signals, the effect on the signal-to-noise ratio is partially compensated by the higher sensitivity of the ECAP hydrophones and the AM sensors. The noise spectrum of the AM sensor displays some structure for frequencies up to about 25 kHz. This is due to coupling of the sensor to the glass spheres. In summary, for studies of the in-situ ambient noise, the HTI hydrophones are the most suited type of sensors.

In Fig. 5.27 a more detailed presentation of the noise data recorded with an HTI hydrophone during the year of 2008 is given. An algorithm to remove strong transient signals (mostly coming from the emitters of the acoustic positioning system) was applied. The relics of such signals and electronics noise show up as spikes between 45 and 75 kHz. The lowest level of recorded noise in situ was confirmed to be consistent with the inherent noise of the system recorded in the laboratory prior to deployment. The observed in-situ noise can be seen to go below the noise level measured in the laboratory for frequencies exceeding 35 kHz. This is due to electronic noise coupling into the system in the laboratory that is absent in the deep sea.

The overall noise levels (i.e. the RMS of the signal amplitudes in each 10 s sample) recorded at the same time with any two active sensors of the same type are correlated at a level above 90%. Furthermore, the noise of the functional sensors with one of the non-functional ones, which is only recording electronic noise, is uncorrelated. This shows that the recorded data are indeed representative of the ambient conditions and not determined by the inherent noise of the system.

To investigate the dependence of the noise recorded with AMADEUS on the weather condition, weather data from several weather stations on the French coast were monitored. Power spectral densities measured with AMADEUS for different sea states are shown in Fig. 5.28.

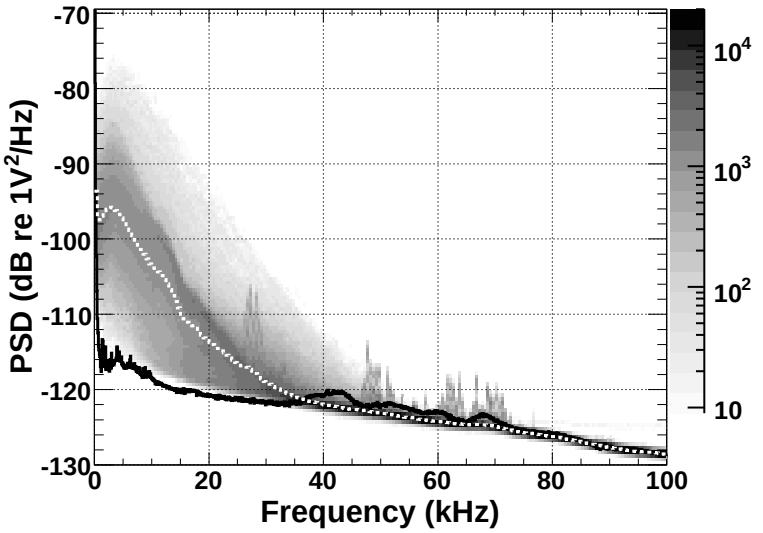

Figure 5.27: Power spectral density (PSD) of the ambient noise recorded with one HTI sensor on the topmost storey of the IL. The voltage used is the calibrated input voltage of the AcouADC board. Shown in shades of grey is the occurrence rate in arbitrary units, where dark colours indicate higher rates. Shown as a white dotted line is the median value of the in-situ PSD and as a black solid line the noise level recorded in the laboratory prior to deployment.

The sea states were determined from the wind conditions at Hyères airport near Toulon at the geographic position 43°05'50"N, 06°08'46"E, roughly 30 km north of the ANTARES site. The slope of the PSD is roughly -10 dB for the octave between 10 and 20 kHz which is much steeper than predicted by the Knudsen curves, in agreement with [236] and the discussion above.
The correlation with the weather station at Cap Cépet at the geographic position 43°4'58.8"N, 5°55'58.8"E about 35 km north-northwest of the ANTARES detector, is shown qualitatively in Fig 5.29. The power spectral density for each minimum bias data sample was integrated from 1 to 50 kHz, being a measure for the standard deviation in that frequency range. A clear correlation is observable, at calm wind the noise level is low and at strong wind it is high, especially at long periods of strong wind. Quantitative measurements are affected by the large distance between the weather station and the ANTARES site. Further cuts can be applied which select only successive data samples for which the RMS change is small, compensating delays between changes of weather conditions at the coast and at the ANTARES site. In this fashion a correlation coefficient of about 0.8 between the wind speed and the noise in the deep sea (1 to 50 kHz range) is obtained [237].

5.4.1.2 Daily Variations and Neutrino Detection Threshold

The ambient background at the ANTARES site determines the energy threshold for neutrino detection. To estimate this threshold, one sensor on the IL07 was evaluated from December 5, 2007 to January 22, 2010, i.e. over a period of about 2 years. During this time, a total of 18462 minimum bias samples was recorded.
Removing samples with large components at high frequencies (e.g. containing signals from

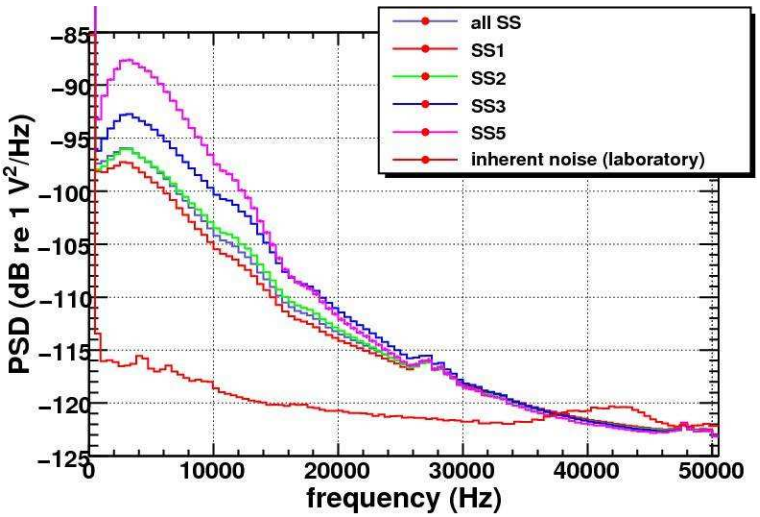

Figure 5.28: Power spectral densities (PSDs) of the ambient noise recorded with one HTI sensor on the topmost storey of the IL for different sea states. The voltage used is the calibrated input voltage of the AcouADC board. Sea states were determined from the wind conditions of the weather station at Hyères airport. Shown is also the noise level recorded in the laboratory prior to deployment.

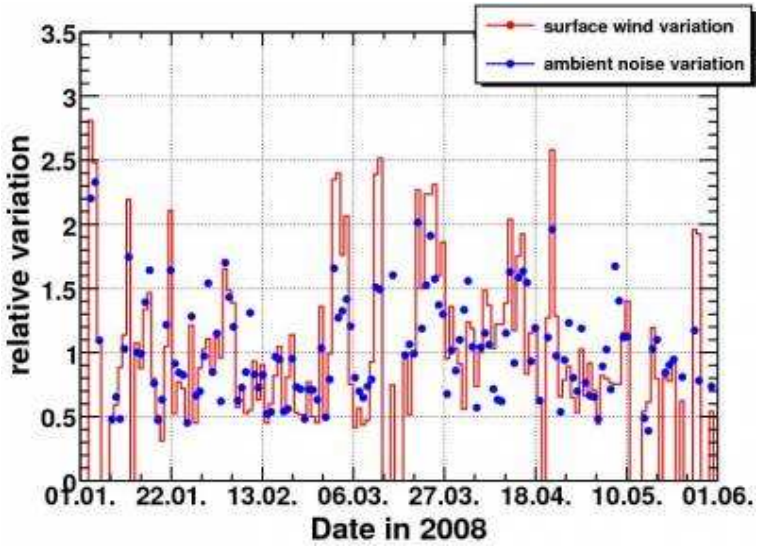

Figure 5.29: Variation of the wind speed (measured at Cap Cépet) and of the ambient noise level measured with an HTI hydrophone on the topmost acoustic storey of the IL over the first half of the year 2008. Plotted is the relative variation for better comparability, i.e. the values which represent daily averages were divided by the yearly average.

the ANTARES acoustic positioning system and non-Gaussian distributions) 13909 samples (75.4%) are remaining. For each of these samples, the noise PSD (units of V^2/Hz) was integrated in the frequency range $1 - 50\,\mathrm{kHz}$, yielding the square of the ambient noise for that sample, as quantified by the output voltage of the hydrophone.
The resulting noise values, relative to the mean noise over all samples, are shown in Fig. 5.30 as a function of the time of the day. Two clear peaks can be observed at about 1 a.m. and 8 to 9 p.m.; the most likely source of this structure is shipping traffic.

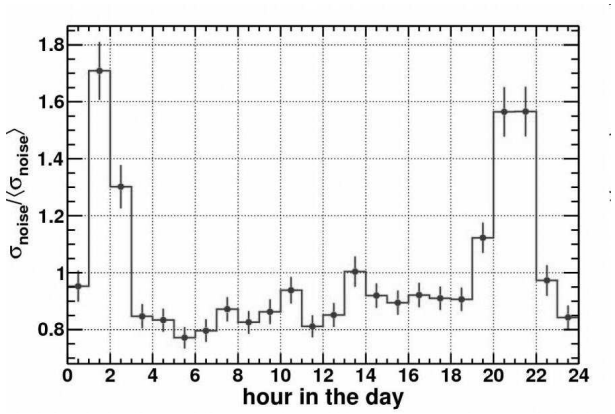

Figure 5.30: Ambient noise in the frequency range $1 - 50\mathrm{kHz}$, measured as described in the text, as a function of the time of the day. The noise is shown relative to the mean noise recorded over the complete period of about two years that was used for the analysis.

Figure 5.31 shows the frequency of occurrence distribution of the same values. Also shown is the corresponding cumulative distribution. For 95% of the samples, the noise level is below $2\langle\sigma_{\mathrm{noise}}^{1\,\mathrm{kHz}}\rangle$, demonstrating that the ambient noise conditions are very stable.

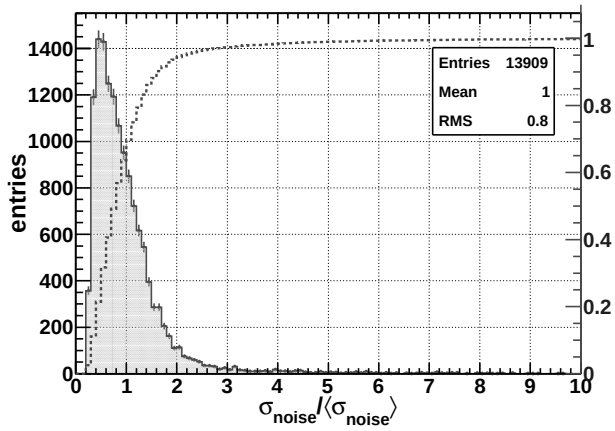

Figure 5.31: Frequency of occurrence distribution for the ambient noise in the range $1 - 50\,\mathrm{kHz}$, relative to the mean ambient noise recorded over the complete period of about two years that was used for the analysis (left scale, filled histogram). Also shown is the cumulative distribution, normalised to the total number of entries of the distribution (right scale, solid line).

The absolute noise level can be estimated by assuming a constant sensor sensitivity[11] of

[11]The ambient noise is originating mainly from the sea surface and hence displays a directivity which has

-145 ± 2 dB re 1V/µPa for the HTI hydrophones, see Sec. 5.2.4. With this value, the mean noise level is $\langle \sigma^{1\,\mathrm{kHz}}_{\mathrm{noise}} \rangle = 25^{+7}_{-5}$ mPa with the median of the distribution at $0.7\langle \sigma^{1\,\mathrm{kHz}}_{\mathrm{noise}} \rangle \sim 17$ mPa.
It must be understood that these noise levels correspond to the specific frequency range chosen. The frequency range investigated so far was *not* optimised for the spectral shape of the expected neutrino signal. Clearly, the noise level can be made arbitrarily small by choosing a correspondingly small frequency range. The most sensible procedure is to choose the frequency range that optimises the signal-to-noise ratio (SNR) for the expected neutrino signal. Preliminary studies using the shower parametrisation and algorithms presented in [156] indicate that this range is about 10 to 50 kHz. In a further study, data taken with the same sensor from the beginning of 2008 until the end of 2010 were evaluated in this frequency range. After quality cuts, 27905 minimum bias samples (79.9% of the total number recorded in that period) were remaining for evaluation. The ambient noise value was derived from the noise PSD in the frequency range $10 - 50$ kHz in the same fashion as describe above. The frequency of occurrence distribution of the resulting noise values and the cumulative distribution, are shown in Fig. 5.32. As for the study of the frequency range $1 - 50$ kHz, see Fig. 5.31, for 95% of the samples the noise level is below $2\langle \sigma^{10\,\mathrm{kHz}}_{\mathrm{noise}} \rangle$. Using the same calibration procedure as described above, the mean noise level is $\langle \sigma^{10\,\mathrm{kHz}}_{\mathrm{noise}} \rangle = 10.1^{+3}_{-2}$ mPa with the median of the distribution at 8.1 mPa.

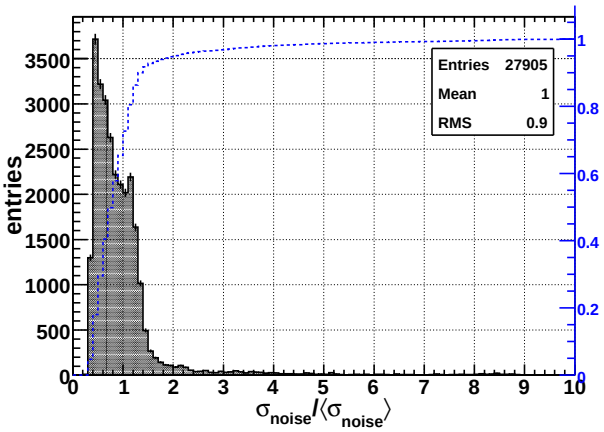

Figure 5.32: Frequency of occurrence distribution for the ambient noise in the range $10 - 50$ kHz, relative to the mean ambient noise recorded over the complete period of three years that was used for the analysis (left scale, filled histogram). Also shown is the cumulative distribution, normalised to the total number of entries of the distribution (right scale, dotted line).

Currently, the detection threshold for bipolar signals corresponds to a SNR of about 2 for an individual hydrophone. For this SNR, the median of the noise distribution corresponds to a signal amplitude of $\sim$15 mPa, equivalent to a neutrino energy of $\sim 1.5\,\mathrm{EeV}$ at a distance of 200 m [148]. By applying pattern recognition methods that are more closely tuned to the expected neutrino signal, this threshold is expected to be further reduced.
In summary, the ambient noise conditions are very favourable for acoustic neutrino detection in the Mediterranean Sea: The noise level is stable at an expected level. Hence it will be

to be folded with the variations of the sensitivity over the polar angle to obtain an effective average sensitivity. For the results presented here the noise has been assumed to be isotropic.

crucial to determine the density of bipolar events to assess the feasibility of an acoustic neutrino detector. Background from transient sources will be discussed now.

5.4.2 Transient Sources

5.4.2.1 Source Direction Reconstruction

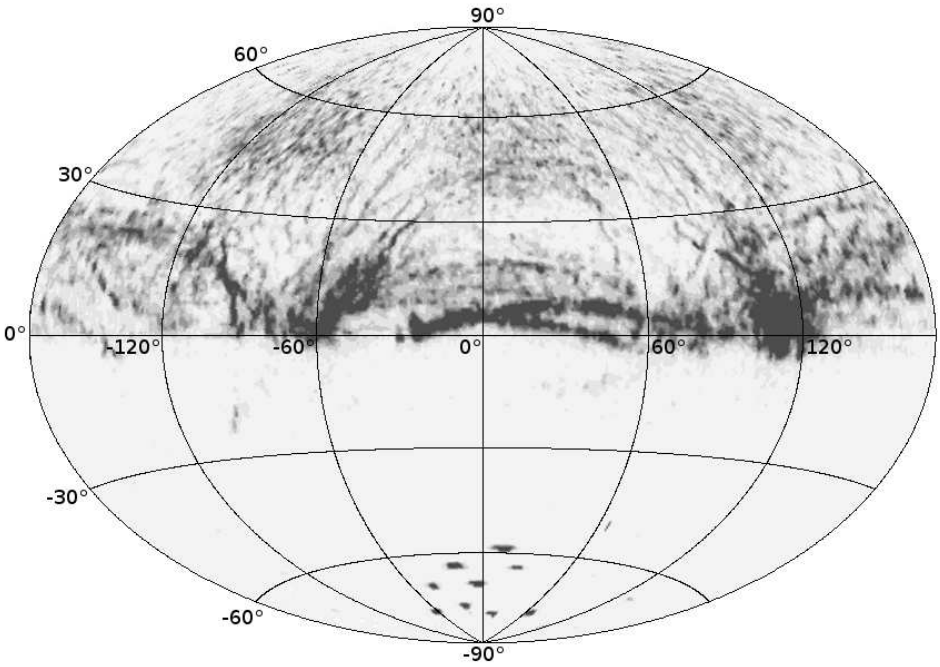

Figure 5.33: Map of directions of sources as reconstructed with an acoustic storey on Line 12. Zero degrees in azimuth correspond to the north direction, the polar angle of zero corresponds to the horizon of an observer on the acoustic storey.

Figure 5.33 shows the reconstructed directions of all sources that were selected during a period of one month by either the amplitude threshold trigger or the pulse shape recognition trigger described in Sec. 5.2.9. In the lower hemisphere, for polar angles between -60° and -90°, the signals from the emitters of the ANTARES acoustic positioning system, located at the anchors of the ANTARES lines, are visible. In the upper hemisphere, dark bands of increased acoustic activity can be observed. These bands can be associated with shipping routes and the points with high activities with the directions of ports. In accordance with the arguments given in Sec. 4.3, the ports themselves are too far away for their acoustic signals to be recorded directly, unless reflection at the sea bottom and surface occur, which would then however strongly reduce the signal strength. It is obvious from Fig. 5.33 that a fiducial volume for the determination of the background rate of bipolar events must exclude the sea surface.
The resolution of the reconstruction is about 3° in azimuth (ϕ) and 0.5° in the polar angle (θ) [238]. While the source direction reconstruction uses methods similar to those used for the position reconstruction of the AMADEUS storeys, for the latter typical $7 \sim 8$ emitters

are used which increases the statistics and hence the precision. For both methods the error includes the resolution of the compass board.
The signals of several sources in Fig. 5.33 associated with port directions reach the detector from directions below the horizon. This is consistent with the effects of refraction discussed in Sec. 4.3. As discussed in that section, for an open water model the most distant signals from the sea surface will reach the uppermost sensor of the AMADEUS device from a distance of about 30 km and from an angle of about -5.5° below the horizon. This is consistent with the direction of the port of Ajaccio on Corsica at a distance of about 240 km and a direction of about 120° from the ANTARES site. For the direction of Marseille at about -60°, the open water model is not valid. Towards the coast in northwards direction, the water depth is reduced to about 200 m within roughly 10 km from the site of the ANTARES detector.

5.4.2.2 Source Position Reconstruction

Using the direction reconstruction from several storeys, the positions of sources can be reconstructed. First investigations over a three month period show that a detailed classification of events triggered by the pulse shape recognition trigger (see Sec. 5.2.9) is necessary to reduce the background of neutrino-like signals [238]. Several methods for a signal classification are currently under investigation [20] and will be discussed in Sec. 5.5.1. Within the geometric volume of the ANTARES detector the background from various transient signals is particularly high, presumably due to reflections of signals from emitters and other sources on the structures of the detector.

5.4.2.3 Background from Environmental Sources and Interdisciplinary Cooperation

Signals from marine mammals and other environmental sources constitute background for the acoustic detection of neutrinos. In particular dolphins emit whistles with frequency spectra that resemble those expected from neutrino interactions. Dolphin can dive to depths of $\sim 500\,\mathrm{m}$ and their whistles constitute the main background of transient signals recorded by the pulse shape recognition trigger. On the other hand, these signals are of great interest to environmental and marine science and the acoustic monitoring of the deep sea has a large potential for interdisciplinary research. As a consequence, efforts for acoustic detection of neutrinos are pursued in cooperation with marine scientists who are using the acoustic data for the study of marine mammals [239, 240] . For the acoustic detection of neutrinos, this cooperation helps to understand and reduce the background from marine mammals. As the AMADEUS device provides a constant stream of acoustic data to shore, currently a unique feature in the Mediterranean Sea, marine scientists are already using the AMADEUS data for dedicated research. A live stream of the data from an AMADEUS hydrophone combined with a real-time analysis focused on marine science is available on the Internet [241].

5.5 Data Analysis Techniques

The search for UHE neutrinos in the presence of a strong background of transient signals as discussed above requires an efficient classification of the acoustic signals. As discussed in Sec. 5.5.1, this is first done on the level of individual hydrophones and storeys. As it has the potential to help classifying the observed transient background, in Sec. 5.4.2.3 interdisciplinary cooperation in the analysis of the acoustic data is discussed. Monte Carlo

simulations, from the neutrino interactions in water to the expected signals in the acoustics sensors, are the subject of Sec. 5.5.2. Finally, the requirements to perform a feasibility study and to calculate a neutrino flux limit is discussed in Sec. 5.5.3.

5.5.1 Source Classification and Identification

The pulse shape recognition trigger described in Sec. 5.2.9 selects a wide range of events each of which can be allocated to one of four classes: Genuine bipolar events that are compatible with signals expected from neutrinos ("neutrino-like signals"), multipolar events, reflections of signals from the acoustic emitters of the ANTARES positioning system and random events, where the latter class contains all events that do not fit into any of the other classes. For the classification, simulated signals representing the four classes in equal proportions were produced and a set of features extracted which are highly discriminant between the classes. This feature vector is then fed into machine learning algorithms [20]. Classification is performed for the signals from individual hydrophones. Subsequently, the results from individual hydrophones are combined to derive a classification for a given acoustic storey. A search for a three-dimensional pressure field consistent with the "pancake" shape expected from neutrino interactions is not part of the classification. The performance of several algorithms was investigated, which will now be discussed.

5.5.1.1 Simulation

A special purpose simulation, generating the four classes of events described above, was designed for testing the feature extraction and classification system, which was also trained with simulated data. Starting from random source positions within a given volume containing the detector, the signals are propagated to the sensors and characteristic ambient noise of different sea levels is added. The output—a continuous data stream—is directed to the filter and from there to the feature extraction.

5.5.1.2 Filtering and Feature Extraction

First, the incoming continuous data stream is subjected to a filter system consisting of the amplitude threshold trigger and the pulse shape recognition trigger described in Sec. 5.2.9. In the next step, the characteristics of the filtered signals are extracted. The resulting feature vector contains time and frequency domain characteristics of the signal as well as the results of a matched filter bank, which was tuned for neutrino-like signals. The bank consists of six reference signals corresponding to angles of $0^\circ - 6^\circ$ in steps of one degree with respect to the plane perpendicular to the axis of a $10^{20}\,\mathrm{eV}$-shower at a distance of 300 m. The plane for 0° in this case was defined to intersect with the position of the neutrino interaction. In the time domain, the number of peaks above a given threshold and the largest peak-to-peak amplitude, its asymmetry and duration are extracted. In the frequency domain, the main frequency component and the excess over the noise background are used as features. From the results of the matched filter bank, the angle for which the best match is obtained is further processed. For the corresponding matched filter output the number of peaks and the amplitude, the width and the integral of the largest peak are stored in the feature vector.

5.5.1.3 Classification

The classification system stems from machine learning algorithms [242] trained and tested with data from the simulation. As input, either the extracted feature vector or the filtered waveform is used; as output, either binary class labels (bipolar or not) or multiple class labels (one for each signal type in the simulation data) are predicted. The following algorithms [243] have been investigated for individual sensors and clusters of sensors:

- Naïve Bayes: This simple classification model is based on applying the Bayes theorem by calculating the most likely class to which a feature vector belongs. It is assumed that the probability of the features to belong to particular class are independent of one another. For a given feature vector, the class is selected using probabilities gained from the training data.
- Decision Tree: This classification model stems from a tree-like structured set of rules. Starting at the root, the tree splits up on each node based on the input variable with the highest information gain. The path from the root of the tree to one of the leaves, which are representing the class labels, defines one rule.
- Random Forest: A Random Forest is a collection of Decision Trees. The classification works as follows: The Random Forest takes the input feature vector, makes a prediction with every tree in the forest, and outputs the class label that received the majority of votes. The trees in the forest are trained with different subsets of the original training data.
- Boosting Trees: They combine the performance of many so-called weak classifiers to produce a powerful classification scheme. A weak classifier is only required to be better than a random choice. Many of them combined in an intelligent fashion, however, result in a strong classifier. Decision Trees are used as weak classifiers in this boosting scheme. In contrast to a Random Forest, the Decision Trees are not necessarily full-grown trees.
- Support Vector Machine (SVM): A SVM maps feature vectors into higher-dimensional space. A hyper-plane is searched so that the margin between this hyper-plane and the nearest feature vectors from both of the two labels of a binary class is maximal.

The algorithms used for Boosting Trees and SVM are restricted to binary class labels as output. The same training and testing data sets were used for the different algorithms. The predictions for the individual sensors are combined to a new feature vector and used as input in order to train and test the models of the clusters of sensors.

5.5.1.4 Results

Two indicators are used to measure the performance of the classification: the *testing error*, which is the failure rate of the prediction for a test sample with respect to the simulation truth, and the *success of training*, which is the ratio between testing error and *training error* (i.e. the failure rate for the training sample) and indicates whether the model is under-trained (<1) or over-trained (>1). As an overall result, multiple class labels as output are less effective than the binary ones, by more than factor of two. The binary class labels are the standard output

of results further presented. Weak classifiers like Naïve Bias and Decision Trees show a high testing error in excess of 14 %, see Fig. 5.34(a), and are neither more robust against changing ambient noise conditions nor significantly faster than other classifiers. Although the SVM is a strong classifier, its high numerical complexity and missing robustness disqualifies it (see Fig. 5.34(b)). Thus the most favourable classifiers are Random Forest and Boosting Trees. In addition, the usage of clusters shows a substantial improvement over individual sensors. Random Forest and Boosting Trees are robust and produce well-trained models. For the individual sensors, a testing error of about 5 % for the Boosting Trees and for the Random Forest of about 10 % is achieved, which is further improved by more than a factor of 4 by combining the sensors to clusters with errors well below 1 %, see Fig. 5.35.

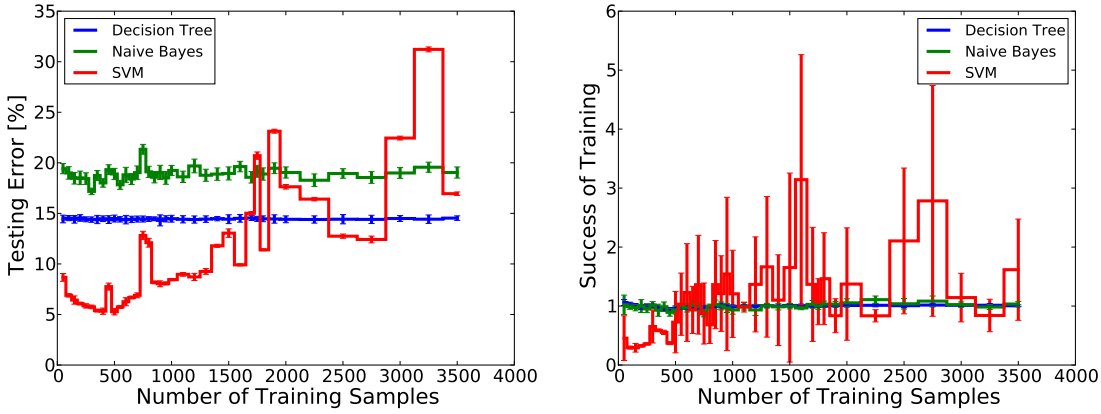

(a) (b)

Figure 5.34: (a) The testing error and (b) the success of the training are shown as a function of the training samples for Decision Tree, Naïve Bias and SVM classifiers. As input, the extracted feature vector is used and the binary class labels as output for individual sensors. A value of 1 in (b) indicates that the model is well-trained.

5.5.2 Monte Carlo Simulations

Simulations of acoustic signals from UHE neutrino interactions consist of the following three separate steps:

- Simulation of the energy distribution of the (hadronic) shower resulting from the interaction of a neutrino in water;
- Propagation of the sound wave from the shower volume to the positions of the acoustic sensors;
- Implementation of measured background noise, both ambient and transient, and of the system response of the acoustic sensors of AMADEUS.

Simulations done for the first step by the ACoRNE collaboration, based on simulations with a modified version of the CORSIKA air shower simulation code [148, 156], were described in Sec. 4.2. The relevant processes for the second step are attenuation (see Sec. 4.2.2) and refraction (see Sec, 4.3), where the former shows a strong frequency dependence and affects

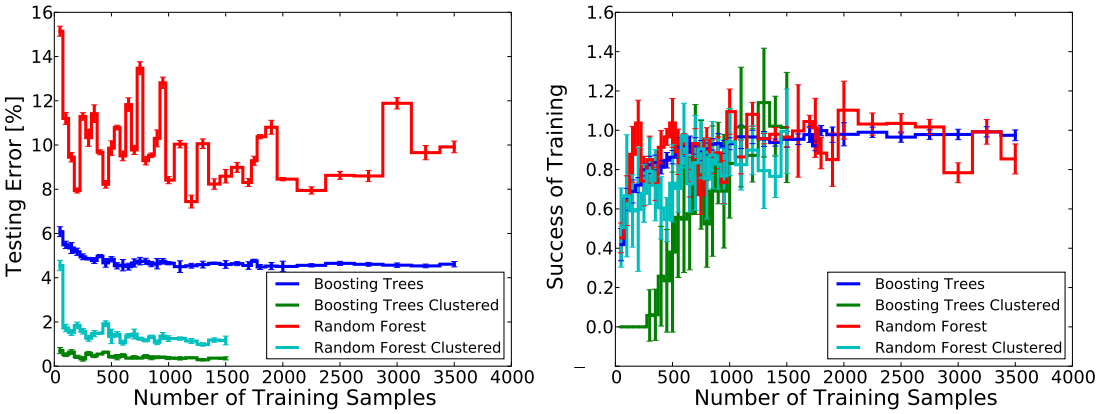

(a) (b)

Figure 5.35: (a) The testing error and (b) the success of the training are shown as a function of the training samples for Random Forest and Boosting Trees classifiers. As input, the extracted feature vector of the signal is used and the binary class labels as output for individual sensors and clusters of sensors (indicated by "clustered"). A value of 1 in (b) indicates that the model is well-trained.

the signal shape as measured with a single hydrophone. For the third step finally parametrisations of the acoustic background in the Mediterranean See (see Sec. 5.4) and of the properties of the AMADEUS hardware (see Sec. 5.2) need to be implemented. In summary, for all required steps the theoretical framework and the formalism exist, and Monte Carlo simulations are currently being implemented for the AMADEUS detector setup, extending the special purpose simulations described in Sec. 5.5.1.

The implementation of Monte Carlo simulations in the context of the AMADEUS project [244] is done using the software framework *SeaTray* which is derived from the framework *IceTray* used by the IceCube collaboration. SeaTray has been chosen as software framework by the KM3NeT consortium, rendering IceTray and SeaTray the de facto standards in neutrino astroparticle physics. It uses a modular approach which e.g. makes it possible to first implement a simple straight line propagation of the sound which then at a later stage can be replaced by a more sophisticated model, taking refraction into account. Furthermore, the AMADEUS detector geometry is implemented in a fashion which allows for an easy replacement with a different geometry, e.g. with that of a potential future large scale detector.

Figure 5.36(a) shows the simulated density of the energy deposition of a 10^{10} GeV hadronic shower, projected into the xz-plane. The energy deposition was calculated using the parametrisations in [148, 156]. The z- and x-coordinates denote the directions along the shower axis and a direction orthogonal to the shower axis, respectively. Figure 5.36(b) shows the distribution of 10^6 points, generated according to the energy distribution shown in Fig. 5.36(a).

As discussed in Sec. 4.2.4, it is mostly the radial energy distribution within the shower which is responsible for the shape and amplitude of the acoustic pulse that is observed in the far field. Figure 5.37(a) shows the modified effective linear energy density $\epsilon_{\mathrm{mod}}(t) \equiv \epsilon_r(r(t))\,\gamma_G/(4\pi\,c_s\,r_0)$ (see Sec. 4.2.3) for different positions of the acoustic sensor receiving the signal. In this notation, Eq. 4.21 can be rewritten

$$\hat{p}_{\mathrm{att}}(\omega) \;=\; i\omega\,\mathcal{F}\{\epsilon_{\mathrm{mod}}(t)\}\,\exp\left(-\frac{\tilde{\mu}(i\omega)}{2}\,r_0\right) \quad . \tag{5.1}$$

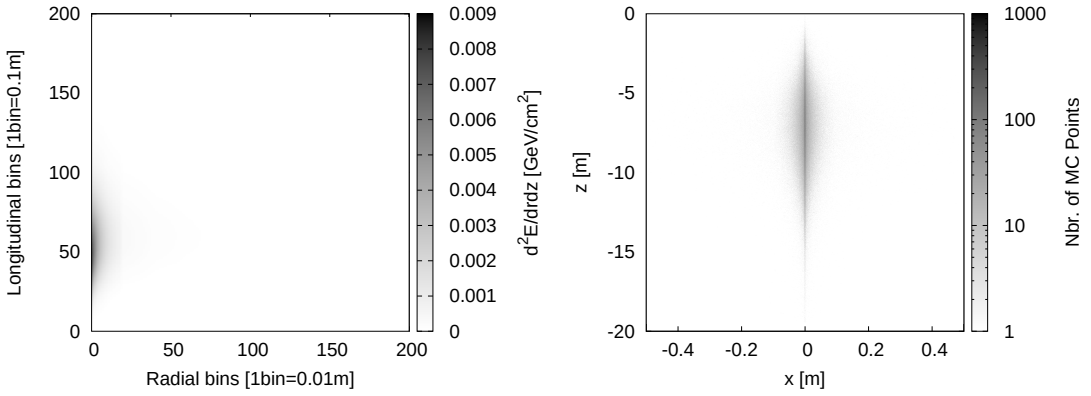

(a) (b)

Figure 5.36: (a) Density of the energy deposition of a 10^{10} GeV hadronic shower resulting from a neutrino interaction in water. (b) Distribution of 10^6 points, generated according to the energy distribution shown in (a) and projected from a three-dimensional distribution upon the xz-plane. Bin sizes are 0.01 m in x and 0.1 m in z. For both plots, the neutrino interaction takes place at a coordinate of $(0, 0)$ in lateral and longitudinal direction and the shower develops in the direction of increasing longitudinal bins for (a) and decreasing z-coordinate for (b).

The neutrino interaction was generated such that the centre of the hadronic shower for a vertically downgoing neutrino lies within the same horizontal plane as a storey denoted "Storey 2", at a distance of 200 m. This way, the storey lies within the "pancake" of the pressure field. "Storey 1" is located 14.5 m below Storey 2. This configuration corresponds to two adjacent acoustic storeys on ANTARES Line 12 or the two lowermost storeys on the Instrumentation Line, see Fig. 5.10. Figure 5.37(b) shows the resulting pressure pulses at the respective positions of the acoustic sensors, derived by calculating the Fourier transform of Eq. 5.1. The simulations illustrate that the characteristic three-dimensional "pancake" pattern expected from neutrino-generated pressure waves can be identified with a setup of acoustic sensors, arranged in clusters along horizontal structures. No signal is observed on Storey 1 when the maximum of the signal is observed in Storey 2. For signals with sufficiently high amplitude, this is a strong experimental signature of a neutrino interaction.
As was pointed out in Secs. 3.4 and 4.2.1, the simulation of hadronic showers for neutrino interactions at ultra-high energies involves extrapolations in energy over several orders of magnitude. It is therefore important to try out alternative approaches to the simulation based on CORSIKA code described above. One alternative is the simulation tool FLUKA[12].

5.5.3 Feasibility Study and Neutrino Flux Limit

The Monte Carlo simulations described in Sec. 5.5.2 indicate that the reconstruction of the "pancake" structure of the three-dimensional pressure field in principle is possible with a large scale detector with a design similar to that of the AMADEUS setup. Once the investigations with the AMADEUS device described in this chapter will have been concluded, a realistic simulation, including effects of ambient and transient background, of a potential future large-scale acoustic neutrino detector will be possible. The feasibility of such a po-

[12] FLUktuierende KAskade ("fluctuating cascade"), http://www.fluka.org/

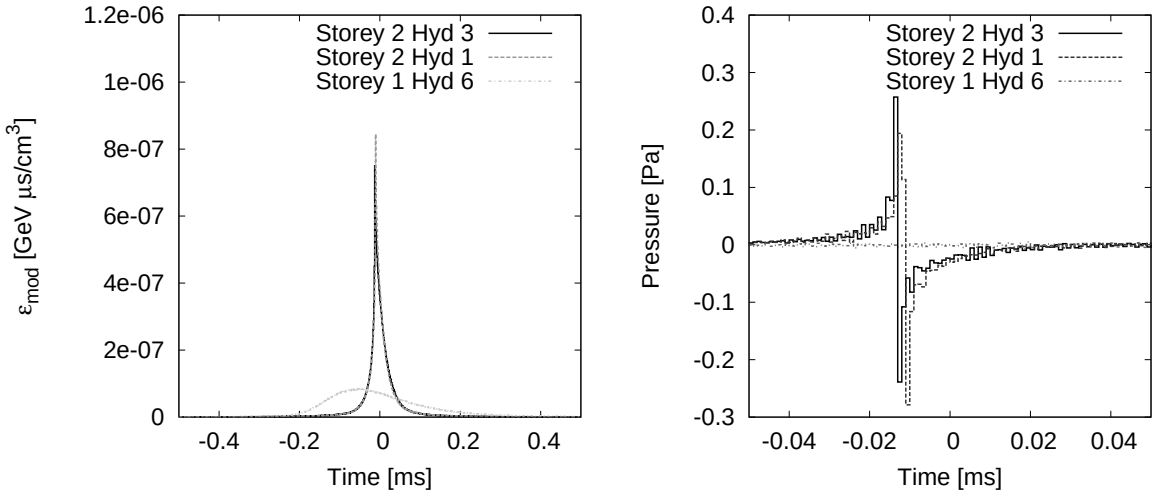

(a) (b)

Figure 5.37: (a) Simulated modified effective linear energy densities ϵ_{mod} (see text) and (b) the derived acoustic signals at the positions of acoustic sensors in two acoustic storeys with a vertical spacing of 14.5 m. See text for details. For Storey 2, signals from two different sensors are shown.

tential detector is essentially a question of whether its size will be within bounds that make its realisation technically and financially possible. For a given flux of UHE neutrinos and a highly efficient and pure reconstruction of neutrino interactions, the required size is mainly determined by the energy threshold for the detection of neutrinos and by how far the effective volume will exceed the geometric volume of the detector, see Sec. 4.4.2. Furthermore it is crucial to develop algorithms to reconstruct neutrinos with high efficiency while rejecting fake neutrino events from random coincidences of transient sources. Given the low expected rate of neutrino interactions, the reconstruction must not yield any fake neutrino events over a period of several years.

The pointing precision of the reconstructed neutrino directions will be important, since cosmogenic neutrinos are expected to point back to their sources. This is so because these neutrinos are produced relatively close ($100 \sim 200\,\mathrm{Mpc}$) to the source of the UHE cosmic rays that generate them. Even if the cosmic rays should be deflected by strong magnetic fields within this range, the angular deviation of a generated neutrino after traversing cosmological distances to reach Earth should be small. The precision of the direction reconstruction from the three-dimensional pressure field will be investigated with the Monte Carlo simulations that are currently being developed. In [175] it was found however that for a set of selection cuts optimising the pointing precision the resolution is not better than 12°.

The methods discussed so far can be applied to the AMADEUS setup to derive a limit on the neutrino flux. While this is an important study that will be performed when the preparatory work has been concluded, the setup is too small to derive a competitive limit on the neutrino flux and from its geometry (two lines spanning up a plane) it is not well suited for the reconstruction of a three-dimensional pressure field.

Chapter 6

Summary and Outlook

As they are the only particles traversing the Universe essentially unobstructed by interactions and electromagnetic fields, neutrinos convey information that neither cosmic rays nor gamma-rays can provide. The production of neutrinos follows from well understood particle physics processes when charged protons or heavier nuclei are accelerated and interact with other particles or with photons. Hence the detection of neutrinos from astrophysical sources, combined with measurements of cosmic rays and gamma-rays, would grant important insights into astrophysical processes. The observation of such neutrinos could help answering the questions of the origin of cosmic rays, of their maximum energy and of their chemical composition.

Charged cosmic rays have been observed on Earth with energies in excess of 10^{20} eV, which implies the production of neutrinos with energies in excess of 10^{19} eV. Measurements with the Pierre Auger Observatory are consistent with the generation of cosmic rays with even higher energies, which however do not reach Earth as a consequence of the Greisen-Zatsepin-Kuz'min-cutoff. While the only known astrophysical objects which are considered capable of accelerating charged particles to such energies are Active Galactic Nuclei and Gamma-Ray Bursts, there is no conclusive evidence that they are indeed the sources of the observed UHE cosmic rays.

The most important process presumably leading to a flux of UHE neutrinos, i.e. neutrinos with $E \geq 1$ EeV, is the production of cosmogenic neutrinos in the interaction of cosmic rays with cosmic microwave background photons. This flux has been termed "guaranteed flux", a notation that however has to be reconsidered since results of the Pierre Auger Observatory indicate that the cosmic ray flux may not be dominantly composed of protons. A wide range of fluxes of UHE neutrinos on Earth is consistent with the chemical composition of cosmic rays measured with the Pierre Auger Observatory, some of which do not result in a measurable neutrino signal. The observation (or non-observation) of a UHE neutrino flux thus would constrain the parameter space of such models. Of highest scientific interest would be the measurement of the neutrino energy spectrum as it would indicate the maximum energy of the cosmic rays at the source and give hints on the cosmological distribution of these sources.

Given their low expected fluxes, the detection of UHE neutrinos requires to survey huge volumes which is technically and financially difficult with the dense instrumentation necessary for optical Cherenkov telescopes. Several alternative detection methods are under investigation that use different detectable signatures of neutrino-induced particle showers (both hadronic and electromagnetic) in various media. To focus the efforts, the "Acoustic and Ra-

dio EeV Neutrino Detection Activities" (ARENA) workshop series was inaugurated in 2003. The ARENA 2012 workshop will be held at the Erlangen Centre for Astroparticle Physics (ECAP).

A promising option for the detection of UHE neutrinos is the radio Cherenkov method, which is based on the detection of electromagnetic radiation, coherently emitted from the excess of electrons present in (hadronic or electromagnetic) showers interacting in the target media. Searches for the resulting radiation have been performed with radio telescopes, observing the lunar regolith, and with balloon- and satellite-borne experiments, surveying the ice of Greenland and the South Pole. Given the success of these experiments, which so far provide the most stringent limits on the neutrino flux in the UHE region, the construction of an in-ice radio array at the South Pole, complementing the IceCube Cherenkov neutrino telescope, is under consideration.

By searching for the Cherenkov and/or fluorescent light from neutrino-induced extended air showers, the Pierre Auger Observatory is searching for neutrinos produced by two mechanisms. First, upgoing, "Earth skimming" tau neutrinos, which interact inside the Earth, produce an upgoing tau lepton. If the tau decays hadronically, an upgoing shower is registered in the Pierre Auger Observatory, which would be a clear signature of a neutrino reaction. Second, neutrinos of any flavour can be identified by down-going, nearly horizontal showers that start deep inside the atmosphere, i.e. after a distance of several interaction lengths up to which a cosmic ray could not propagate without initiating a shower beforehand.

The main subject of this report is the method of acoustic detection of neutrinos by measuring pressure pulses in underwater acoustic arrays. The pressure signals are produced by the particle showers that evolve when neutrinos interact with nuclei in water. The resulting energy deposition in a cylindrical volume of a few centimetres in radius and several metres in length leads to a local heating of the medium which is instantaneous with respect to the hydrodynamic time scales. This temperature change induces an expansion or contraction of the medium depending on its volume expansion coefficient. According to the thermo-acoustic model, the expansion of the heated volume creates a pressure pulse of bipolar shape which propagates through the surrounding medium within a characteristic disk-like volume, typically referred to as "pancake".

To investigate the potential of acoustic neutrino detection, several experiments are currently pursued or have been pursued until recently. Studies in sea water have been done using military arrays of hydrophones (SAUND, ACoRNE) or using the infrastructure of other existing deep sea infrastructures (OνDE). In addition, ice (SPATS) and fresh water (Lake Baikal) are investigated as media for the acoustic detection of neutrinos.

The feasibility of a large-scale acoustic neutrino detector in the Mediterranean Sea has been a subject of research at the Erlangen Centre for Astroparticle Physics. Building on previous work, the thermo-acoustic model has been confirmed in proton and laser beam experiments. Simulations based on the thermo-acoustic model were shown to fit the data well and the disappearance of the signal for the temperature with the highest density of water, 4°C at normal pressure, could be confirmed. Following these studies, the AMADEUS system for the investigation of techniques for acoustic particle detection in the deep sea was integrated into the ANTARES neutrino detector in the Mediterranean Sea. The system started to take data in December 2007 and was completed in May 2008. It comprises 36 acoustic sensors, arranged in six acoustic storeys (or clusters) at water depths between 2050 and 2300 m. The signal amplification can be adjusted to adapt to special circumstances, e.g. to record dedicated runs with high-amplitude signals, as they are emitted by the ANTARES positioning system. The

sensitivity of the hydrophones and the digitisation are chosen such that signals exceeding the ambient noise background can be recorded with high resolution, both in amplitude and time, over a frequency range of about 1 to 50 kHz. The inherent noise of the system was kept low, at about the same level as the ambient noise expected at sea state 0, i.e. a completely calm sea. The in-situ performance of AMADEUS is in full accordance with expectations. Data taking is going on continuously and the data are recorded if one of three adjustable trigger conditions is met.

The analysis of the AMADEUS data is on-going as the data volume is constantly increasing. The position calibration of the acoustic storeys has been performed with the required precision. The ambient noise has been studied over a period of about three years by now. Preliminary results indicate that the threshold for the detection of hadronic showers from neutrino interactions is of the order of 1 EeV shower energy. The observed background of transient signals is very diverse. An online trigger, performing a cross correlation with the expected bipolar neutrino signal, is not sufficient to effectively reject the background of transient signals. For this purpose, currently a classification scheme for transient signals is being developed. Furthermore, Monte Carlo simulations are under development. This is done in a software framework that allows for an easy adaption to the detector setup, so that simulations can be easily transferred from the AMADEUS setup to a potential future detector configuration. Among other things, the simulation will allow for a realistic determination of the effective volume of an acoustic neutrino detector, which in turn will help to determine the required instrumented volume and sensor configuration.

The determination of the energy and incident direction of a neutrino from the three-dimensional pressure field is a great challenge. With an array of acoustics sensors, the energy of a particle shower can be determined from the observed pulse heights if the position of the interaction has been reconstructed. The energy distribution in the shower is however subject to large event-by-event fluctuations and in average only 20% of the neutrino energy is transferred to the hadronic shower. The case of charged current interactions of electron neutrinos, where the complete energy is deposited in the hadronic and electromagnetic showers, requires dedicated simulations. Only a lower limit on the energy of the incident neutrino can thus be estimated. This situation is quite similar to that of optical detection of muon tracks from neutrino interactions, where the energy of the hadronic shower in most cases cannot be measured and the energy reconstruction of the muon has a large uncertainty.

A further subject of interest are hybrid studies, i.e. the search for coincidences between signals in the optical and acoustic sensors within the ANTARES detector. Even though coincidences are only expected for the very small subset of contained events at high or ultra-high energies, the AMADEUS setup is perfectly suited to pursue these investigations. Since the optical telescope can be used as a trigger and interactions close to an AMADEUS sensor can be selected, the energy threshold may be reduced w.r.t. that of $\sim$1 EeV discussed above. It is foreseen to operate the ANTARES detector until 2016 and given the excellent reliability of the AMADEUS hardware so far, the device can be expected to continue data taking until that date. The total lifetime of AMADEUS will then have been about nine years and within this time a unique data set will be accumulated. The time span of several years will allow for the investigation of seasonal and long term trends of background noise for acoustic neutrino detection. At the same time the data are also of great interest to environmental and marine science. Given the large potential for interdisciplinary research, efforts for acoustic detection of neutrinos are pursued in cooperation with marine scientists who are using the acoustic data for the study of marine mammals. For the acoustic detection of neutrinos, this cooperation

helps to understand and reduce the background from marine mammals. As the AMADEUS device provides a constant stream of acoustic data to shore, currently a unique feature in the Mediterranean Sea, marine scientists are already using the AMADEUS data for dedicated research.

The future deep-sea research infrastructure KM3NeT in the Mediterranean Sea will contain an optical neutrino telescope exceeding the volume of the ANTARES detector by more than two orders of magnitude. Acoustic sensors will be installed for the calibration of the positions of the photomultiplier tubes (PMTs). As the experience with ANTARES shows, the "all data to shore" concept is useful also for acoustic positioning, since systematic effects can be studied and algorithms can be adjusted to in-situ conditions. Hence, acoustic sensors can be designed to comply with the requirements for acoustic detection and marine science besides that for acoustic positioning. The relevant filter and analysis routines can then be implemented on on-shore computer clusters, a concept that is already successfully pursued with the AMADEUS project. European research groups involved in the field of acoustic neutrino detection in sea water are jointly focusing their efforts on the KM3NeT detector. The software framework under development for the analysis of AMADEUS data will allow for an easy adaption to any potential future setup.

As indicated by the current state of research, even an extensive instrumentation of KM3NeT with acoustic sensors will not be sufficient to detect cosmogenic neutrinos. An acoustic neutrino detector capable of precisely measuring the flux of UHE neutrinos or set limits that would allow for severely constraining the parameter space of existing theories would need an instrumented volume of at least several tens of cubic kilometres. A measurement of UHE neutrinos by means of acoustic detection therefore cannot be expected in the near future. It would require a major effort by an international, and presumably interdisciplinary, collaboration that is not likely to be undertaken before the research programme with the KM3NeT detector has produced results. Whether or not a large scale acoustic neutrino detector will be built then depends on the outcome of the on-going feasibility studies, on technological developments and on the scientific results of both KM3NeT and the alternative methods pursued for the detection of UHE neutrinos.

Appendix A

Cosmic Acceleration

A.1 A Generic Model

A first serious attempt to explain the cosmic ray spectrum was done by Fermi [75]. Before returning to this theory, a more general approach will be taken, following the argumentation of [76], in which the power law distribution of primordial cosmic rays is derived for a "generic" particle accelerator. Only a number of generalises assumptions are made. The first assumption is that some acceleration regions exist where charged particles are injected which gain energy at a rate that is proportional to their energy with a characteristic time constant τ_{acc} according to

$$\frac{dE}{dt} = \frac{E}{\tau_{acc}} \quad . \tag{A.1}$$

If it is further assumed that particles are ejected from the acceleration region at an average rate of $1/\tau_{esc}$, then this process follows a Poisson distribution

$$P(t) = \exp\left(-\frac{t}{\tau_{esc}}\right) \quad , \tag{A.2}$$

where $P(t)$ is the probability that the particle will be ejected *after* the time t, or stated differently, the probability that it has not yet been ejected at the time t and assuming that ejection will take place eventually. Since the probability for the particle to be ejected after the time $t = 0$ is $P(t = 0) = 1$ and decreases from thereon, dP/dt is negative,

$$\frac{dP}{dt} = -\frac{1}{\tau_{esc}} \exp\left(-\frac{t}{\tau_{esc}}\right) \quad . \tag{A.3}$$

Defining $N(t)$ as the number of particles ejected from the accelerator up to time t (and therefore joining the ranks of primordial cosmic rays) for a total number N_0 of accelerated particles then one gets

$$N(t) = N_0 \left(1 - P(t)\right) \tag{A.4}$$

$$\Rightarrow \frac{dN}{dt} = \frac{N_0}{\tau_{esc}} \exp\left(-\frac{t}{\tau_{esc}}\right) \quad . \tag{A.5}$$

Solving Eq. A.1, an expression for the energy of the accelerated particle at the time t is obtained,

$$E(t) = E_0 \cdot \exp\left(\frac{t}{\tau_{acc}}\right) \quad , \tag{A.6}$$

which can be solved for t and inserted into Eq. A.5 together with the expression for dt derived from Eq. A.1 to yield

$$\begin{aligned} \frac{dN}{dE} &= \frac{N_0}{\tau_{esc}} \exp\left(\frac{-\ln(E/E_0)\cdot\tau_{acc}}{\tau_{esc}}\right)\cdot\frac{\tau_{acc}}{E} \\ &= N_0\,\frac{\tau_{acc}}{\tau_{esc}}\,{E_0}^{-1}\cdot\left(\frac{E}{E_0}\right)^{-(1+\tau_{acc}/\tau_{esc})} \quad . \end{aligned} \tag{A.7}$$

The result is the sought after power law for the spectral distribution of particles emitted from a cosmic accelerator. The mathematical shape of Eqs. A.1 and A.2 shall now be derived by postulating a mechanism by which a particle gains energy by repetitively going through some process, where it gains some amount of energy in each cycle. Denoting the number of cycles by n, where it gains in average a relative energy of ϵ in each cycle, then the energy gain between cycles n and $n+1$ is

$$E_{n+1} - E_n = E_n\,\epsilon \quad . \tag{A.8}$$

Denoting the time between two cycles as Δt, one can find a time constant τ_{acc} such that $\epsilon = \Delta t/\tau_{acc}$. With the transition $E_n \rightarrow E(t)$ and with $E_{n+1} - E_n \equiv \Delta E$ one gets

$$\Delta E = E(t)\frac{\Delta t}{\tau_{acc}} \quad , \tag{A.9}$$

which in the transition to differentials is equivalent to Eq. A.1.
The ejection probability, Eq. A.2, can be derived from the assumption of a successive number of interactions, where for each interaction, the particle will be ejected from the acceleration region with a probability of p. Then the probability P_n that the particle will *not* have been ejected in the n-th cycle is

$$P_n = (1-p)^n \quad . \tag{A.10}$$

P_n is equivalent to the probability that the particle will be ejected *after* the n-th cycle. Again a time constant τ_{esc} can be found such that $p = \Delta t/\tau_{esc}$ with $t = n\Delta t$. For large values of n (i.e. small p) this yields

$$P_n = \left(1 - \frac{t/\tau_{esc}}{n}\right)^n \overset{n\rightarrow\infty}{\longrightarrow} P(t) = \exp(-\frac{t}{\tau_{esc}}) \quad , \tag{A.11}$$

which is equivalent to Eq. A.2. As can be easily verified, for the term τ_{acc}/τ_{esc} in the exponent of Eq. A.7 the relation

$$\tau_{acc}/\tau_{esc} = p/\epsilon \tag{A.12}$$

holds. For completeness it should be noted that from Eq. A.10 alternatively the relation

$$\Delta P := P_{n+1} - P_n = -p\,P_n \quad , \tag{A.13}$$

can be derived and evaluated in the same fashion as Eq. A.8. This will yield the same result as Eq. A.11.

A.2 Fermi Acceleration of Second Order

In Sec. A.1, the processes that lead to the successive energy gain of the accelerated particles were left open. In his original paper [75], Fermi assumed interactions of charged particles with magnetic clouds. If a cloud is treated as a "brick wall" that moves with velocity u, then after the collision with a particle with velocity $v > 0$, the particle will have a velocity $(-v + u)/(1 - vu/c^2)$. The collision will increase the kinetic energy of the particle if u and v are anti-parallel ($u < 0$) or decrease the kinetic energy if they are parallel; for simplicity, the situation is treated in one dimension only. For the velocities holds $|u| \ll |v| \approx c$. The difference in energy is given by

$$E' - E = (\gamma' - \gamma)mc^2 \quad ,$$

where the prime denotes the quantities after the collision. Using $\beta \equiv v/c$ and $\xi \equiv u/c$ one obtains

$$\begin{aligned} \gamma' &= \frac{1}{\sqrt{1 - \left(\frac{-\beta+\xi}{1-\beta\xi}\right)^2}} \\ &= \gamma \frac{1 - \beta\xi}{\sqrt{1 - \xi^2}} \end{aligned} \tag{A.14}$$

where the second line is the result of a straight forward calculation. Expanding the expression for γ' from Eq. A.14 to second order in ξ it follows

$$\begin{aligned} E' - E &= \gamma(-\beta\xi + \frac{1}{2}\xi^2)mc^2 \\ \Rightarrow (E' - E)/E \equiv \epsilon_\pm &= -\beta\xi + \frac{1}{2}\xi^2 \quad , \end{aligned} \tag{A.15}$$

where ϵ was introduced in Eq. A.8. The subscript '$\pm$' is added because one cycle results either in an energy gain ($\beta\xi < 0$) or in an energy loss ($\beta\xi > 0$). The crucial point is that independent of the sign of ξ, the quadratic term is positive, meaning that if ξ is negative, a bit more energy is gained than is lost if ξ is positive. Assuming there will be in average an equal number of scatterings with parallel and anti-parallel velocities, then the average gain is

$$\epsilon \equiv \epsilon_+ + \epsilon_- = \xi^2 \equiv (u/c)^2 \quad .$$

The result is altered numerically if an isotropic distribution of the velocity vectors of the particles w.r.t. that of the clouds is assumed [77]. Important is that in either case, ϵ only grows in second order of u/c, which is the reason why this mechanism has been dubbed "Fermi mechanism of second order".

This theory leads to three problems [76], some of which are already addressed in Fermi's paper. First, given velocities of interstellar clouds in the Galaxy of $u/c < 10^{-4}$ and a mean free path of the order of 1 pc [77], the fact that the process is second order makes it very slow. Second, between collisions with magnetic clouds, the accelerated particle will collide with other particles and suffer ionisation losses. This requires an injection of particles exceeding $\sim 100\,\mathrm{MeV}$ to allow for an energy gain by acceleration that exceeds the energy loss by ionisation. And third, the assumption that the ratio of the time constants τ_{acc}/τ_{esc} is a universal constant, independent of energy, which Fermi made to derive the cosmic ray spectrum observed on Earth, can not easily be justified. In the following section, the process of shock acceleration will be introduced, which overcomes the first problem.

A.3 Shock Acceleration

Generally speaking, a shock wave is a flow of matter (gas in the present case) that moves through a medium at speeds much higher than the speed of sound or the Alfvén speed, respectively, in that medium. For the process of shock acceleration, first the presence of an interstellar gas is assumed, considered at rest in the observer's frame, into which relativistic particles are injected that shall be further accelerated to highest energies. The gas is then traversed by a shock wave of ionised plasma.
A gas can be characterised by its pressure ρ, temperature T and velocity u. The subscripts 1 and 2 will be used to label the gas upstream and downstream of the shock, respectively. Then continuity requires $\rho_1 u_1 = \rho_2 u_2$ and it can be shown that for a fully ionised plasma (treated as an ideal gas) in the rest frame of the shock front $\rho_2/\rho_1 = 4$ and therefore $u_2/u_1 = 1/4$. In the rest frame of the upstream gas, the passing of the shock front with velocity U increases the velocity of the gas to $3/4\,U$. Hence, in the rest frame of the upstream gas, the downstream gas is approaching with this speed, while in the rest frame of the downstream gas, the same is true for the upstream gas.
The relativistic particles to be shock accelerated will traverse the shock front with hardly noticing it at all. Instead, they are affected by the gas upstream and downstream of the shockfront in such a manner that turbulences behind and irregularities ahead of the shock front randomise the direction of the particles w.r.t. the rest frame of the respective gas without loss of energy [77]. If the momenta of the relativistic particles upstream of the shock front have an isotropic distribution, at a given time half of the particles will travel towards the shock front with momentum $p\cos\theta$, where θ is defined w.r.t. the normal on the shock front. When traversing the shock front, the particle vectors are isotropised behind the shock front. Allowing for sufficient time to elapse, most of them will cross the shock front back into the upstream region, which in their reference frame is approaching with a velocity of $3/4\,U$. This way, by virtue of the condition that the particles assume an isotropic distribution in the reference frame of the respective gas they are in, they manage to gain an energy boost each time they cross the shock front, irrespective of the direction in which they do this.

For a quantitative examination, the particle flux per area (and time) Φ_A through the shock front will be defined, such that $d^2\Phi_A/d\theta d\phi$ is the "conventional" flux per area, time and solid angle. The polar angle θ is defined w.r.t. the normal on the shock front $\vec{n}$ and after integration over the azimuthal angle ϕ the expression $d\Phi_A = C\,2\pi\,\sin\theta\,\vec{n}\cdot\vec{n}_v d\theta$ is obtained. Here $\vec{n}_v$ is the unit vector in the direction of the velocity of the particle and C some normalisation constant[1]. The vector product can be substituted by $-\cos\theta$. If now a set of protons with the same absolute value of the momentum (and hence of the velocity) is considered, the particle flux through the shock front from all directions can be calculated by integrating the expression above over a half sphere,

$$\Phi_A \;= -C2\pi \int_0^{\pi/2} \sin\theta\,\cos\theta d\theta = -C\pi \quad .$$

The minus sign is owed to the fact that the direction of the flux is into the shock front, and the normal on the front is defined as pointing into the direction of the movement of the shock. The average momentum in the direction of the shock front for a particle with velocity $\vec{v}$ is

[1]The dependence of Φ_A on area and time is presumed to be constant and is contained in C.

$v\ \cos\theta$, and the average over the particles constituting the above flux is

$$\langle v\cos\theta\rangle = \frac{-C2\pi\int_0^{\pi/2} v\cos\theta\sin\theta\ \cos\theta d\theta}{-C\pi} = \frac{2}{3}v \quad .$$

Revisiting Eq. A.15, particle and gas velocities now have opposite directions, independent of the direction in which the shock front is crossed. Using a first order approximation, the energy gain for a "back-and-forth trip" across the shock front with $\beta = v/c$ and $\xi = 3/4{\cdot}U/c$ can be written as

$$\epsilon = 2\langle\beta\cos\theta\rangle\xi = 2\,\frac{2}{3}\,\xi = \frac{U}{c} \quad , \tag{A.16}$$

where in the second step, β was approximated by 1. To determine the ejection probability per cycle, the arguments given in [245] will be followed. In kinetic theory, the rate per area with which a perfect gas with particle density n hits a wall is given by $\frac{1}{4}n\langle v\rangle$, where $\langle v\rangle$ denotes the average velocity of the gas particles. Starting with the gas upstream of the shock, the flux of particles across the shock front is given by $\frac{1}{4}nc$. Once the particles have crossed the shock front into the downstream gas, they will be scattered by the magnetic fields which will, if only enough time elapses, sooner or later scatter the particle back across the shock front. However, the particle velocity is isotropic within the downstream gas, which moves with a flux of $n|u_2| = n\frac{1}{4}|U|$ away from the shock front. This is the flux of the particles that are swept away, or advected, from the shock front. At an "infinite" distance away from the shock front, this gives the flux of particles never crossing back into the upstream area. Hence, within one cycle, the fraction of particles that is removed is $p = \frac{1}{4}nU/(\frac{1}{4}nc) = U/c$. Here p is identical to the probability introduced in Eq. A.10 and with ϵ from Eq. A.16 it follows $p/\epsilon = 1$. This can now, using the identity of Eq. A.12 be inserted into Eq. A.7 to give a power law of the form E^{-2} for the production of cosmic rays in cosmic accelerators.

Bibliography

[1] K. Hirata et al., *Observation of a Neutrino Burst from the Supernova SN1987A*, Phys. Rev. Lett. 58 (1987) 1490.

[2] R.M. Bionta et al., *Observation of a neutrino burst in coincidence with supernova 1987A in the Large Magellanic Cloud*, Phys. Rev. Lett. 58 (1987) 1494.

[3] J. G. Learned and K. Mannheim, *High-Energy Neutrino Astrophysics*, Ann. Rev. Nucl. Part. Sci. 50 (2000) 679.

[4] A. Avrorin et al., *The Baikal neutrino experiment*, in: Proceedings of the 4th International Workshop on a Very Large Volume Neutrino Telescope for the Mediterranean Sea (VLVnT 2009), Athens, Greece, 13–15 Oct 2009, Nucl. Inst. and Meth. A 626–627, 2011, p. S13.

[5] M. Ageron et al. (ANTARES Coll.), *ANTARES: the first undersea neutrino telescope*, accepted for publication by Nucl. Inst. and Meth. A, arXiv:1104.1607v1 [astro-ph.IM].

[6] A. Achterberg et al. (IceCube Coll.), *First Year Performance of the IceCube Neutrino Telescope*, Astropart. Phys. 26 (2006) 155, arXiv:astro-ph/0604450.

[7] J.A. Hinton for the HESS Coll., *The Status of the H.E.S.S. Project*, in: Proceedings of the 2nd VERITAS Symposium on TeV Astrophysics, Chicago, IL, USA, April 24–26, 2003, Vol. 48 of New Astron. Rev., 2004, p. 331, arXiv:astro-ph/0403052v1.

[8] J. Cortina, F. Goebel and T. Schweizer for the MAGIC Coll., *Technical Performance of the MAGIC Telescopes*, in: Proceedings of the 31st Int. Cosmic Ray Conf. (ICRC2009), Lodz, Poland, July 7–15, 2009, arXiv:0907.1211v1 [astro-ph.IM].

[9] H. Kubo et al., *Status of the CANGAROO-III Project*, in: Proceedings of the 2nd VERITAS Symposium on TeV Astrophysics, Chicago, IL, USA, April 24–26, 2003, Vol. 48 of New Astron. Rev., 2004, p. 323.

[10] T.C. Weekes et al., *VERITAS: the Very Energetic Radiation Imaging Telescope Array System*, Astropart. Phys. 17 (2002) 221, arXiv:astro-ph/0108478v1.

[11] A.A. Abdo et al., *Milagro Observations of Multi-TeV Emission from Galactic Sources in the Fermi Bright Source List*, Astrophys. J. 700 (2009) L127, erratum-ibid.703:L185,2009, arXiv:0904.1018v3 [astro-ph.HE].

[12] U.F. Katz for the KM3NeT Consortium, *The KM3NeT Project*, in: Proceedings of the 4th International Workshop on a Very Large Volume Neutrino Telescope for the Mediterranean Sea (VLVnT 2009), Athens, Greece, 13–15 Oct 2009, Nucl. Inst. and Meth. A 626–627, 2011, p. S57, doi:10.1016/j.nima.2010.06.207.

[13] KM3NeT Consortium, *Technical Design Report for a Deep-Sea Research Infrastructure in the Mediterranean Sea Incorporating a Very Large Volume Neutrino Telescope*, ISBN 978-90-6488-033-9, http://www.km3net.org/TDR/KM3NeTprint.pdf (2011).

[14] *The ARENA workshop series*, *http://www-zeuthen.desy.de/arena/*, Zeuthen (Germany) 2005; Newcastle (UK) 2006; *http://www.roma1.infn.it/arena2008/index.htm*, Rome (Italy) 2008, *http://arena2010.in2p3.fr/*, Nantes (France) 2010.

[15] I. Allekotte et al. for the Pierre Auger Coll., *The Surface Detector System of the Pierre Auger Observatory*, Nucl. Inst. and Meth. A 586 (2008) 409, arXiv:0712.2832v1 [astro-ph].

[16] J. Abraham, *The Fluorescence Detector of the Pierre Auger Observatory*, Nucl. Inst. and Meth. A 620 (2010) 227, arXiv:0907.4282v1 [astro-ph.IM].

[17] K. Graf et al., *Thermo-acoustic Sound Generation in the Interaction of Pulsed Proton and Laser Beams in a Water Target*, to be submitted to Nucl. Inst. and Meth.

[18] J.A. Aguilar et al. (ANTARES Coll.), *AMADEUS–The acoustic neutrino detection test system of the ANTARES deep-sea neutrino telescope*, Nucl. Inst. and Meth. A 626-627 (2011) 128, arXiv:1009.4179v2 [astro-ph.IM].

[19] R. Lahmann for the ANTARES Coll., *Status and Recent Results of the Acoustic Neutrino Detection Test System AMADEUS*, in: Proceedings of the 4th International Workshop on Acoustic and Radio EeV Neutrino Detection Activities (ARENA 2010), Nantes, France, June 29–July 2, Nucl. Inst. and Meth. A, 2010, arXiv:1104.3041v1 [astro-ph.IM].

[20] M. Neff et al., *Signal Classification for Acoustic Neutrino Detection*, in: Proceedings of the 4th International Workshop on Acoustic and Radio EeV Neutrino Detection Activities (ARENA 2010), Nantes, France, June 29–July 2, Nucl. Inst. and Meth. A, 2010, arXiv:1104.3248v1 [astro-ph.IM].

[21] A.M. Hillas, *The origin of ultra-high-energy cosmic rays*, Ann. Rev. Astron. Astrophys. 22 (1984) 425.

[22] F. Halzen and D. Hooper, *High-energy Neutrino Astronomy: The Cosmic Ray Connection*, Rep. Prog. Phys. 65 (2002) 1025, arXiv:astro-ph/0204527v2.

[23] D. Torres and L.A. Anchordoqui, *Astrophysical origins of ultrahigh energy cosmic rays*, Rep. Prog. Phys. 67 (2004) 1663, arXiv:astro-ph/0402371v3.

[24] J.H. Krolik, *Active Galactic Nuclei*, 3rd Edition, Princeton Series in Astrophysics, Princeton University Press, 1999, ISBN 0-691-01151-6.

[25] C.M. Urry, *AGN Unification: An Update*, in: G.T. Richards and P.B. Hall (Ed.), Princeton meeting on "AGN Physics with the Sloan Digital Sky Survey" (July 2003), Vol. 311 of ASP Conf. Series, 2004, p. 49, arXiv:astro-ph/0312545v1.

[26] K. Mannheim, *High-energy neutrinos from extragalactic jets*, Astropart. Phys. 3 (1995) 295.

[27] P. Padovani, *Gamma-ray emitting AGN and unified schemes*, in: Proceedings of the 32nd Rencontres de Moriond: Very high energy phenomena in the universe, Les Arcs, France, 18–25 Jan 1997, p. 7, astro-ph/9704002.

[28] C. Spiering, private communication (Oct. 2009).

[29] M. Böttcher, *Modeling the Emission Processes in Blazars*, Astrophys. Space Sci. 309 (2007) 95, arXiv:astro-ph/0608713v1.

[30] L.A. Anchordoqui, D. Hopper, S. Sarkar, and A.M. Taylor, *High-energy neutrinos from astrophysical accelerators of cosmic ray nuclei*, Astropart. Phys. 29 (2008) 1, arXiv:astro-ph/0703001v4.

[31] R.U. Abbasi et al. (IceCube Coll.), *Search for muon neutrinos from Gamma-Ray Bursts with the IceCube neutrino telescope*, Astrophys. J. 710 (2010) 346, arXiv:0907.2227v2 [astro-ph.HE].

[32] S.E. Woosley, *Gamma-ray bursts from stellar mass accretion disks around black holes*, Astrophys. J. 405 (1993) 273.

[33] D. Eichler, M. Livio, T. Piran, and D.N. Schramm, *Nucleosynthesis, Neutrino Bursts and Gamma-Rays from Coalescing Neutron Stars*, Nature 340 (1989) 126.

[34] E. Waxman and J. Bahcall, *High Energy Neutrinos from Cosmological Gamma-Ray Burst Fireballs*, Phys. Rev. Lett. 78 (1997) 2292, arXiv:astro-ph/9701231v1.

[35] J.K. Becker, *High-energy neutrinos in the context of multimessenger astrophysics*, Phys. Rep. 458 (2008) 173, arXiv:0710.1557v2 [astro-ph].

[36] T. Piran, *The Physics of Gamma-Ray Bursts*, Rev. Mod. Phys. 76 (2004) 1143, arXiv:astro-ph/0405503v1.

[37] P. Mészáros, *Theories of gamma-ray bursts*, Ann. Rev. Astro. Astrophys. 40 (2002) 137.

[38] E. Waxman, *Cosmological Gamma Ray Bursts and the Highest Energy Cosmic Rays*, Phys. Rev. Lett. 75 (1995) 386, arXiv:astro-ph/9505082v1.

[39] E. Waxman and J. Bahcall, *Neutrino Afterglow from Gamma-Ray Bursts:* $\sim 10^{18}$ *eV*, Astrophys. J. 541 (2000) 707, arXiv:hep-ph/9909286v2.

[40] V.S. Berezinsky and G.T. Zatsepin, *Cosmic rays at ultra high energies (neutrino?)*, Phys. Lett. B 28 (1969) 423.

[41] J.V. Narlikar, *An Introduction to Cosmology*, 3rd Edition, Cambridge University Press, 2002, ISBN 0-521-79367-9.

[42] S. Yoshida, G. Sigl, and S. Lee, *Extremely High Energy Neutrinos, Neutrino Hot Dark Matter, and the Highest Energy Cosmic Rays*, Phys. Rev. Lett. 81 (1998) 5505, arXiv:hep-ph/9808324v1.

[43] T.J. Weiler, *Cosmic Ray Neutrino Annihilation on Relic Neutrinos Revisited: A Mechanism for Generating Air Showers above the Greisen-Zatsepin-Kuzmin Cut-off*, Astropart. Phys. 11 (1999) 303, arXiv:hep-ph/9710431v2.

[44] C. Barbot, M. Drees, F. Halzen, and D. Hooper, *Neutrinos Associated With Cosmic Rays of Top-Down Origin*, Phys. Lett. B 555 (2003) 22, arXiv:hep-ph/0205230v1.

[45] D. Semikoz and G. Sigl, *Ultra-High Energy Neutrino Fluxes: New Constraints and Implications*, J. Cosm. Astropart. Phys. 0404 (2004) 003, arXiv:hep-ph/0309328v1.

[46] P.W. Gorham et al., *Experimental Limit on the Cosmic Diffuse Ultra-high Energy Neutrino Flux*, Phys. Rev. Lett. 93 (2004) 041101, arXiv:astro-ph/0310232v3.

[47] G. Sigl, *Some Current Theoretical Issues around Ultra-High Energy Cosmic Rays*, Acta Phys. Pol. B 35 (2004) 1845, arXiv:astro-ph/0404074v1.

[48] P.W. Gorham et al. (ANITA Coll.), *Observational Constraints on the Ultra-high Energy Cosmic Neutrino Flux from the Second Flight of the ANITA Experiment*, Phys. Rev. D 82 (2010) 022004, arXiv:1003.2961v3 [astro-ph.HE]; Erratum: arXiv:1011.5004v1 [astro-ph.HE].

[49] P. Bhattacharjee and G. Sigl, *Origin and Propagation of Extremely High Energy Cosmic Rays*, Phys. Rep. 327 (2000) 109, arXiv:astro-ph/9811011v2.

[50] R. Aloisio, V. Berezinsky, and M. Kachelrieß, *On the status of superheavy dark matter*, Phys. Rev. D 74 (2006) 023516, arXiv:astro-ph/0604311v1.

[51] H. Ohoka et al., *Further development of data acquisition system of the Akeno Giant Air Shower Array*, Nucl. Inst. and Meth. A 385 (1997) 268.

[52] M. Takeda et al., *Extension of the Cosmic-Ray Energy Spectrum Beyond the Predicted Greisen-Zatsepin-Kuz'min Cutoff*, Phys. Rev. Lett. 81 (1998) 1163, arXiv:astro-ph/9807193v1.

[53] M. Kachelrieß, *The rise and fall of top-down models as main UHECR sources*, in: Proceedings of the 20th Rencontres de Blois 'Challenges in Particle Astrophysics', Blois, France, 18–23 May 2008, arXiv:0810.3017v2 [astro-ph].

[54] J. Blümer, R. Engel, and J. Hörandel, *Cosmic Rays from the Knee to the Highest Energies*, Prog. Part. Nucl. Phys. 63 (2009) 293, arxiv:0904.0725v1[astro-ph.HE].

[55] T. Stanev, *Ultra High Energy Cosmic Rays*, arXiv:astro-ph/0411113v1.

[56] C. Grupen, *Astroparticle Physics*, Springer Verlag, 2005, ISBN 3-540-25312-2.

[57] J. Abraham et al. (Pierre Auger Coll.), *Measurement of the energy spectrum of cosmic rays above* 10^{18} *eV using the Pierre Auger Observatory*, Phys. Lett. B 685 (2010) 239, arXiv:1002.1975v1 [astro-ph.HE].

[58] J. Hörandel, *Cosmic rays from the knee to the second knee:* 10^{14} *to* 10^{18} *eV*, Mod. Phys. Lett. A22 (2007) 1533, arXiv:astro-ph/0611387v1.

[59] J.W. Cronin, T.K. Gaisser and S.P. Swordy, *Cosmic Rays at the Energy Frontier*, Sci. Am. (1997) 32.

[60] S. Ostapchenko, *Status of QGSJET*, in: Proceedings of the International Conference 'Colliders to Cosmic Rays 2007' (C2CR07), Granlibakken (CA), USA, 25 Feb. – 1 Mar., Vol. 928 of AIP Conf. Proc., 2007, p. 118, arXiv:0706.3784v1 [hep-ph].

[61] E.-J. Ahn et al., *Cosmic ray event generator Sibyll 2.1*, Phys. Rev. D 80 (2009) 094003, arXiv:0906.4113v3 [hep-ph].

[62] T. Antoni et al. (KASCADE Coll.), *KASCADE measurements of energy spectra for elemental groups of cosmic rays: Results and open problems*, Astropart. Phys. 24 (2005) 1, arXiv:astro-ph/0505413v1.

[63] A. Haungs for the KASCADE-Grande Coll., *The Cosmic Ray Energy Spectrum Measured with KASCADE-Grande*, in: Proceedings of the 31st Int. Cosmic Ray Conf. (ICRC2009), Lodz, Poland, July 7–15, 2009, arXiv:0910.4824v1 [astro-ph.HE].

[64] R. Aloisio, V. Berezinsky, P. Blasi, and S. Ostapchenko, *Signatures of the transition from galactic to extragalactic cosmic rays*, Phys. Rev. D 77 (2008) 025007, arXiv:0706.2834v2 [astro-ph].

[65] K. Nakamura et al. (Particle Data Group), *The Review of Particle Physics*, J. Phys. G 37 (2010) 075021, *http://pdg.lbl.gov/*.

[66] D. Allard et al., *UHE nuclei propagation and the interpretation of the ankle in the cosmic-ray spectrum*, Astron. & Astrophys. 443 (2005) L29, arXiv:astro-ph/0505566v2.

[67] D. Allard, E. Parizot and A.V. Olinto, *On the transition from Galactic to extragalactic cosmic-rays: spectral and composition features from two opposite scenarios*, Astropart. Phys. 27 (2007) 61, arXiv:astro-ph/0512345v2.

[68] P. Sommers and S. Westerhoff, *Cosmic Ray Astronomy*, New J. Phys. 11 (2009) 055004, arXiv:0802.1267v1 [astro-ph].

[69] T. Abu-Zayyad et al., *The prototype high-resolution Fly's Eye cosmic ray detector*, Nucl. Inst. and Meth. A 450 (2000) 253.

[70] J.H. Boyer, B.C. Knapp, E.J. Mannel and M. Seman, *FADC-based DAQ for HiRes Fly's Eye*, Nucl. Inst. and Meth. 482 (2002) 457.

[71] R.U. Abbasi et al. (HiRes Coll.), *Measurement of the Flux of Ultra High Energy Cosmic Rays by the Stereo Technique*, Astropart. Phys. 32 (2009) 53, arXiv:0904.4500v1 [astro-ph.HE].

[72] N. Hayashida et al. (AGASA Coll.), *The Anisotropy of Cosmic Ray Arrival Directions around* 10^{18}*eV*, Astropart. Phys. 10 (1999) 303, arXiv:astro-ph/9807045v2.

[73] M. Takeda et al., *Small-Scale Anisotropy of Cosmic Rays above* 10^{19} *eV Observed with the Akeno Giant Air Shower Array*, Astrophys. J. 522 (1999) 225.

[74] P. Abreu et al. (Pierre Auger Coll.), *Update on the correlation of the highest energy cosmic rays with nearby extragalactic matter*, Astropart. Phys. 34 (2010) 314, arXiv:1009.1855v2 [astro-ph.HE].

[75] E. Fermi, *On the Origin of the Cosmic Radiation*, Phys. Rev. 75 (1949) 1169.

[76] R. Blandford and D. Eichler, *Particle Acceleration at Astrophysical Shocks: A Theory of Cosmic Ray Origin*, Phys. Rep. 154 (1987) 1.

[77] M.S. Longair, *High Energy Astrophysics*, 2nd Edition, Vol. 2, Cambridge University Press, 1992, ISBN 0-521-38374-9.

[78] E. Waxman, *High energy cosmic ray and neutrino astronomy*, to be published in: Astronomy at the Frontiers of Science, Springer Verlag, 2011, arXiv:1101.1155v1 [astro-ph.HE].

[79] P. Blasi, *Cosmic Ray Acceleration in Supernova Remnants*, in: Proceedings of the International Conference on Advanced Technology and Particle Physics (ICATPP 2010), Villa Olmo, Como, 7–8 October 2010, arXiv:1012.5005v1 [astro-ph.HE].

[80] F.W. Stecker and M.H. Salamon, *Photodisintegration of Ultrahigh Energy Cosmic Rays: A New Determination*, Astrophys. J. 512 (1999) 521, arXiv:astro-ph/9808110v3.

[81] F.W. Stecker, M.A. Malkan and S.T. Scully, *Intergalactic Photon Spectra from the Far IR to the UV Lyman Limit for* $0 < z < 6$ *and the Optical Depth of the Universe to High Energy Gamma-Rays*, Astrophys. J. 648 (2006) 774, arXiv:astro-ph/0510449v4.

[82] R. Kayser, P. Helbig, and T. Schramm, *A general and practical method for calculating cosmological distances*, Astron. & Astrophys. 318 (1997) 680, arXiv:astro-ph/9603028v3.

[83] E. Waxman and J. Bahcall, *High energy neutrinos from astrophysical sources: An upper bound*, Phys. Rev. D 59 (1998) 023002, arXiv:hep-ph/9807282v2.

[84] A. Mücke et al., *Monte-Carlo simulations of photohadronic processes in astrophysics*, Comp. Phys. Comm. 124 (2000) 290, arXiv:astro-ph/9903478v1.

[85] K. Huang, *Statistical Mechanics*, 2nd Edition, John Wiley & Sons, 1987, ISBN 0-471-81518-7.

[86] G.R. Blumenthal, *Energy Loss of High-Energy Cosmic Rays in Pair-Producing Collisions with Ambient Photons*, Phys. Rev. D 1 (1970) 1596.

[87] V. Berezinsky, A. Gazizov, and S. Grigorieva, *On astrophysical solution to ultrahigh energy cosmic rays*, Phys. Rev. D 74 (2006) 043005, arXiv:hep-ph/0204357v3.

[88] R. Engel, D. Seckel, and T. Stanev, *Neutrinos from propagation of ultrahigh energy protons*, Phys. Rev. D 64 (2001) 093010, arXiv:astro-ph/0101216v2.

[89] K. Greisen, *End to the cosmic-ray spectrum?*, Phys. Rev. Lett. 16 (1966) 748.

[90] G.T. Zatsepin and V.A. Kuz'min, *Upper limit of the spectrum of cosmic rays*, JETP Lett. 4 (1966) 78, russian original: Pis'ma Zh. Éksp. Teor. Fiz. **4** (1966) 114.

[91] M.S. Longair, *High Energy Astrophysics*, 2nd Edition, Vol. 1, Cambridge University Press, 1992, iSBN 0-521-38374-9.

[92] R.J. Protheroe and P.A. Johnson, *Propagation of ultra high energy protons and gamma rays over cosmological distances and implications for topological defect models*, Astropart. Phys. 4 (1996) 253, arXiv:astro-ph/9506119v1.

[93] F.A. Aharonian and J.W. Cronin, *Influence of the universal microwave background radiation on the extragalactic cosmic-ray spectrum*, Phys. Rev. D 50 (1994) 1892.

[94] D. Allard et al., *Cosmogenic Neutrinos from the propagation of Ultra High Energy Nuclei*, J. Cosm. Astropart. Phys. 0609 (2006) 005, arXiv:astro-ph/0605327v2.

[95] R.J. Protheroe, A.-C. Donea and A. Reimer, *TeV gamma rays and cosmic rays from the nucleus of M87, a mis-aligned BL Lac object*, Astropart. Phys. 19 (2003) 559, arXiv:astro-ph/0210249v2.

[96] P.L. Biermann et al., *Active Galactic Nuclei with Starbursts: Sources for Ultra High Energy Cosmic Rays*, Int. J. Mod. Phys. D18 (2009) 1577, arXiv:0904.1507v2 [astro-ph.HE].

[97] K. Mannheim, R.J. Protheroe and J.P. Rachen, *Cosmic ray bound for models of extragalactic neutrino production*, Phys. Rev. D 63 (2000) 023003.

[98] B. Katz, R. Budnik, and E. Waxman, *The Energy Production Rate & the Generation Spectrum of UHECRs*, J. Cosm. Astropart. Phys. 03 (2009) 20, arXiv:0811.3759v2 [astro-ph].

[99] E. Waxman, *Cosmological Origin for Cosmic Rays Above* 10^{19} *eV*, Astrophys. J. 452 (1995) L1, arXiv:astro-ph/9508037v1.

[100] J. Abraham et al. (Pierre Auger Coll.), *Measurement of the Depth of Maximum of Extensive Air Showers above* 10^{18} *eV*, Phys. Rev. Lett. 104 (2010) 091101, arXiv:1002.0699v1 [astro-ph.HE].

[101] P. Sokolsky for the HiRes Coll., *Final Results from the High Resolution Fly's Eye (HiRes) Experiment*, in: Proceedings of the XVIth International Symposium on Very High Energy Cosmic Ray Interactions (ISVHECRI 2010), Batavia, IL, USA, 28 June–2 July, 2010, arXiv:1010.2690v2 [astro-ph.HE].

[102] R. Ulrich et al., *Proton-Air Cross Section and Extensive Air Showers*, in: Proceedings of the XVth International Symposium on Very High Energy Cosmic Ray Interactions 2008 (ISVHECRI 2008), Paris, France, Sept. 1–6, Vol. 196 of Nucl. Phys. Proc. Suppl., 2009, p. 335, arXiv:0906.3075v1 [astro-ph.HE].

[103] D. Hooper, A.M. Taylor and S. Sarkar, *Cosmogenic photons as a test of ultra-high energy cosmic ray composition*, Astropart. Phys. 34 (2011) 340, arXiv:1007.1306v1 [astro-ph.HE].

[104] D. Hooper, A. Taylor, and S. Sarkar, *The Impact of Heavy Nuclei on the Cosmogenic Neutrino Flux*, Astropart. Phys. 23 (2005) 11, arXiv:astro-ph/0407618v2.

[105] L.A. Anchordoqui et al., *Prediction of the cosmogenic neutrino flux in light of new data from the Pierre Auger Observatory*, Phys. Rev. D 76 (2007) 123008, arXiv:0709.0734v1 [astro-ph].

[106] D. Hooper, S. Sarkar and A.M. Taylor, *The intergalactic propagation of ultra-high energy cosmic ray nuclei*, Astropart. Phys. 27 (2007) 199, arXiv:astro-ph/0608085v4.

[107] R. Aloisio, V. Berezinsky and A. Gazizov, *Ultra High Energy Cosmic Rays: The disappointing model*, Astropart. Phys. 34 (2011) 620, arXiv:0907.5194v2 [astro-ph.HE].

[108] E.G. Berezhko, *Composition of cosmic rays accelerated in active galactic nuclei*, Astrophys. J. 698 (2009) L138, arXiv:0905.4785v1 [astro-ph.HE].

[109] M. Ahlers et al., *Neutrinos as a diagnostic of cosmic ray Galactic/extra-galactic transition*, Phys. Rev. D 72 (2005) 023001, arXiv:astro-ph/0503229v2.

[110] J. Bahcall and E. Waxman, *High energy astrophysical neutrinos: The upper bound is robust*, Phys. Rev. D 64 (2001) 023002, arXiv:hep-ph/9902383v2.

[111] D.J. Thompson, *Gamma ray astrophysics: the EGRET results*, Rep. Prog. Phys. 71 (2008) 116901, arXiv:0811.0738v1 [astro-ph].

[112] J.A. Aguilar et al. (ANTARES Coll.), *Search for a diffuse flux of high-energy ν_μ with the ANTARES neutrino telescope*, Phys. Lett. B 696 (2011) 16, arXiv:1011.3772v1 [astro-ph.HE].

[113] R. Abbasi et al. (IceCube Coll.), *A Search for a Diffuse Flux of Astrophysical Muon Neutrinos with the IceCube 40-String Detector*, arXiv:1104.5187v1 [astro-ph.HE].

[114] K. Murase and J.F. Beacom, *Neutrino Background Flux from Sources of Ultrahigh-Energy Cosmic-Ray Nuclei*, Phys. Rev. D 81 (2010) 123001, arXiv:1003.4959v1 [astro-ph.HE].

[115] F. Halzen, *Lectures on High-Energy Neutrino Astronomy*, presented at the International WE Heraeus Summer School on Physics with Cosmic Accelerators, arXiv:astro-ph/0506248v1 (2005).

[116] R. Abbasi et al. (IceCube Coll.), *The energy spectrum of atmospheric neutrinos between 2 and 200 TeV with the AMANDA-II detector*, Astropart. Phys. 34 (2010) 48, arXiv:1004.2357v2 [astro-ph.HE].

[117] G.D. Barr et al., *A three-dimensional calculation of atmospheric neutrinos*, Phys. Rev. D 70 (2004) 023006, arXiv:astro-ph/0403630v1.

[118] C.G.S. Costa, *The prompt lepton cookbook*, Astropart. Phys. 16 (2001) 193, arXiv:hep-ph/0010306v3.

[119] S. Yoshida and M. Teshima, *Energy Spectrum of Ultra-High Energy Cosmic Rays with Extra-Galactic Origin*, Prog. Theor. Phys. 89 (1993) 833.

[120] O.E. Kalashev, V.A. Kuzmin, D.V. Semikoz, and G. Sigl, *Ultra-High Energy Neutrino Fluxes and Their Constraints*, Phys. Rev. D 66 (2002) 063004, arXiv:hep-ph/0205050v3.

[121] Z. Fodor, S.D. Katz, A. Ringwald, and H. Tu, *Bounds on the cosmogenic neutrino flux*, J. Cosm. Astropart. Phys. 0311 (2003) 015, arXiv:hep-ph/0309171v1.

[122] K. Kotera, D. Allard, and A.V. Olinto, *Cosmogenic Neutrinos: parameter space and detectabilty from PeV to ZeV*, J. Cosm. Astropart. Phys. 1010 (2010) 013, arXiv:1009.1382v2 [astro-ph.HE].

[123] T. Stanev, D. De Marco, M.A. Malkan, and F.W. Stecker, *Cosmogenic Neutrinos from Cosmic Ray Interactions with Extragalactic Infrared Photons*, Phys. Rev. D 73 (2006) 043003, arXiv:astro-ph/0512479v1.

[124] M. Ave et al., *Cosmogenic Neutrinos from Ultra-High Energy Nuclei*, Astropart. Phys. 23 (2005) 19, arXiv:astro-ph/0409316v2.

[125] H. Yüksel and M.D. Kistler, *Enhanced Cosmological GRB Rates and Implications for Cosmogenic Neutrinos*, Phys. Rev. D 75 (2007) 083004, arXiv:astro-ph/0610481v3.

[126] A.A. Abdo et al. (Fermi-LAT Coll.), *The Spectrum of the Isotropic Diffuse Gamma-Ray Emission Derived From First-Year Fermi Large Area Telescope Data*, Phys. Rev. Lett. 104 (2010) 101101, arXiv:1002.3603v1 [astro-ph.HE].

[127] M. Ahlers et al., *GZK Neutrinos after the Fermi-LAT Diffuse Photon Flux Measurement*, Astropart. Phys. 34 (2010) 106, arXiv:1005.2620v2 [astro-ph.HE].

[128] V. Berezinsky, A. Gazizov, M. Kachelrieß, and S. Ostapchenko, *Restricting UHE-CRs and cosmogenic neutrinos with Fermi-LAT*, Phys. Lett. B 695 (2011) 13, arXiv:1003.1496v3 [astro-ph.HE].

[129] R.U. Abbasi et al. (HiRes Coll.), *First Observation of the Greisen-Zatsepin-Kuzmin Suppression*, Phys. Rev. Lett. 100 (2008) 101101, arXiv:astro-ph/0703099v2.

[130] S. Sarkar, private communication (June 2011).

[131] H. Athar, M. Jeżabek, and O. Yasuda, *Effect of neutrino mixing on high-energy cosmic neutrino flux*, Phys. Rev. D 62 (2000) 103007, arXiv:hep-ph/0005104v2.

[132] L. Stanco, *Neutrinos Oscillations with Long-Base-Line Beams (Past, Present and very near Future)*, in: Proceedings of the Int. Conf. Beyond the Standard Models of Particle Physics, Cosmology and Astrophysics (BEYOND 2010), Cape Town, South Africa 1–6 February 2010, arXiv:1006.4826v1 [hep-ph].

[133] F. Halzen and A.D. Martin, *Quarks & Leptons*, John Wiley & Sons, Inc., 1984, ISBN 0-471-88741-2.

[134] K.O. Mikaelian and I.M. Zheleznykh, $\overline{\nu}_e e$ *annihilitions*, Phys. Rev. D 22 (1980) 2122.

[135] R. Gandhi, C. Quigg, M.H. Reno, and I. Sarcevic, *Ultrahigh-Energy Neutrino Interactions*, Astropart. Phys. 5 (1996) 81, arXiv:hep-ph/9512364v1.

[136] M. Fukugita and T. Yanagida, *Physics of Neutrinos*, Springer Verlag, 2003, ISBN 3-540-43800-9.

[137] R.N. Mohapatra and P.B. Pal, *Massive Neutrinos in Physics and Astrophysics*, 3rd Edition, Vol. 72 of World Scientific Lecture Notes in Physics, World Scientific Publishing Co., 2004, ISBN 981-238-070-1.

[138] A. Cooper-Sarkar and S. Sarkar, *Predictions for high energy neutrino cross-sections from the ZEUS global PDF fits*, JHEP 01 (2008) 75, arXiv:0710.5303[hep-ph].

[139] R. Gandhi, C. Quigg, M.H. Reno, and I. Sarcevic, *Neutrino Interactions at Ultrahigh Energies*, Phys. Rev. D 58 (1998) 093009, arxiv:hep-ph/9807264v1.

[140] E.L. Berger M.M. Block, D.W. McKay, and C. Tan, *Ultra-high energy neutrino scattering*, Phys. Rev. D 77 (2008) 053007, arXiv:0708.1960v2[hep-ph].

[141] A.M. Dziewonski and D.L. Anderson, *Preliminary reference Earth model*, Phys. Earth Planetary Interiors 25 (1981) 297.

[142] S.I. Klimushin, E.V. Bugaev, and I.A. Sokalski, *Precise parametrizations of muon energy losses in water*, in: Proceedings of the 27th Int. Cosmic Ray Conf. (ICRC2001), Hamburg, Germany, August 7–15, 2001, arXiv:hep-ph/0106010v1.

[143] L.D. Landau and I.J. Pomeranchuk, *The Limits of Applicability of the Theory of Bremsstrahlung by Electrons and of the Creation of Pairs at Large Energy*, Dokl. Akad. Nauk. SSSR 92 (1953) 535, English Reprint in *The Collected Papers of L.D. Landau*, Pergamon Press, 1965, p. 586.

[144] L.D. Landau and I.J. Pomeranchuk, *Electron-Cascade Processes at Ultra-High Energies*, Dokl. Akad. Nauk. SSSR 92 (1953) 735, English Reprint in *The Collected Papers of L.D. Landau*, Pergamon Press, 1965, p. 589.

[145] A.B. Migdal, *Bremsstrahlung and Pair Production in Condensed Media at High Energies*, Phys. Rev. 103 (1956) 1811.

[146] V.N. Baier and V.M. Katkov, *Concept of Formation Length in Radiation Theory*, Phys. Rep. 409 (2005) 261, arXiv:hep-ph/0309211v2.

[147] S.R. Klein, *Suppression of Bremsstrahlung and Pair Production due to Environmental Factors*, Rev. Mod. Phys. 71 (1999) 1501, arXiv:hep-ph/9802442v2.

[148] S. Bevan et al. (ACoRNE Coll.), *Simulation of Ultra High Energy Neutrino Interactions in Ice and Water*, Astropart. Phys. 28 (2007) 366, arXiv:0704.1025v1 [astro-ph].

[149] D. Heck et al., *CORSIKA: A Monte Carlo Code to Simulate Extensive Air Showers* , Report FZKA 6019, Forschungszentrum Karlsruhe, *http://www-ik.fzk.de/corsika/physics_description/corsika_phys.html* (1998).

[150] V. Niess and V. Bertin, *Underwater Acoustic Detection of Ultra High Energy Neutrinos*, Astropart. Phys. 26 (2006) 243, arXiv:astro-ph/0511617v3.

[151] P.L. Anthony et al., *An Accurate measurement of the Landau-Pomeranchuk-Migdal effect*, Phys. Rev. Lett. 75 (1995) 1949.

[152] S. Böser, *Acoustic detection of ultra-high energy cascades in ice*, Ph.D. thesis, Humboldt-Universität zu Berlin, *http://www-zeuthen.desy.de/~sboeser* (2006).

[153] G.A. Askariyan, B.A. Dolgoshein, A.N. Kalinovsky, and N.V. Mokhov, *Acoustic Detection of High Energy Particle Showers in Water*, Nucl. Inst. and Meth. 164 (1979) 267.

[154] J.G. Learned, *Acoustic Radiation by Charged Atomic Particles in Liquids: An Analysis*, Phys. Rev. D 19 (1979) 3293.

[155] L.D. Landau and E.M. Lifschitz, *Course of Theoretical Physics, Vol.6: Fluid Mechanics*, 2nd Edition, Pergamon Press, 1987.

[156] S. Bevan et al. (ACoRNE Coll.), *Study of the Acoustic Signature of UHE Neutrino Interactions in Water and Ice*, Nucl. Inst. and Meth. A 607 (2009) 398, arXiv:0903.0949v2 [astro-ph.IM].

[157] M.A. Ainslie and J.G. McColm, *A simplified formula for viscous and chemical absorption in sea water*, J. Acoust. Soc. Am. 103 (1998) 1671.

[158] L. Liebermann, *Sound Propagation in Chemically Active Media*, Phys. Rev. 76 (1949) 1520.

[159] L. Liebermann, *The Origin of Sound Absorption in Water and in Sea Water*, J. Acoust. Soc. Am. 20 (1948) 868.

[160] R.J. Urick, *Principles of Underwater Sound*, Peninsula publishing, 1983, ISBN 0-932146-62-7.

[161] R.E. Francois and G.R. Garrison, *Sound absorption based on ocean measurements: Part I: Pure water and magnesium sulfate contributions*, J. Acoust. Soc. Am. 72 (1982) 896.

[162] R.E. Francois and G.R. Garrison, *Sound absorption based on ocean measurements: Part II: Boric acid contribution and equation for total absorption*, J. Acoust. Soc. Am. 72 (1982) 1879.

[163] V. Niess, *Détection acoustique sous-marine de neutrinos de ultra haute énergie dans le cadre de l'experience ANTARES*, Ph.D. thesis, Université de la Méditerranée – Aix-Marseille II, http://tel.archives-ouvertes.fr/tel-00132273/ (annexe h) (2005).

[164] N.G. Lehtinen et al., *Sensitivity of an underwater acoustic array to ultra-high energy neutrinos*, Astropart. Phys. 17 (2002) 279, arXiv:astro-ph/0104033v1.

[165] A.V. Butkevich et al., *Prospects for radio-wave and acoustic detection of ultra- and superhigh-energy cosmic neutrinos (cross sections, signals, thresholds)*, Phys. Part. Nucl. 29 (1998) 266.

[166] J. Alvarez-Muñiz and E. Zas, *Cherenkov radio pulses from EeV neutrino interactions: the LPM effect*, Phys. Lett. B 411 (1997) 218, arXiv:astro-ph/9706064v1.

[167] J. Alvarez-Muñiz and E. Zas, *The LPM effect for EeV hadronic showers in ice: implications for radio detection of neutrinos*, Phys. Lett. B 434 (1998) 396, arXiv:astro-ph/9806098v1.

[168] J. Vandenbroucke, G. Gratta, and N. Lehtinen, *Experimental Study of Acoustic Ultra-High-Energy Neutrino Detection*, Astrophys. J. 621 (2005) 301, arXiv:astro-ph/0406105v2.

[169] The International Association for the Properties of Water and Steam (IAPWS), *Revised Release on the IAPWS Industrial Formulation 1997 for the Thermodynamic Properties of Water and Steam* (Aug. 2007), *Release on the IAPWS Formulation 2008 for the Thermodynamic Properties of Seawater* (Sept. 2008), *http://www.iapws.org/*.

[170] *Data from an INSU sea campaign at the ANTARES site Aug. 2007*, V. Bertin, private communication (Aug. 2009).

[171] *Data from an INSU sea campaign at the ANTARES site March 2010*, D. Lefèvre, private communication (Nov. 2010).

[172] National Oceanographic Data Center (USA), *World Ocean Atlas 2005*, *http://www.nodc.noaa.gov/OC5/WOA05/pr_woa05.html*.

[173] W.R. Leo, *Techniques for Nuclear and Particle Physics Experiments*, 2nd Edition, Springer-Verlag, 1994, ISBN 0-387-57280-5.

[174] F. Halzen, *Astroparticle Physics with High Energy Neutrinos: from AMANDA to IceCube*, Eur. Phys. J. C 46 (2006) 669, arxiv:astro-ph/0602132.

[175] T. Karg, *Detection of ultra high energy neutrinos with an unterwater very large volume array of acoustic sensors: A simulation study*, Ph.D. thesis, Univ. Erlangen-Nürnberg, FAU-PI4-DISS-06-002, arXiv:astro-ph/0608312v1 (2006).

[176] J. Perkin for the ACORNE Coll., *The sensitivity of km^3 hydrophone arrays to fluxes of ultra high energy neutrinos*, in: Proceedings of the 3rd International Workshop on Acoustic and Radio EeV Neutrino Detection Activities (ARENA 2008), Rome, Italy, June 25–27, Nucl. Inst. and Meth. A 604, 2009, p. 193.

[177] G.J. Feldman and R.D. Cousins, *A Unified Approach to the Classical Statistical Analysis of Small Signals*, Phys. Rev. D 57 (1998) 3873, arXiv:physics/9711021v2 [physics.data-an].

[178] D. Seckel, Internet, *ftp://ftp.bartol.udel.edu/../seckel/ess-gzk/*; "ESS model (2005)": file flux_n3_8_flat_om0p3.txt; "Proton model, Auger": file 2008/export_data/ss_135_a.txt; "Proton model, HiRes": file 2008/export_data/ss_135_h.txt; "Mixed comp model, HiRes": file 2008/export_data/ss_151_h.txt.

[179] N.G. Lehtinen, P.W. Gorham, A.R. Jacobson, and R.A. Roussel-Dupré, *FORTE satellite constraints on ultra-high energy cosmic particle fluxes*, Phys. Rev. D 69 (2004) 013008, arXiv:astro-ph/0309656v2.

[180] G. Manthei, J. Eisenblätter, and T. Spies, *Experience on acoustic wave propagation in rock salt in the frequency range 1–100 kHz and conclusions with respect to the feasibility of a rock salt dome as neutrino detector*, in: Proceedings of the 1st International Workshop on Acoustic and Radio EeV Neutrino detection Activities (ARENA 2005), Zeuthen, Germany, May 17–19, Int. J. Mod. Phys. A21S1, World Scientific, 2006, p. 30, ISBN 981-256-755-0.

[181] P.B. Price, *Attenuation of acoustic waves in glacial ice and salt domes*, J. of Geophys. Res 111 (2006) B02201, arXiv:astro-ph/0506648v1.

[182] R. Nahnhauer, A.A. Rostovtsev, and D. Tosi, *Permafrost – An Alternative Target Material for Ultra High Energy Neutrino Detection?*, Nucl. Inst. and Meth. A 587 (2008) 29, arXiv:0707.3757v1 [astro-ph].

[183] A. Roberts, *The birth of high-energy neutrino astronomy: A personal history of the DUMAND project*, Rev. Mod. Phys. 64 (1992) 259.

[184] L.G. Dedenko et al., *Sadco: Hydroacoustic Detection of Super-High Energy Cosmic Neutrinos*, arXiv:astro-ph/9705189v1 (1997).

[185] R. Nahnhauer, *Acoustic particle detection – from early ideas to future benefits*, in: Proceedings of the 4th International Workshop on Acoustic and Radio EeV Neutrino Detection Activities (ARENA 2010), Nantes, France, June 29–July 2, Nucl. Inst. and Meth. A, 2010, arXiv:1010.3082v2 [astro-ph.IM].

[186] M. Taiuti et al., *The NEMO project: A status report*, in: Proceedings of the 4th International Workshop on a Very Large Volume Neutrino Telescope for the Mediterranean Sea (VLVnT 2009), Athens, Greece, 13–15 Oct 2009, Nucl. Inst. and Meth. A 626–627, 2011, p. S25.

[187] T. Karg, for the IceCube Coll., *Status and recent results of the South Pole Acoustic Test Setup*, in: Proceedings of the 4th International Workshop on Acoustic and Radio EeV Neutrino Detection Activities (ARENA 2010), Nantes, France, June 29-July 2, Nucl. Inst. and Meth. A, 2010, arXiv:1010.2025v1 [astro-ph.IM].

[188] Y. Abdou et al. (IceCube Coll.), *Design and performance of the South Pole Acoustic Test Setup*, submitted to Nucl. Inst. and Meth. A, arXiv:1105.4339v1 [astro-ph.IM] (2011).

[189] R. Abbasi et al. (IceCube Coll.), *Measurement of sound speed vs. depth in South Pole ice for neutrino astronomy*, Astropart. Phys. 33 (2010) 277, arXiv:0909.2629v1 [astro-ph.IM].

[190] R. Abbasi et al. (IceCube Coll.), *Measurement of Acoustic Attenuation in South Pole Ice*, Astropart. Phys. 34 (2011) 382, arXiv:1004.1694v2 [astro-ph.IM].

[191] R. Abbasi et al. (IceCube Coll.), *Background studies for acoustic neutrino detection at the South Pole*, submitted to Astropart. Phys., arXiv:1103.1216v1 [astro-ph.IM] (2011).

[192] K. Antipin et al. (BAIKAL Coll.), *A prototype device for acoustic neutrino detection in Lake Baikal*, in: Proceedings of the 30th International Cosmic Ray Conference (ICRC2007), Merida, Mexico, July 3–11, 2007, arXiv:0710.3113 [astro-ph].

[193] V. Aynutdinov et al., *Acoustic Search for High-Energy neutrinos in the Lake Baikal: Results and Plans*, in: Proceedings of the 4th International Workshop on Acoustic and Radio EeV Neutrino Detection Activities (ARENA 2010), Nantes, France, June 29–July 2, Nucl. Inst. and Meth. A, 2010, doi:10.1016/j.nima.2010.11.153.

[194] V. Aynutdinov et al., *Acoustic search for high-energy neutrinos in Lake Baikal: status and perspectives*, in: Proceedings of the 31st Int. Cosmic Ray Conf. (ICRC2009), Lodz, Poland, July 7–15, 2009, arXiv:0910.0678v1 [astro-ph.HE].

[195] G. Riccobene for the NEMO Coll., *Long-term measurements of acoustic noise in very deep sea*, in: Proceedings of the 3rd International Workshop on Acoustic and Radio EeV Neutrino Detection Activities (ARENA 2008), Rome, Italy, June 25–27, Nucl. Inst. and Meth. A 604, 2009, p. 149.

[196] N. Kurahashi, J. Vandenbroucke, and G. Gratta, *Search for acoustic signals from ultra-high energy neutrinos in 1500 km^3 of sea water*, Phys. Rev. D 82 (2010) 073006, arXiv:1007.5517v1 [hep-ex].

[197] S. Bevan, *Data analysis techniques for UHE acoustic astronomy*, in: Proceedings of the 3rd International Workshop on Acoustic and Radio EeV Neutrino Detection Activities (ARENA 2008), Rome, Italy, June 25–27, Nucl. Inst. and Meth. A 604, 2009, p. 143.

[198] S. Danaher for the ACoRNE Coll. , *First Data from ACoRNE and Signal Processing Techniques*, in: Proceedings of the 2nd International Workshop on Acoustic and Radio EeV Neutrino detection Activities (ARENA 2006), Newcastle, UK, 28–30 June, Vol. 81 of J. Phys. Conf. Ser., IOP Publishing, Philadelphia, 2007, p. 012011.

[199] G.A. Askariyan, *Excess Negative Charge of an Electron-Photon Shower and its Coherent Radio Emission*, Sov. Phys. JETP 14 (1962) 441, Russian original: Zh. Éksp. Teor. Fiz. **41** (1961) 616.

[200] I. Kravchenko et al., *RICE Limits on the Diffuse Ultra-High Energy Neutrino Flux*, Phys. Rev. D 73 (2006) 082002, arXiv:astro-ph/0601148v1.

[201] I. Kravchenko et al., *Updated Neutrino Flux Limits from the RICE Experiment at the South Pole*, arXiv:1106.1164v1 [astro-ph.HE] (2011).

[202] P. Allison et al., *Design and Initial Performance of the Askaryan Radio Array Prototype EeV Neutrino Detector at the South Pole*, arXiv:1105.2854v1 [astro-ph.IM] (2011).

[203] A good overview of projects is given by the talks from the ARENA2010 workshop, *http://arena2010.in2p3.fr/* .

[204] R.D. Dagkesamanskii, A.R. Beresnyak, A.V. Kovalenko, and I.M. Zheleznykh, *The upper limit to the EHE neutrino flux from observations of the moon with Kalyazin radio telescope*, in: Proceedings of the 1st International Workshop on Acoustic and Radio EeV Neutrino detection Activities (ARENA 2005), Zeuthen, Germany, May 17–19, Vol. A21S1 of Int. J. Mod. Phys., World Scientific Publishing Co., 2006, p. 142.

[205] S. ter Veen et al., *A new limit on the Ultra-High-Energy Cosmic-Ray flux with the Westerbork Synthesis Radio Telescope*, Phys. Rev. D82 (2010) 103014, arXiv:1010.6061v1 [astro-ph.HE].

[206] J.D. Bray et al., *Status and Strategies of Current LUNASKA Lunar Cherenkov Observations with the Parkes Radio Telescope*, in: Proceedings of the 4th International Workshop on Acoustic and Radio EeV Neutrino Detection Activities (ARENA 2010), Nantes, France, June 29–July 2, Nucl. Inst. and Meth. A, 2010, arXiv:1010.1997v2 [astro-ph.HE].

[207] T.R. Jaeger, R.L. Mutel, and K.G. Gayley, *Project RESUN, a Radio EVLA Search for UHE Neutrinos*, Astropart. Phys. 34 (2010) 293.

[208] M. Mevius et al., *Detecting ultra high energy neutrinos with LOFAR*, in: Proceedings of the 4th International Workshop on Acoustic and Radio EeV Neutrino Detection Activities (ARENA 2010), Nantes, France, June 29–July 2, Nucl. Inst. and Meth. A, 2010, doi:10.1016/j.nima.2010.11.018.

[209] A. Connolly for the SalSA Collaboration, *SalSA Status*, in: Proceedings of the 4th International Workshop on Acoustic and Radio EeV Neutrino Detection Activities (ARENA 2010), Nantes, France, June 29–July 2, 2010, arXiv:1010.4347v1 [astro-ph.IM].

[210] R. Milincic for the HASRA Coll., *Results of the radio-detection experiment HASRA (Hawaii Askaryan in Salt Radio Array) and prospect for UHE neutrino detection in salt*, in: Proceedings of the 11th International Conference on Topics in Astroparticle and Underground Physics (TAUP 2009), Gran Sasso, Assergi, Italy, 1–5 July, J. Phys. Conf. Ser. 203, 2010, p. 012138.

[211] J. Abraham et al. (Pierre Auger Coll.), *Limit on the diffuse flux of ultrahigh energy tau neutrinos with the surface detector of the Pierre Auger Observatory*, Phys. Rev. D 79 (2009) 102001, arXiv:0903.3385 [astro-ph.HE].

[212] J. Tiffenberg for the Pierre Auger Coll., *Limits on the diffuse flux of ultra high energy neutrinos set using the Pierre Auger Observatory*, in: Proceedings of the 31st Int. Cosmic Ray Conf. (ICRC2009), Lodz, Poland, July 7–15, 2009.

[213] A. Haungs, *Radio Detection of Particles from the Cosmos*, in: Proceedings of the 3rd International Workshop on Acoustic and Radio EeV Neutrino Detection Activities (ARENA 2008), Rome, Italy, June 25–27, Nucl. Inst. and Meth. A 604, 2009, p. 236, arXiv:0811.2361v1 [astro-ph].

[214] H. Falcke and P. Gorham, *Detecting Radio Emission from Cosmic Ray Air Showers and Neutrinos with a Digital Radio Telescope*, Astropart. Phys. 19 (2003) 477, arXiv:astro-ph/0207226v1.

[215] G. Medina-Tanco et al. for the JEM-EUSO Coll., *JEM-EUSO Science Objectives*, in: Proceedings of the 31st Int. Cosmic Ray Conf. (ICRC2009), Lodz, Poland, July 7–15, 2009.

[216] G.A. Askariyan, *Hydrodynamic Radiation From the Tracks of Ionizing Particles in Stable Liquids*, Sov. J. At. En. 3 (1957) 921, Russian original: *At. Energ.* **3**, 152 (1957).

[217] L. Sulak et al., *Experimental studies of the acoustic signature of proton beams traversing fluid media*, Nucl. Inst. and Meth. 161 (1979) 203.

[218] S.D. Hunter et al., *Acoustic signals of nonthermal origin from high energy protons in water*, J. Acoust. Soc. Am. 69 (1981) 1557.

[219] S.D. Hunter, W.V. Jones, and D.J. Malbrough, *Nonthermal acoustic signals from absorption of a cylindrical laser beam in water*, J. Acoust. Soc. Am. 69 (6) (1981) 1563.

[220] V.I. Albul et al., *Measurements of the Parameters of the Acoustic Radiation Accompanying the Moderation of an Intense Proton Beam in Water*, Instr. Exp. Tech. 44 (2001) 327.

[221] G. Anton et al., *Study of piezo based sensors for acoustic particle detection*, Astropart. Phys. 26 (2006) 301.

[222] M. Ageron et al. (ANTARES Coll.), *Performance of the First ANTARES Detector Line*, Astropart. Phys. 31 (2009) 277, arXiv: 0812.2095 v1 [astro-ph].

[223] P. Amram et al. (ANTARES Coll.), *The ANTARES optical module*, Nucl. Inst. and Meth. A 484 (2002) 369.

[224] M. Ardid for the ANTARES Coll., *Positioning system of the ANTARES neutrino telescope*, in: Proceedings of the 3rd International Workshop on a Very Large Volume Neutrino Telescope for the Mediterranean Sea (VLVnT 2008), Toulon, France, April 22–24, Nucl. Inst. and Meth. A 602, 2009, p. 174.

[225] C. Richardt et al., *Reconstruction methods for acoustic particle detection in the deep sea using clusters of hydrophones*, Astropart. Phys. 31 (2009) 19, arXiv:0906.1718v1 [astro-ph.IM].

[226] K. Graf, *Experimental Studies within ANTARES towards Acoustic Detection of Ultra-High Energy Neutrinos in the Deep Sea*, Ph.D. thesis, Univ. Erlangen-Nürnberg, FAU-PI1-DISS-08-001 (2008).

[227] R.J. Urick, *Ambient Noise in the Sea*, Peninsula publishing, 1986, ISBN 0-932146-13-9.

[228] C.L. Naumann, *Development of sensors for the acoustic detection of ultra high energy neutrinos in the deep sea*, Ph.D. thesis, Univ. Erlangen-Nürnberg, FAU-PI4-DISS-07-002 (2007).

[229] J.A. Aguilar et al. (ANTARES Coll.), *The data acquisition system for the ANTARES neutrino telescope*, Nucl. Inst. and Meth. A 570 (2007) 107, arXiv:astro-ph/0610029v1.

[230] J.A. Aguilar et al. (ANTARES Coll.), *Performance of the front-end electronics of the ANTARES neutrino telescope*, Nucl. Inst. and Meth. A 622 (2010) 59, arXiv:1007.2549v2 [astro-ph.IM].

[231] I. Antcheva et al., *ROOT – A C++ framework for petabyte data storage, statistical analysis and visualization*, Comp. Phys. Comm. 180 (2009) 2499.

[232] M. Neff, *Studie zur akustischen Teilchendetektion im Rahmen des ANTARES-Experiments: Entwicklung und Integration von Datennahmesoftware*, Diploma thesis, Univ. Erlangen-Nürnberg, FAU-PI1-DIPL-07-003 (2007).

[233] S. Brehm, *Studien zur Positionsbestimmung der akustischen ANTARES-Stockwerke*, Diploma thesis, Univ. Erlangen-Nürnberg, ECAP-2008-022 (2009).

[234] G.M. Wenz, *Acoustic Ambient Noise in the Ocean: Spectra and Sources*, J. Acoust. Soc. Am. 34 (1962) 1936.

[235] V.O. Knudsen, R.S. Alford and J.W. Emling, *Underwater ambient noise*, J. Mar. Res. 3 (1948) 410.

[236] N. Kurahashi and G. Gratta, *Oceanic Ambient Noise as a Background to Acoustic Neutrino Detection*, Phys. Rev. D 78 (2008) 092001, arXiv:0712.1833v2 [physics.ao-ph].

[237] B. Bergmann, *Untersuchungen zum Tiefsee-Hintergrundrauschen am ANTARES-Standort*, Bachelor's thesis, Univ. Erlangen-Nürnberg, ECAP-2010-042 (2010).

[238] C. Richardt, *Acoustic particle detection – Direction and source location reconstruction techniques*, Ph.D. thesis, Univ. Erlangen-Nürnberg, ECAP-2010-046 (2010).

[239] N. Nosengo, *The neutrino and the whale*, Nature 462 (2009) 560, News Feature.

[240] H. Rietz, *Walgesang als Beifang*, published in the German newspaper "Die Zeit" on March 14th, *http://www.zeit.de/2011/11/N-Neutrinodetektoren* (2011).

[241] Web page of the LIDO (Listening to the Deep-Ocean Environment) project, *http://listentothedeep.org/*.

[242] T. Mitchell, *Machine Learning*, McGraw Hill, 1997, ISBN 0-07-042807-7.

[243] *Implementation of the Open Computer Vision Library*, *http://www.opencv.org* (Sept. 2010).

[244] A. Würstlein, *Development of a Software Framework for the ANTARES Acoustic Data and Simulations within the Framework*, Diploma thesis, Univ. Erlangen-Nürnberg, ECAP-2010-047 (2009).

[245] A.R. Bell, *The acceleration of cosmic rays in shock fronts – I*, Mon. Not. Roy. Astron. Soc. 182 (1978) 147.